

# Single-Phase and Boiling Flow in Microchannels with High Heat Flux

by

Elmer Galvis

A thesis

presented to the University of Waterloo

in fulfillment of the

thesis requirement for the degree of

Doctor of Philosophy

in

Mechanical Engineering

Waterloo, Ontario, Canada, 2012

© Elmer Galvis 2012

I hereby declare that I am the sole author of this thesis. This is a true copy of the thesis, including any required final revisions, as accepted by my examiners.

I understand that my thesis may be made electronically available to the public.

## Abstract

A cooling system for high heat flux applications is examined using microchannel evaporators with water as the working fluid and boiling as the heat transfer mechanism. Experimental studies are performed using single channel microevaporators allowing for better control of the flow mechanics unlike other investigations where multiple, parallel, flow channels can result in a non-uniform distribution of the working fluid. High-speed flow visualizations are performed in conjunction with heat transfer and pressure drop measurements to support the quantitative experimental data. Flow patterns associated with a range of boundary conditions are characterized and then presented in the form of novel flow regime maps that intrinsically reflect the physical mechanisms controlling two-phase pressure distributions and heat transfer behavior. Given the complexity associated with modeling of boiling heat transfer and the lack of a universal model that provides accurate predictions across a broad spectrum of flow conditions, flow regime maps serve as a valuable modeling aid to assist in targeted modeling over specific flow regimes. This work represents a novel and original contribution to the understanding of boiling mechanisms for water in microchannels.

The flow patterns in this work are found to be closely coupled with mass flux, heat flux, and channel size; where re-wetting and pressure oscillations play a crucial role, and are likely responsible for its development and evolution. Reversed flow, typically attributed to a non-uniform fluid distribution in multiple channel microevaporators by other researchers, is shown to be a result of the upstream expansion of confined bubbles. During flow boiling, the pressure drop in the microchannel increases with the heat flux for a constant flow rate due to the significant acceleration effects associated with smaller channels, unlike in single-phase flow where the pressure drop is constant. Water flow boiling in rectangular microchannels, although not extensively explored in the published literature, provides an extremely high cooling capacity, with dissipation rates approaching  $440\text{ W/cm}^2$ , making this an ideal candidate for cooling of next generation electronic systems.

Single-phase flow studies revealed that pressure and heat transfer coefficient macroscale models are transferable to microchannels with hydraulic diameters down to  $200\text{ }\mu\text{m}$ , when

the entrance effects and minor losses are properly considered. These studies include laminar developing flow conditions not commonly considered in the literature and fully developed flow. Since the applicability of macroscale theories to microchannels is often questioned, this investigation helps clarify this issue for microchannels within the range of experimental conditions explored in this work. Finally, new correlations for the hydrodynamic entrance length are proposed for rectangular microchannels and good agreement is found when compared with published experimental data over a wide range of Reynolds number. These correlations are more accurate, and original in the sense that they incorporate the effects of channel aspect ratio, and include creeping flow conditions which are currently unavailable for rectangular microchannels.

This work represents a major advance in the development of new cooling systems for high heat flux applications requiring dissipation rates in excess of  $100\text{ W/cm}^2$ .

## Acknowledgements

It is a pleasure to express my sincere gratitude to my supervisor Dr. Richard Culham for his guidance and support throughout the course of my research. The financial supports from Natural Sciences and Engineering Research Council of Canada (NSERC), Ontario Graduate Scholarship (OGS), and University of Waterloo are gratefully acknowledged. Also, sincere gratitude to the Microelectronics Heat Transfer Laboratory (MHTL) for providing research facilities during this project. I would like to thank the many members of the Mechanical and Mechatronics Engineering Department and staff whose assistance and encouragement helped through this journey. Finally, to my friend Bong Joo Lee, thank you very much for helping me with the proof-reading.

## **Dedication**

This thesis is dedicated to my parents Jaime Galvis and Rosa Amalia Luna. A special feeling of gratitude to my wife who has supported me throughout this journey.

# Table of Contents

List of Tables	xv
List of Figures	xxi
Nomenclature	xxvi
<b>1 Introduction</b>	<b>1</b>
1.1 Background . . . . .	1
1.2 Problem Statement . . . . .	5
1.3 Motivation . . . . .	7
1.4 Approach . . . . .	9
1.5 Outline . . . . .	10
<b>2 Fundamentals and Literature Review</b>	<b>12</b>
2.1 Fundamentals of boiling . . . . .	12
2.1.1 Macro flow boiling . . . . .	13
2.1.2 Micro flow boiling . . . . .	21
2.2 Single-phase liquid flow in microchannels . . . . .	22
2.2.1 Friction factor . . . . .	23

2.2.2	Heat transfer coefficient . . . . .	26
2.3	Boiling two-phase flow . . . . .	27
2.4	Flow boiling heat transfer correlations . . . . .	31
2.4.1	Kandlikar model . . . . .	33
2.4.2	Lee and Mudawar model . . . . .	33
2.4.3	Gungor and Winterton model . . . . .	34
2.4.4	Lee and Garimella model . . . . .	34
2.4.5	Schrock and Grossman model . . . . .	35
<b>3</b>	<b>Experimental Facility</b>	<b>36</b>
3.1	Experimental setup and procedures . . . . .	36
3.1.1	Test rig . . . . .	36
3.1.2	Microchannels . . . . .	43
3.2	Data reduction . . . . .	46
3.2.1	Single-phase flow . . . . .	46
3.2.2	Two-phase flow . . . . .	50
3.3	Uncertainty analysis . . . . .	55
<b>4</b>	<b>Single-Phase Flow and Heat Transfer</b>	<b>58</b>
4.1	Single-phase friction factor . . . . .	59
4.2	Single-phase heat transfer . . . . .	67
<b>5</b>	<b>Two-phase Flow Visualization</b>	<b>71</b>
5.1	Experimental Results . . . . .	71
5.2	Flow patterns . . . . .	73



5.3	Bubble size and bubbly frequency . . . . .	75
5.4	Flow reversal and intermittent flow patterns . . . . .	80
5.5	Pressure drop and channel wall temperature . . . . .	83
5.6	Flow regime maps . . . . .	89
5.7	Macro and micro flow regime maps comparison . . . . .	93
5.7.1	Macroscale flow regime maps . . . . .	93
5.7.2	Microscale flow regime maps . . . . .	95
<b>6</b>	<b>Experimental Heat Transfer Coefficient, <math>HTC</math></b>	<b>99</b>
6.1	Experimental Results . . . . .	99
6.2	Boiling curve . . . . .	101
6.3	Heat Transfer Coefficient, $HTC$ . . . . .	104
6.4	Comparison of the experimental $HTCs$ with published correlations . . . .	108
<b>7</b>	<b>Conclusions and Recommendations</b>	<b>116</b>
7.1	Single-phase flow and heat transfer . . . . .	117
7.1.1	Applicability of macroscale theory to mini and microchannels . . .	117
7.1.2	Entrance length in microchannels . . . . .	118
7.2	Boiling two-phase flow . . . . .	119
7.2.1	Two-phase flow visualizations . . . . .	120
7.2.2	Boiling heat transfer and thermal performance on microevaporators	121
7.2.3	Heat transfer coefficient models . . . . .	122
7.3	Recommendations . . . . .	123
	<b>Permissions</b>	<b>125</b>

<b>References</b>	<b>146</b>
<b>Appendices</b>	<b>147</b>
<b>A Uncertainty Analysis</b>	<b>148</b>
A.1 Method . . . . .	148
A.2 Uncertainty in Measured Values . . . . .	149
A.2.1 Temperature Measurements . . . . .	149
A.2.2 Heater Voltage . . . . .	150
A.2.3 Heater Current . . . . .	150
A.2.4 Pressure . . . . .	152
A.2.5 Properties . . . . .	154
A.2.6 Channel Dimensions . . . . .	155
A.2.7 Time . . . . .	155
A.3 Uncertainty in Calculated Quantities . . . . .	156
A.3.1 Mass flow, $\dot{m}$ . . . . .	156
A.3.2 Channel cross sectional area, $A$ . . . . .	157
A.3.3 Channel surface area, $A_s$ . . . . .	157
A.3.4 Channel perimeter, $P$ . . . . .	158
A.3.5 Hydraulic diameter, $d_h$ . . . . .	159
A.3.6 Mass flux, $G$ . . . . .	159
A.3.7 Reynolds number, $Re$ . . . . .	159
A.3.8 Heat flux, $q_w$ . . . . .	160
A.3.9 Heat transfer coefficient, $h$ . . . . .	162
A.3.10 Nusselt number, $Nu$ . . . . .	162

A.3.11 Friction factor, $f$ . . . . .	164
A.3.12 Vapor quality, $x$ . . . . .	165
<b>B Detailed Drawings of Microevaporator Assembly Unit</b>	<b>166</b>
<b>C Finite Element Models and Thermal Conductivity Measurements</b>	<b>177</b>
C.1 Finite Element Models, FEMs . . . . .	177
C.2 Thermal conductivity . . . . .	180
<b>D Channel Size Measurements</b>	<b>184</b>
<b>E Fluid Properties Correlations</b>	<b>187</b>
E.1 Thermal conductivity, $k$ ( $W/mK$ ) . . . . .	187
E.2 Specific heat, $c_p$ ( $J/kgK$ ) . . . . .	187
E.3 Density, $\rho$ ( $kg/m^3$ ) . . . . .	188
E.4 Dynamic viscosity, $\mu$ ( $Pa.s$ ) . . . . .	188
E.5 Saturation temperature, $T_{sat}$ ( $^{\circ}C$ ) . . . . .	188
E.6 Liquid, $h_f$ and vapor, $h_g$ enthalpy and latent heat of vaporization, $h_{fg}$ ( $kJ/kg$ )	190
<b>F Heat Loss Correlations for Microevaporators</b>	<b>193</b>
F.1 Microchannel . . . . .	194
F.2 Minichannel . . . . .	196
<b>G Experimental Data</b>	<b>198</b>
G.1 Single-phase friction factor for $198 \times 241 \mu m$ microchannel after pressure drop correction . . . . .	198
G.2 Average Nusselt numbers for $198 \times 241 \mu m$ microchannel (isothermal bound- ary condition) . . . . .	201

G.3	Vapor and liquid slug positions and lengths . . . . .	203
G.4	Bubble diameter . . . . .	210
G.5	Number of active cavities . . . . .	211
G.6	Two-phase flow pressure drop and channel wall temperature . . . . .	212
G.7	Heat transfer coefficient . . . . .	221

# List of Tables

2.1	Saturated flow boiling correlations . . . . .	32
3.1	Channel dimensions . . . . .	44
3.2	Uncertainties for experimental data (*includes precision and bias errors. The high uncertainty of $\approx 44\%$ is only for the two highest heat fluxes at each mass flux tested). . . . .	57
4.1	Correlations for dimensionless entrance length for mini and microchannels ( $100 \leq d_h \leq 500$ ; $0.5 \leq Re \leq 2000$ , Galvis et al. (2012)) . . . . .	66
5.1	Results for the positions and vapor slug lengths in the microchannel $198 \times 241 \mu m$ at 9 watts and $1 ml/min$ , (video capture rate 20000 <i>fps</i> ) . . . . .	77
5.2	Pressure drop in minichannel $378 \times 471 \mu m$ , mass flux $G \simeq 364 kg/m^2 s$ . . . . .	84
6.1	Results for thermal performance study (microchannel $198 \times 241 \mu m$ ) . . . . .	100
6.2	Results for experimental and predicted <i>HTCs</i> ( $198 \times 241 \mu m$ microchannel) . . . . .	110
6.3	Results for experimental and predicted <i>HTCs</i> ( $378 \times 471 \mu m$ minichannel) . . . . .	111
6.4	<i>MAEs</i> in the prediction of <i>HTCs</i> after sub-cooling correction . . . . .	113
C.1	Thermal conductivity measurement . . . . .	183
E.1	Saturation temperature vs pressure (Babcock and Wilcox, 1992) . . . . .	189

E.2	Enthalpy and latent heat vs temperature (Babcock and Wilcox, 1992) . . .	191
G.1	Results for single-phase friction factor . . . . .	199
G.2	Results for Nusselt number for single-phase ( $Re = 198$ , $Pr = 3.8$ ) . . . . .	202
G.3	Slug position microchannel $198 \times 241 \mu m$ (10 watts, 1 $ml/min$ , video capture 20000 $fps$ ) . . . . .	203
G.4	Slug position microchannel $198 \times 241 \mu m$ (15 watts, 1 $ml/min$ , video capture 20000 $fps$ ) . . . . .	204
G.5	Slug position microchannel $198 \times 241 \mu m$ (22.5 watts, 1 $ml/min$ , video capture 20000 $fps$ ) . . . . .	204
G.6	Slug position microchannel $198 \times 241 \mu m$ (11 watts, 2 $ml/min$ , video capture 20000 $fps$ , vapor slug #1) . . . . .	205
G.7	Slug position microchannel $198 \times 241 \mu m$ (11 watts, 2 $ml/min$ , video capture 20000 $fps$ , vapor slug #2) . . . . .	206
G.8	Slug position microchannel $198 \times 241 \mu m$ (11 watts, 2 $ml/min$ , video capture 20000 $fps$ , vapor slug #3) . . . . .	207
G.9	Slug position microchannel $198 \times 241 \mu m$ (11 watts, 2 $ml/min$ , video capture 20000 $fps$ , vapor slug #4) . . . . .	208
G.10	Slug position microchannel $198 \times 241 \mu m$ (12 watts, 2 $ml/min$ , video capture 20000 $fps$ ) . . . . .	209
G.11	Bubble diameter microchannel $198 \times 241 \mu m$ . . . . .	210
G.12	Active cavities microchannel $198 \times 241 \mu m$ . . . . .	211
G.13	Pressure drop microchannel $198 \times 241 \mu m$ , mass flux $G \simeq 340 \text{ kg}/m^2s$ . . .	212
G.14	Pressure drop microchannel $198 \times 241 \mu m$ , mass flux $G \simeq 680 \text{ kg}/m^2s$ . . .	213
G.15	Pressure drop microchannel $198 \times 241 \mu m$ , mass flux $G \simeq 1024 \text{ kg}/m^2s$ . .	214
G.16	Pressure drop microchannel $198 \times 241 \mu m$ , mass flux $G \simeq 1296 \text{ kg}/m^2s$ . .	215

G.17 Pressure drop minichannel $378 \times 471 \mu m$ , mass flux $G \simeq 730 \text{ kg/m}^2 s$ . . .	216
G.18 Pressure drop minichannel $378 \times 471 \mu m$ , mass flux $G \simeq 1097 \text{ kg/m}^2 s$ . . .	218
G.19 Pressure drop minichannel $378 \times 471 \mu m$ , mass flux $G \simeq 1373 \text{ kg/m}^2 s$ . . .	220
G.20 HTC microchannel $198 \times 241 \mu m$ . . . . .	222
G.21 HTC minichannel $378 \times 471 \mu m$ . . . . .	223

# List of Figures

1.1	Typical thermal resistances for various coolants and heat transfer mechanisms (Kraus and Bar-Cohen, 1995). Reprinted with the permission of John Wiley and Sons . . . . .	3
1.2	Cooling system problem statement flow diagram . . . . .	6
2.1	Flow and heat transfer regimes in a uniformly heated horizontal tube with moderate heat flux (Ghiaasiann, 2008). Reprinted with the permission of Cambridge University Press . . . . .	14
2.2	Flow regime map for gas-liquid flow in horizontal pipes (Mandhane et al., 1974). Reprinted with the permission of Cambridge University Press . . . .	18
2.3	Typical flow boiling curve at low quality conditions and transition of flow through regimes of sub-cooled boiling. Adapted from Ghiaasiann (2008) and Carey (2008) . . . . .	19
2.4	Major flow boiling regimes in small passages. Adapted from (Cornwell and Kew, 1992) . . . . .	21
2.5	Comparison of normalized Poiseuille number $C^* = (Po)_{experimental}/(Po)_{theory}$ vs Reynolds number: ( $\circ$ ), ( $\bullet$ ) circular micro-tubes, ( $\nabla$ ) trapezoidal microchannels, ( $\square$ ) rectangular microchannels (Sharp et al., 2006) . . . . .	24
2.6	Apparent friction factor, $f$ , as a function of $Re$ for smooth and rough-wall conditions (Natrajan and Christensen, 2010b) . . . . .	25



3.1	(a): main components and fluid flow direction, (b): microevaporator assembly unit, (c): sight glass section view . . . . .	37
3.2	Photograph of the experimental facility . . . . .	38
3.3	(a),(b): microevaporator assembly unit, (c) mini and microevaporator, (d) wiring board . . . . .	39
3.4	Schematic thermocouple locations in evaporator and heater block (dimensions are shown in Appendix C, Figure C.2) . . . . .	42
3.5	Microchannel design and manufacturing process . . . . .	43
3.6	Channel width measurement techniques, top: with surface roughness profile, bottom: with electronic microscope . . . . .	45
3.7	Schematic representation for pressure drop measurements in microevaporator (location of inlet pressure sensor shown in Appendix B, Figure B.3) . . . . .	46
3.8	Control volume and boundary conditions for the channel . . . . .	48
3.9	Heat removed by fluid for $378 \times 471 \mu m$ microevaporator at $G = 1373 kg/m^2s$ . . . . .	51
3.10	Measurement of the gradient of temperature in microevaporator and heater block . . . . .	52
3.11	Test rig for thermal conductivity measurements . . . . .	54
4.1	Experimental friction factor for single-phase adiabatic and diabatic rectangular channel with $d_h \approx 200 \mu m$ . . . . .	59
4.2	Experimental friction factor with and without minor losses correction . . . . .	60
4.3	Comparison of experimental friction factor with traditional correlations for macrochannels . . . . .	61
4.4	Computational model . . . . .	62
4.5	Streamwise normalized velocity profiles from simulations for microchannel ( $a = b = 100 \mu m$ , $Re = 50$ ) . . . . .	63

4.6	Centerline velocity ratio vs. dimensionless position for microchannel $a = b = 100 \mu m$ , $0.5 \leq Re \leq 200$ . . . . .	64
4.7	Normalized entrance length $L_e/d_h$ from experimental data reported by Ahmad and Hassan (2006) and from numerical simulation by Galvis et al. (2012) at $b/a = 1$ . . . . .	65
4.8	Experimental and theoretical average Nusselt number vs Reynolds number for rectangular channel ( $d_h = 217 \mu m$ , $b/a = 0.822$ ) . . . . .	68
4.9	Experimental results for the average Nusselt number for developing flow conditions vs Graetz number . . . . .	69
5.1	Flow patterns: left: actual image, right: enhanced with Matlab image processing tool, vapor quality estimated from Equation 3.20, (a): bubbly flow $x \approx 0$ , (b): slug flow $x = 0.12$ , (c): churn flow $x = 0.19$ , (d): annular flow $x = 0.24$ , (e): wavy annular flow $x = 0.31$ , (f): inverted annular flow $x = 0.47$ 73	
5.2	Sketch for a vapor slug growth . . . . .	76
5.3	Typical meniscus position for vapor and liquid slugs (11 watts, volumetric flow rate $2 \text{ ml/min}$ , channel $198 \times 241 \mu m$ ) . . . . .	79
5.4	Vapor slug growth at different heat fluxes (volumetric flow rate $1 \text{ ml/min}$ , channel $198 \times 241 \mu m$ ) . . . . .	79
5.5	Reverse flow, $378 \times 471 \mu m$ , $G = 365 \text{ kg/m}^2\text{s}$ , $q = 546 \text{ kW/m}^2$ : (a): bubbly flow, (b): bubble on the left starts to grow, (c) to (f): bubble is confined by the channel wall and the expansion upstream causes flow reversal. . . . .	81
5.6	Meniscus displacement: (a)-(c): bubbly expansion and tail meniscus displacement against flow direction, (d)(f): pressure gradient in the channel overcomes evaporating momentum and tension forces and moves the tail meniscus towards the outlet. . . . .	81

5.7	Intermittent flow, $378 \times 471 \mu m$ , $G = 1373 kg/m^2s$ , $q = 3146 kW/m^2$ : (a): bubbly flow, (b): churn flow, (c): annular flow, (d): Localized dry out condition, (e): re-wetting of the channel, (f): wavy annular flow, (g): bubbly flow. . . . .	82
5.8	Results for pressure drop and channel wall temperature for microchannel $198 \times 241 \mu m$ at constant mass flux $G \simeq 340 kg/m^2s$ . . . . .	86
5.9	Pressure drop for two different channel sizes as a function of the heat flux for a constant mass flux $G \approx 1300 kg/m^2s$ . . . . .	87
5.10	Pressure drop oscillations for $378 \times 471 \mu m$ minichannel . . . . .	88
5.11	Summary of boiling flow patterns in a $198 \times 241 \mu m$ microchannel. <i>SP</i> : single-phase, <i>S</i> : slug flow, <i>S – A</i> : slug and annular flow, <i>I</i> : inverted annular flow . . . . .	89
5.12	Flow regime map for $198 \times 241 \mu m$ microchannel. <i>S</i> : slug flow, <i>S – A</i> : slug and annular flow, <i>I</i> : inverted annular flow . . . . .	91
5.13	Flow regime map for $378 \times 471 \mu m$ minichannel. <i>B</i> : bubbly flow, <i>B – S</i> : bubbly-slug flow, <i>S</i> : slug, <i>A</i> : annular flow, <i>INT</i> : intermittent flow . . . . .	92
5.14	Comparison between present flow regime map ( $198 \times 241 \mu m$ microchannel) and the experimental transition lines of Mandhane et al. (1974) . . . . .	94
5.15	Comparison between present flow regime map ( $198 \times 241 \mu m$ microchannel) and transitions lines predicted by Taitel and Dukler (1976) . . . . .	94
5.16	Comparison between flow regime maps: Present flow regime map ( $198 \times$ $241 \mu m$ microchannel) and pipe ( $D = 0.509 mm$ ) by Revellin and Thome (2007b) . . . . .	95
5.17	Comparison between flow regime maps: Present flow regime map ( $198 \times$ $241 \mu m$ microchannel) and minichannel ( $250 \times 400 \mu m$ ) by Harirchian and Garimella (2009b) . . . . .	96

5.18	Comparison between flow regime maps: Present flow regime map ( $198 \times 241 \mu m$ microchannel) and microchannel ( $119 \times 173 \mu m$ ) by Singh et al. (2009)	97
6.1	Boiling curves for microevaporator $198 \times 241 \mu m$ microchannel . . . . .	102
6.2	Boiling curves for minievaporator $378 \times 471 \mu m$ minichannel . . . . .	102
6.3	Average $HTC$ vs vapor quality $198 \times 241 \mu m$ microchannel . . . . .	104
6.4	Average $HTC$ vs vapor quality $378 \times 471 \mu m$ minichannel . . . . .	104
6.5	$HTC$ vs heat flux $198 \times 241 \mu m$ microchannel . . . . .	105
6.6	$HTC$ vs heat flux $378 \times 471 \mu m$ minichannel . . . . .	105
6.7	Microevaporators thermal performance curves at $G \simeq 1300 kg/m^2s$ . . . . .	107
6.8	Microevaporators thermal performance curves at $G \simeq 350 kg/m^2s$ . . . . .	107
6.9	Comparison of saturated flow boiling $HTCs$ ( $198 \times 241 \mu m$ microchannel)	112
6.10	Comparison of saturated flow boiling $HTCs$ ( $378 \times 471 \mu m$ minichannel) .	112
6.11	Estimation of heat flux due to sub-cooling using the boiling curve . . . . .	113
6.12	Comparison of saturated flow boiling $HTCs$ after sub-cooling correction ( $198 \times 241 \mu m$ microchannel) . . . . .	114
A.1	Shunt resistance linear fit . . . . .	151
B.1	Microevaporator assembly unit - side views . . . . .	167
B.2	Microevaporator assembly unit - isometric and exploded views . . . . .	168
B.3	Cover plate . . . . .	169
B.4	Side insulation . . . . .	170
B.5	Side insulation-internal . . . . .	171
B.6	Microevaporator single straight channel . . . . .	172
B.7	Heater block . . . . .	173

B.8	Lateral gasket . . . . .	174
B.9	Lateral insulation . . . . .	175
B.10	Bottom insulation . . . . .	176
C.1	FEM for thermocouple locations at isothermal planes in oxygen free copper sample . . . . .	178
C.2	FEM for thermocouple locations at isothermal planes in heater block and microevaporator . . . . .	179
C.3	Heat, sample temperature and conductivity vs time (case 70 °C) . . . . .	181
C.4	Gradient of temperature in sample and calibrated blocks (case 90 °C) . . .	182
D.1	Dimension in microchannel . . . . .	185
D.2	Dimension in minichannel . . . . .	186
F.1	Heat losses vs channel wall temperature, 1 ml/min ( $G \approx 350 \text{ kg/m}^2\text{s}$ ) . . .	194
F.2	Heat losses vs channel wall temperature, 2 ml/min ( $G \approx 700 \text{ kg/m}^2\text{s}$ ) . . .	194
F.3	Heat losses vs channel wall temperature, 3 ml/min ( $G \approx 1050 \text{ kg/m}^2\text{s}$ ) . .	195
F.4	Heat losses vs channel wall temperature, 3.8 ml/min ( $G \approx 1300 \text{ kg/m}^2\text{s}$ ) .	195
F.5	Heat losses vs channel wall temperature, 4 ml/min ( $G \approx 350 \text{ kg/m}^2\text{s}$ ) . . .	196
F.6	Heat losses vs channel wall temperature, 8 ml/min ( $G \approx 700 \text{ kg/m}^2\text{s}$ ) . . .	196
F.7	Heat losses vs channel wall temperature, 12 ml/min ( $G \approx 1050 \text{ kg/m}^2\text{s}$ ) . .	197
F.8	Heat losses vs channel wall temperature, 15 ml/min ( $G \approx 1300 \text{ kg/m}^2\text{s}$ ) . .	197

# Nomenclature

$A$	: channel cross sectional area, ( $m^2$ )
$A_h$	: header cross sectional area, ( $m^2$ )
$A_s$	: heated transfer surface area, ( $m^2$ )
$a$	: channel width, ( $m$ )
$Bo$	: Boiling number $\equiv q/Gh_{fg}$
$b$	: channel height, ( $m$ )
$c_p$	: specific heat capacity, ( $J/kgK$ )
$d_h$	: hydraulic diameter $\equiv 4A/P$ , ( $m$ )
$d_s$	: smallest channel dimension, ( $\mu m$ )
$f$	: friction factor coefficient $\equiv d_h\Delta p/2L\rho u^2$
$G$	: mass flux, ( $kg/m^2s$ )
$G_z$	: Graetz number $\equiv (d_h/x)RePr$
$h$	: local heat transfer coefficient, ( $W/m^2K$ ); specific enthalpy, ( $J/kg$ )
$h_{fg}$	: latent heat of evaporation, ( $J/kg$ )
$I$	: electrical current, ( $A$ )

$j_f$	: liquid superficial velocity, ( $m/s$ )
$j_g$	: gas superficial velocity, ( $m/s$ )
$K$	: Hagenbach's factor
$K_b$	: loss coefficient for bends
$K_c$	: loss coefficient for contraction
$K_e$	: loss coefficient for expansion
$k$	: thermal conductivity, ( $W/mK$ )
$L$	: channel length, ( $m$ )
$L_e$	: entrance length, ( $m$ )
$n$	: number of data
$P$	: channel wetted perimeter, ( $m$ )
$Q$	: heat flow rate, ( $W$ )
$q$	: heat flux, ( $W/m^2$ )
$R$	: electrical resistance, ( $Ohm$ ); thermal resistance, ( $K/W$ )
$R_a$	: surface roughness, ( $\mu m$ )
$Re$	: Reynolds number $\equiv ud_h/\nu$
$T$	: temperature, ( $K$ )
$U_o$	: inlet velocity, ( $m/s$ )
$u$	: velocity component in x-direction, ( $m/s$ )
$V_{shunt}$	: shunt voltage, ( $V$ )
$v$	: velocity component in y-direction, ( $m/s$ )

$We$  : Weber number  $\equiv \rho u^2 d_h / \sigma$   
 $w$  : velocity component in z-direction,  $(m/s)$   
 $X$  : Martinelli parameter  
 $x$  : vapor quality; channel axial distance from the inlet,  $m$   
 $x, y, z$  : Cartesian coordinates

### Greek Symbols

$\alpha$  : channel aspect ratio  $\equiv b/a$   
 $\Delta p$  : pressure drop,  $(Pa)$   
 $\Delta T_{\ell n}$  : log mean temperature difference,  $(K)$   
 $\mu$  : dynamic viscosity,  $(Pa \cdot s)$   
 $\nu$  : kinematic viscosity  $\equiv \mu/\rho$ ,  $(m^2/s)$   
 $\rho$  : density,  $(kg/m^3)$   
 $\sigma$  : standard deviation

### Other Symbols

$\dot{m}$  : mass flow,  $(kg/s)$   
 $\bar{h}$  : average heat transfer coefficient,  $(W/m^2K)$   
 $\overline{Nu}$  : average Nusselt number  $\equiv \bar{h}d_h/k_f$   
 $\Re$  : shunt electrical thermal resistance,  $(Ohm)$



## Subscripts

$a$	: ambient
$app$	: apparent
$avg$	: average
$c$	: centerline, channel
$cb$	: convective boiling
$corr$	: corrected
$exp$	: experimental
$FD$	: fully developed
$f$	: fluid
$in$	: inlet
$j$	: junction
$l$	: liquid
$max$	: maximum
$min$	: minor
$nb$	: nucleate boiling
$opt$	: optimum
$out$	: outlet
$sat$	: saturation
$sub$	: sub-cooled
$tp$	: two-phase

$v$  : vapor

$w$  : wall

## Acronyms

$A$  : Annular flow

$B$  : Bubbly flow

$CHF$  : Critical Heat Flux

$HTC$  : Heat Transfer Coefficient

$I$  : Inverted flow

$IB$  : Incipient Boiling

$INT$  : Intermittent flow

$MAE$  : Mean Average Error

$MFB$  : Minimum Film Boiling

$MHE$  : Micro Heat Exchanger

$ONB$  : Onset of Nucleate Boiling

$OSV$  : Onset of Significant Void

$PIV$  : Particle Image Velocity

$S$  : Slug flow

$SP$  : Single-Phase

$TDP$  : Thermal Design Power, ( $W$ )

# Chapter 1

## Introduction

In this chapter, the rapid increases of the heat flux in electronics applications is discussed in addition to some of the most promising heat transfer solutions for high heat flux applications. Although, there is not a generalized criterion for the transition from macro to microscale, the criterion adopted in this thesis is also presented. Finally, this chapter contains the problem statement, motivation, approach, and outline of this thesis.

### 1.1 Background

Over the past few years many people in the electronics industry have become concerned with the increase in heat density at both the chip and package module level. The microelectronics and power electronics industries are now facing the challenge of removing very high heat fluxes of  $100\text{ W/cm}^2$  and this number keeps rising and might reach  $300\text{ W/cm}^2$  in the next few years (Agostini et al., 2007; Ali, 2010). While conventional cooling solutions have been adequate to meet heat dissipation requirements until recently, no straightforward extension is possible for such high heat fluxes. Many system architects are hoping for a technology advancement that will help alleviate their current heat flux concerns. The heat dissipation of current and future microprocessors has reached values where new cooling systems are required to satisfy the high heat flux demand. Even with the incorporation of

heat transfer enhancements, e.g. thermal interface materials or heat spreaders, the power dissipation in integrated circuits and other electronics equipment has reached a threshold where air-cooling technologies can no longer be relied upon to effectively maintain reliable operating conditions, and liquid cooling systems must be used.

Traditionally, microelectronic designers have increased chip performance by adding more transistors onto the surface of the chip. Unfortunately, with this practise, more heat is generated by the chip. Also, the surface temperature of high heat dissipating microchips has to be maintained below 80 to 85 °C in order to ensure the effective and reliable operation of the electronic circuitry. Cooling systems for integrated circuits are constrained by both operating temperature and heat flux, making the design of effective, reliable solutions even more challenging.

The heat flow path in a microprocessor can be represented as a thermal network consisting of a combination of thermal resistances ( $R$ ), represented as a temperature difference divided by the heat dissipation or Thermal Design Power ( $TDP$ <sup>1</sup>)

$$R = \frac{T_j - T_a}{TDP} \quad (1.1)$$

For a given ambient temperature  $T_a$  and chip safe operating junction temperature  $T_j$ , the  $TDP$  can be increased by reducing the overall thermal resistance, which can be achieved by improving the cooling system (i.e. improving thermal attach technologies, using different coolants or heat transfer mechanisms, among others).

---

<sup>1</sup>The  $TDP$ , also referred to as the thermal guideline, is the maximum amount of heat that a component must dissipate to allow the processor to operate at safe/reliable operating conditions.

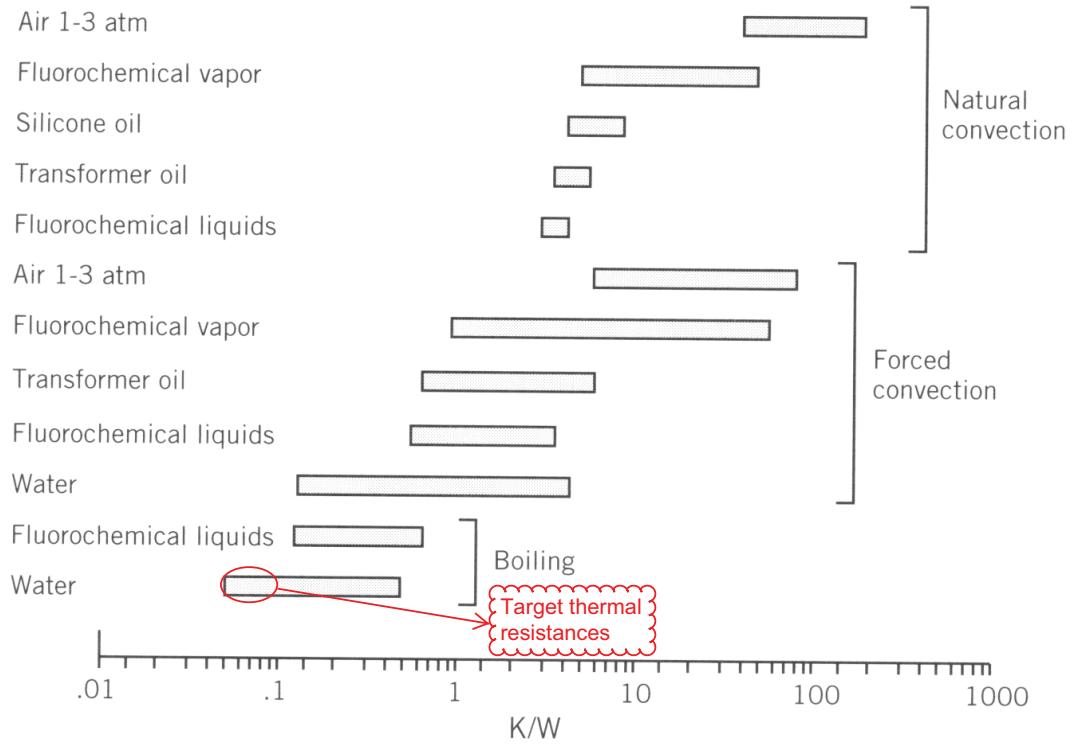


Figure 1.1: Typical thermal resistances for various coolants and heat transfer mechanisms (Kraus and Bar-Cohen, 1995). Reprinted with the permission of John Wiley and Sons

The thermal resistances for a variety of working fluids and heat transfer mechanisms are shown in Figure 1.1. Values of thermal resistance are seen to decrease from a nominal  $100\text{ K/W}$  for natural convection in air, to  $30\text{ K/W}$  for forced convection in air, to  $0.8\text{ K/W}$  in water liquid forced convection, and less than  $0.2\text{ K/W}$  for boiling with water. As a reference, a microprocessor with a typical die size surface area of  $2.25\text{ cm}^2$  and a heat dissipation of  $300\text{ W/cm}^2$  could reach a thermal resistance of  $R \simeq 0.09\text{ K/W}$  (assuming a differential temperature  $T_j - T_a = 85 - 24 = 61\text{ }^\circ\text{C}$ ). This value of thermal resistance or lower can be attained by a cooling system using water as the working fluid and boiling as the heat transfer mechanism. From Figure 1.1, clearly boiling of fluorochemical liquids or water can achieve lower thermal resistance than other heat transfer mechanisms such as forced or natural convection. In particular, the thermal resistance follows a globally decreasing trend with increasing heat flux and decreasing hydraulic diameter. Therefore, boiling of water seems to be a promising heat transfer mechanism to be used to solve the

challenge of cooling the next generation of high heat flux computer chips.

Some liquid cooling techniques are already in production or at a research stage, circulating liquid through separate cooling modules attached to the integrated circuits, or through microchannels fabricated onto the back of chips using high-temperature bonding techniques. Enhanced heat transfer capability using microchannels has been demonstrated in the literature in both single and two-phase flow as compared to their macro counterparts. Therefore the combination between microchannels, boiling as heat transfer mechanism, and water as the working fluid is very promising for the development of cooling systems for high heat flux applications.

There is no generalized criterion in the literature to define a threshold for transition from macro to a microscale channel, but for the purpose of this research, the criterion suggested by Kandlikar et al. (2006a) is adopted.

- Conventional channels:  $d_s > 3\text{ mm}$
- Minichannels:  $3\text{ mm} \geq d_s > 200\text{ }\mu\text{m}$
- Microchannels:  $200\text{ }\mu\text{m} \geq d_s > 10\text{ }\mu\text{m}$

$d_s$ : smallest channel dimension

Although, boiling in microchannels seems to be an attractive solution, it has been somewhat limited because of flow boiling instability. Also, it is difficult to have low boiling temperatures in the evaporator using water as the coolant, unless the cooling system is operated at sub-atmospheric pressures. The flow boiling approach has several potential advantages over competing technologies, such as providing nearly uniform chip base temperature, cooling of hot spots, higher heat transfer coefficient, and minimizing energy consumption. Even though flow boiling has these advantages, some operational challenges need to be addressed like the need for low pressure water or a suitable refrigerant to match the saturation temperature with the range of operating temperatures found in electronic systems, unstable operation, higher junction temperatures after critical heat flux, and

the lack of fundamental understanding of the flow boiling phenomenon in microchannel passages.

In spite of intensive research activity in recent years, many issues related to the heat transfer characteristics in small geometries still need to be clarified. It appears that boiling heat transfer, pressure drop and flow patterns in microchannels cannot be properly predicted by the existing macroscale theories. This is commonly explained by the fact that the physical mechanisms that are potentially dominant in microchannels are less important in macrochannels e.g. inertial and/or capillary forces are dominant compared with gravitational forces.

Although there are extensive applications of flow-boiling in refrigeration, air conditioning, and cooling of electronics among others, there is still a need for improved understanding of the two-phase flow involving boiling and condensing of working fluids in microchannels.

## 1.2 Problem Statement

Miniaturization of electronics, motivated by new and exciting application areas and modern fabrication techniques, has led to increases in chip power and high packaging densities. Although, most chip manufacturers have implemented design alternatives to increase chip performance, the ability to dissipate heat remains the principal impediment to future performance enhancements. Therefore, effective solutions are required that control the production of heat, which seems unlikely unless a technology breakthrough occurs (i.e. bipolar to CMOS technology) or more effective methods of cooling are developed that liberate excess heat, thereby controlling integrated circuit temperatures.

Alternative techniques, such as Core technology or other novel techniques are expected to increase chip performance. However, they are currently limited by the available cooling technologies. Therefore, new novel cooling technologies are required to allow for advances in chip performance. Figure 1.2 summarizes the cooling system problem flow diagram. In order to increase chip capacity, several techniques are used (more transistors, parallel

processing or long term solutions). Unfortunately, many of these performance enhancements result in excessive heat generation that cannot be controlled by present day cooling solutions. Therefore, new cooling strategies are required.

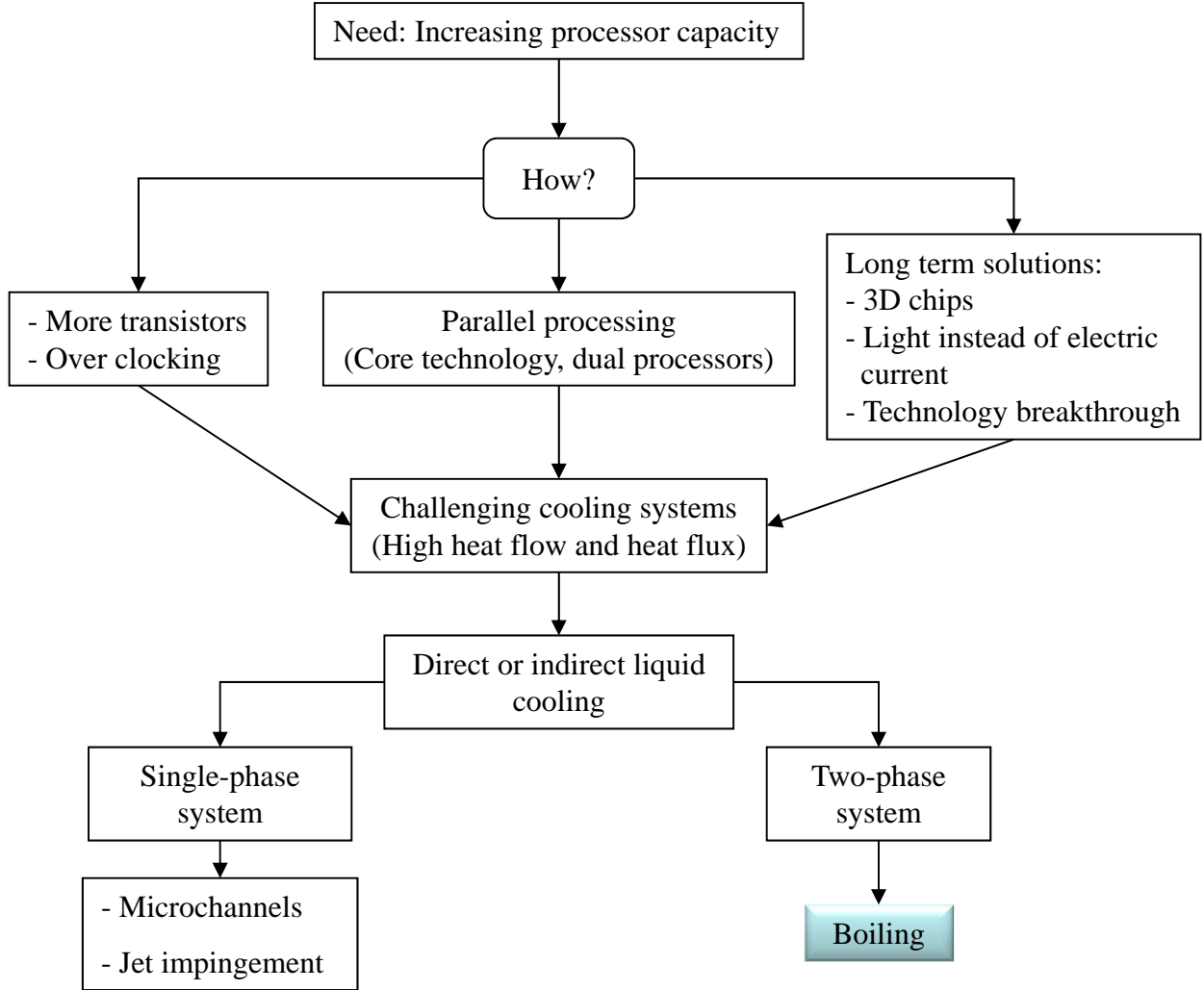


Figure 1.2: Cooling system problem statement flow diagram

Boiling is one of the most promising heat transfer mechanisms for electronics cooling but the understanding of the boiling process mechanisms in microchannels is still a challenge for the future development of two-phase cooling systems. An understanding of heat transfer mechanisms associated with microchannels boiling is not well understood, and this uncertainty is further complicated in microchannels where capillarity forces, and



experimental accuracy, among others factors are more crucial.

Two-phase flow mixtures can form a variety of flow patterns. The behavior of a vapor-liquid mixture including many of the constitutive relations that are needed for the solution of two-phase conservation equations depends strongly on the flow patterns. Although, simplified models can be obtained from the mass, momentum and energy equations ignoring the details of the flow patterns in the channel, knowing the flow patterns allows more suitable assumptions to be applied for each particular flow pattern, leading to more accurate models. Therefore, methods for predicting the occurrence of the major two-phase flow patterns are thus useful, and also required for more accurate modeling and analysis of two-phase flow systems.

Current methods for predicting the flow patterns are far from perfect. The difficulty and challenges arise out of the extremely varied morphological configurations that a vapor-liquid mixture can acquire, and these are affected by numerous parameters. Knowledge of dominant two-phase flow patterns in mini or microchannels is a key factor in developing accurate and physically sound predictive tools for designing cooling systems. Unfortunately, interfacial interactions between the vapor and liquid phases during flow boiling are often far too complex to permit accurate quantitative assessment of flow patterns.

Some attributes of two-phase flow in microchannels are not fully understood, and there are inconsistencies among experimental observations, phenomenological interpretation, and theoretical models. Therefore, experimental observations of the two-phase flow boiling are required in order to better understand the two-phase flow mechanisms. These observations may provide improved information that can lead to more accurate analytical and empirical models, and better cooling system designs that can be used for dissipating the heat demand of current and future electronics.

## 1.3 Motivation

The capacity of integrated circuits is traditionally increased by adding more transistors on the surface of the chip. The number of transistor on integrated circuits double ap-

proximately every two years according to Moore's law. However, the 2010 update to the International Technology Roadmap for Semiconductors suggests that for the first time in more than half a century, this trend will begin to slow near the end of 2013, after which time transistor counts and densities are to double only every 3 years. This drastic change from Moore's law is an indication of the limitation on the heat dissipation capacity of current cooling systems.

Natural, and forced air convection cooling systems are no longer satisfactory solutions for the current high heat flux applications, and even liquid cooling technologies are lagging behind. Therefore, new cooling systems are required for current and future high heat flux applications.

In this thesis, a potential cooling system is experimentally studied to satisfy the high heat flux demand for future applications. A successful novel cooling system will allow chip manufacturers to produce more powerful integrated circuits. The study is performed in microchannels because these systems are capable of rejecting large heat loads while being relatively small in size. In this thesis, an increase in the heat transfer coefficient is also considered using flow boiling instead of single-phase forced convection as the heat transfer mechanism.

There are several studies of two-phase flow in microchannels in the open literature but most involve adiabatic conditions at the boundary between the fluid and the channel wall. Although, there are some studies involving diabatic two-phase flow (boiling), these are with fluorocarbons instead of water as the working fluid. Using water as the working fluid in microchannels and boiling as the heat transfer mechanism seems to be one of the most promising techniques for the development of cooling systems for future applications. Unfortunately, the study of boiling in microchannels is very complex, and needs to be better understood before being implemented with confidence in a cooling system. It is important to mention that there is not much research with water as the working fluid in micro boiling systems, but it is attractive for its high latent heat of vaporization.

All observations and analysis in this research are expected to help with a better understanding of the physical mechanisms during boiling of water in mini and microchannels

which is a key factor in the development of cooling systems for future high heat flux applications.

## 1.4 Approach

New cooling systems for high heat flux applications require high heat transfer coefficients and compact size. This can be achieved with microchannels and boiling as the heat transfer mechanism. Therefore, this thesis is focused on the experimental investigation and analysis of boiling two-phase flow data performed in horizontal channel microevaporators. Single channel microevaporators with a rectangular cross sectional area are used in order to characterize the two-phase flow boiling since previously developed experiments containing multiple channels have a non-uniform distribution of the flow in the channels. Water is used as the working fluid because it offers thermal advantages over other coolants.

Microevaporators with different channel size are used to investigate the flow patterns, the effect of the mass flow, channel size, and heat flux in the heat transfer coefficient and pressure drop. The flow patterns are characterized through high-speed visualization and then presented in a flow regime map which is compared with the traditional flow regime map proposed by Taitel and Dukler (1976) and other flow regime maps available in the literature for microchannels. These flow patterns and flow regime maps will provide important information to better understand the complexity of the two-phase flow mechanisms. Simultaneously with the high-speed visualization, pressure drop, mass flow, heat flux, and temperatures at different locations on the microevaporators are recorded in order to evaluate the thermal performance in the microevaporators. Once the flow patterns and heat transfer study is performed, published correlations for heat transfer coefficient are assessed based on the measurement data.

Prior to conducting the two-phase flow boiling experiments, single-phase flow studies are performed to quantify heat losses and to assess the applicability of pressure and heat transfer coefficient macroscale models to microchannels. This study is achieved by comparing experimental data for friction factor and Nusselt number with theoretical values

obtained from macroscale models. The experimental data were obtained from a single channel heat exchanger.

## 1.5 Outline

This dissertation provides a detailed experimental study of boiling two-phase flow in microchannels with rectangular cross sections. The thesis is arranged in the following order with additional detail given in the appendices when deemed necessary.

1. Introduction: Contains the background, problem statement, motivation, and approach.
2. Fundamentals and Literature Review. A review of the fundamentals and state-of-the-art on boiling, two-phase flow patterns, and boiling heat transfer are discussed. The fundamentals of boiling at the macroscale are initially introduced. The discussion is focused on the heat transfer coefficient, flow regime maps, and boiling curves, followed by the fundamentals of boiling at the microscale. The discussion then turns to a brief overview of single-phase flow and boiling two-phase flow in microchannels. Attention is paid to a comparison between predictions of the conventional theory and experimental data, obtained during the last decade, as well as to a discussion of possible sources of unexpected effects which were revealed by a number of previous investigations.
3. Experimental Facility: The experimental test rig and data reduction are described and validated against single-phase data.
4. Single-Phase Flow and Heat Transfer Coefficient: This chapter presents and discusses the pressure drop and heat transfer results from the single-phase experiments in a microchannel with water as the working fluid. The experimental data are used to validate the applicability of macroscale theory to microchannels and the identification of heat losses in the test fixture.

5. Two-phase Flow Visualizations: The results from the two-phase flow visualization are presented. Flow patterns are presented in the form of flow regime maps and compared with other experimental data reported in the literature. Flow reversal, bubble size, bubbly frequency, intermittent flow, and pressure drop oscillations in two-phase flow boiling are also discussed.
6. Experimental Heat Transfer Coefficient: The effect of the inlet sub-cooling, mass flux, heat flux, and channel size on the heat transfer coefficient are reported. The results are shown in the form of boiling curves and heat transfer coefficient vs quality and heat flux. Some models for the heat transfer coefficient reported in the literature are compared with the experimental data.
7. Conclusions and Recommendations: The major contribution resulting from this work are summarized and recommendations for extensions to the work presented here are suggested.

# Chapter 2

## Fundamentals and Literature Review

This chapter contains fundamentals of boiling heat transfer where the two types of boiling are discussed. Flow boiling heat transfer, flow regime maps, boiling curves in conventional and microscale, and a brief description of the typical approaches for modeling in two-phase flow are also discussed. Finally, a literature review of single-phase liquid flow in microchannels and two-phase flow boiling is presented.

### 2.1 Fundamentals of boiling

Boiling is the process in which heat transfer leads to a phase change of a substance from a liquid to a gas. Boiling will not occur if the wall temperature is below the saturation temperature. Saturation flow boiling occurs when the bulk liquid reaches saturation temperature and sub-cooled flow boiling exists when the bulk liquid temperature remains below its saturation value but the surface is hot enough for bubbles to form. Bubbles formed at the wall will condense as they move out of the developing saturation boundary layer, but the appearance of these bubbles will affect the heat transfer between the wall and the fluid. Sub-cooled internal flow boiling has been of particular interest as a mean of providing high heat flux cooling. At the present time, one of the simplest ways to achieve high heat flux cooling in microelectronics is with a sub-cooled flow boiling process (Carey, 2008).

There are two types of boiling: *pool boiling* refers to boiling from a heated surface submerged in a large volume of stagnant liquid, where the fluid flow is caused by a natural convective phenomena only, and *flow boiling*, where the boiling occurs in a fluid which is flowing over a heated surface. Flow boiling is considerably more complicated than pool boiling, owing to the coupling between hydrodynamics and the boiling heat transfer process. There are three different boiling heat transfer mechanisms: in *nucleate boiling*, steam bubbles form at the heat transfer surface and then break away to be carried into the main stream of the fluid. There is also *convective boiling*, where heat is conducted through the liquid which evaporates at the liquid-vapor interface. Finally, in *film boiling*, the heat is transferred by conduction and radiation through a film of vapor that covers the heated surface and the liquid vaporizes at the vapor-liquid interface.

Experimental observations and physical arguments indicate that the basic phenomenology of flow boiling in microchannels is similar to that in large channels as long as there are defects on the heated surface that have characteristic sizes that are smaller than the flow channel cross sectional dimensions. Therefore, bubbles nucleate on the heated wall crevices in such small channels, leading to the onset of nucleate boiling and further downstream the bubbles are released into the bulk flow and lead to the development of a two-phase flow field. The confinement resulting from the small size channel can affect the bubble dynamics.

### 2.1.1 Macro flow boiling

**Heat Transfer Coefficient:** Boiling is first initiated at the Onset of Nucleate Boiling, *ONB*, when some of the bubbles forming on crevices can survive condensation (e.g. no collapse of the vapor bubble). As the vaporization process proceeds, the vapor content of the flow increases with the distance along the tube and different flow pattern such as bubbly, plug, annular, and mist flow are observed as shown in Figure 2.1.

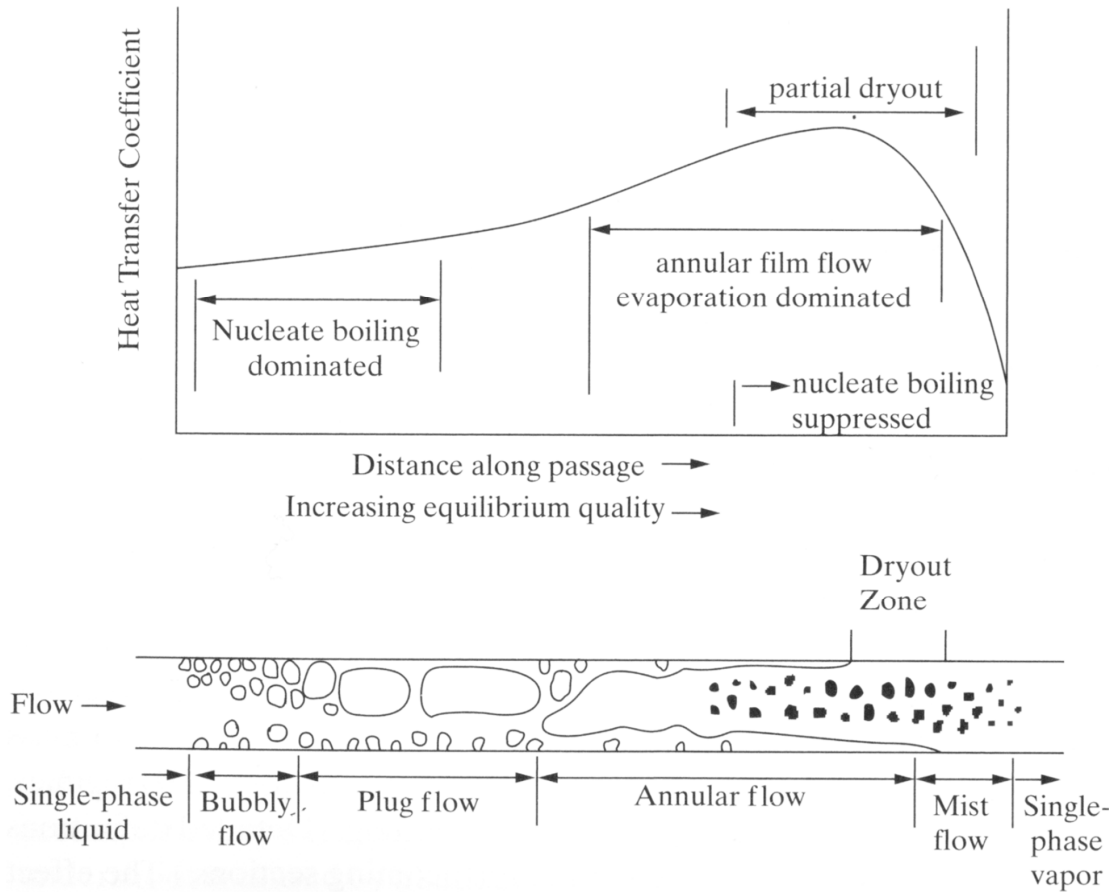


Figure 2.1: Flow and heat transfer regimes in a uniformly heated horizontal tube with moderate heat flux (Ghiaasiann, 2008). Reprinted with the permission of Cambridge University Press

Regimes of slug, stratified, or wavy flow may also be observed depending on the flow conditions. The qualitative axial variation of the heat transfer coefficient is also shown in the figure. The heat transfer coefficient often (but not always) increases with the downstream distance prior to the onset of dry-out. Furthermore, as the wetted fraction of the wall decreases with downstream distance, more of the wall becomes “inactive” (dries) and the heat transfer coefficient progressively decreases.

Nucleate boiling is usually the dominant heat transfer mechanism near the *ONB* and low equilibrium quality. As the liquid film on the wall thins, film evaporation may become so effective that it is the dominant mechanism. The film may disappear completely from



portions of the tube wall leading to partial dry-out. Between low and moderated qualities, both mechanisms may be important. In some cases nucleate boiling may be completely suppressed, leaving film evaporation as the only active vaporization mechanism.

The two-phase flow modeling for heat transfer and pressure drop has typically been treated analytically or empirically. Analytical models use the mass, momentum, and energy equations, but the difficulty in applying these equations in the interpretation of the two-phase flow systems is that detailed information on the local mass flux, velocity and density is practically never available. Data on the distribution of these parameters across the channel are needed. The distribution depends on the respective total flow rates of the two-phases, upon their physical properties, geometry, and is closely linked with the flow pattern. In order to evaluate the momentum and energy balances, it is therefore necessary to measure the distribution of local values across the channel of some variables (e.g. density, phasic mass flows, phasic velocities). In most practical cases, however, experimental techniques are not available to make these measurements, and approximations are used as a reasonable alternative. The most basic approximations are considered in the homogenous and separated flow models. The homogenous model, also known as the “friction factor” or “fog flow” model, considers the two-phases to flow as a single-phase, possessing mean fluid properties, and the separated model considers the phases to be artificially segregated in two streams, one of liquid and one of vapor with constant but not necessarily equal velocities.

Empirical models have been extensively proposed. Several researches compare their own experimental results with published correlations. Most of the conclusion are that the empirical models are not able to predict their experimental data even under a similar range of operating conditions for which the correlations were obtained. These models are typically adjusted (if possible) to match their experimental data through modifying selected “calibration” parameters in the model. In summary, analytical or empirical modelling of two-phase flow is a very difficult task, and a generalized model for heat transfer or pressure drop is still not available. Therefore, most of the current efforts in modeling are concentrated on the generation of models valid for a particular flow pattern instead of a

generalized model trying to cover all flow patterns which is difficult or may be an impossible task.

**Flow Regime Maps:** Flow patterns are widely used predictive tools for two-phase flow studies and are presented in the form of so-called flow regime maps, a two-dimensional plot attempting to separate the flow patterns into particular areas. They are often empirical and generally plotted based on the phasic superficial velocities ( $j_f$ : liquid superficial velocity,  $j_g$ : gas superficial velocity) or coordinates that include the physical properties of the gas and liquid phases. Recent two-phase flow regime maps found in the literature are plotted in the form proposed by Steiner (1993) with quality on the horizontal axis and mass flux on the vertical.

Baker(1954) developed one of the earliest empirical flow regime maps and numerous other attempts to develop a generalized flow regime map followed (Mandhane et al., 1974; Taitel and Dukler, 1976; Weisman et al., 1979). Most noteworthy among these was the pioneering effort by Taitel and Dukler, defining and mapping the four predominant flow regimes (stratified, intermittent, bubble, and annular) with superficial gas and superficial liquid coordinates and proposing physics based criteria for the transition from one regime to the next. A comprehensive method of predicting flow pattern transitions over the complete range of pipe inclinations has been put forward by Taitel (1990). This model relies on the previous work by Taitel and Dukler (1976, 1977); Dukler (1978); Barnea and Taitel (1976). Taitel used the term *intermittent flow* to cover elongated bubbles, slug and churn flows.

The Taitel and Dukler (1976) methodology relies on adiabatic models that ignore the thermal interactions between phases when heat is added or extracted from the flowing two-phase mixture in diabatic conditions. Such an adiabatic model can be expected to provide better flow regime predictions as the applied heat flux decreases (Bar-Cohen et al., 1979). Nevertheless, the model has proven to be exceedingly useful for diabatic conditions and has demonstrated its first-order accuracy in numerous studies, including those performed by Taitel et al. (1978); Frankum et al. (1997).

Most flow maps are only valid for a specific set of operating conditions (type of fluid, channel geometry, size, and orientation, adiabatic or diabatic flow, etc.). Therefore, efforts

are being made to propose generalized flow maps. One of the first unified models for predicting flow regime transitions in channels of any orientation, based on simple physical criteria and using familiar two-phase non-dimensional groupings was proposed by Taitel and Dukler (1976). When the theoretical equations are solved in dimensionless form, five dimensionless groups emerge in their analysis: modified Froude number (relating inertial force to gravitational force), the  $T$  parameter (relating liquid pressure drop to buoyancy), the Martinelli number (relating liquid pressure drop to gas pressure drop), the  $K$  parameter (product of the modified Froude number and the square root of the superficial Reynolds number of the liquid), and the  $Y$  parameter (forces acting on the liquid due to gravity and pressure drop,  $Y=0$  to horizontal orientation). Since the original study, several attempts modifying Taitel's approach or using more suitable dimensionless parameters have been used in order to generalize the flow regime maps.

Flow regime maps in adiabatic and diabatic conditions are important in the study of two-phase flow. In fact, the physical mechanisms controlling two-phase pressure drops and heat transfer coefficients are intrinsically related to the local flow patterns (Collier and Thome, 1994; Carey, 2008; Kattan et al., 1998; Cheng et al., 2008a,b), and thus flow pattern prediction is an important aspect of two-phase heat transfer and pressure drop.

The majority of the widely used regime maps are based on data for vertical or horizontal tubes with small and moderated diameters (typically  $1 \leq d \leq 10$  cm). The flow regime map of Mandhane et al. (1974), displayed in Figure 2.2, is probably the most widely accepted map for gas-liquid flow in horizontal pipes. They defined and mapped four predominant flow regimes (stratified, intermittent, bubble, and annular) with superficial gas and superficial liquid coordinates and proposed a physical criteria for the transition from one regime to the next. The difficulty of identifying flow regimes and their transitions comes mainly from the subjectivity of the observer and the lack of agreement in the description and classification of the flow patterns.

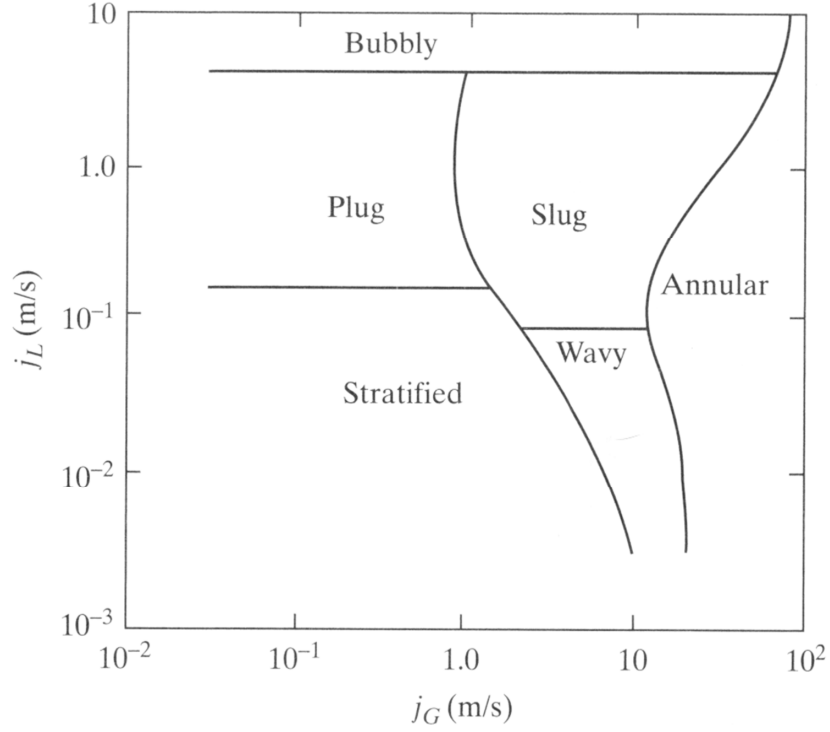


Figure 2.2: Flow regime map for gas-liquid flow in horizontal pipes (Mandhane et al., 1974). Reprinted with the permission of Cambridge University Press

A large number of experiments have been conducted with adiabatic macroscale smooth channels over the past decades in horizontal, vertical, and inclined orientations using gas-liquid as working fluids. Compared to the flow regime maps available for adiabatic circular tubes, non-circular channel data show little difference if the hydraulic diameter is bigger than  $10\text{ mm}$ . Flow regime boundaries are also similar between small rectangular channels and small circular tubes ( $1\text{-}5\text{ mm}$ ) in horizontal and possibly vertical orientation (Kandlikar et al., 1999). Typically, at low gas and high liquid flow rates, bubbly flow occurs, and at high gas flow rates and low liquid flow rates, an annular flow regime is observed. At intermediate gas and liquid flow rates, different flow regimes such as slug, wavy, plug, etc. may occur.

**Boiling Curve:** The thermal performance during pool and flow boiling is being studied using the boiling curve introduced by Nukiyama (1934). The effect of mass flux in the

flow boiling curve and the sequence of regimes associated with sub-cooled boiling for an horizontal pipe flow are shown in Figure 2.3. The effect of local equilibrium quality in the boiling curve is rather complicated, with increasing in the Critical Heat Flux,  $CHF$  as the equilibrium quality decreases Ghiaasiann (2008). The boiling curve is divided in sub-cooled boiling (after the  $ONB$  point), saturated boiling, transition boiling (after Critical Heat Flux point,  $CHF$ ), and film boiling region (after Minimum Film Boiling point,  $MFB$ ). The boiling curve or heat transfer coefficient is particularly sensitive to mass flux  $G$  in single-phase liquid forced-convection, partial sub-cooled boiling, and post- $CHF$  regimes but it is insensitive to mass flux in the fully developed sub-cooled boiling and saturated boiling regions as illustrated on Figure 2.3.

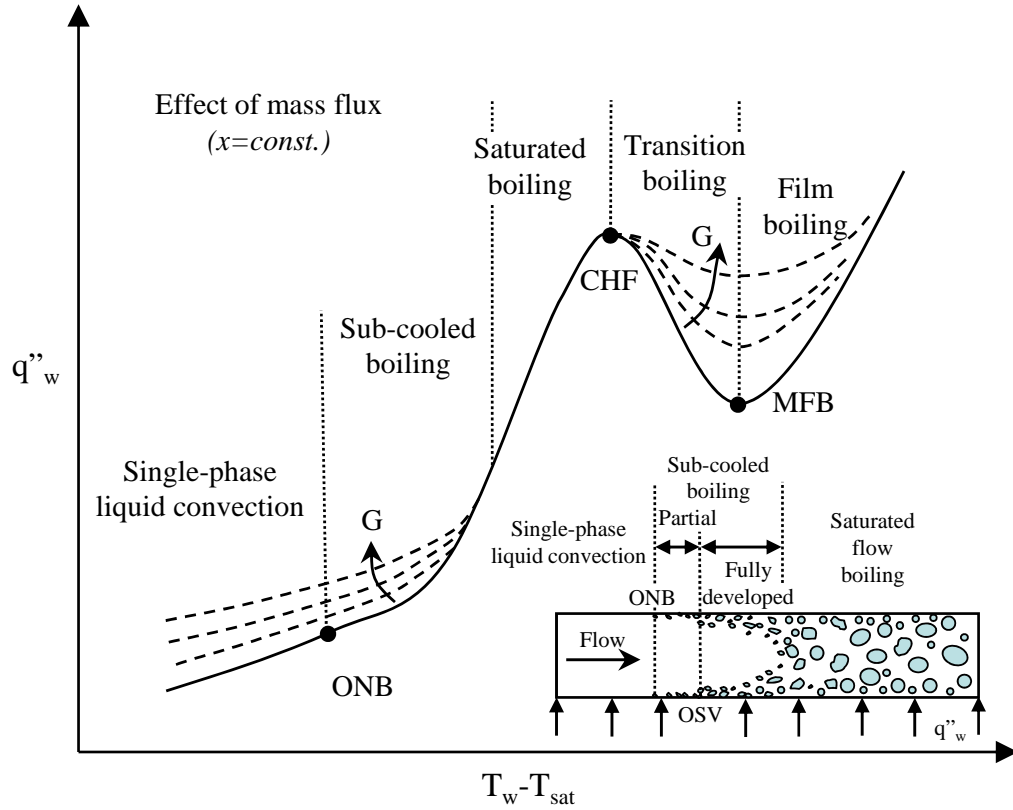


Figure 2.3: Typical flow boiling curve at low quality conditions and transition of flow through regimes of sub-cooled boiling. Adapted from Ghiaasiann (2008) and Carey (2008)

Sub-cooled boiling can be partial and fully developed after Onset of Significant Void, OSV, where bubbles typically depart from the surface. During partial sub-cooled flow, both forced-convective and nucleate boiling effects are important, with nucleate boiling effects increasing in strength as the flow proceeds downstream. Eventually, the nucleation site density becomes so high that the nucleate boiling completely dominates the heat transfer process. In saturated forced-flow boiling (region between vapor quality  $x=0$  and the *CHF* point) nucleated boiling is predominant where quality is low (a few percent), and force convective evaporation is predominant at high qualities representing annular flow, and elsewhere both mechanisms can be important.

Nucleated boiling heat transfer ( $h_{nb}$ ) and forced-convective boiling heat transfer ( $h_{cb}$ ) both contribute to the total heat transfer coefficient ( $h$ ) in saturated flow boiling. Nucleate boiling is characterized by the formation of vapor bubbles at the heated wall. Convective boiling is characterized by conduction and convection through a liquid film at the heated wall, and vaporization at the liquid/vapor interface. From numerous macroscale investigations it is known that when flow boiling is dominated by the nucleate boiling mechanism, the heat transfer coefficient increases with increasing heat flux (or wall superheat) and saturation pressure, and is independent of mass flux and vapor quality. Furthermore in convective-dominated flow boiling, the heat transfer coefficient is independent of heat flux and increases with increasing mass flux and vapor quality.

The heat transfer coefficient correlations can generally be divided into three groups (Ghiaasiann, 2008): *The summation rule*, proposed by Chen (1966), where the heat transfer coefficient is considered to be the addition of the nucleate and convective boiling contribution ( $h = h_{nb} + h_{cb}$ ), *the asymptotic model*, which assumes one of the two mechanisms to be dominant, ( $h^n = h_{nb}^n + h_{cb}^n$ , with  $n > 1$ ,  $h$  asymptotically approaches to  $h_{nb}$  or  $h_{cb}$ ). The third group constitutes the *flow-pattern dependent correlations*, this methodology consists of a flow regime map and regime-specific models and correlation for heat transfer.

### 2.1.2 Micro flow boiling

Flow boiling is attractive over single-phase liquid cooling because of its high heat transfer coefficient and higher heat removal capacity for a given mass flow rate of coolant (Kandlikar et al., 2006a). Flow boiling systems can carry larger amounts of thermal energy through the latent heat of vaporization, whereas single-phase systems rely only on the sensible heat.

It is believed that nucleation criteria in small channels are not significantly different from the conventional theories for large channels. With flow boiling in small channels the bubble growth is similar to that in pool boiling, except that the flow causes the bubbles to depart early. In fact, most of the recent theories for small channels are extension of the pool boiling nucleation model proposed by Hsu (1962). One of the main differences observed between conventional and small size channels is that buoyancy in small channels is insignificant but inertial viscous and capillary effect are crucial (e.g. stratified flow is not observed in microchannels, effect of tension force must be considered in small size channels).

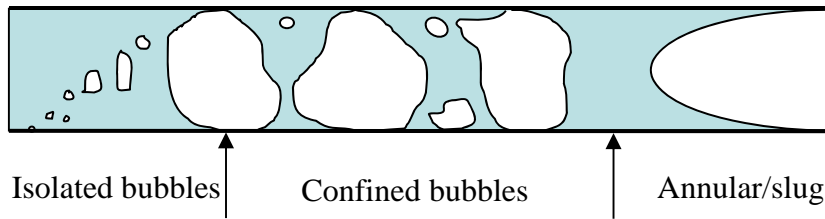


Figure 2.4: Major flow boiling regimes in small passages. Adapted from (Cornwell and Kew, 1992)

Typical flow regimes in small passages are shown schematically in Figure 2.4. The departing and growing bubbles contribute to isolated bubble flow which eventually spans the entire smaller dimension of the channel forming a confined bubbles regime. Finally, the bubbles grow significantly in the axial direction and eventually lead to the collapse and dispersal of some of the liquid slugs that separated neighboring bubbles. The confinement of bubbles in microchannels leads to a different growth pattern of bubbles between conventional and small channels.

Flow boiling in microchannels can be affected by superficial tension forces, boundary conditions that behave differently in comparison with macrochannels (e.g. jump wall temperature, wall velocity slip at Knudsen number much bigger than 1;  $Kn \gg 1$ ), or even continuity is not valid and rarefied gas dynamics theory is needed.

Studies on microscale flow regime maps have increased greatly in recent years but most of these studies are focused on adiabatic conditions rather than on diabatic two-phase flows. The develop of diabatic flow maps is more challenging due to the coupled effects between the flow dynamics and heat transfer, and the scale effects at the microscale level. Important factors influencing these flows are nucleate boiling, evaporation or condensation of liquid films, dry-out, heat flux, mass flux, acceleration/deacceleration of the flows, and surface tension among others.

There are a number of studies on flow patterns and flow maps in microscale channels but there is no proven consistency of observations for similar fluids under similar test conditions taken by different researchers, also the effects of channel shapes and physical properties in the flow regime maps need to be clarified. Cheng et al. (2008c) presented a comprehensive review of the studies of microscale gas-liquid two-phase flow patterns and flow patterns maps at adiabatic and diabatic conditions. Although, it appears that the adiabatic flow regime maps and flow transition models perform reasonably well with diabatic flow boiling data (Celata et al., 1991; Frankum et al., 1997), there is no proven evidence that this is also applicable at the microscale level. In general, compared to macroscale geometries, the study of flow patterns in microscale and diabatic conditions needs to be developed.

## 2.2 Single-phase liquid flow in microchannels

Thirty years ago Tuckerman and Pease (1981) introduced the concept of microchannels to the electronics cooling industry. Since the heat transfer coefficient generally increases with decreasing size, the passage size should be made as small as possible. This results in a dense package with higher heat transfer and a larger surface area-to-volume ratio than a conventional cooling device. However, the benefits are tempered by increased pressure



losses with small passages, in addition to manufacturing challenges. In order to minimize pressure drop but maximize thermodynamic performance, Khan et al. (2006) and Galvis and Culham (2010) used an entropy generation minimization method where pressure drop and heat transfer were simultaneously evaluated.

The early applications of microchannels involved micromachined devices (e.g., micropumps, microvalves, and microsensors), and more current advancements are used in the development of inkjet printer heads, lab-on-a-chip technology, micro-propulsion, micro-thermal technologies, and even cooling of turbine blades (Galvis et al., 2008). In engineering thermofluid systems, such as heat exchangers, laminar flow in non-circular ducts is encountered, for example, in automotive coolers, cold plates, and microchannel heat sinks.

In dealing with liquid flows in minichannels and microchannels with low Knudsen numbers ( $Kn < 10^{-3}$ ), the flow is not expected to experience any fundamental changes from the continuum approximation employed in macroscale theories (Kandlikar et al., 2006a). Channels larger than  $1 \mu m$  using water can be treated as continuous media and the classical macroscale theory is applicable (Gad-el-Hak, 1999). However, there are a number of contradictory studies on the friction factor in microchannels and the transition from laminar to turbulent flow.

### 2.2.1 Friction factor

Several authors evaluated the applicability of the classical macroscale correlations to microchannel fluid flow and heat transfer (Park and Punch, 2008; Hrnjak and Tu, 2007; Yang and Lin, 2007; Qi et al., 2007; Papautsky et al., 2001; Jiang et al., 1995; Brody and Yager, 1996). Through a comparative analysis of results from several studies, Park and Punch (2008), Sharp et al. (2006) and Papautsky et al. (2001) showed that Poiseuille numbers  $Po = f Re$ , where  $f$  is the friction factor and  $Re$  is the Reynolds number at the microscale, can be similar or vary appreciably from those expected based on conventional macro Hagen-Poiseuille theory as shown in Figure 2.5.

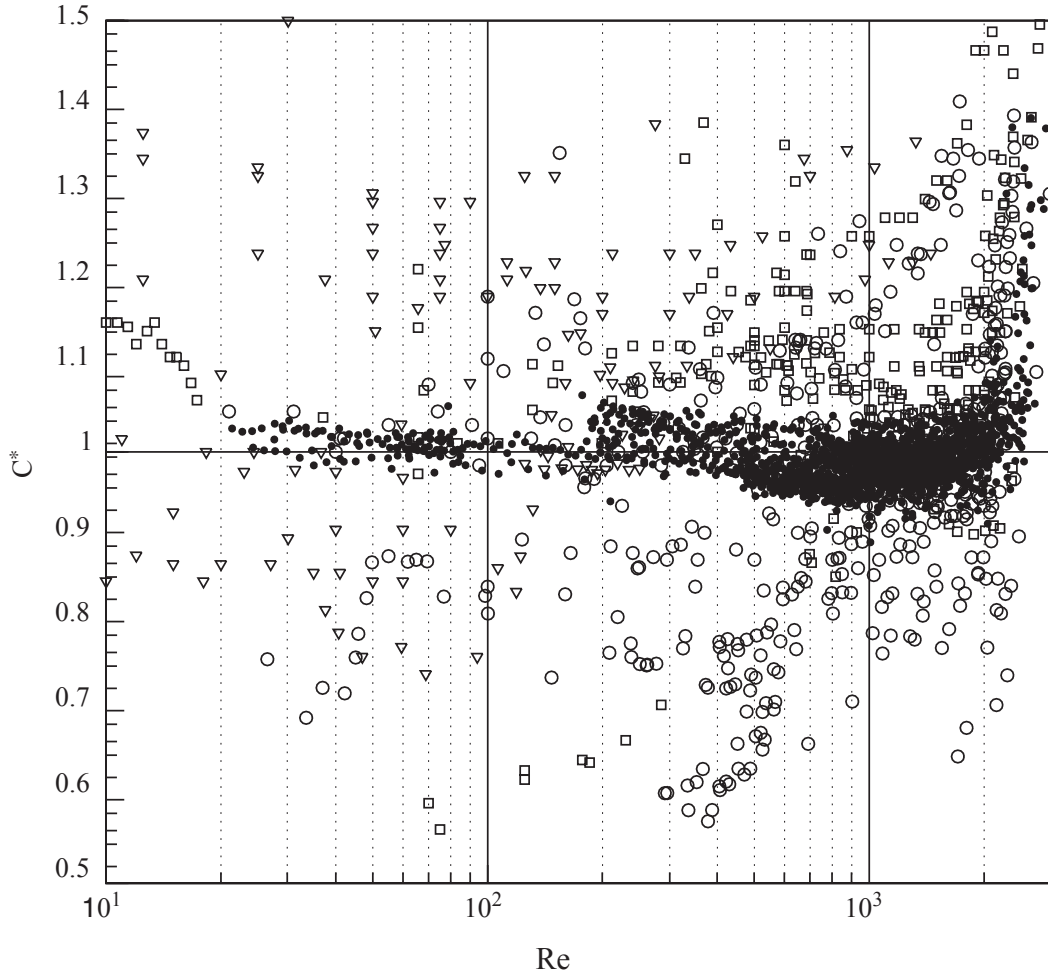


Figure 2.5: Comparison of normalized Poiseuille number  $C^* = (Po)_{experimental}/(Po)_{theory}$  vs Reynolds number: ( $\circ$ ), ( $\bullet$ ) circular micro-tubes, ( $\nabla$ ) trapezoidal microchannels, ( $\square$ ) rectangular microchannels (Sharp et al., 2006)

Yarin et al. (2009) suggested possible reasons for disparity between the theoretical predictions and measurements obtained for single-phase flow in microchannels. The analysis was performed using experimental data from several publications including smooth and rough microchannels. They attribute the inconsistency between theory and experimental friction factor to the discrepancy between the actual conditions of a given experiment and the assumptions used in deriving the theoretical value, error in measurements, and effects associated with decreasing the characteristic scale of the problem.

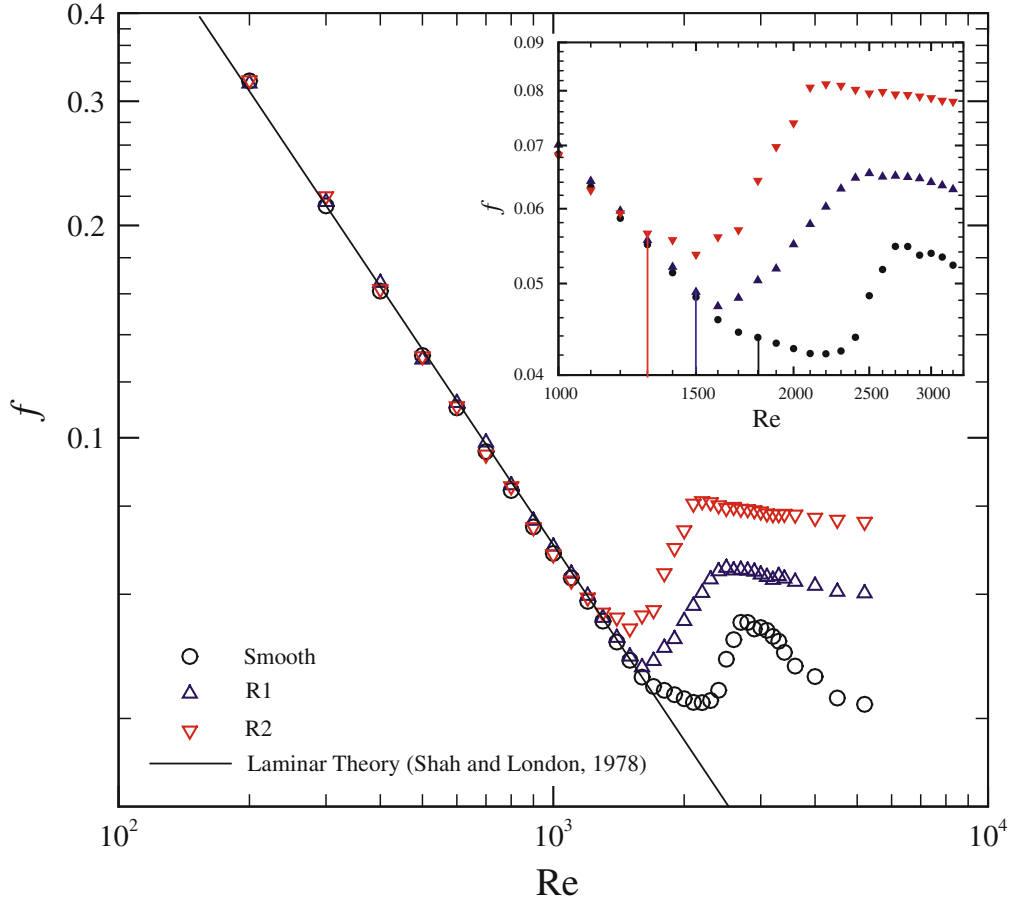


Figure 2.6: Apparent friction factor,  $f$ , as a function of  $Re$  for smooth and rough-wall conditions (Natrajan and Christensen, 2010b)

Furthermore, the results of many groups have indicated that the transition from laminar to turbulent flow occurs at anomalously low  $Re$  in comparison to macroscale transition (Hsieh et al., 2004; Qu et al., 2000; Peng et al., 1994; Mala and Li, 1999; Peng and Peterson, 1996). The onset of early transition as shown in Figure 2.6 was attributed to relatively high surface roughness that can have a pronounced effect on the flow behavior at these scales (Natrajan and Christensen, 2011, 2010a,b). In contrast, experiments by other researchers have revealed transitional  $Re$  that are quite comparable to that observed at the macroscale (Barlak et al., 2011; Natrajan and Christensen, 2007; Li and Olsen, 2006; Sharp and Adrian, 2004; Qu and Mudawar, 2002; Judy et al., 2002).

In light of this, conventional formulations that are applicable to macro-size channels may not be valid for microchannels. As the field of microfluidics continues to grow, it is becoming increasingly important to understand the physical phenomena governing fluid flow and heat transfer in microchannels as well as the limitations associated with applying design correlations developed for macroscale flows in microfluidics.

### 2.2.2 Heat transfer coefficient

Heat transfer in straight tubes and channels has been a subject of much research. In many cases theoretical predictions in this field agree fairly well with known experimental data related to heat transfer in the conventional size channels. Single-phase heat transfer in microchannels may be affected by viscous energy dissipation, axial heat conduction, electro-osmotic effects, property variation effects, channel surface conditions (relative roughness), and experimental uncertainties (Gözükara, 2010; Tso and Mahulikar, 1998, 1999, 2000; Tunc and Bayazitoglu, 2001; Koo and Kleinstreuer, 2004; Maranzana et al., 2004). Comprehensive surveys can be found in Hetsroni et al. (2005a,b); Morini (2004); Sobhan and Garimella (2001); Kandlikar and Grande (2002); Guo and Li (2003); Celata et al. (2004)

The influence of the geometric parameters of the channel and the thermophysical properties of the fluid on the flow and heat transfer were studied by Li et al. (2004) using numerical simulation in a micro-heat sink model with a 10 *mm* long silicon substrate, with rectangular microchannels, 57  $\mu\text{m}$  wide and 180  $\mu\text{m}$  deep. The results indicated that thermophysical properties of the liquid can significantly influence both the flow and heat transfer in the microchannel heat sink. The effect of axial conduction, viscous dissipation, and variable properties were studied by Ramiar and Ranjbar (2011). The results showed that increasing the thermal conductivity of water (e.g. using nano-particles) enhances heat transfer characteristics of the channel and in contrast, viscous dissipation causes the Nusselt number and friction factor to decrease.

Giudice et al. (2007) studied numerically the effects of viscous dissipation and temperature dependent viscosity in thermally and simultaneously developing laminar flows of

liquids in straight microchannels. They concluded that, in laminar forced convection in straight microchannels, both temperature dependence of viscosity and viscous dissipation effects cannot be neglected for a wide range of operating conditions.

Lelea et al. (2004) experimentally evaluated the developing heat transfer and fluid flow of water in tubes with internal diameters 0.1, 0.3, and 0.5 *mm* with  $100 < Re < 800$ . The experimental results confirmed that, including the entrance effects, and boundary conditions imposed in the experiments, the conventional or classical theoretical approach can be employed in predicting heat transfer behavior in microchannels. A similar conclusion was reported by Lee et al. (2005) using rectangular channels ranging in width from 194  $\mu m$  to 534  $\mu m$ , with the channel depth being nominally five times the width and  $300 < Re < 3500$ .

The thermal transport characteristics of transitional and turbulent flow through smooth and rough wall rectangular minichannels with hydraulic diameter  $d_h = 600 \mu m$  and  $1300 \leq Re \leq 5200$  under constant heat flux conditions was investigated by Natrajan and Christensen (2011). A determination of the bulk Nusselt number indicated enhancement in convective heat transfer over the smooth-wall case with increasing surface roughness in both the transitional and turbulent regimes. In addition, their data support the applicability of macroscale convective heat transfer correlations for the design and optimization of smooth wall micro-fluidic systems where axial conduction and viscous heating are negligible.

By comparing the available experimental data on single-phase convective heat transfer through microchannels, it is evident that further systematic studies are required to generate a sufficient body of knowledge of the transport mechanism responsible for the variation of the flow structure and heat transfer in microchannels.

## 2.3 Boiling two-phase flow

When a liquid is vaporized in a heated channel, the liquid and the vapor interact based on the relative phase constituents to form a range of flow patterns. The particular flow

pattern depends on the conditions of pressure, flow, heat flux, and channel geometry. Since it is extremely difficult to “track” the continuous change of all the thermal and hydraulic properties of the flow (on time and position), the study of boiling to date is largely empirical rather than analytical (Collier and Thome, 1994). The methods used to analyze two-phase flow are based on the basic equations governing the conservation of mass, momentum, and energy. The difficulty in applying these equations arises from the need to provide detailed information of mass flux, velocity, and density in order to achieve reliable results. Unfortunately, these data are not easily recorded using experimental techniques and most modeling procedures are based on simplifying assumptions. The main assumptions that have been made are considered in the homogeneous, separated, and flow pattern models. The flow pattern model is a more sophisticated approach to the two-phase flow where the equations are solved within the framework of each flow pattern.

Various techniques are available for the study of two-phase flow patterns in diabatic and adiabatic channels. At higher velocities, where the patterns become indistinct, the flow patterns are directly observed using cinematography, X-radiography, or high-speed video recording. Probes are also used as an indirect method to provide information to deduce the flow patterns (Revellin et al., 2006; Hewitt, 1978). While the terminology used to describe flow patterns can be subjective, the conventional pattern regimes are classified as bubbly, slug, churn, annular, and inverted annular flows (Harirchian and Garimella, 2009b; Revellin and Thome, 2007a; Kandlikar, 2006; Chen and Garimella, 2006; Lee and Mudawar, 2005).

Despite the present deficiencies in the understanding of various flow patterns and transitions from one pattern to another, there is a widely felt need for simple methods to give some idea of the particular pattern likely to occur for a given set of local parameters. One method of representing the various transitions is in the form of a flow pattern map. Although, there are pattern maps available for macrochannels, it has been conclusively shown that applying or extrapolating two-phase macroscale flow pattern maps to microscale two-phase flows is unrealistic (Callizo, 2010; Ali, 2010). This is because surface tension effects often play a stronger role in microchannels than in larger flow passages

(Carey, 2008). Other reasons for observed deviation from classical “macro theories” are surface roughness (Shen et al., 2006; Wu and Chen, 2003; Kandlikar et al., 2003) and unaccounted systematic errors due to the small dimensions of microchannels that make some experimental parameters difficult to measure with sufficient accuracy (Morini, 2004). In addition, the occurrence of flow instabilities reported in flow boiling in microchannels by several authors complicate modeling efforts (Wu and Cheng, 2004; Kandlikar et al., 2006b; Lee et al., 2010).

Flow regime maps at the microscale are also typically represented in graphs, where the co-ordinates are the superficial phase velocities or generalized parameters containing these velocities. The use of the superficial phase velocities in a flow pattern map restricts its application to one particular situation, whereas the choice of more generalized parameters may be preferable to represent the transitions. In fact, Harirchian and Garimella (2010, 2012); Ong and Thome (2011) proposed new pattern maps based on dimensionless parameters instead of superficial phase velocities. Also, Felcar et al. (2007) using the methodology proposed by Taitel and Dukler (1976) and incorporating surface tension effects (using the Weber and Eötvös numbers) proposed an adiabatic flow regime map and transition models for channels varying between hydraulic diameters 1 and 5 *mm*. However, these methods cannot be generalized until more well characterized data become available but they are an initial step towards a better understanding of the mechanisms acting on the flow pattern transitions.

A better understanding of the two-phase flow patterns will help to formulate accurate predictions of heat transfer and pressure drop which are fundamental parameters for safe operation and optimal design of heat exchangers. In spite of intensive activity in the recent years, heat transfer characteristics in small geometries still need clarification. The difference between a micro and macro “approach” in single-phase flow has been commonly attributed to the fact that the physical mechanisms that are potentially dominant in microchannels are less important in macrochannels, and vice versa. Some publications agree that considering entrance effects, viscous energy dissipation, wall roughness, axial heat conduction, and high measurement accuracy can lead to comparable results between

micro and macroscale theories. However, there are also studies in microchannels based on experimental and numerical simulation of the full Navier-Stokes and energy equations, which demonstrate fairly good agreement with macro experimental data. These do not appear to be conclusive evidence as to the applicability of macro theory when analyzing microchannels. Unfortunately, the governing phenomena in microchannels are not well understood and before predictions of flow and heat transfer rates can be made with confidence, high-quality, reliable experimental data are needed to resolve discrepancies in the literature.

Regarding the two-phase flow Heat Transfer Coefficient ( $HTC$ ), there are a large number of correlations available in the literature on flow boiling of saturated liquids. Most of these consider the contribution of two heat transfer mechanisms (nucleate and convective)

The mechanism of flow boiling heat transfer in microchannels has been a subject of disagreement, due to the sometimes contradictory trends in various experimental data. The trends in the experimental data in some publications are consistent with the predominance of nucleate boiling and indicate that the heat transfer coefficient is a strong function of the heat flux and increases with saturation pressure, being essentially independent of mass flux ( $G$ ) and vapor quality ( $x$ ) as reported by Bao et al. (2000). In contrast, Lee and Lee (2001) showed that the  $HTC$  increases with  $G$  and is sensitive to  $x$  which is consistent with the convective boiling mechanisms observed in an annular flow regime. These observations are both correct and simply refer to two different heat transfer regimes that can in fact simultaneously occur in different parts of the same heated channel. Experimental data supporting these observations can be found in Lee and Lee (2001); Bertscha et al. (2008, 2009); Lee and Mudawar (2005); Thome (2004), and Kandlikar (2004).

In this experimental work, high-speed visualization covering a range of vapor qualities with simultaneous heat transfer and pressure drop measurements are performed in two different microchannel evaporators to provide important insights into flow boiling in microchannels. The visualized flow patterns are expected to serve in developing of flow pattern maps which can also provide valuable information for proper modeling assumptions. Also, the effects of the channel size, heat flux and mass flux on the boiling curve



and heat transfer coefficient on flow boiling in microchannels are explored.

Macroscale flow boiling heat transfer may be decomposed into nucleate and convective boiling contributions at the microscale. The extent of these two important mechanisms remain unclear (Kakaç et al., 2009). Although, many experimental papers conclude that nucleation boiling is dominant in their data because of the heat flux dependency, a heat flux dependency does not prove that nucleate boiling is dominant or present (Jacobi et al., 2002). Since, nucleate boiling requires only small superheat; it is the most convenient flow regime for electronics cooling applications. If a microevaporator operates before the critical heat flux ( $CHF$ ) overheating in the microprocessor could be avoided. Therefore, this research will be focused on the main flow regimes observed during the visualization tests before  $CHF$ .

## 2.4 Flow boiling heat transfer correlations

Typically nucleate boiling is dominant at low qualities while at moderate to high qualities nucleate boiling is suppressed and film evaporation dominates. At intermediate qualities, both nucleated boiling and film evaporation effects are important. Experimental  $HTCs$  are compared with correlations that use a superposition technique to account for the gradual transition between nucleate and convective boiling.

Five empirical correlations for the saturated flow boiling  $HTC$  in macro and microchannels were assessed. Table 2.1 summarizes the references, operation range, and working fluid for the flow boiling correlations which are briefly described below. These correlations were chosen in this study because they have been used with some success to correlate flow boiling heat transfer data over a finite range of flow conditions, are appropriated for water, and their operation conditions are closer to the experiments in this work. It is important to mention that it is difficult to find correlations that cover a similar range of operating conditions in microchannels with water as the working fluid.

Table 2.1: Saturated flow boiling correlations

<i>Model</i>	<i>References</i>	<i>Working fluid and geometry</i>	<i>Experimental conditions</i>
Kandlikar	Kandlikar and Balasubramanian (2004)	water, refrigerants, and cryogenic fluids (round tubes)	$d_h = 190 \mu m - 2.92 mm$ $G = 50 - 570 kg/m^2 s$ $q = 5.5 - 90.8 kW/m^2$ $h_{tp} = 1 - 60 kW/m^2$ $x = 0 - 1$
Lee and Mudawar	Lee and Mudawar (2004)	R134a, water (rectangular channel)	$d_h = 349 \mu m$ $G = 127 - 654 kg/m^2 s$ $q = 159 - 938 kW/m^2$ $h_{tp} = 3 - 57 kW/m^2$ $x = 0.26 - 0.87$
Gungor and Winterton	Gungor and Winterton (1986) Carey (2008)	water, refrigerants, and ethylene glycol (round tubes)	$d_h = 2.95 - 32 mm$ $G = 12.4 - 61518 kg/m^2 s$ $q = 0 - 1 kW/m^2$ $h_{tp} = 2 - 5 kW/m^2$ $x = 0 - 0.99$
Lee and Garimella	Lee et al. (2008)	water (rectangular channels)	$d_h = 160 - 539 \mu m$ $G = 218 - 934 kg/m^2 s$ $q = 100 - 3400 kW/m^2$ $h_{tp} = 10 - 70 kW/m^2$ $x = -0.02 - 0.20$
Schrock and Grossman	Schrock and Grossman (1959)	water (round tubes)	$d_h = 2.9 - 10.8 mm$ $G = 239 - 4447 kg/m^2 s$ $q = 189 - 4574 kW/m^2$ $h_{tp}$ (not available) $x = 0.05 - 0.57$

### 2.4.1 Kandlikar model

The original correlation by Kandlikar (1990, 1991) on boiling  $HTC$  was developed using a large data bank consisting over 10,000 data points with ten different fluids, including water, refrigerants, and cryogenic fluids. The tube diameter ranged from 3 to 25  $mm$  considering all flow in the liquid phase in the turbulent region ( $Re_{Lo} > 3000$ ). This correlation was extended to mini and microchannels in the laminar and transition regions by Kandlikar and Balasubramanian (2004). The overall trend in  $HTC$  versus quality, is that nucleate boiling contributions decrease with quality and the convective boiling contribution increases with quality. Depending on the boiling number and the liquid to vapor density ratio, the  $HTC$  trends are seen to be increasing, decreasing or flat with an increase in quality. Typically, in flow boiling data with small channels, the first two or three experimental data points at low qualities always report considerably higher  $HTCs$ . This is believed to be due to the increased heat transfer rate associated with the  $ONB$  (Kandlikar and Balasubramanian, 2004). This effect is not predicted by this correlation in addition to experimental results under sub-cooling conditions or the liquid deficient region at high qualities generally observed above 0.7 or 0.8.

### 2.4.2 Lee and Mudawar model

This correlation was initially obtained for R134a as the working fluid but its applicability to other fluids such as water was validated by correlating the R134a and water data with the Martinelli parameter ( $X$ ) and incorporating the boiling ( $Bo$ ) and the Weber ( $We_{Lo}$ ) numbers in the model of Lee and Mudawar (2004). The experiments were performed in a multiple channel microevaporator with a 231  $\mu m$  and 713  $\mu m$  channel width and depth respectively. For better predictions, the model was divided into three quality ranges that provided adequate coverage of both water and R134a databases. The low and high quality regions are based only on the Martinelli parameter while the mid range includes the effects of  $Bo$  and  $We_{Lo}$  as well. The low viscosity of the R134a vapor leads to vapor Reynolds numbers corresponding to turbulent flow at high heat flux conditions despite the small

hydraulic diameter of the microchannel. Thus the single-phase vapor term in the high quality correlation allows for both laminar or turbulent vapor flow.

### 2.4.3 Gungor and Winterton model

This correlation was developed with a data bank of over 4300 data points for water, refrigerants, and ethylene glycol. Mostly for saturated boiling in vertical and horizontal tubes with internal diameters between 2.95 and 32 *mm*. The correlation assumes that the two-phase flow *HTC* is a combined effect between single-phase and pool boiling. An enhancement factor *E* for the single-phase term and a suppression factor *S* for the pool boiling term were incorporated into this model. The *E* factor was correlated with the vapor quality *x* and liquid to vapor density ratio ( $\rho_l/\rho_v$ ). The original publication for this model can be found in (Gungor and Winterton, 1986) but a compact expression of this correlation for saturated boiling presented in Carey (2008) was used to compare with the experimental data in this thesis.

### 2.4.4 Lee and Garimella model

The correlation is a superposition-type model between convective and nucleate boiling heat transfer mechanisms. The experiments were performed with water as the working fluid in mini and microchannels with hydraulic diameters between 160 and 539  $\mu m$ . Similar to Gungor and Winterton's model, Lee et al. (2008) used enhancement and suppression factors for the convective and nucleate boiling terms respectively. The postulate for this correlation is that convective *HTC* is promoted as the flow is agitated by bubble nucleation and growth, while nucleate boiling is suppressed owing to the reduced superheat in the near-wall region caused by the bulk fluid. The convective term of the model was represented as the single-phase *HTC* multiplied by the enhancement factor. Since, the flow in microchannels is typically laminar, they proposed a correlation suitable for predicting laminar and thermally developing *HTC* in rectangular microchannels. The enhancement and suppression factors were obtained from regression analysis following the methodology proposed by Liu

and Garimella (2007). For the nucleated boiling  $HTC$  term, the correlation proposed by Gorenflo (1993) for water was used.

#### **2.4.5 Schrock and Grossman model**

This correlation was developed using vertical upward flow boiling heat transfer data for water in round tubes with internal diameters ranging from 2.9 to 10.8  $mm$ . This is one of the first models that correlates the two-phase flow  $HTC$  with the single-phase  $HTC$  in addition to the use of the Boiling number and the Martinelli's parameter to take into account the effects of nucleate boiling and forced convection in the two-phase flow  $HTC$ . Details of this correlation can be found in the original publication (Schrock and Grossman, 1959).

# Chapter 3

## Experimental Facility

Single-phase experiments using water as the working fluid were performed to quantify heat losses from the microchannel test apparatus to the surrounding ambient and to validate the applicability of friction factor and heat transfer macro theories in microchannels. The data could then be used as a starting condition for the two-phase flow experiments. The chapter begins with a description of the experimental setup, followed by the data reduction and an uncertainty analysis.

### 3.1 Experimental setup and procedures

#### 3.1.1 Test rig

Schematic representation and photos of the experimental set-up are shown in Figures 3.1-3.3 respectively. The sketch shown in Figure 3.1(a) illustrates the main components and fluid flow direction in the flow-regime-observation system. A steady flow of liquid to the microchannel evaporator was supplied by a Harvard Apparatus PHD2000 syringe pump for low flow rates ( $1 - 15 \text{ ml/min}$ ) or a Fluid-o-Tech DGD09A02 gear pump for higher flow rates ( $15 - 63 \text{ ml/min}$ ). The channel was tested in a horizontal orientation and given its small size, the driving force for buoyancy driven flow in a direction along the

gravity vector was minimal in comparison to the other forces acting on the control volume; therefore considered negligible. Surface tension, and evaporation momentum forces play a dominant role at the microscale (Dang et al., 2011; Kandlikar, 2010; Kandlikar et al., 2006a).

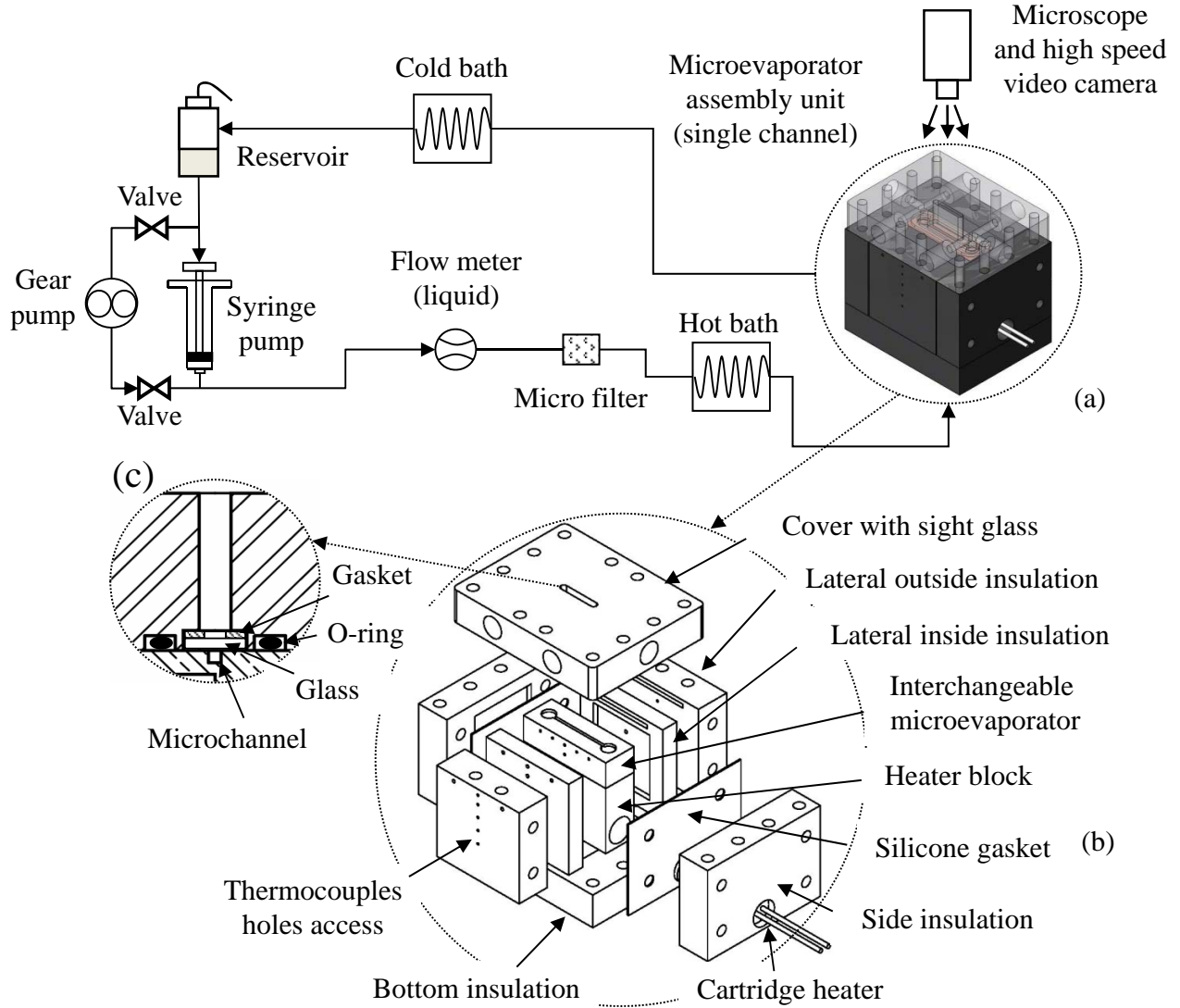


Figure 3.1: (a): main components and fluid flow direction, (b): microevaporator assembly unit, (c): sight glass section view

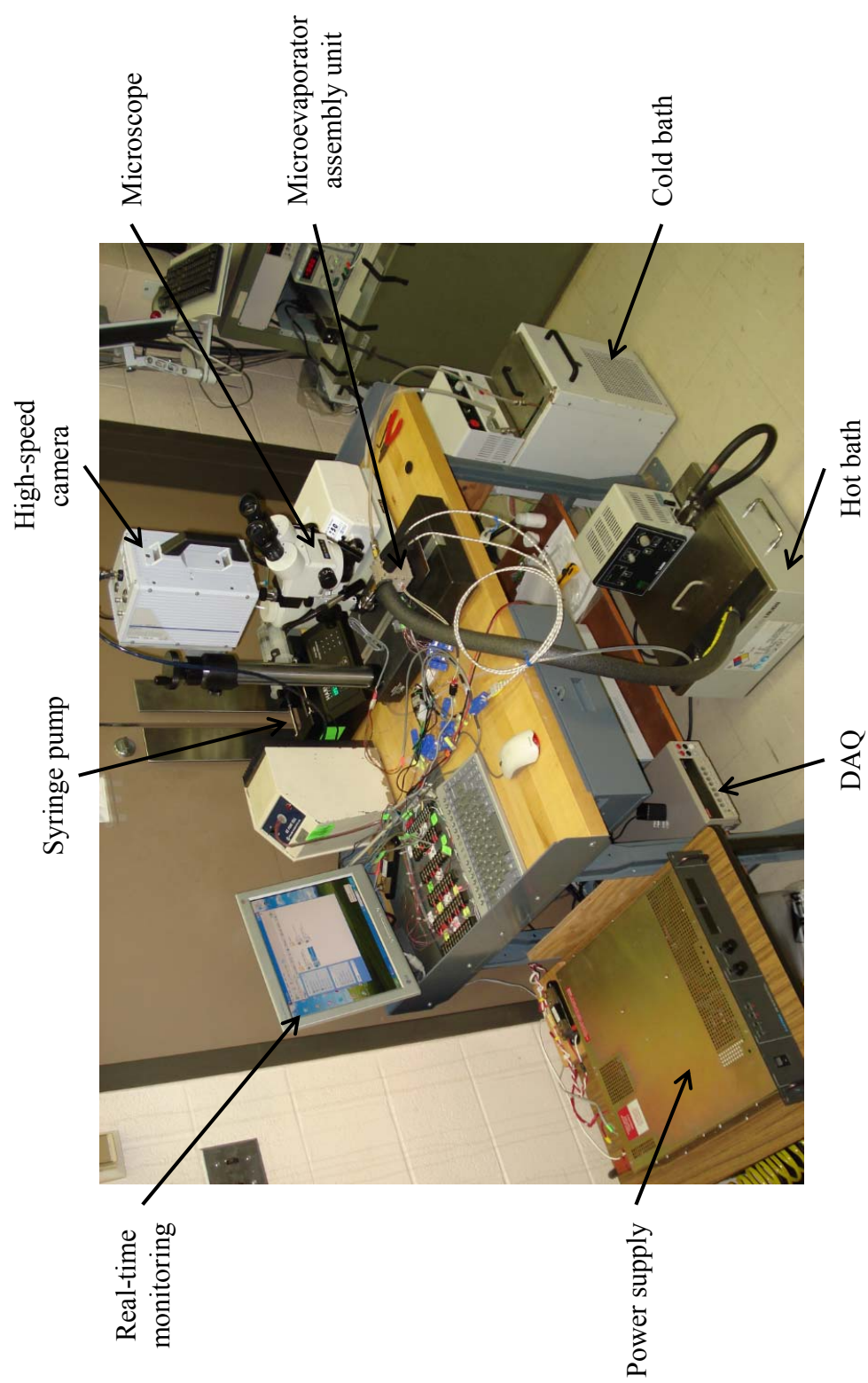
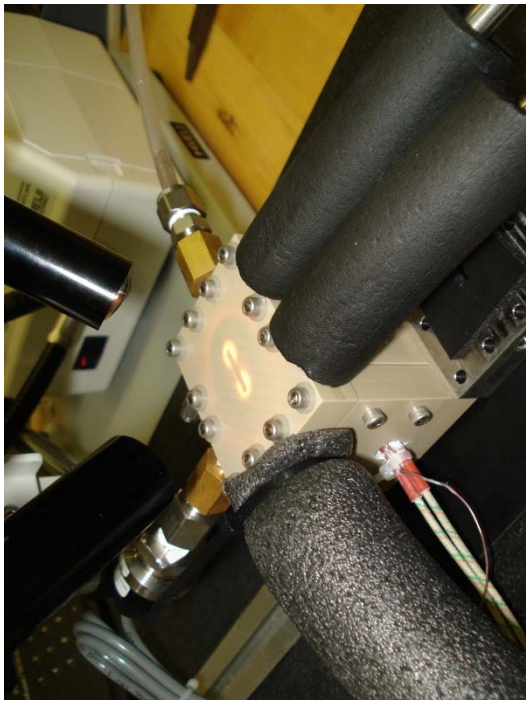
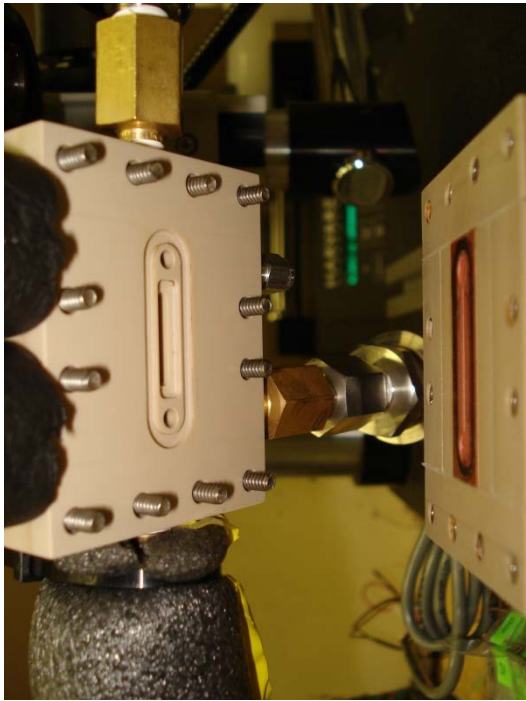


Figure 3.2: Photograph of the experimental facility





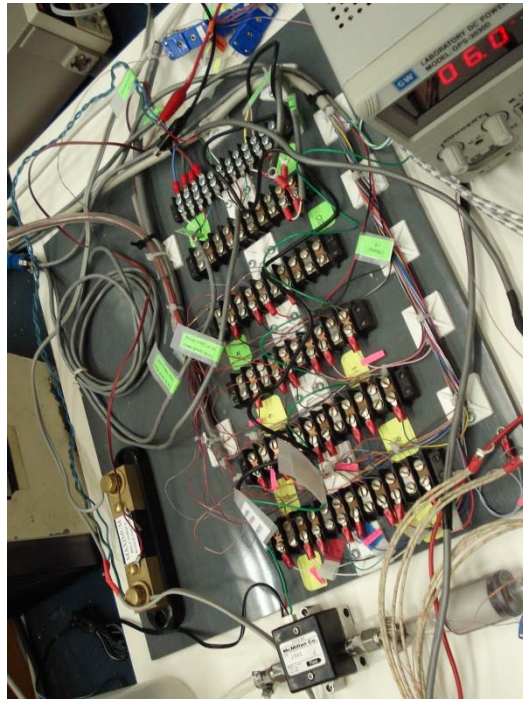
(a)



(b)



(c)



(d)

Figure 3.3: (a),(b): microevaporator assembly unit, (c) mini and microevaporator, (d) wiring board

Four different mass fluxes ( $G \simeq 350, 700, 1000, \text{ and } 1300 \text{ kg/m}^2\text{s}$ ) were evaluated during these experiments with ultra pure water as the working fluid. The outlet pressure was kept constant at atmospheric pressure, and the inlet pressure changed with the mass and heat flux. A correlation for the saturation temperature as a function of the pressure was obtained using water vapor tables to take into account the pressure drop along the channel. Since the inlet pressure was allowed to float and the inlet temperature was constant, the sub-cooling was different for each test. However in these experiments, the average sub-cooling was almost the same, ranging between  $50.7$  and  $54.2^\circ\text{C}$ . Ultra pure water was used as the working fluid. The water was boiled in the experimental facility before data were collected and possible air or gases dissolved in the water were removed in a settling reservoir open to the ambient. Any possible re-entrainment of air in the water can cause formation of bubbles before saturation temperature and can be confused with the *ONB*. In most of the cases the first bubble appeared near the saturation temperature. Cases where the first bubble formed below the saturation temperature were easily identified because bubbles formed due to trapped gases do not appear in the same location after being moved downstream by the fluid while a bubble formed at the wall by boiling re-appears in the same cavity. A Haake F3 circulating bath was used to maintain a temperature of  $50^\circ\text{C}$  at the inlet of the evaporator. The liquid flow rate to the test section was monitored by the electronic display of the syringe pump but also measured with a McMillan liquid microturbine Flo-sensor model 104. Prior to running any test, the microchannel was cleaned with liquid soldering flux and then thoroughly rinsed before filling the system with the test liquid. The soldering flux removes any layer of oxide formed at the channel surface. A miniature high-efficiency inline filter was used to remove from 93 to 99.99 % of the foreign particles at a 25 micron rating.

The convective boiling process was studied using a special microevaporator assembly unit as shown in Figure 3.1(b), with detailed drawings shown in Appendix B. The unit included a top cover plate with sight glass window which allowed flow pattern visualization, an interchangeable microevaporator, heater block, cartridge heater, and thermal insulation. The sight glass was fabricated with a  $20 \times 5 \text{ mm}$  and  $1.2 \text{ mm}$  thick gold seal glass microscope

slide and sealed with a Bisco HT-6240 transparent silicone gasket (thickness 0.020”), and an O-ring as shown in Figure 3.1(c). The microevaporator was machined from a  $44 \times 10 \times 12.7$  mm block of oxygen free copper. The microevaporator consisted of a single straight channel with rectangular cross sectional profile to avoid the non-uniform flow distribution observed with multiple channels microevaporators. In order to evaluate the effect of the channel size on flow patterns, two different microevaporators with a channel depth, width and length of  $198 \times 241 \times 21900$  and  $378 \times 471 \times 21900$   $\mu m$  were experimentally evaluated. These channel dimensions were chosen in order to fall into the range of classification for microchannel and minichannel suggested by Kandlikar et al. (2006a). Also, manufacturing smaller channels in copper is more challenging with micromilling technology.

The microevaporator was heated along its lower boundary using a 400 watt Watlow cartridge heater embedded in the oxygen free copper heater block. The heat flow provided to the microevaporator was controlled with the supplied power (e.g. controlling the voltage) to the cartridge heater ranging between 5 and 130 watts until steady state was reached or when the maximum temperature reached  $180^{\circ}C$  to avoid damage to the silicone gaskets. This heater block provides a virtually uniform channel wall temperature along the length of the channel. Heat was conducted from the heater along the heater block to the microevaporator where it was transferred to the fluid in the microchannel. The single channel evaporator and the heater block were completely enclosed in insulation so that heat leakage to the surroundings was minimized. Polyetheretherketone known as “PEEK” was used as insulation material and two gaskets fabricated with Bisco HT6135 solid silicone (thickness 0.015”) were used in the side insulation blocks to take into account thermal expansion. Additionally, cavities in the insulation blocks were machined in order to trap air and minimize heat losses.

A Fisher Scientific ice point cell RC-140 was used as an external reference junction for more accurate temperature readings (down to  $0.2^{\circ}C$ ). Nine T-type thermocouples were embedded in the evaporator and heater block along the middle plane of the evaporator to determine the temperature gradient and channel surface temperature as shown schematically in Figure 3.4, with detailed drawings shown in Appendix B (Figures B.6 and B.7).

T-Type thermocouples and Omega pressure sensors PX481A-060G5V were also located at the inlet and outlet of the microchannel to measure the local fluid temperature and pressure drop along the microchannel with an accuracy of 0.2% FS. For the lowest pressure drops in the experiments (below  $\approx 6.3 \text{ kPa}$ ), an Omega differential pressure sensor PX26-005GV was used to decrease uncertainty (accuracy 1% FS). The measured temperature gradient was used to calculate the surface temperature at the channel wall by extrapolation.

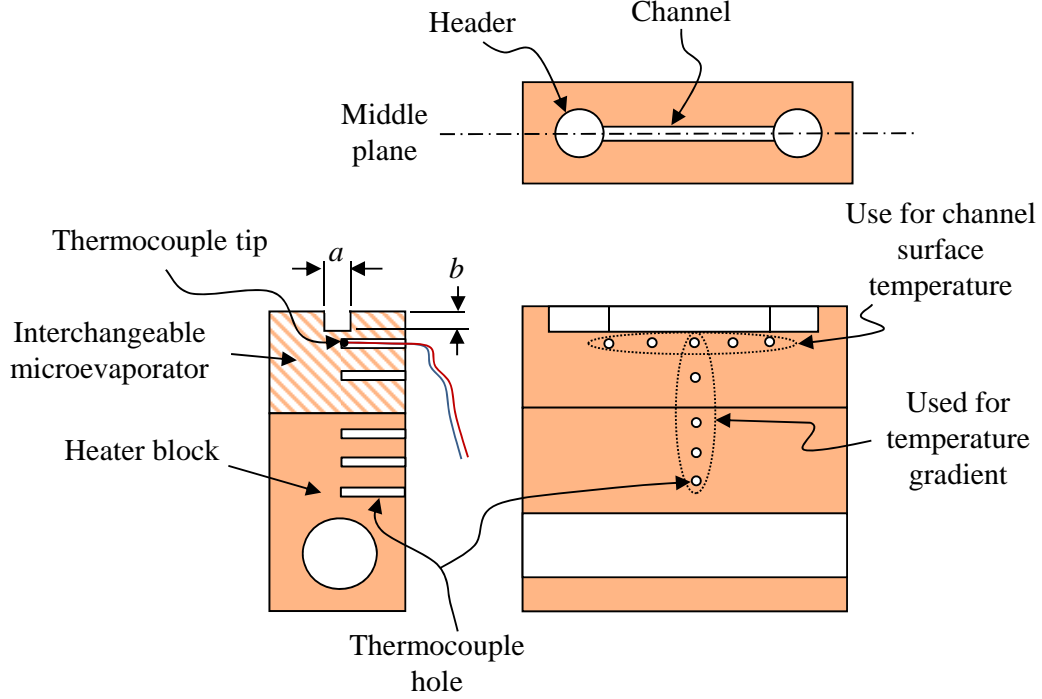


Figure 3.4: Schematic thermocouple locations in evaporator and heater block (dimensions are shown in Appendix C, Figure C.2)

The heat supplied to the microchannel was estimated based on the heater power (voltage $\times$ current) minus the heat losses. During steady state conditions, 50 experimental data points for each measured parameter were recorded using a Keithley DAQ system with a 7700-20 channels multiplex module, and ExceLINX software. Simultaneously, the flow patterns were also recorded using a high-speed digital video camera (Photron FastCam S1A) installed in a Meiji-EZ-13 stereo microscope. The high-speed videos were recorded at  $128 \times 60$  pixels and between 2,000 and 30,000 frames per second. Some images recorded

at higher frame rates were post-processed using Matlab image processing tools to enhance the quality. Finally, the fluid leaving the evaporator was condensed using a spiral copper tube immersed into a Haake A81 circulating bath at  $24^{\circ}\text{C}$  and returned to a reservoir at atmospheric pressure.

### 3.1.2 Microchannels

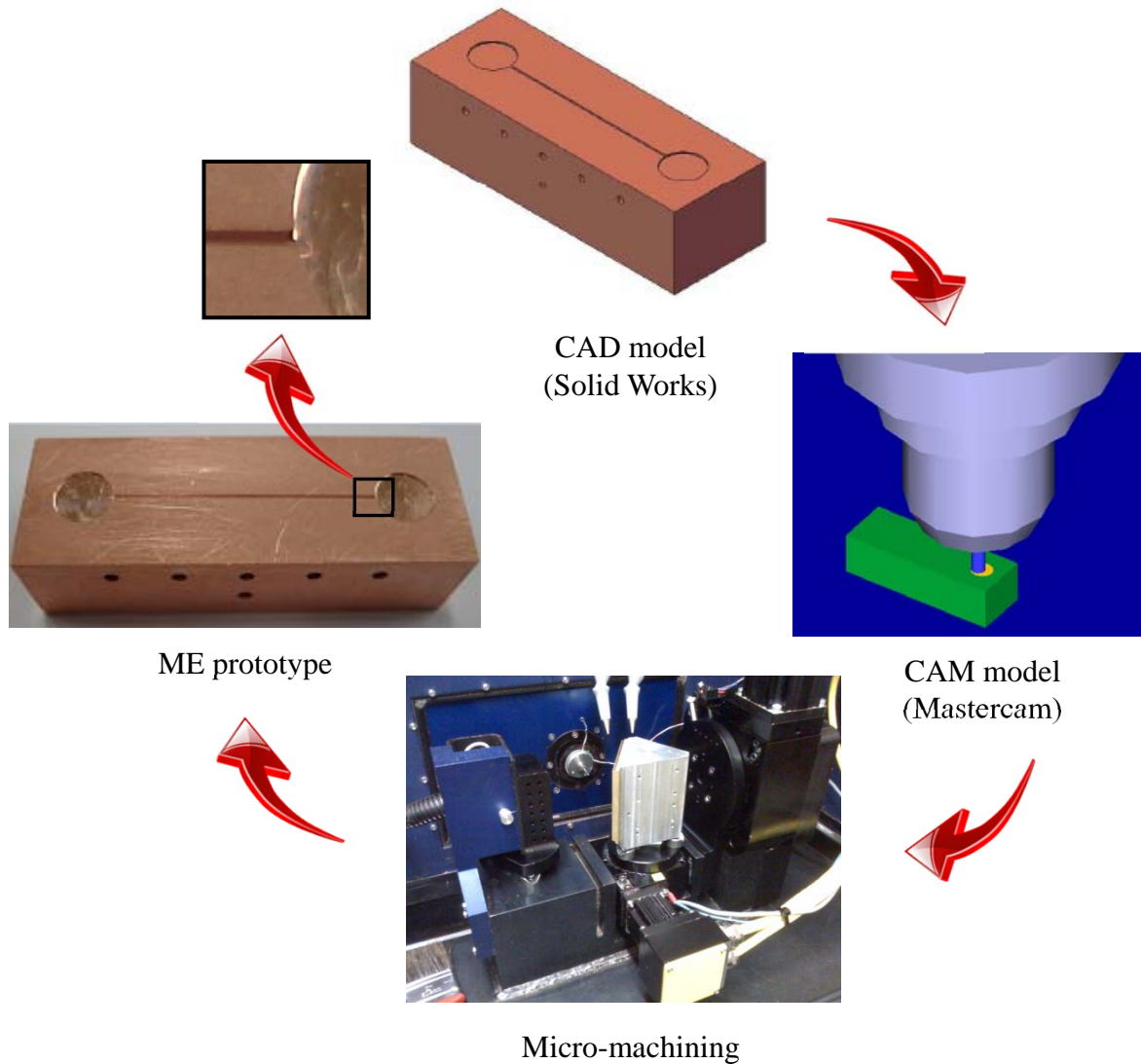

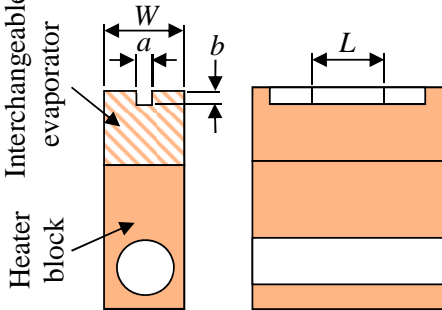


Figure 3.5: Microchannel design and manufacturing process

Two microevaporators were used in the experimental investigations. Figure 3.5 shows the design and manufacturing process for the microevaporators. The mini and microchannel were designed and manufactured in-house using CAD (Solid Works), CAM (MasterCam) software, and the “G-code” generated in MasterCam was transferred to a micro-milling machine for the cutting process.

The microevaporator prototype (ME prototype as shown in Figure 3.5) consists of a circular header (diameter =  $5\text{ mm}$   $\times$  depth = channel depth) at the inlet and outlet connected by a channel approximately  $19\text{ mm}$  in length. The headers provide an equalization of fluid pressure at the inlet and exit of the channel (see Appendix B for headers dimensions). The appropriate location of the thermocouples in the microevaporator and in the heater block were estimated using a 3D steady state finite element model, where results are shown in Appendix C.

Table 3.1: Channel dimensions

<i>Channel geometry</i>		<i>L, mm</i>	<i>b, <math>\mu\text{m}</math></i>	<i>a, <math>\mu\text{m}</math></i>	<i>R<sub>a</sub>, <math>\mu\text{m}</math></i>
 198x241 378x471	 Interchangeable evaporator Heater block	21.9	198	241	0.65
		21.9	378	471	0.54

$W=12,7\text{ mm}$

Channel dimensions and surface roughness ( $R_a$ <sup>1</sup>) of the microevaporators are shown in Table 3.1. The channel dimensions were measured using a Mitutoyo SJ-400 surface roughness tester and confirmed with an Olympus U-PMTVC optical microscope (with a Photometrics CoolSNAP CCD camera, and image Pro Plus software), both methods differ by less than 2 % in the channel size measurements. A typical channel width registered by both methods is shown in Figure 3.6. For this particular location in the channel, the

<sup>1</sup>Defined as the arithmetical mean of the absolute values of the profile deviations from the mean line.

surface roughness tester registered a channel width of  $242\text{ }\mu\text{m}$  which is comparable with the  $238\text{ }\mu\text{m}$  observed with the microscope (see Appendix D for more channel size registered data).

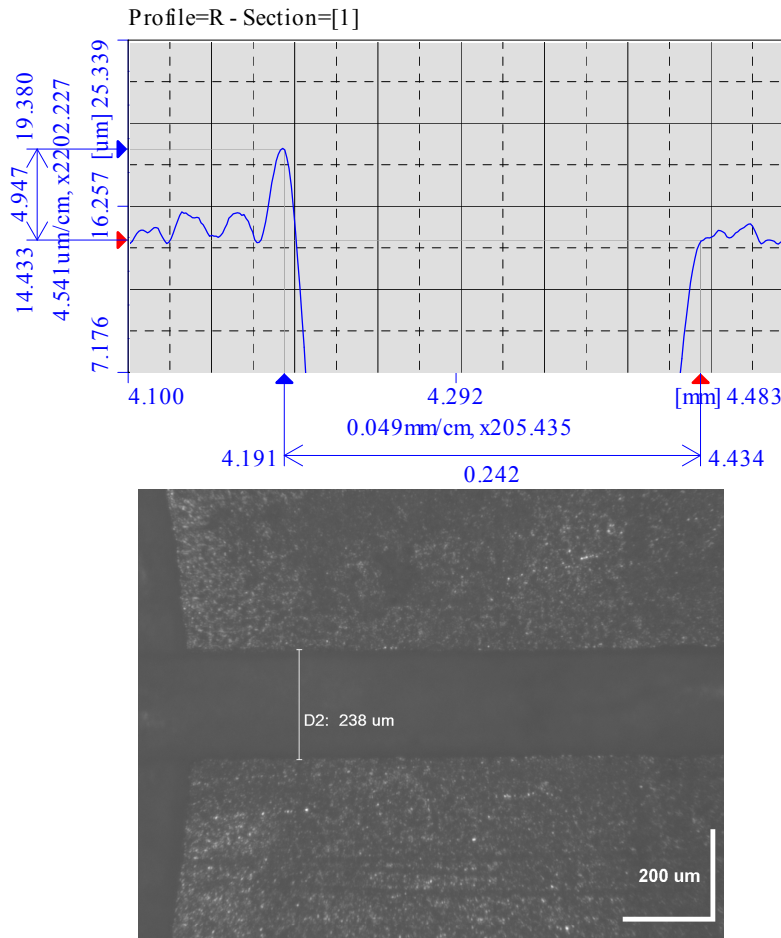


Figure 3.6: Channel width measurement techniques, top: with surface roughness profile, bottom: with electronic microscope



## 3.2 Data reduction

### 3.2.1 Single-phase flow

#### Friction factor

Measuring the local pressure along the flow is difficult in microchannels and normally the experimental pressure drop represents the combined effect of the losses in the bends, entrance and exit losses, developing region effects and the core frictional losses. The schematic representation of the pressure drop measurements is shown in Figure 3.7.

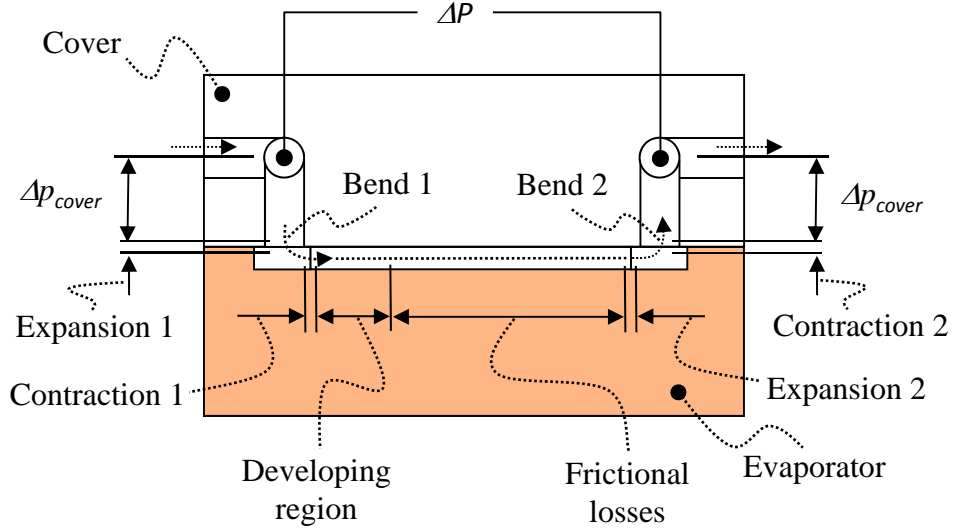


Figure 3.7: Schematic representation for pressure drop measurements in microevaporator (location of inlet pressure sensor shown in Appendix B, Figure B.3)

The pressure drop for bends, fluid contraction and expansion losses (usually called minor losses,  $\Delta p_{min}$ ) was obtained from Phillips (1990) and shown in Equation 3.1. The pressure drop for the cover, first expansion and second contraction ( $\Delta p_{cover}$ , Expansion 1, and Contraction 2, in Figure 3.6) were between 0.4 and 4.8% of the minor losses, therefore they were neglected.



$$\Delta p_{min} = \frac{\rho u^2}{2} \left[ \left( \frac{A}{A_h} \right)^2 2K_b + K_c + K_e \right] \quad (3.1)$$

In Equation 3.1  $A$  and  $A_h$  are the channel and header cross sectional area respectively.  $K_b$  is the loss coefficient for the bends,  $K_c$  and  $K_e$  respectively represent the contraction and expansion loss coefficients due to area changes. Phillips (1990) recommended  $K_b$  to be approximately 1.2 for a 90 degree and a contraction and expansion loss coefficient  $K_c = 0.8$  @  $Re \leq 2000$ ,  $K_c = 0.5$  @  $Re > 2000$  and  $K_e = 0.9$ . Finally, the experimental pressure drop in the channel after correction can be calculated from the experimental pressure measured minus the minor losses.

$$\Delta p_{exp} = \Delta p_{measured} - \Delta p_{min} \quad (3.2)$$

The experimental single-phase friction factor  $f_{exp}$ , was calculated using the experimental channel frictional pressure drop  $\Delta p$ , measured across the whole length of the test section  $L$ , in the Darcy-Weisbach equation:

$$f_{exp} = \Delta p_{exp} \frac{d_h}{2L\rho u^2} \quad (3.3)$$

where, the hydraulic diameter is defined as  $d_h = 4A/P$  ( $A$ : channel cross sectional area,  $P$ : channel wetted perimeter). The fluid properties were evaluated at the arithmetic mean temperature between the inlet and outlet  $(T_{in} + T_{out})/2$ .

The experimental friction factor obtained from the above equation was compared with the friction factor  $f$ , calculated for laminar fully developed flow proposed by Shah and London (1978) (Equation 3.4) and the Blasius equation for turbulent flow (Equation 3.5).

$$f Re = 24(1 - 1.3553\alpha + 1.9467\alpha^2 - 1.7012\alpha^3 + 0.9564\alpha^4 - 0.2537\alpha^5) \quad (3.4)$$

In Equation 3.4 the channel aspect ratio  $\alpha = b/a$  if  $b \leq a$ , or  $\alpha = a/b$  if  $b > a$ .

$$f = 0.0791Re^{-0.25} \quad (3.5)$$

To account for the developing region, the microchannel pressure drop equation was presented in terms of an apparent friction factor in the following form:

$$\Delta p = \frac{2f_{app}L\rho u^2}{d_h} = \frac{2fL\rho u^2}{d_h} + K\frac{\rho u^2}{2} \quad (3.6)$$

$K$  represents the Hagenbach's factor for rectangular channels obtained by Steinke and Kandlikar (2006).

$$K = 0.6796 + 1.2197\alpha + 3.3089\alpha^2 - 9.5921\alpha^3 + 8.9089\alpha^4 - 2.9959\alpha^5 \quad (3.7)$$

### Heat transfer coefficient

For single-phase flow, the average heat transfer coefficient is traditionally expressed in its dimensionless form by means of the average Nusselt number,  $\overline{Nu}$ , which may be defined as the ratio of convective to conductive heat transfer across the boundary with the expression:

$$\overline{Nu} = \frac{\bar{h} d_h}{k_f} \quad (3.8)$$

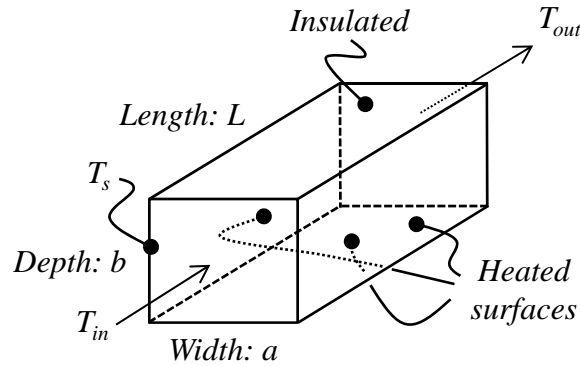


Figure 3.8: Control volume and boundary conditions for the channel

The channel was heated along three surfaces and insulated on the top surface as shown Figure 3.8. Since the measurements of the experimental surface temperature along the channel indicated isothermal boundary condition, the average heat transfer coefficient  $\bar{h}$  was calculated as:

$$\bar{h} = \frac{Q_{fluid}}{A_s \Delta T_{\ell n}} \quad (3.9)$$

where  $A_s$  and  $\Delta T_{\ell n}$  are the heat transfer surface area and the log mean temperature difference respectively as shown in Equations 3.10 and 3.11.

$$A_s = (a + 2b)L \quad (3.10)$$

$$\Delta T_{\ell n} = \frac{\Delta T_{out} - \Delta T_{in}}{\ln \left( \frac{\Delta T_{out}}{\Delta T_{in}} \right)} \quad (3.11)$$

$\Delta T_{out}$  and  $\Delta T_{in}$  in Equation 3.11 are expressed in terms of the channel surface temperature  $T_s$  and the inlet and outlet fluid temperature as:

$$\Delta T_{out} = T_s - T_{out} \quad \text{and} \quad \Delta T_{in} = T_s - T_{in} \quad (3.12)$$

The heat absorbed by the fluid  $Q_{fluid}$  can be obtained from:

$$Q_{fluid} = \dot{m} c_p (T_{out} - T_{in}) \quad (3.13)$$

Substituting Equation 3.11 and Equation 3.13 into Equation 3.9, the heat transfer coefficient can be expressed as:

$$\bar{h} = -\ln \left( \frac{\Delta T_{out}}{\Delta T_{in}} \right) \frac{\dot{m} c_p}{A_s} \quad (3.14)$$

Fluid properties were calculated at the mean fluid temperature,  $(T_{out} + T_{in})/2$  using the correlations shown in Appendix E.

### 3.2.2 Two-phase flow

An energy balance can be written for the microevaporator assembly unit as:

$$Q_{total} = Q_{fluid} + Q_{loss} \quad (3.15)$$

in which,  $Q_{total}$  is the total heat supplied by the cartridge heater,  $Q_{fluid}$  is the heat removed by the fluid, and  $Q_{loss}$  is the heat loss. The total heat was obtained directly as  $Q_{total} = VI$  ( $V$ , is the applied voltage and  $I$ , is the current in the heater). The current in the heater was estimated measuring the voltage through a calibrated 0.01 ohm shunt resistance  $I = V_{shunt}/R$ . The heat loss to the ambient from the test section was estimated from the difference between the total heat and the sensible heat gain by the fluid under single-phase condition as:

$$Q_{loss} = Q_{total} - \dot{m}c_p(T_{f,out} - T_{f,in}) \quad (3.16)$$

The previous equation is only valid for single-phase experiments. However, to extend its applicability for two-phase flow, a similar methodology proposed by Liu and Garimella (2007) was used. The heat loss obtained from Equation 3.16 was correlated with the average channel wall temperature. Therefore, a linear correlation of the heat loss as a function of channel wall temperature was obtained [ $Q_{loss}(T_w) = mT_w + b$ ]. Then, the heat removed by the fluid for single and two-phase flow experiments can be estimated from Equation 3.17. Values of  $m$  and  $b$  values for the  $Q_{loss}$  correlations associated with each mass flux and channel size tested in this work are shown in Appendix F.

$$Q_{fluid}(T_w) = Q_{total} - Q_{loss}(T_w) \quad (3.17)$$

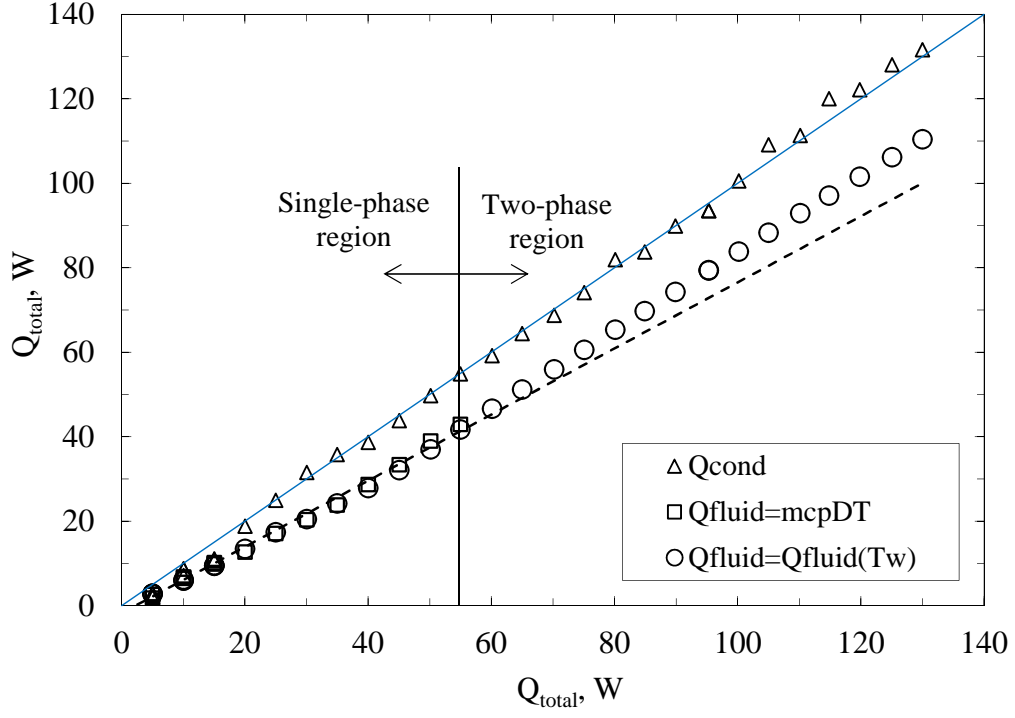


Figure 3.9: Heat removed by fluid for  $378 \times 471 \mu m$  microevaporator at  $G = 1373 kg/m^2s$

Figure 3.9, shows the variation of the heat transfer by conduction through the copper heater block ( $Q_{cond}$ ), the fluid removed by the fluid as sensible heat ( $Q_{fluid} = \dot{m}c_p\Delta T$ ), and the heat removed by the fluid  $Q_{fluid}(T_w)$  with respect to the total heat supplied by the heater ( $Q_{total}$ ) for the channel size  $378 \times 471 \mu m$  at  $G = 1373 kg/m^2s$ . From Figure 3.9, it can be clearly seen that  $Q_{fluid}(T_w)$  follows a different slope in the two-phase flow region which can be attributed to the high heat transfer coefficient associated with latent heat.

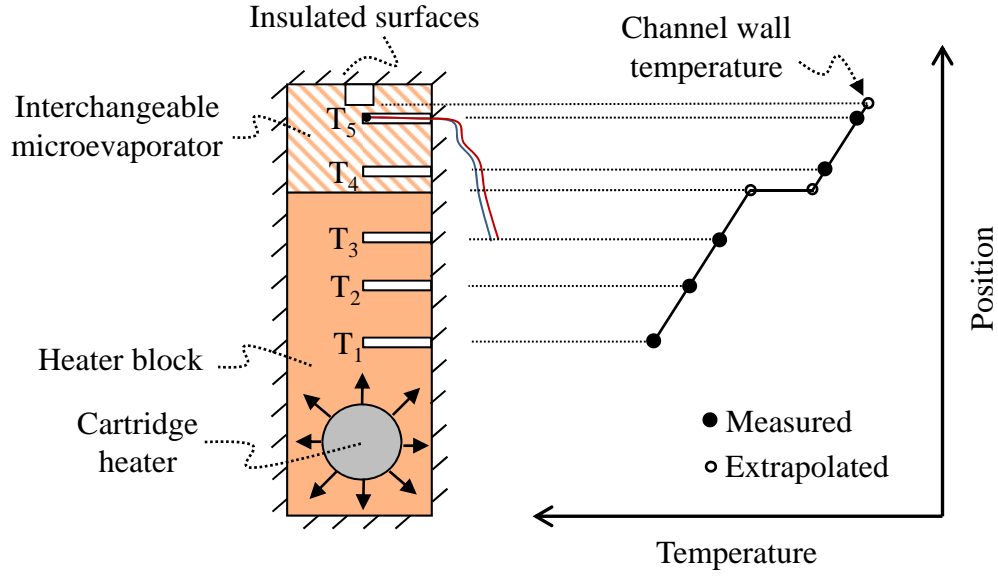


Figure 3.10: Measurement of the gradient of temperature in microevaporator and heater block

The heat by conduction was calculated with the thermal conductivity of the oxygen free copper and the gradient of temperature along the the heater block and the interchangeable evaporator as shown in Figure 3.10. Note that the heat transfer by conduction ( $Q_{cond}$ , in Figure 3.9) was very similar to the total heat, showing a linear behavior which indicates that most of the losses are by conduction.

The local two-phase flow heat transfer coefficient for the microevaporator was calculated from:

$$h = \frac{q_w}{T_w - T_{sat}} \quad (3.18)$$

where  $T_w$  is the local channel wall temperature (measured by extrapolation),  $T_{sat}$  is the local saturation temperature which decreases in the flow direction due to changes in pressure along the channel. Therefore, a correlation for the local saturation temperature as a function of the pressure was developed and a linear pressure drop from the inlet to the exit of the channel was assumed. Fluid properties such as thermal conductivity, specific

heat, density, dynamic viscosity, saturation temperature, enthalpy, and latent heat of vaporization were corrected for temperature and the correlations can be found in Appendix E.

The thermal conductivity of the oxygen free copper was experimentally measured in accordance with ASTM D5470. The experiments were performed in a vacuum chamber to minimize heat losses by convection. Figure 3.11 shows the test rig for measurement of thermal conductivity of oxygen free copper. Since this method requires measurement of the gradient of temperature along the sample, thermocouples were located in the isothermal planes which were identified through finite element simulation (see Appendix C for finite element model, and the experimental results for the thermal conductivity). Since negligible effects on temperature in the range of study were observed, and an average of  $384 \text{ W/mK}$  was used for the thermal conductivity. The fin effect in the microevaporator was neglected since the channel wall thickness was much larger than the channel depth.

The wall heat flux  $q_w$ , is defined as:

$$q_w = \frac{Q_{fluid}}{(a + 2b)L} \quad (3.19)$$

where  $a$ ,  $b$ , and  $L$  are the channel width, depth, and length respectively.

The exit vapor quality  $x$ , was calculated from an energy balance in the channel as:

$$x = \frac{1}{h_{fg}} \left[ \frac{Q_{fluid}}{\dot{m}} - c_p(T_{sat} - T_{in}) \right] \quad (3.20)$$

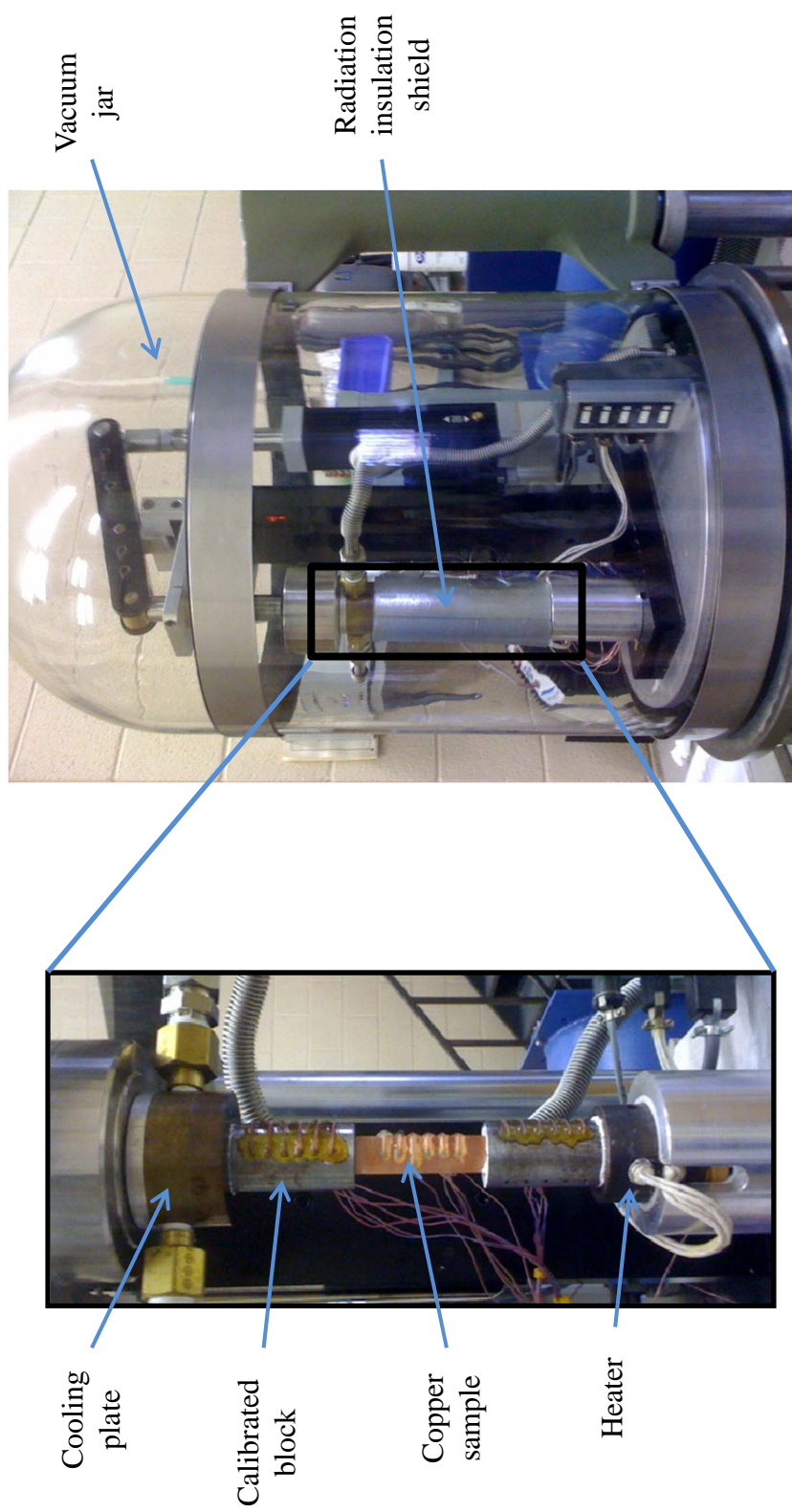


Figure 3.11: Test rig for thermal conductivity measurements



### 3.3 Uncertainty analysis

The overall uncertainty can be obtained by adding uncertainties of type A and B. Type A (also called random uncertainty or precision error) is statistical in nature and can be estimated by the standard deviation, ( $\sigma$ ) of the mean value for a quantity which has been measured a sufficiently large number of times (usually measured more than 20 times). Type B (also called systematic uncertainty or bias error) is however, not statistical in nature and most of the time is constant and can be estimated from previously available measurement data, experience or general knowledge of the instruments, manufacturer's specifications, data provided in calibration and other reports, and uncertainties assigned to reference data taken from handbooks.

$$U = [(Type\ A)^2 + (Type\ B)^2]^{1/2} \quad (3.21)$$

The various sources of error of type B are independent and can be combined using the root-sum-square (RSS) method to calculate the total uncertainty due to type B. According to BIPM/ISO standards, the overall uncertainty  $U$  of a quantity due to the two types of uncertainties (i.e. type A and B) is thus determined by RSS method as shown in Equation 3.21.

Random uncertainty was typically neglected for most of the data given that it would only affect the overall uncertainty by less than 1%. In some instances, such as two-phase flow with pressure drops in excess of 24  $kPa$ , where oscillation are significant, random uncertainty was considered. In these cases precision error increased from 1 to 44 % and the bias error decreased from 3.4 to 0.7 %

The uncertainty type B for the measured and calculated variables was estimated based on the method described by Coleman and Steele (1989). In this method is assumed that a quantity  $R$ , it is determined from a set of measured values,  $X_j$ :

$$R = R(X_1, X_2, X_3, \dots, X_N) \quad (3.22)$$

where each measured value  $X_j$  has an associated uncertainty represented by the notation  $\delta X_j$ , the effect of the uncertainty in  $X_j$  on the result  $R$  is calculated by:

$$\delta R_{X_j} = \frac{\partial R}{\partial X_j} \delta X_j \quad (3.23)$$

where  $\delta R_{X_j}$  refers to the uncertainty in  $R$  as a result of the uncertainty in the  $X_j$  measurement. Then the uncertainty in the result is given in general form as:

$$\delta R = \pm \left\{ \left( \frac{\partial R}{\partial X_1} \delta X_1 \right)^2 + \left( \frac{\partial R}{\partial X_2} \delta X_2 \right)^2 + \dots + \left( \frac{\partial R}{\partial X_j} \delta X_j \right)^2 \right\}^{1/2} \quad (3.24)$$

Detailed calculation of the uncertainty on the measured and calculated variables is shown in Appendix A, and a summary of the uncertainties for the experimental data in this thesis is shown in Table 3.2.

In these experiments, all measured variables were registered in a DAQ through sensors that produce a voltage signal proportional to the measured variable. Although, the DAQ has very low uncertainty in the reading of voltage ( $\pm 0.4\%$ ), and each transducer has low uncertainty ( $\leq 5\%$ ), the uncertainties of some calculated variables such heat transfer coefficient and friction factor reached values up to 17.7 and 29.8 % respectively. It is important to mention that these high uncertainties are only present in a small portion of the measurement range. Moreover, high values of uncertainties in calculated variables are normally presented in micro and microchannels due to the error propagation (addition of each individual error as shown in Equation 3.24). This is one of the reasons that making measurements in microchannels is very challenging. As a reference, uncertainties ranging between 17 and 25 % were also reported by Callizo (2010); Megahed (2010) in round pipes and rectangular channels with hydraulic diameters between 268 and 640  $\mu m$ .

Table 3.2: Uncertainties for experimental data (\*includes precision and bias errors. The high uncertainty of  $\approx 44\%$  is only for the two highest heat fluxes at each mass flux tested).

<i>Variable</i>	<i>Range</i>	<i>Uncertainty, %</i>
Voltage	1-25 mV 5-100 V	$\pm 0.4$ negligeble
Current	1-2.5 A	$\pm (0.6-0.1)$
Temperature	24-180, °C	$\pm (0.8-0.1)$
Pressure single-phase flow	6.3-237 kPa	$\pm (13.1-0.3)$
Pressure two-phase flow	6.3-24 kPa 24-113 kPa	$\pm (13.1-3.4)$ $\pm (3.4-44.0)^*$
Flow rate	1-15 ml/min 15-64 ml/min	$\pm 0.4$ $\pm 2.7$
Channel dimensions (bxa) 198x241 $\mu m$ 378x471 $\mu m$	198-241 $\mu m$ 378-471 $\mu m$	$\pm 4.7$ $\pm 2.8$
Reynolds number, $R_e$ channel (198x241 $\mu m$ ) channel (378x471 $\mu m$ )	119-863 280-1725	$\pm 3.2$ $\pm 1.9$
Mass flux, $G$ channel (198x241 $\mu m$ ) channel (378x471 $\mu m$ )	340-1297 kg/m <sup>2</sup> s 364-1373 kg/m <sup>2</sup> s	$\pm 6.2$ $\pm 2.8$
Heat flux (single-phase), $q_w$ channel (198x241 $\mu m$ ) channel (378x471 $\mu m$ )	50-2900 kW/m <sup>2</sup> 112-3720 kW/m <sup>2</sup>	$\pm 9.1$ $\pm 8.6$
Heat flux (two-phase), $q_w$ channel (198x241 $\mu m$ ) channel (378x471 $\mu m$ )	63-2700 kW/m <sup>2</sup> 55-4300 kW/m <sup>2</sup>	$\pm (11.6-3.3)$ $\pm (2.9-1.1)$
Heat transfer coefficient, $h_{tp}$ channel (198x241 $\mu m$ ) channel (378x471 $\mu m$ )	40-713 kW/m <sup>2</sup> K 89-960 kW/m <sup>2</sup> K	$\pm (17.7-3.4)$ $\pm (13.8-1.4)$
Single-phase Nusselt number, $\overline{Nu}$ channel (198x241 $\mu m$ )	47.7-4.6	$\pm (28.8-5.5)$
Single-phase friction factor, $f$ channel (198x241 $\mu m$ )	0.011-0.444	$\pm (29.8-16.3)$
Vapor quality, $x$ channel (198x241 $\mu m$ ) channel (378x471 $\mu m$ )	0.04-0.49 0.04-0.54	$\pm (25.0-9.0)$

# Chapter 4

## Single-Phase Flow and Heat Transfer

Single-phase heat transfer and pressure drop experiments were performed prior to the boiling tests mainly to check the energy balance, validate measurement equipment, experimental procedures and the applicability of conventional macro theory for friction factor and Nusselt number in rectangular channels with a hydraulic diameter of approximately  $200\ \mu m$ . The heat loss in the sample was evaluated in the insulated microchannel during single-phase, based on the heat provided by a cartridge heater ( $Q_{total}$ ) and the heat removed by the fluid ( $Q_{fluid}$ ). After, the heat loss was properly quantified (as described in section 3.2.2), the friction factor and Nusselt number were experimentally measured and compared with traditional macro theories.

## 4.1 Single-phase friction factor

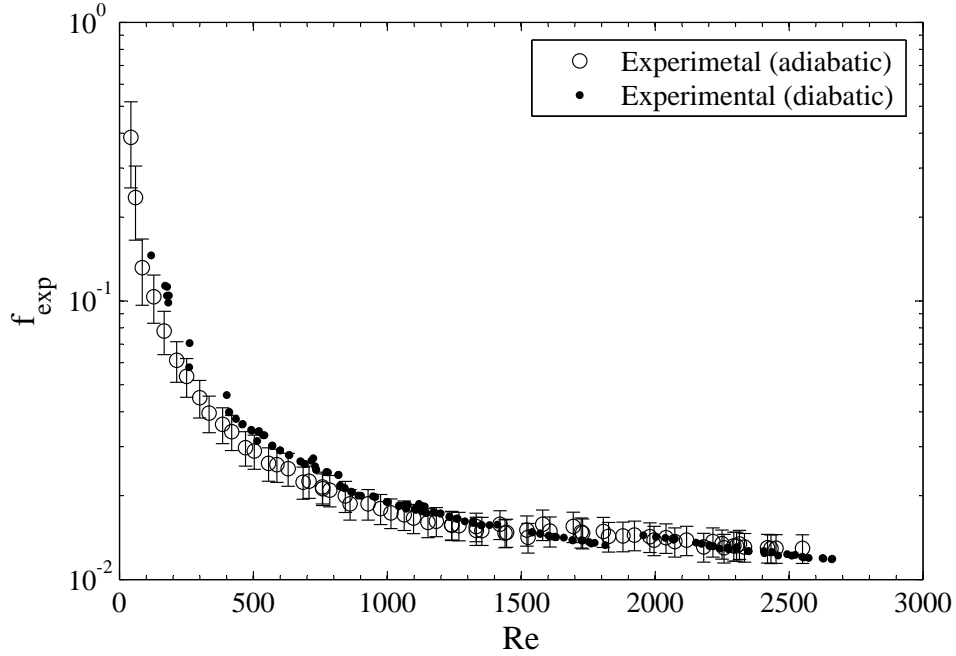


Figure 4.1: Experimental friction factor for single-phase adiabatic and diabatic rectangular channel with  $d_h \approx 200 \mu m$

Single-phase pressure drop experiments have been performed in the smallest channel ( $198 \times 241 \mu m$ ) size during adiabatic and diabatic conditions (heat input between 0 and 50 W). The experimental single-phase friction factor vs Reynolds number for adiabatic and diabatic conditions is shown in Figure 4.1. Only the uncertainty on the friction factor for the adiabatic case is shown in this figure for easy reading. Clearly, the friction factor for diabatic and adiabatic cases are comparable after  $Re \geq 900$ . For  $Re < 900$ , the uncertainty in the friction factor and Reynolds number are higher, and both cases (diabatic and adiabatic) are also comparable within the uncertainties of the measurements.

The calculation of the friction factor using the Darcy-Weisbach (Eq. 3.3) requires the local pressure drop along the microchannel which is difficult to measure experimentally. Normally, the experimental pressure drop in microchannels includes the effects of bends,

and fluid contraction and expansion as described in section 3.2.1 as the minor losses. Since the minor losses increase with the square of the velocity, it is possible to find an appreciable difference between the measured pressure drop and the pressure drop along the microchannel as the Reynolds number increases.

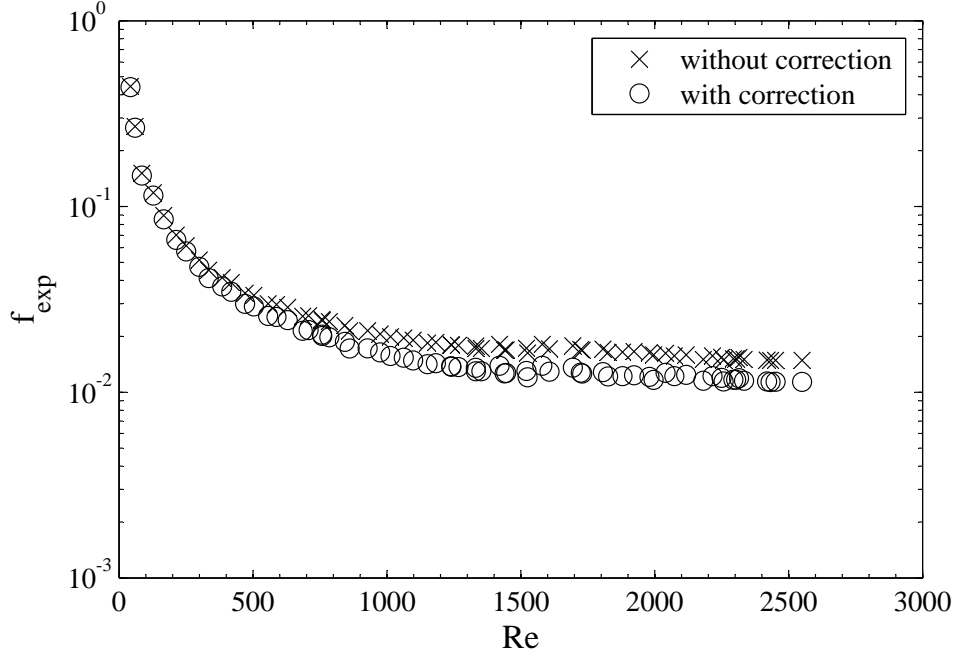


Figure 4.2: Experimental friction factor with and without minor losses correction

The experimental friction factor calculated with and without minor losses as a function of the Reynolds number is shown in Figure 4.2. The results of the friction factor with minor losses correction are tabulated in Appendix G section G.1. The friction factor with minor losses correction is smaller than the friction factor without correction for  $Re \geq 500$ . This is attributed to the fact that minor losses increase with the velocity. Therefore, minor losses have a strong effect on the friction factor as the Reynolds number increases. The minor losses were estimated between 1 and 30 % of the measured pressure drop. Therefore, in these experiments, the measure pressure drop was corrected for the minor losses in order to estimate the experimental pressure drop along the channel. Once the pressure drop along the microchannel was estimated, the theoretical and experimental friction factors

were compared. It is important to mention that in the calculation of friction factor, the density of the fluid was temperature dependent and estimated based on the correlation shown in Appendix E.

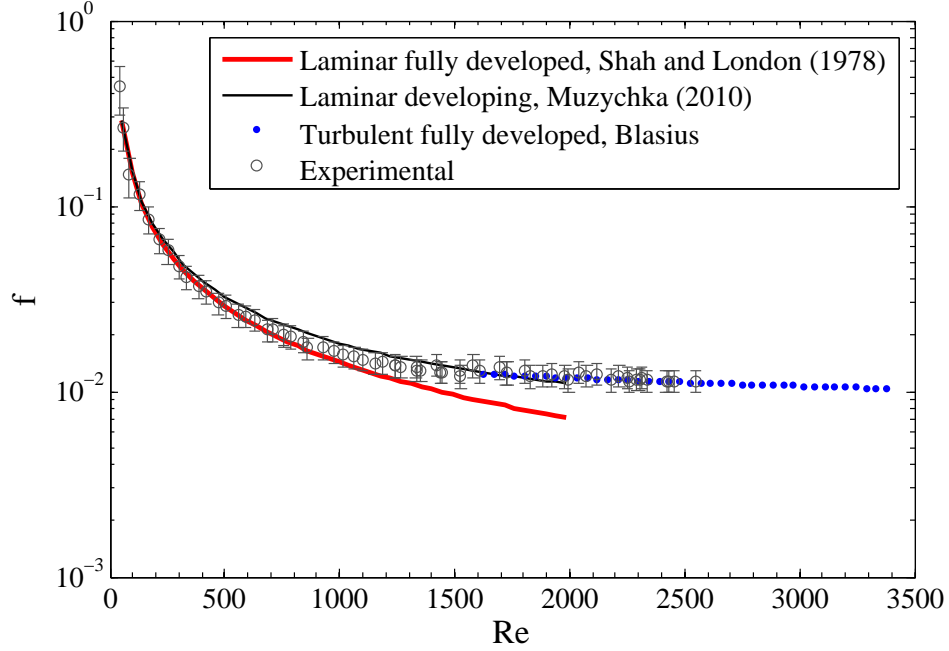


Figure 4.3: Comparison of experimental friction factor with traditional correlations for macrochannels

Figure 4.3 shows the variation of the experimental friction factor (after minor losses correction) with respect to the Reynolds number. The figure also shows the friction factors obtained for laminar fully developed flow (Equation 3.4), laminar developing flow (Muzychka and M.M.Yovanovich, 2010), and the Blasius equation for fully developed turbulent flow (Equation 3.5) in conventional macro theory. The experimental data show good agreement with the laminar fully developed theory for  $Re \leq 500$ . For  $Re > 500$  the entrance effects may cause increases in pressure drop and the laminar fully developed macro theory cannot predict the experimental data. A transition between fully developed and developing flow is observed at  $500 < Re \leq 1600$ . Considering the uncertainty in the friction factor, both laminar developing or turbulent theory can predict the experimental data for  $1600 < Re \leq 2600$ .

As shown in Figure 4.3, the experimental data deviated from the laminar fully developed theory at  $Re \approx 500$ . To confirm if this deviation is directly related to the developing entrance length, the effects of Reynolds number, hydraulic diameter, and channel aspect ratio on the entrance length in rectangular microchannels were investigated in microchannels. Details of this study using numerical methods were published in the paper Galvis et al. (2012) and a brief description of the methodology and results are described as follows:

Laminar flow in a rectangular channel was modeled using incompressible laminar Navier-Stokes equations using ANSYS CFX 12.1. The simulations were performed for a range of Reynolds numbers from 0.5 to 200. Square channels 100, 200, 400, and 500  $\mu m$  wide and rectangular mini and microchannels of comparable dimensions with channel aspect ratios ( $\alpha = b/a$ ) between 1 and 5 were investigated. The fluid properties were assumed to be constant, neglecting viscous dissipation, which was shown to be a valid assumption for water in microchannels with  $d_h \geq 100 \mu m$  (Celata et al., 2006; Morini, 2005; Koo and Kleinstreuer, 2004). The simulations were compared with available experimental data and new correlations for estimating the entrance length in mini and microchannels were proposed.

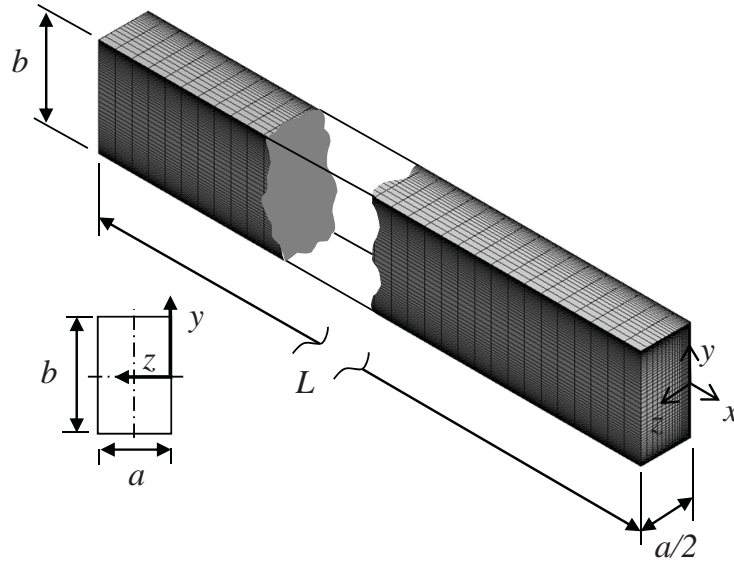


Figure 4.4: Computational model



The computational domain is depicted in Figure 4.4. No-slip boundary conditions were applied at the top ( $y = b/2$ ), back ( $z = 0$ ), and bottom ( $y = -b/2$ ) boundary of the domain and the symmetry condition was applied at the front boundary, corresponding to the channel center plane ( $z = a/2$ ). At the inlet, a uniform velocity profile,  $(u, v, w) = (U_o, 0, 0)$  was prescribed, and zero static pressure was set at the outlet. A structured mesh was employed, with mesh refinement near the walls. Both non-uniform and uniform mesh configurations in the streamwise direction were considered.

Traditionally the hydrodynamic entrance length is defined as the length from the inlet of a channel to a location where the velocity profile has attained 99% of the fully developed velocity profile (Kandlikar et al., 2006a). In the present study, this was approximated as the location where the centerline velocity ( $u_c$ ) of a developing flow reaches 99 % of the centerline velocity expected in the fully developed profile ( $u_{FD}$ ).

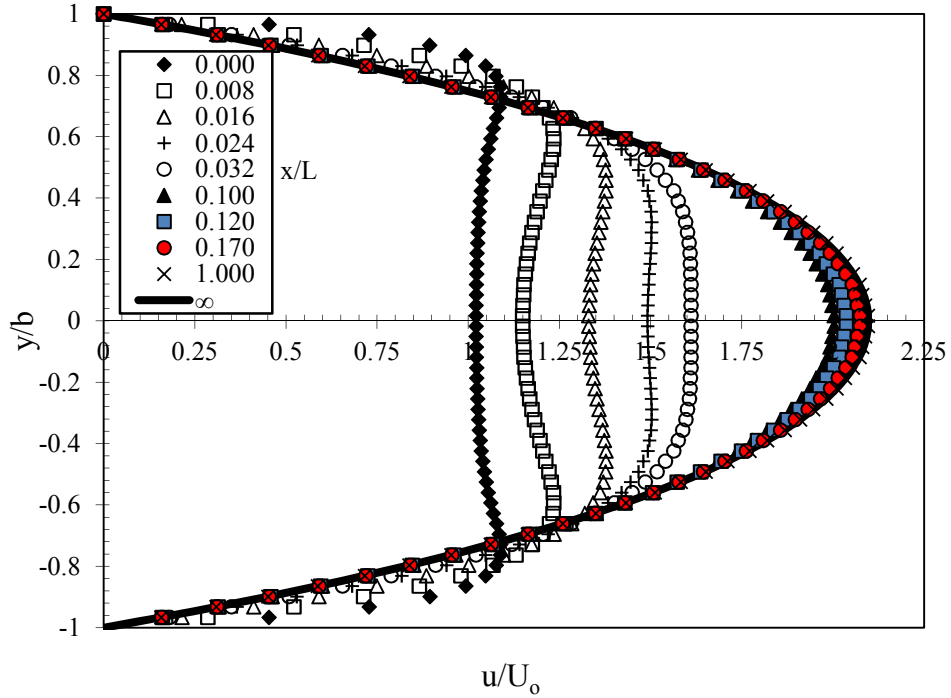


Figure 4.5: Streamwise normalized velocity profiles from simulations for microchannel ( $a = b = 100 \mu m$ ,  $Re = 50$ )

Figure 4.5 depicts the evolution of streamwise velocity profiles for a channel  $100 \times 100 \mu m$  and  $Re = 50$  obtained from the numerical simulations. The velocity profiles and position were normalized with inlet velocity  $U_o$  and the channel side dimensions (e.g.  $u/U_o$ ,  $y/b$ ,  $z/a$ ). Figure 4.5 illustrates how the velocity profiles gradually approached the fully developed profile as the flow develops along the length of the microchannel.

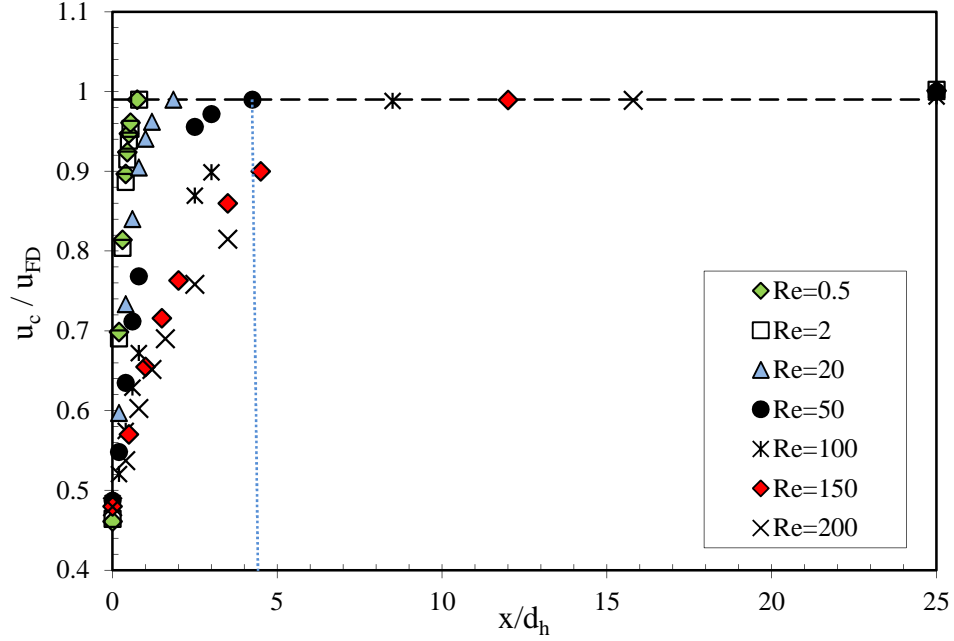


Figure 4.6: Centerline velocity ratio vs. dimensionless position for microchannel  $a = b = 100 \mu m$ ,  $0.5 \leq Re \leq 200$

Figure 4.6 shows the variation of centerline velocity ( $u_c/u_{FD}$ ) with the downstream position ( $x/d_h$ ) for the normalized velocities profiles at different Reynolds numbers for the channel  $100 \times 100 \mu m$ . The dashed line corresponds to  $u_c/u_{FD} = 0.99$ . For example, for  $Re = 50$  the normalized axial position ( $x/d_h$ ) corresponds to a normalized entrance length ( $L_e/d_h = 4.25$ ).

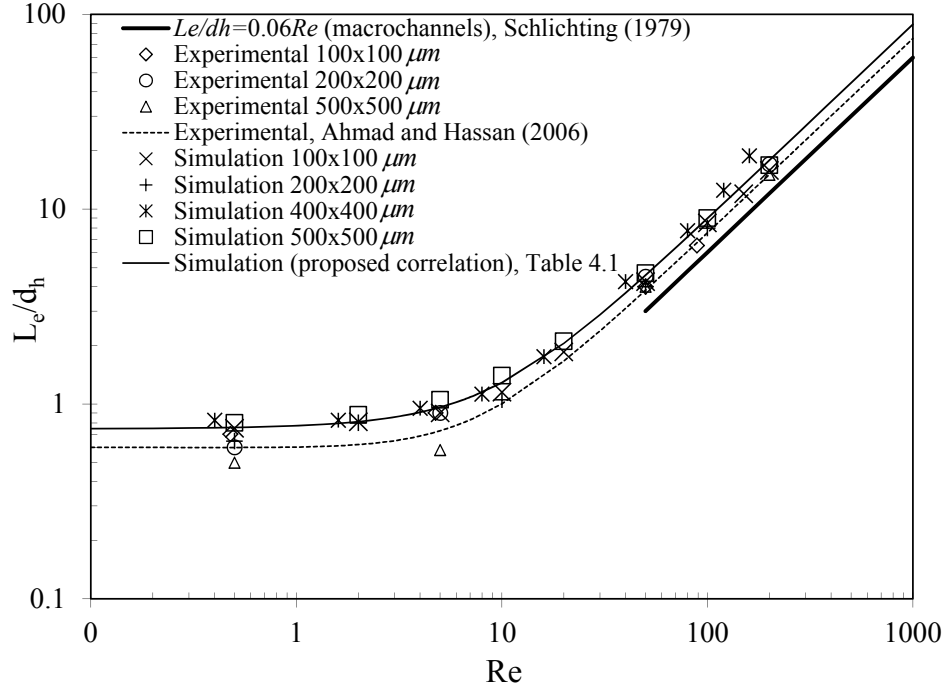


Figure 4.7: Normalized entrance length  $L_e/d_h$  from experimental data reported by Ahmad and Hassan (2006) and from numerical simulation by Galvis et al. (2012) at  $b/a = 1$

Further simulations at different channel sizes (e.g.  $200 \times 200$ ,  $400 \times 400$ , and  $500 \times 500 \mu m$ ) permitted the variation of the entrance length as the channel size was increased. Figure 4.7 shows the variation of the normalized entrance length  $L_e/d_h$  with the Reynolds number using the numerical results obtained in this study, the experimental data from Ahmad and Hassan (2006), and the well known correlation for macrochannels  $L_e/d_h = 0.06Re$  (Schlichting, 1979). Considering experimental uncertainty in micro PIV, there is excellent agreement between experimental and numerical results for channel sizes of 100 and 200  $\mu m$ . Experimental data for these two channel sizes and the numerical results for all channel sizes investigated, i.e., 100, 200, 400, and 500  $\mu m$ , tightly follow a similar trend line (e.g. relative difference between 1.8 and 20 %<sup>1</sup>). However, the experimental data set pertaining to a channel size of 500  $\mu m$  deviates from the general trend at lower  $Re$ . Since no slip

<sup>1</sup>The highest relative difference was for the lowest Reynolds number. Higher uncertainties in microchannels are typical, as mentioned in section 3.3

effect is expected for all the channel sizes investigated, this deviation may be attributed to uncertainty in experimental measurements. Ahmad and Hassan (2006) do not provide any explanation for the observed deviation of the data pertaining to the larger channel (500  $\mu m$ ) from other results obtained in their study.

The results show that the dimensionless entrance length changes nonlinearly with Reynolds number for  $Re < 50$ , while exhibiting a nearly linear dependence within  $50 \leq Re \leq 1000$ . The observed trends were found to be independent of the microchannel size for  $b/a = 1$ .

Table 4.1: Correlations for dimensionless entrance length for mini and microchannels ( $100 \leq d_h \leq 500$ ;  $0.5 \leq Re \leq 2000$ , Galvis et al. (2012))

$\frac{L_e}{d_h} = \frac{C_1}{C_2 Re + 1} + C_3 Re$	<i>Coefficients</i>		
<i>b/a</i>	<i>C<sub>1</sub></i>	<i>C<sub>2</sub></i>	<i>C<sub>3</sub></i>
1.00	0.740	0.090	0.0889
1.25	0.715	0.115	0.0825
2.50	1.000	0.098	0.9890
5.00	1.471	0.034	0.0818

In order to evaluate the effect of the channel aspect ratio on the entrance length, simulations were performed for channel aspect ratios  $1 \leq b/a \leq 5$  and  $0.5 \leq Re \leq 200$ . The results obtained from the simulations and the proposed correlations are shown in Table 4.1. It was also verified that the estimates made for  $L_e/d_h$  based on streamwise velocity profiles measured in either  $xy$ , or  $xz$  planes were the same. The results show that there is no significant effect of the channel aspect ratio on the dimensionless entrance length for  $Re \geq 50$ . However, for  $Re < 50$ , the dimensionless entrance length increases as the channel aspect ratio increases for a given Reynolds number. Since, for  $Re \geq 50$ , there is essentially linear dependence of the dimensionless entrance length on Reynolds number, the correlation can be extrapolated to higher Reynolds numbers within the laminar flow regime. Similarly, a linear dependence of the  $L_e/d_h$  on  $Re$  for  $50 \leq Re \leq 1000$  was also

observed by Renksizbulut and Niazmand (2006) and Wiginton and Dalton (1970). Thus, the correlations in Table 4.1 can be applied to rectangular microchannels with  $1 \leq b/a \leq 5$  and for  $0.5 \leq Re$  within the laminar flow regime.

It was possible to identify that 50 % of the channel length was in developing flow conditions at  $Re = 500$  by using the appropriate coefficients from Table 4.1 for the channel size  $198 \times 241 \mu m$  ( $b/a \approx 0.8$ ). As the Reynolds number increases from 500 to 1600, the percentage of the developing length increases from 50 to 100 %. Therefore, the friction factor obtained from experiments will clearly follow a different path from that of the laminar fully developed theory in the range of Reynolds number between  $500 < Re \leq 1600$  as shown in Figure 4.3.

In summary, macro theory predicts the friction factor but entrance effects and minor losses must be considered in the calculations. The deviation from the fully developed laminar flow in this channel was observed at  $Re \approx 500$ , and the developing and turbulent flow macroscale correlations were able to predict the experimental friction factor for Reynolds number between 1600 and 2600.

## 4.2 Single-phase heat transfer

It was reported by Callizo (2010) and Ali (2010) that the Nusselt number in micro cylinders ( $0.6 \leq D \leq 1.7 mm$ ) can be properly obtained using single-phase classical macro theory. Their experiential work was for refrigerants in laminar fully developed flow and turbulent conditions. Different to the work reported by Callizo (2010) and Ali (2010), in this thesis, water was used as the working fluid and the experiments were performed in a rectangular channel with smaller hydraulic diameter ( $d_h = 217 \mu m$ ). Also, the applicability of classical macro theory to microchannels was studied under developing flow conditions.

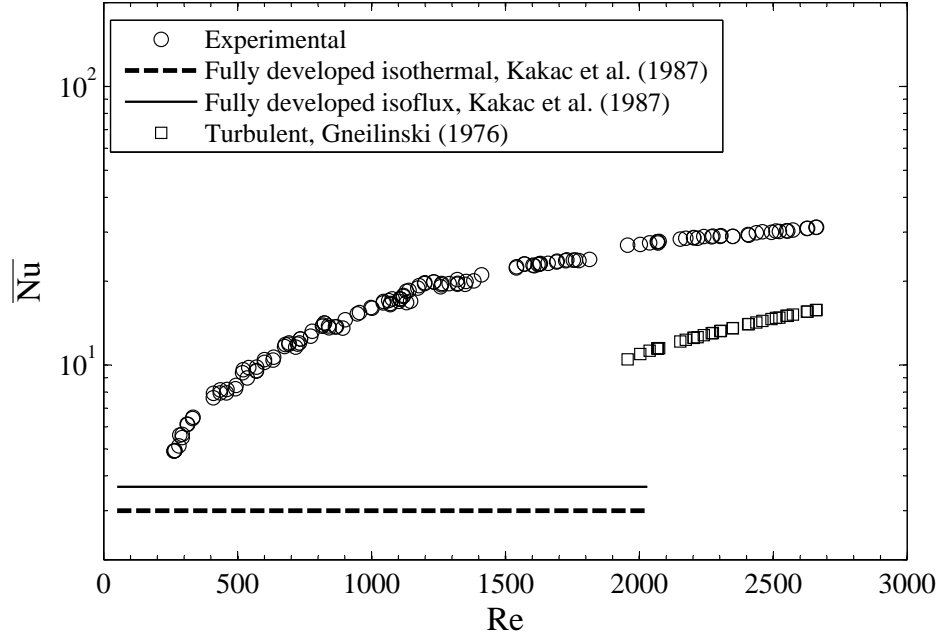


Figure 4.8: Experimental and theoretical average Nusselt number vs Reynolds number for rectangular channel ( $d_h = 217 \mu m$ ,  $b/a = 0.822$ )

In Figure 4.8, the experimental average heat transfer coefficient, expressed in the form of dimensionless Nusselt number was compared with correlations for fully developed flow (Kakaç et al., 1987) and turbulent flow (Gneilinski, 1976) for conventional macro theory. For fully developed flow conditions, the Nusselt number is constant (3.00 isothermal or 3.65 isoflux for a channel aspect ratio  $b/a = 0.822$ ) or increases with Reynolds number for turbulent flow regime as shown in Figure 4.8. It is evident from Figure 4.8 that the experimental Nusselt number differs from the fully developed and turbulent cases. Since, turbulent flow is not expected for these experimental conditions, and the experimental data are not indicating a fully developed flow condition ( $\overline{Nu}$  is not constant), the experimental data may correspond to a developing flow condition. Therefore, the experimental data should be compared with developing flow correlations instead of fully developed or turbulent flow models.

The Nusselt number under developing flow conditions or entry length problem is typical plotted against the Graetz number  $G_z \equiv (d_h/x) Re Pr$  instead of the Reynolds number.

The entry length problem corresponds to the case for which the temperature and velocity profiles develop simultaneously. In a  $\overline{Nu}$  vs  $G_z$  plot, the Nusselt number is infinity at the inlet of the channel  $x = 0$  and decays to an asymptotic (fully developed) value with increasing  $x$ . When plotted against the Graetz number, the Nusselt number is independent of the Prandtl number if the velocity profile is independent of the fluid viscosity. In contrast, for the combined entry length problem or simultaneously developing flow, the results depend on the manner in which the velocity distribution develops, which is highly sensitive to the fluid properties. Hence, the heat transfer results depend on the Prandtl number for the combined entry length case.

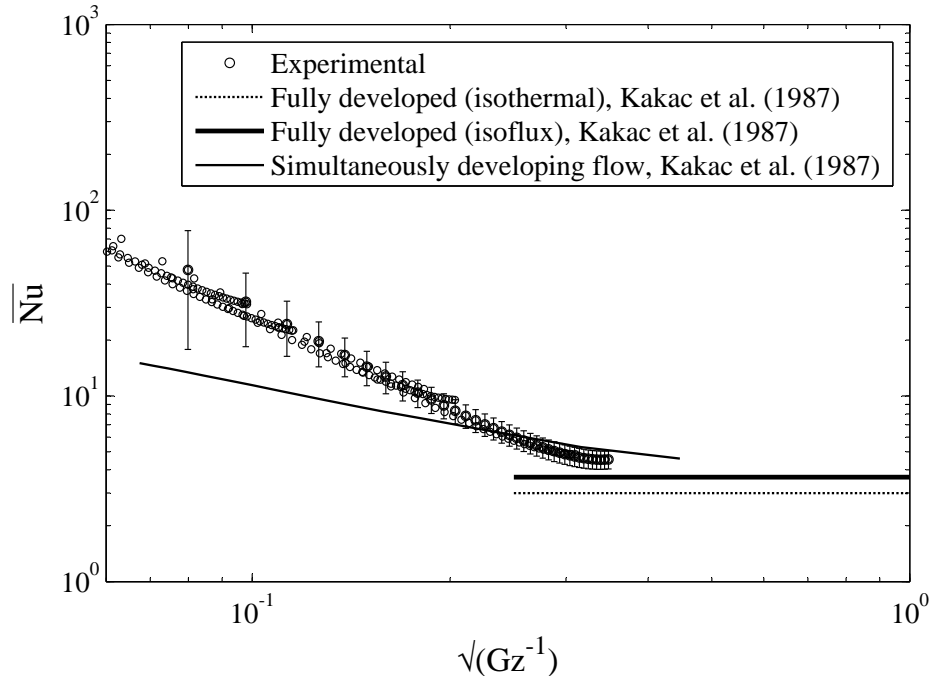


Figure 4.9: Experimental results for the average Nusselt number for developing flow conditions vs Graetz number

Figure 4.9 shows the experimental average Nusselt number against the square-root of the reciprocal of the Graetz number. The results for single-phase Nusselt number are tabulated in Appendix G section G.2. The experimental Nusselt numbers correspond to Reynolds numbers between 190 and 2660 and Prandtl numbers between 3.8 and 5.

The experimental average Nusselt number approaches the fully developed condition as the Graetz number increases. Typically, the fully developed conditions are reached for  $\sqrt{Gz^{-1}} \approx 0.22$  in laminar flow in a circular tube, for this microchannel the fully developed condition seems to be reached for  $\sqrt{Gz^{-1}} \approx 0.30$ .

For the channel size tested it was not possible to decrease the Reynolds number below  $Re \leq 189$  or have the term  $\sqrt{Gz^{-1}}$  in Figure 4.9 below 0.34. This can be achieved with volumetric flow rates lower than 1 ml/min but at this condition, just a small amount of heat<sup>2</sup> added to the water will produce boiling inside the microchannel which is not desirable for the purpose of this analysis. Based on these experimental results, conventional macro theory for heat transfer is applicable at microscale level for microchannels with hydraulic diameters  $d_h \geq 217 \mu m$ . It is important to mention that in this work, developing flow conditions in microchannels were experimentally evaluated. According to the best knowledge of the author this kind of study in microchannels is mostly considered using numerical simulations.

In summary, the experimental results on microchannel single-phase liquid flow and heat transfer characteristics obtained in this study confirm that, including the entrance effects, conventional macroscale theory for laminar flow is applicable for water as the working fluid through rectangular microchannel with hydraulic diameters as small as  $200 \mu m$ . This observation is meaningful considering the large scatter in the results existing in the literature.

The single-phase investigation also permitted a proper identification of the heat losses to the environment which was used for the estimation of the heat removed by the microevaporator during the two-phase flow experiments. It would be interesting for future work to evaluate the effects of different working fluids on the Nusselt number and friction factor and modify the current test rig in order to allow a larger range of Graetz number that includes fully developed flow conditions (e.g. longer channel).

---

<sup>2</sup>2.5 W will produce boiling inside the microchannel if the volumetric flow rate is  $\simeq 0.5 \text{ ml/min}$ . Therefore, it is not possible to collect substantial data for single-phase at low flow rates.



# Chapter 5

## Two-phase Flow Visualization

In this section the results for two-phase flow boiling using high-speed visualization are presented<sup>1</sup>. Six different flow patterns are defined and an explanation of the flow reversal typically observed in two-phase flow is given. General observations for the bubble growth, bubble frequency, and pressure oscillations in microchannels are reported. Finally, the flow patterns from this study are presented in the form of flow regime maps and compared with published flow regime maps for macrochannels and microchannels.

### 5.1 Experimental Results

The morphology of the two-phase flow plays a critical role in the determination of pressure drop heat and mass transfer during vaporization and condensation processes. Traditionally, flow patterns are plotted as flow regime maps where the boundaries between the flow patterns have been established through visual observations. Analogous to predicting the transitions from laminar to turbulent flow in single-phase, two-phase flow pattern maps are used for predicting the transition from one type of two-phase flow pattern to another. In addition, flow regime maps are required and will be a step forward for future modeling

---

<sup>1</sup>A summary of the results for flow patterns, boiling curves, HTC, and pressure drop can be found in Galvis and Culham (2012)

based on individual flow regimes instead of the development of a model that covers all observed flow patterns.

The purpose of the two-phase flow visualizations in this research is to contribute to a better understanding of the physical mechanism of two-phase flow boiling in microchannels and propose new flow regime maps for mini and microchannels. For that reason, the flow patterns are recorded using high-speed videos and then presented in the form of a flow regime map. The flow visualization was useful for the identification of the flow patterns but also for the study of bubble growth, bubbly frequency, and flow reversal in mini and microchannels. Simultaneously with the two-phase flow visualizations, experimental variables such as pressure drop, mass flow, heat input, and temperatures in the microevaporators were monitored. This information is used to investigate the dependence of the heat flux on the pressure drop. These experimental data are also used to investigate the thermal performance in microevaporators which is discussed in the Chapter 6.

The flow patterns were recorded with a high-speed video camera with a steady supply of water flow and heat input to the microevaporators. Details of the experimental conditions and procedure are shown in Chapter 3 section 3.1 but a short summary is given as follows. The temperature of the fluid was kept constant at approximately  $50\text{ }^{\circ}\text{C}$  at the inlet of the evaporator. For a fixed mass flow and heat input, videos of the flow patterns were recorded when steady state conditions in the microevaporator were reached. The steady state condition was determined when the temperature values from the thermocouples in the microevaporator and heater block (as shown in Figure 3.4) did not vary with time. The steady state condition was visually monitored with a real time plot of these temperatures in the data acquisition system. In order to identify the dependency of the heat and mass flux on the flow patterns, the heat input was set to a new value while the mass flux was kept constant. The heat input supplied by the carriage heater ranged between 5 and 130 watts and the mass flux from 350 to  $1300\text{ kg/m}^2\text{s}$ . Approximately 34 GB of memory with 606 high-speed videos were recorded and classified during this study.

## 5.2 Flow patterns

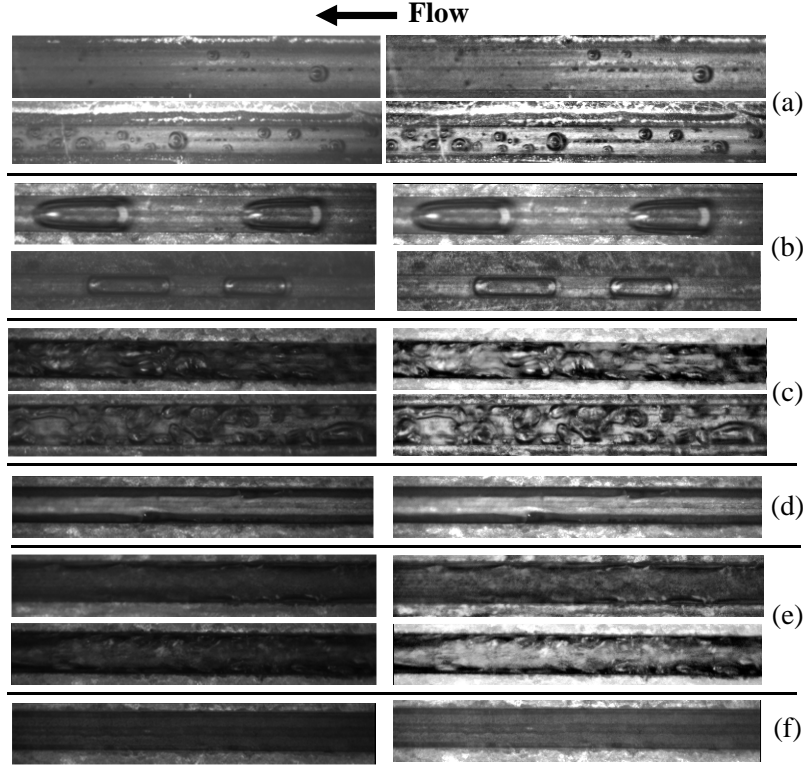


Figure 5.1: Flow patterns: left: actual image, right: enhanced with Matlab image processing tool, vapor quality estimated from Equation 3.20, (a): bubbly flow  $x \approx 0$ , (b): slug flow  $x = 0.12$ , (c): churn flow  $x = 0.19$ , (d): annular flow  $x = 0.24$ , (e): wavy annular flow  $x = 0.31$ , (f): inverted annular flow  $x = 0.47$

After a detail analysis of the videos, the flow patterns in the microchannel evaporators were classified in terms of the most commonly accepted terms and descriptions. Figure 5.1 shows the actual and the enhanced flow pattern images observed during these experiments, where the flow direction is from right to left. A single flow pattern is observed everywhere along the channel, and the images captured in this work are all taken at the midpoint of the channel length. The purpose of this figure is to illustrate the representative flow patterns observed in the microevaporators during all the experimental conditions in this study. The conditions associated with these flow patterns are discussed in section 5.6,

where the flow patterns are a function of the heat flux, mass flux, channel size, and phasic superficial velocities.

Figure 5.1(a) shows bubbly flow, where the vapor phase is distributed in discrete bubbles within a liquid continuum. Small cavities on the heated surface trap vapor and serve as nucleation sites. If the heated surface temperature exceeds the saturation temperature, a bubble may grow inside the cavity and appear at its mouth. As the heat flux increases, the bubble generation rate at the wall increases, bubbles become larger but small compared to the channel size and eventually are detached from the wall surface and move along with the stream fluid. When a bubble spans the entire smaller lateral dimension of the channel (mainly due to bubbles growing or bubbles coalescing), the bubbly flow changes to slug flow. The slug flow as shown in Figure 5.1(b) is characterized by confined bubbles separated by liquid slugs which may or may not contain a dispersion of smaller vapor bubbles. The nose of the bubble has a characteristic spherical cap and the vapor in the bubble is separated from the wall surface by a descending film of liquid. The length of the elongated bubbles vary considerably with the heat flux. The evaporating rate increases with the heat flux which increases the length of the vapor slug.

If the velocity of the two-phase mixture flow in slug flow is increased (e.g. adding heat to the system resulting in increased vapor quality), the structure of the large vapor bubbles becomes unsteady. This instability results in a chaotic motion of the irregular-shaped vapor pockets, with literally no discernible interfacial shape. Both phases may appear to be contiguous, and incessant “churning” flow is observed as shown in Figure 5.1(c). Although “churn” flow is usually reserved for vertical geometries, the same name is used here due the similar appearance. In fact several authors are also using the term “churn” in horizontal channels (Saisorn et al., 2010; Harirchian and Garimella, 2009b,a; Ekberg et al., 1999). At much higher quality levels, the two-phase flow assumes an annular flow as shown in Figure 5.1(d). This consists of a liquid layer film on the channel walls with a continuous interface to a vapor flowing in the center core. When the vapor velocity is high, a wavy annular flow is observed, where the interface becomes unsteady, leading to the formation of waves at the interface as shown in Figure 5.1(e). At very high fluxes,

dry-out is observed where most channel walls are dry, except for a fluid that apparently is flowing on the top wall of the channel, this type of flow is referred to as inverted annular flow as shown in Figure 5.1(f).

### 5.3 Bubble size and bubbly frequency

The completed process of liquid heating, nucleation, bubble growth and release, collectively referred to as the ebullition cycle (Carey, 2008; Kim, 2009) is the central mechanism of heat transfer from a superheated wall during nucleate boiling. In macro heat transfer two features of this process that impact the rate of heat transfer during the ebullition cycle are the bubble diameter at departure and the frequency at which bubbles are generated and released.

In macro boiling, the bubble diameter at release is primarily determined by the net effect of forces acting on the bubble as it grows on the surface. Interfacial tension acting along the contact acts to hold the bubble in place on the surface. Buoyancy is often a major player in the force balance and depends of the channel orientation. Also, the inertia associated with the induced liquid flow field around the bubble may also tend to pull the bubble away from the surface. All these similar effects reported during bubble growth in macro boiling were observed in the microevaporators with the exception of the gravitational effects due to the dominant inertial and surface forces.

The bubble size and bubbly frequency are studied from the high-speed videos. The bubble diameter and location of the bubbles at each frame of the video are analyzed using Photron Fascam viewer software for high-speed digital imaging processing. The position of the vapor and liquid slugs in the microevaporators is identified using a “measuring tool” provided by the software after a scale calibration procedure.<sup>2</sup>

---

<sup>2</sup>Setting a distance between 2 points on the image. The channel width is used as the calibrating parameter.

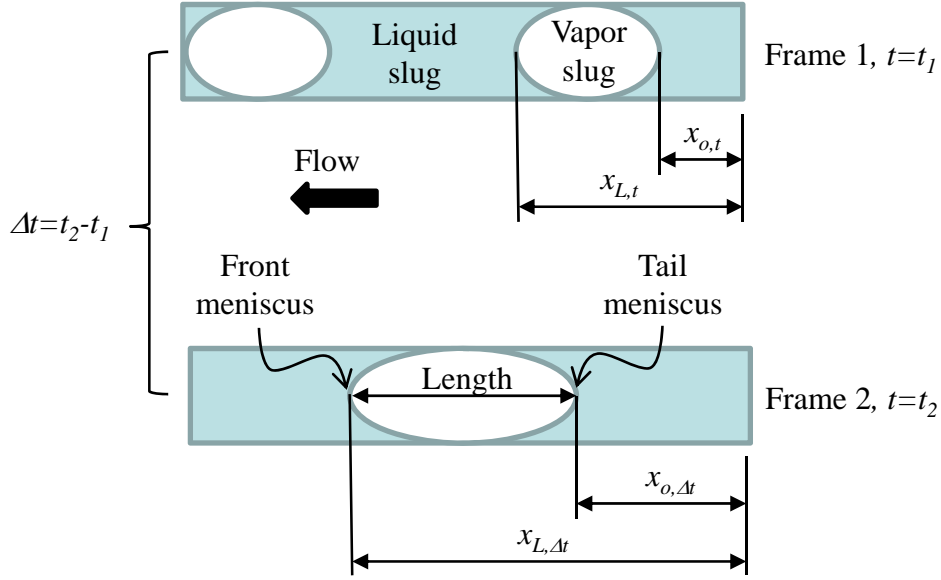


Figure 5.2: Sketch for a vapor slug growth

Figure 5.2 shows a sketch of the growth evolution for a vapor slug. Typically, the vapor slug expands along the length of the microchannel. The vapor slug growth is estimated based on its length change per unit time. The length of the slug is measured based on the position of the meniscus. In frame 1 (at  $t = t_1$  as shown in Figure 5.2), the position of the tail and front meniscus of the vapor slug is defined as  $x_{o,t}$  and  $x_{L,t}$  respectively. In frame 2 (at  $t = t_2$ ), the vapor slug moves, and the new positions of the meniscus are defined as  $x_{o,\Delta t}$  and  $x_{L,\Delta t}$ . The length of the vapor slug in frame 1 is calculated from  $x_{L,t} - x_{o,t}$  and for frame 2  $x_{L,\Delta t} - x_{o,\Delta t}$ . The vapor slug growth is estimated from the change of length as:

$$slug\ growth = \left[ \frac{(x_{L,\Delta t} - x_{o,\Delta t}) - (x_{L,t} - x_{o,t})}{\Delta t} \right] \quad (5.1)$$

Table 5.1: Results for the positions and vapor slug lengths in the microchannel  $198 \times 241 \mu m$  at 9 watts and 1  $ml/min$ , (video capture rate 20000  $fps$ )

$x_{o,t}, \mu m$	$x_{L, \Delta t}, \mu m$	<i>Frame</i>	<i>Length, <math>\mu m</math></i>	<i>Time, <math>\mu s</math></i>
0	996.0	89203	996.0	0.00
56.8	1068.4	89208	1011.6	0.25
136.6	1148.8	89213	1012.2	0.50
192.8	1229.1	89218	1036.3	0.75
233.1	1309.5	89223	1076.4	1.00
297.3	1381.7	89228	1084.4	1.25
377.6	1462.1	89233	1084.5	1.50
466.0	1630.8	89243	1164.8	2.00
610.5	1783.4	89253	1172.9	2.50
698.9	1944.1	89263	1245.2	3.00
843.5	2096.7	89273	1253.2	3.50
939.9	2265.4	89283	1325.5	4.00
1084.5	2434.1	89293	1349.6	4.50
1172.9	2602.8	89303	1429.9	5.00
1309.4	2795.6	89313	1486.2	5.50
1413.9	3028.6	89323	1614.7	6.00

Table 5.1 shows the results for positions and vapor slug lengths for the channel  $198 \times 241 \mu m$  at 9 watts and 1  $ml/min$  of heat input and liquid volumetric flow rate respectively. Results for other conditions are shown in Appendix G section G.3.

Higher magnification in the microscope is required in order to capture more detail associated with bubble and slug growth processes. Unfortunately, only a small portion of the channel length can be observed at higher magnification. Therefore, for evaluating a longer length of the channel without sacrificing magnification, videos are recorded at different portions of the channels until approximately 3/4 of the total length of the channel is covered.

In order to identify the bubble growth dependency on the flow rate and heat flux, the heat flow and volumetric flow rate are varied between 9 and 22 watts and 1 to 3.8  $ml/min$  respectively. Due to instabilities in the flow patterns, in addition to the rapid change of the bubbly or slug flow into annular flow, it was not possible to perform any further studies in

terms of the bubble growth, number of active nucleation sites, etc. However, the following general observations were possible from the steady bubbly and slug flow patterns:

- A general trend observed was a decreasing of the bubble departure diameter with the heat flux. It is also expected that as the flow rate increases, the bubbles may detached quicker from the surface as a result of the increasing drag forces over the bubble.
- A number of active nucleation sites were observed at the middle of channel at different flow rates and heat flux. The active cavities were identified when bubbles in the channel surface appear. It was evident that the number of active cavities increases with the heat flux.
- The positions of the front and tail meniscus of a vapor and liquid slug vs time were measured for a steady slug flow pattern. Figure 5.3 shows a typical trend of the position vs time for the menisci of a vapor and liquid slug. Since the slope of the line represents the velocity, it can be concluded that the vapor and liquid slug are moving at constant and similar velocities. Therefore, for this case, the homogenous flow model, which assumes equal vapor and fluid velocities should be applicable. It is important to mention that Figure 5.3 also implies a constant length of the slugs. However, a change of length in the vapor slug was also observed as the heat flux increases due to evaporation of the film liquid or increases in the vapor slug pressure. Figure 5.4 shows the change of length of a vapor slug per unit time (or vapor slug growth velocity) at different heat fluxes. From Figure 5.4, it can be concluded that the rate of growth of a vapor slug increases with the heat flux.
- Successive slug bubbles that flow in tandem down the passages were observed, this resulted in high frequency of repeated nucleation in a single cavity or nucleation at multiple sites. The vapor slugs may eventually merge into longer slugs due to different menisci velocities or the vapor slug can expand to subsequently evolve into annular flow.



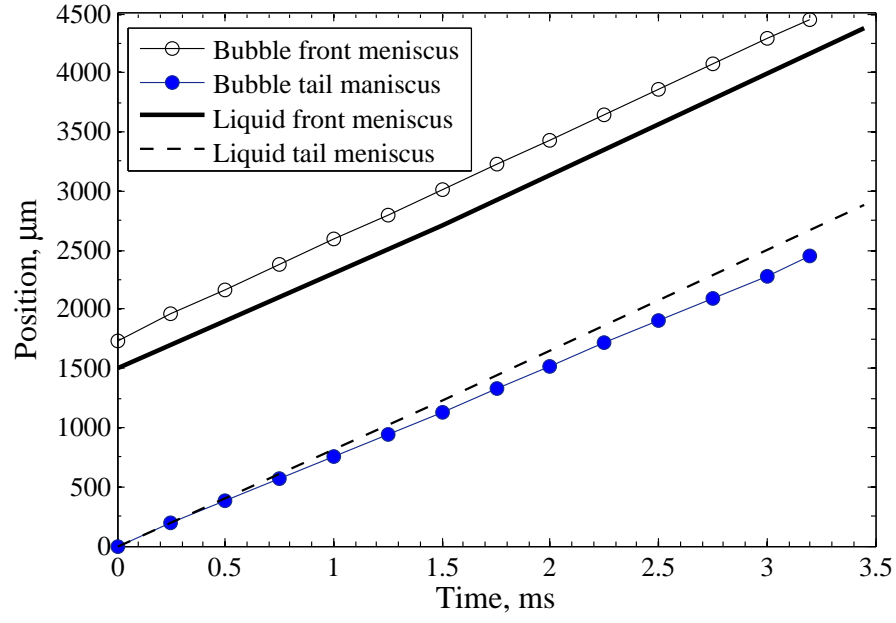


Figure 5.3: Typical meniscus position for vapor and liquid slugs (11 watts, volumetric flow rate  $2 \text{ ml/min}$ , channel  $198 \times 241 \text{ } \mu\text{m}$ )

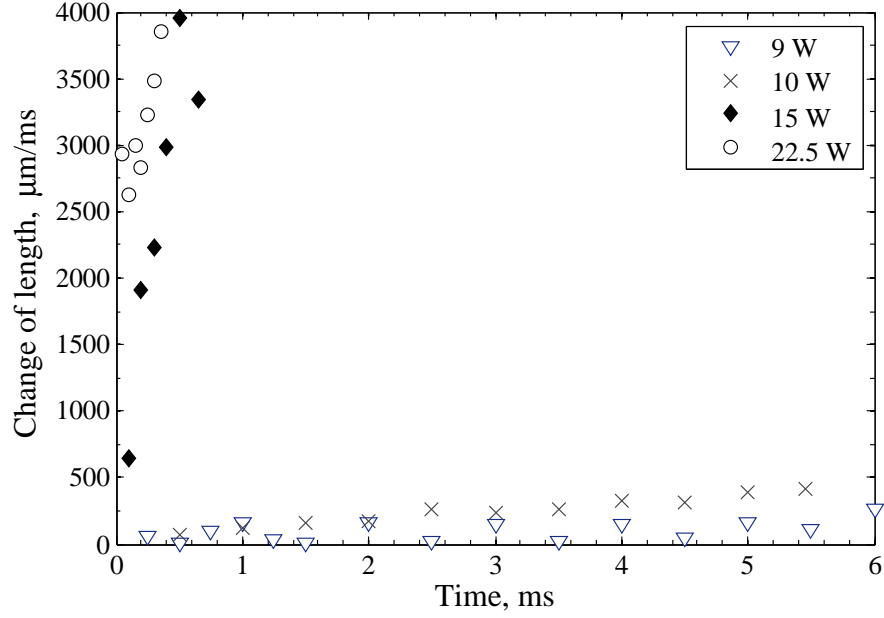


Figure 5.4: Vapor slug growth at different heat fluxes (volumetric flow rate  $1 \text{ ml/min}$ , channel  $198 \times 241 \text{ } \mu\text{m}$ )

## 5.4 Flow reversal and intermittent flow patterns

During the analysis of the high-speed videos used for the identification of the flow patterns, flow reversal was observed in the microevaporators. Typically, in the literature, the flow reversal is attributed to a non-uniform distribution of the fluid in the microchannels. The purpose of the high-speed videos of the flow patterns is also to identify if flow reversal is presented in single channel microevaporators and what may cause its formation. Flow reversal can be prevented using nucleation sites at the surface of the channel wall (Kandlikar et al., 2006b), using an inlet orifice upstream of the channel, or expanding the microchannel in the flow direction (Lee et al., 2010). In order to understand the natural development of the flow reversal in a straight single channel, none of these procedures were used in this study. It is important to mention that having a single channel in the microevaporator, the problem with non-uniform distribution of the fluid in the channel is avoided.

Figure 5.5 shows a sequence of vapor expansion during slug flow for a low heat flux ( $q = 546 \text{ kW/m}^2$ ). Figure 5.5(a) shows a typical bubbly flow moving in the flow direction toward the channel exit, the bubble on the left side grows as shown in Figure 5.5 (b). This bubble continues growing but is confined by the channel walls and expanding in both directions. The expansion of the bubble upstream, opposite to the the flow direction causes reversed flow as shown in Figures 5.5(c) to (f). The flow reversal was attributed to the expansion upstream of confined bubbles. Flow reversal in parallel microchannels has also been reported by Kandlikar (2004) and Steinke and Kandlikar (2004) multiple channel microevaporators. The bubble expansion is caused by a large enough evaporating momentum force that overcomes the relatively low dynamic pressure of the flow, and/or manifold pressure at the channel inlet.

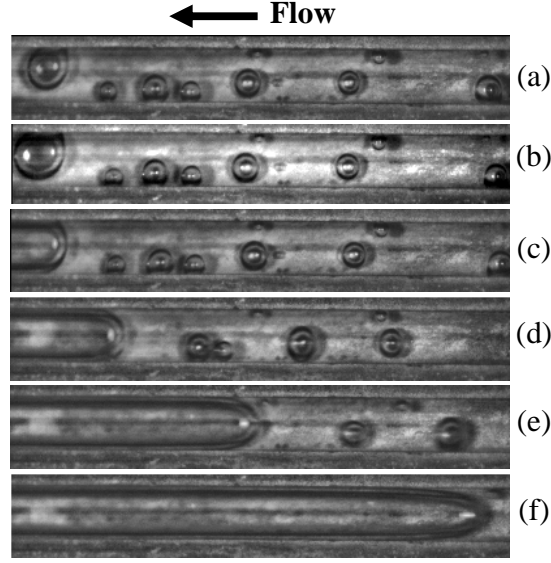


Figure 5.5: Reverse flow,  $378 \times 471 \mu m$ ,  $G = 365 \text{ kg}/m^2 s$ ,  $q = 546 \text{ kW}/m^2$ : (a): bubbly flow, (b): bubble on the left starts to grow, (c) to (f): bubble is confined by the channel wall and the expansion upstream causes flow reversal.

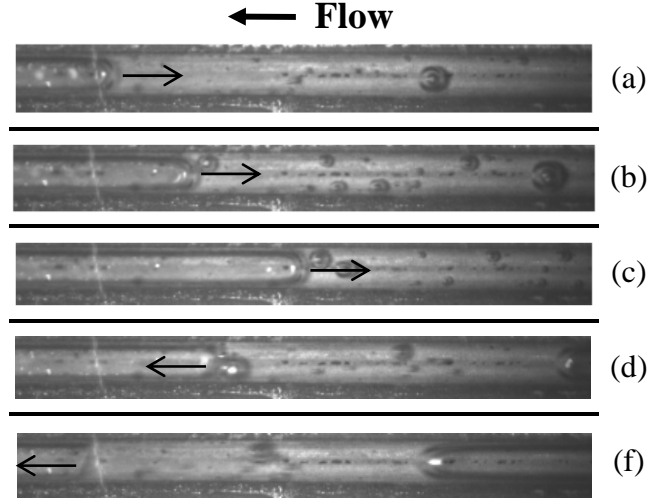


Figure 5.6: Meniscus displacement: (a)-(c): bubbly expansion and tail meniscus displacement against flow direction, (d)(f): pressure gradient in the channel overcomes evaporating momentum and tension forces and moves the tail meniscus towards the outlet.

The bidirectional growth of the slug may slow as growth proceeds and eventually stops as superheat in the fluid is consumed. The displacement of the tail meniscus of a vapor slug opposite to the flow direction is shown in Figures 5.6 (a) to (c). Eventually, the pressure drop gradient along the channel acts to move the slug bubble towards the outlet as shown in Figure 5.6 (d) and (c).

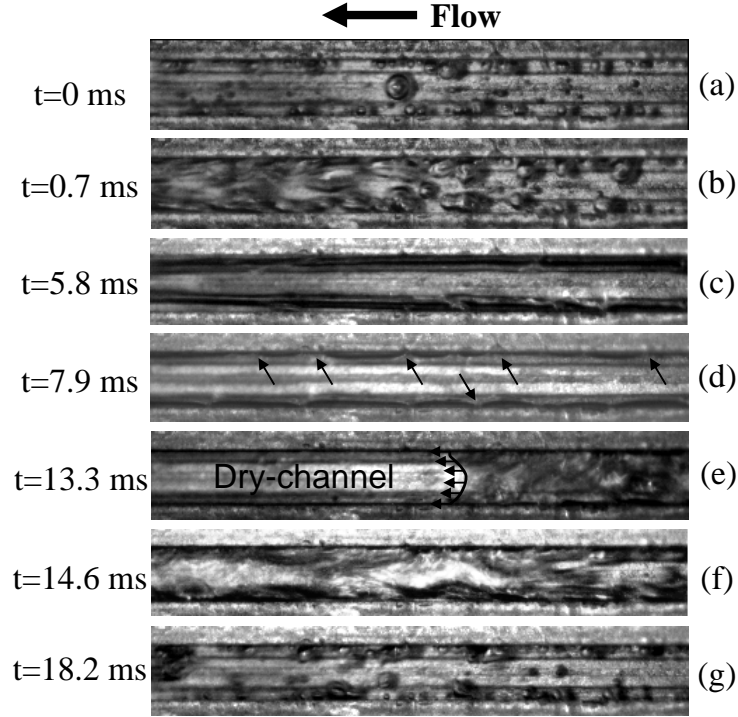


Figure 5.7: Intermittent flow,  $378 \times 471 \mu m$ ,  $G = 1373 kg/m^2s$ ,  $q = 3146 kW/m^2$ : (a): bubbly flow, (b): churn flow, (c): annular flow, (d): Localized dry out condition, (e): re-wetting of the channel, (f): wavy annular flow, (g): bubbly flow.

Two flow patterns are expected during transitional flow (e.g. bubbly flow to slug and slug flow to bubbly). When more than two patterns are observed, the pattern is referred to as intermittent flow. A typical intermittent flow is shown in Figure 5.7, where a bubbly flow, as shown in Figure 5.7(a) turns to a churn flow and annular flow in less than 6 ms as shown in Figures 5.7(b) and (c). The liquid film boiling in the annular flow decreases and eventually shows dry-out spots as shown in Figure 5.7 (d). Figure 5.7(e) shows the

instant where almost half of the channel length is re-wetted. Finally, the flow pattern turns into wavy annular flow (Figure 5.7(f)) before reaching its original bubbly flow condition as shown in Figure 5.7(g). During this intermittent flow pattern, an oscillating pressure drop was also observed, this is discussed in next section.

In summary, flow reversal is presented in single channel microevaporators and it is attributed to the expansion upstream of confined bubbles. Microevaporators can experience multiple flow patterns in a very short time (e.g. approximately 20 ms) even under steady input conditions such as heat and mass flux. These “unsteady” flow patterns called intermittent flow in this research, could be one of the reasons for the discrepancies between experimental results and models for two-phase flow boiling in microchannels.

## 5.5 Pressure drop and channel wall temperature

To achieve normal flow conditions in a microevaporator, the pump must overcome the total pressure drop of the system. Therefore, it is important to know how the pressure drop changes during flow boiling in order to select a proper pump capacity. Simultaneously to the flow visualization, data for pressure drop and channel wall temperature are recorded as describe in section 5.1. The purpose of these measurements is to identify the maximum pressure drop in the microevaporators and the dependency of the pressure drop on the heat flux. The measurements of the channel wall temperature are used to assist with the identification of dry-out conditions in the microchannel.

Table 5.2: Pressure drop in minichannel  $378 \times 471 \mu m$ , mass flux  $G \simeq 364 \text{ kg/m}^2 s$

<i>Heat flux, <math>\text{kW/m}^2</math></i>	<i>Channel wall temperature, <math>^\circ\text{C}</math></i>	<i>Pressure drop, kPa</i>	
		<i>kPa</i>	<i>psi</i>
55	60.8	3.0	0.4
52	61.3	3.1	0.5
49	62.0	2.9	0.4
157	77.9	3.0	0.4
170	75.4	3.2	0.5
163	76.8	3.1	0.5
276	91.3	3.5	0.5
268	93.1	3.5	0.5
283	90.0	3.5	0.5
324	97.0	3.6	0.5
328	96.2	3.7	0.5
326	96.6	3.6	0.5
421	100.1	3.8	0.5
420	100.3	3.8	0.5
420	100.3	3.7	0.5
525	101.8	4.8	0.7
524	102.0	4.9	0.7
524	102.0	4.9	0.7
634	102.4	5.4	0.8
631	102.9	6.3	0.9
631	102.9	6.6	1.0
771	104.3	8.0	1.2
771	104.3	8.1	1.2
947	106.3	11.1	1.6
947	106.2	11.2	1.6
1123	108.4	14.4	2.1
1124	108.4	14.7	2.1
1301	110.3	19.1	2.8
1299	110.7	20.2	2.9
1475	112.6	24.3	3.5

Table 5.2: Pressure drop in minichannel  $378 \times 471 \mu m$ , mass flux  $G \simeq 364 \text{ kg}/m^2 s$  (cont)

<i>Heat flux, <math>kW/m^2</math></i>	<i>Channel wall temperature, <math>^{\circ}C</math></i>	<i>Pressure drop, <math>kPa</math></i>	
		<i><math>kPa</math></i>	<i><math>psi</math></i>
1474	112.9	24.8	3.6
1649	113.8	27.7	4.0
1655	114.3	28.7	4.2
1833	116.0	32.5	4.7
1832	116.1	32.3	4.7
2012	117.0	37.1	5.4
2009	117.6	36.3	5.3
2011	117.1	37.4	5.4
2181	120.1	41.2	6.0
2354	123.5	50.0	7.3
2516	127.7	60.0	8.7
2683	132.8	74.7	10.8
2834	139.2	91.6	13.3
3001	143.1	102.3	14.8

Table 5.2 shows the results of the pressure drop and channel wall temperature for the minichannel  $378 \times 471 \mu m$  for a fixed mass flux ( $G \simeq 364 \text{ kg}/m^2 s$ ) and different heat fluxes. Results for other mass fluxes and channel sizes are shown in Appendix G section G.6. Each data point corresponds to an average of 50 data at steady state conditions. These data are collected using the same process used during the two-phase flow visualization. The mass flow and heat flux are kept constant until steady stated is reached. The process is repeated at different heat fluxes.

In contrast to single-phase flow, where the pressure drop is constant for a fixed heat flux, in boiling two-phase flow, the pressure drop increases with the heat flux. From Table 5.2, the pressure drop increases from 3.0 to 102.3  $kPa$  as the heat flux increases from 55 to 3001  $kW/m^2$ . The maximum average pressure drop reached during the experiments was  $\approx 113 \text{ kPa}$  (16  $psi$ ).

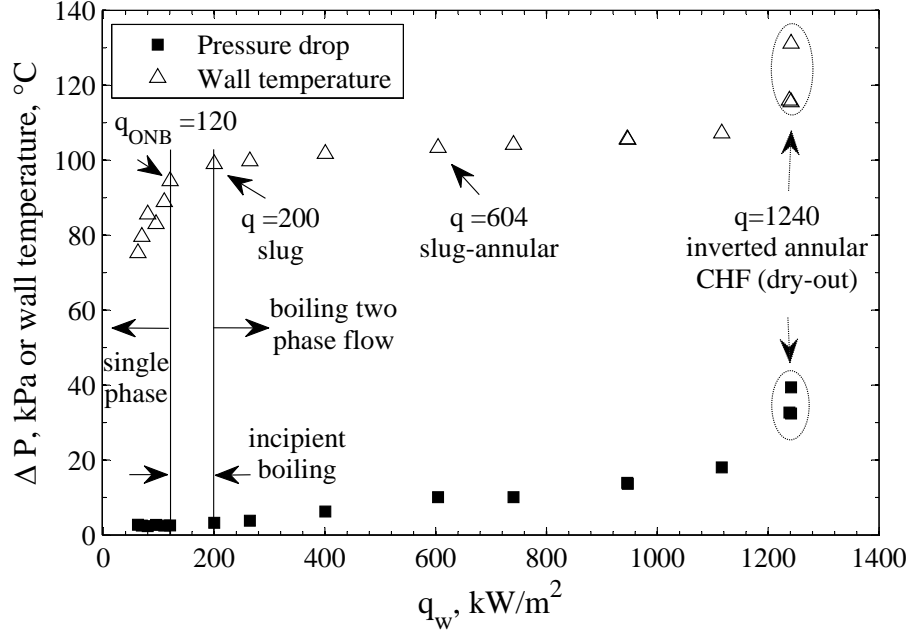


Figure 5.8: Results for pressure drop and channel wall temperature for microchannel  $198 \times 241 \mu m$  at constant mass flux  $G \simeq 340 \text{ kg/m}^2 s$

Figure 5.8 shows the behavior of the pressure drop and channel wall temperature for the  $198 \times 241 \mu m$  microchannel at constant mass flux  $G = 340 \text{ kg/m}^2 s$  as the heat flux is varied from 63 to  $1240 \text{ kW/m}^2$ . This figure is divided into three regions, single-phase, incipient boiling, and boiling two-phase flow. The single-phase is found before  $ONB$  and the boiling two-phase flow when at least one of the flow patterns defined in Figure 5.1 is observed. The incipient boiling located between the single and two-phase regions, was characterized by bubbles that grow in cavities and are attached to the channel wall (this avoids confusion with bubbly flow where bubbles travel with the fluid). For this configuration,  $ONB$  commenced at a heat flux  $q_{ONB} = 120 \text{ kW/m}^2$  and incipient boiling was observed between 120 and  $200 \text{ kW/m}^2$ . As seen in Figure 5.8, the heat flux of  $200 \text{ kW/m}^2$  marks the point where boiling two-phase flow begins (slug flow pattern commenced at this point). The pressure drop in the channel did not show any dependency on the heat flux for the single-phase and incipient boiling regions; however, it increases with the



heat flux in the boiling two-phase flow region. This characteristic was observed in both microchannel evaporators for all flow rates evaluated. It is important to mention that the incipient boiling region was not observed during all experiments where a flow pattern was observed immediately after *ONB*.

The channel wall temperature shows almost a linear behavior with respect to the heat flux for both evaporators regardless of the flow rates for single and incipient boiling regions. A significant change of temperature-heat flux slope is observed during the transition between incipient and two-phase flow regions at  $q = 200 \text{ kW/m}^2$  as shown in Figure 5.8. For this particular case, *CHF* (dry-out condition) is observed with an inverted annular flow pattern. At this condition, the pressure drop and channel wall temperature increased significantly with a very small increment on the heat flux as shown in Figure 5.8. Similar trends for pressure drop and channel wall temperature were reported by Chen and Garimella (2006).

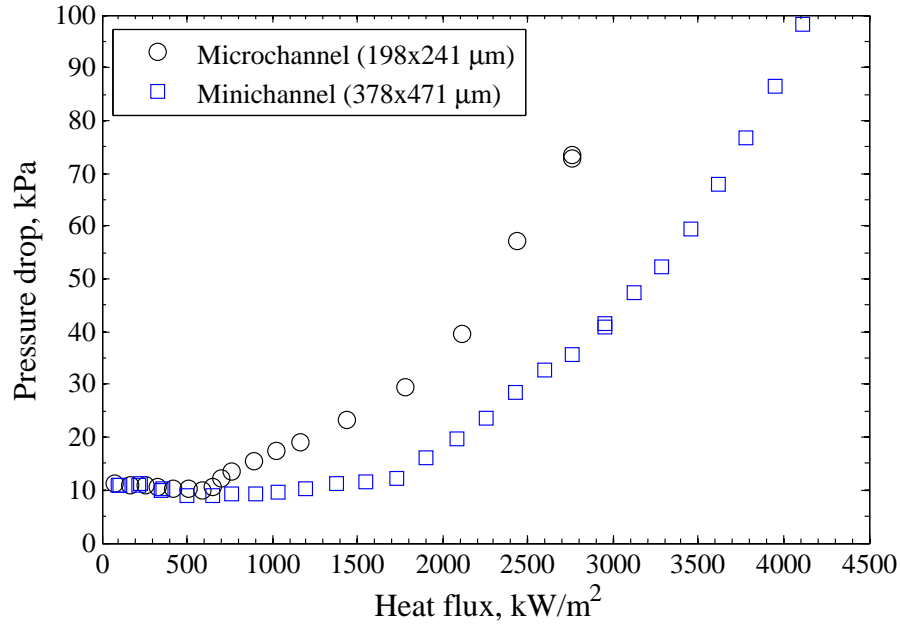


Figure 5.9: Pressure drop for two different channel sizes as a function of the heat flux for a constant mass flux  $G \approx 1300 \text{ kg/m}^2\text{s}$

It is well known that for single-phase flow, the pressure drop in a channel increases as the channel size decreases for a given flow rate of coolant. It is interesting to know if this can be applicable for two-phase flow. Figure 5.9 shows the variation of the pressure drop with the heat flux for two microevaporators with different channel size for a given mass flux. The near horizontal line in the first portion of the curves represent single-phase data, where no effects of heat flux are expected on the pressure drop. As the heat increases, boiling commences, and the pressure drop begins to show dependency on the heat flux. It is evident from Figure 5.9 that for a given mass and heat flux, the pressure drop is higher in the smaller microchannel. This is analogous to the single-phase case, where the pressure drop increases as the channel size decreases for a constant mass flow rate. Therefore, for a given mass flux of coolant, the two-phase flow pressure drop increases as the channel size decreases or the heat flux increases.

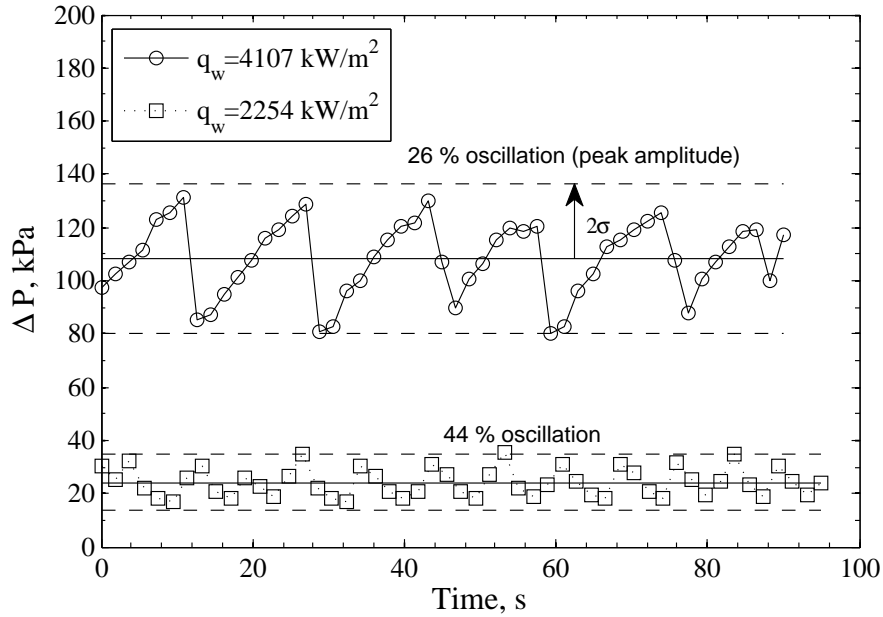


Figure 5.10: Pressure drop oscillations for  $378 \times 471 \mu m$  minichannel

A direct consequence of high heat flux is a fluctuation in the wall channel temperature and the measured pressure drop across the microchannel. Figure 5.10 shows the pressure drop time traces for the  $378 \times 471 \mu m$  minichannel at two different heat fluxes and constant

mass flux. The fluctuation strength or peak amplitude, quantified as two times the standard deviation ( $\sigma$ ) of pressure drop measurements was approximately 26 % and 44 % for  $q_w = 4107 \text{ kW/m}^2$  and  $q_w = 2254 \text{ kW/m}^2$  respectively as shown in Figure 5.10. The amplitude of the oscillations in the pressure drop and channel wall temperature increases with the heat flux and can be attributed to the growth of confined bubbles, re-wetting, and flow reversal.

## 5.6 Flow regime maps

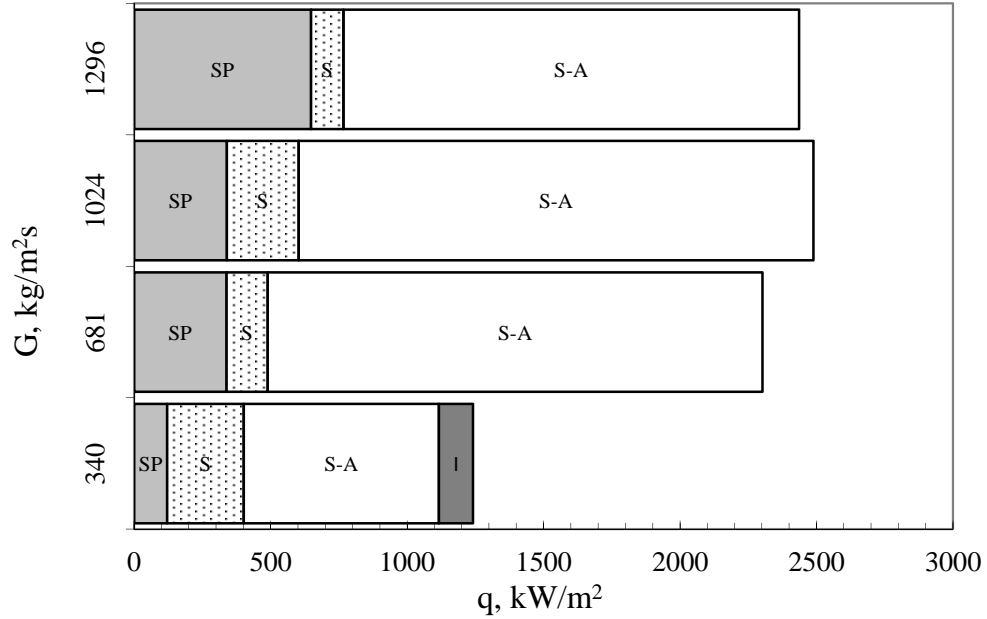


Figure 5.11: Summary of boiling flow patterns in a  $198 \times 241 \mu\text{m}$  microchannel. *SP*: single-phase, *S*: slug flow, *S – A*: slug and annular flow, *I*: inverted annular flow

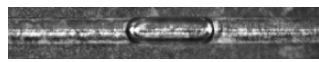
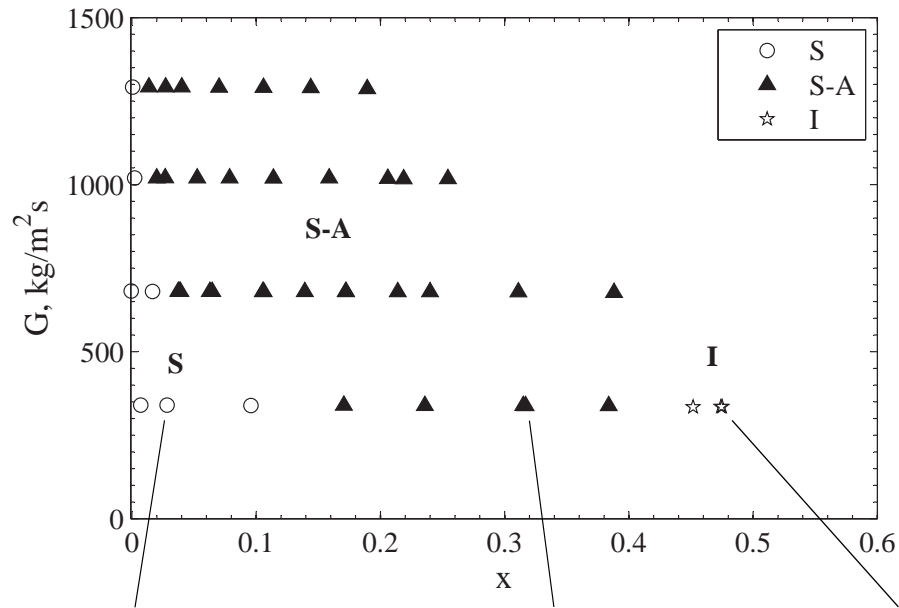
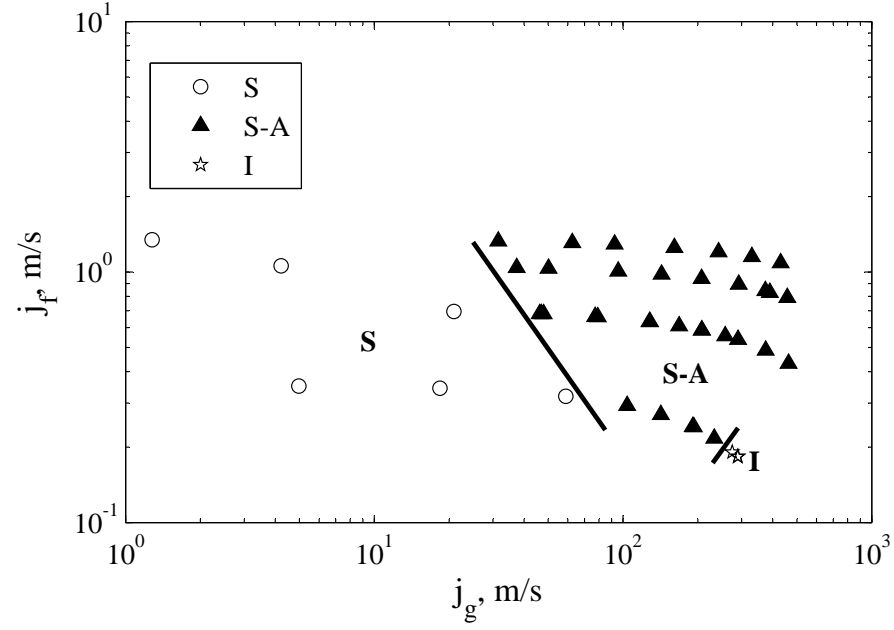
Flow patterns are typically presented in a convenient form called flow regime maps. Figure 5.11 shows a non-conventional representation of a flow regime map but this form seems to be more practical for electronics cooling since it includes the heat flux and mass flux. Figure 5.11 shows a summary of the flow patterns observed in a  $198 \times 241 \mu\text{m}$  microchannel at heat

fluxes up to  $2500 \text{ kW/m}^2$  and four different mass fluxes  $G = 340, 681, 1024, 1296 \text{ kg/m}^2\text{s}$ ). Any single flow pattern occurs along the channel. At this microchannel size, bubbly flow was not established at the visualization location, and instead, slug flow commenced early after the *ONB*. The slug flow started at heat fluxes 120, 338, 339, and  $647 \text{ kW/m}^2$  for mass fluxes 340, 681, 1024 and  $1296 \text{ kg/m}^2\text{s}$ , respectively. As the heat flux increases, the flow pattern changes to slug-annular flow. This flow is characterized by the expansion of a confined bubble upstream and downstream that eventually takes up the total length of the channel transitioning into annular flow. Note that as the mass flux is increased, the transition lines are shifted towards higher heat flux.

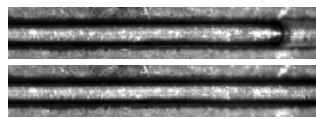
A dry-out condition was reached for the lowest mass flux ( $G = 340 \text{ kg/m}^2\text{s}$ ) and the smallest channel size  $198 \times 241 \text{ }\mu\text{m}$ . During this dry-out condition, inverted annular flow was observed, starting at approximately  $1100 \text{ kW/m}^2$  as shown in Figure 5.11. This kind of flow pattern is undesirable, not only because the channel wall temperature drastically increases but also because the heat transfer coefficient deteriorates due to the fact that the heat is transferred by conduction and radiation through a film of vapor instead of a liquid film.

As the mass flux increases, boiling or *ONB* commences at a higher heat flux, this has also been reported by Harirchian and Garimella (2010) and Bertscha et al. (2009). This can be attributed to a thinner thermal boundary layer or an increase in the saturation temperature due to higher pressure in the channel as the mass flux increases.

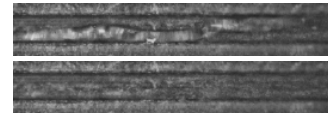
Flow pattern maps for the  $198 \times 241 \text{ }\mu\text{m}$  microchannel plotted using liquid vs. vapor superficial velocities ( $j_f, j_g$ ) and mass flux ( $G$ ) vs. vapor quality ( $x$ ) are shown in Figure 5.12. Boiling typically starts at *ONB*, followed by incipient boiling (*IB*), slug flow (*S*), slug and annular flow (*S – A*: where a vapor slug expands and occupies the total length of the channel), and inverted annular flow (*I*). This progression from incipient boiling to inverted annular flow is shown in Figure 5.12 for a fixed mass flux  $G \simeq 340 \text{ kg/m}^2\text{s}$  as the heat flux increases.



$q=264 \text{ kW/m}^2$   
 $x=0.03$



$q=946 \text{ kW/m}^2$   
 $x=0.32$



$q=1238 \text{ kW/m}^2$   
 $x=0.47$

Figure 5.12: Flow regime map for  $198 \times 241 \mu\text{m}$  microchannel. *S*: slug flow, *S* – *A*: slug and annular flow, *I*: inverted annular flow

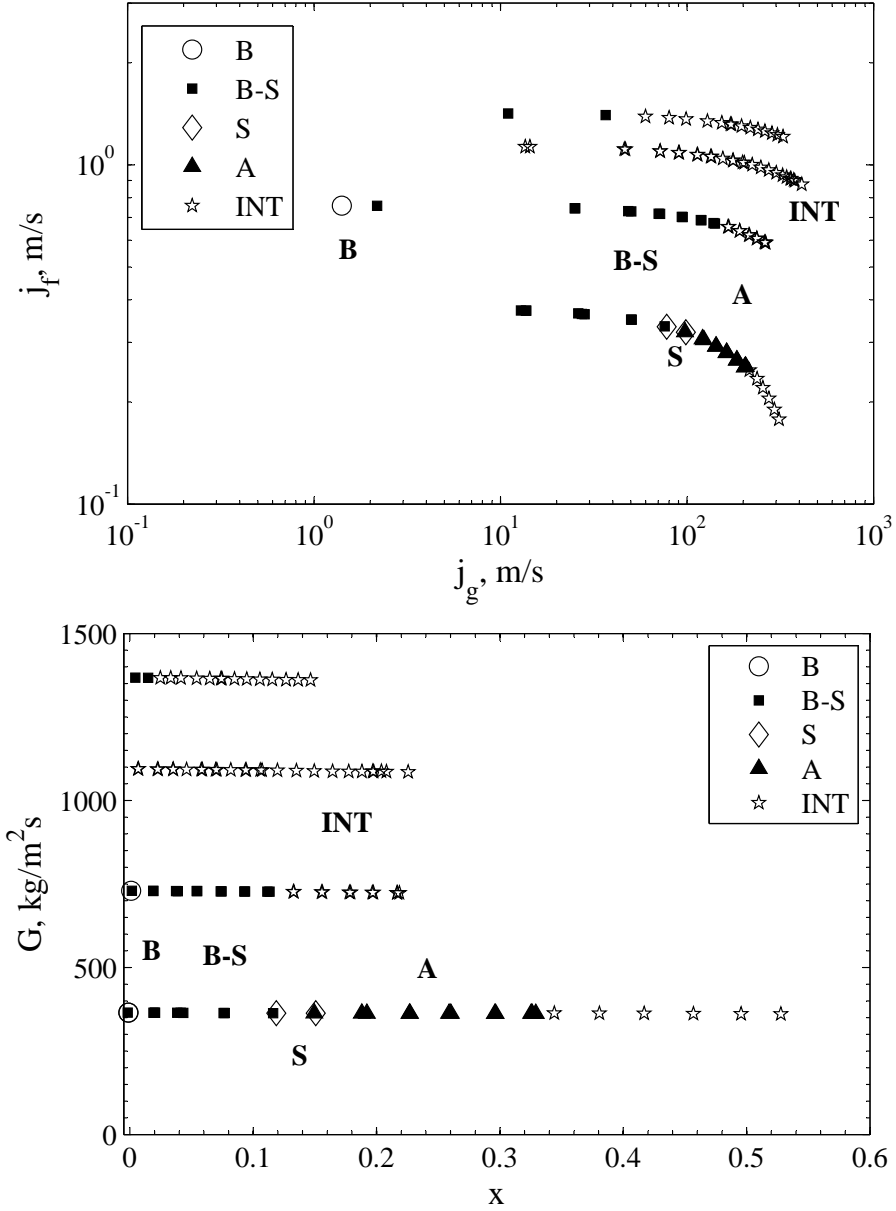


Figure 5.13: Flow regime map for  $378 \times 471 \mu\text{m}$  minichannel. *B*: bubbly flow, *B – S*: bubbly-slug flow, *S*: slug, *A*: annular flow, *INT*: intermittent flow

Figure 5.13 shows the flow regime map for the larger channel tested. This flow map shows patterns that were not observed in the smaller channel (e.g. bubbly and intermittent flows). The bubbly flow pattern appears in the conventional size channels typically at high liquid and low vapor superficial velocities, due to turbulence in the liquid breaking up the

vapor phase into small bubbles. In this microchannel, bubbly flow commenced early after  $IB$  at lower mass flux but quickly changed to bubbly-slug flow. Intermittent flow was the most predominant flow pattern in this minichannel which was observed at higher vapor or liquid superficial velocities, where turbulence and agitation of the vapor-liquid interface will result in much more chaotic patterns. It is evident that the higher the mass flux, the earlier the transitions between the different flow patterns occur, this characteristic behavior of the transition lines was also reported by Callizo (2010).

## 5.7 Macro and micro flow regime maps comparison

Although, there have been recent efforts to study the diabatic two-phase flow at the microscale, there are a limited number of publications considering water as the working fluid in rectangular channels with hydraulic diameters less than one millimeter. In this section, the diabatic flow regime map obtained in this work is compared with existing adiabatic and diabatic two-phase flow regime maps and experimental transition lines for horizontal flow in the conventional size channels as well as in microchannels.

### 5.7.1 Macroscale flow regime maps

As mentioned in section 2.1.1, one of the earliest flow regime maps available for horizontal flow is that of Mandhane et al. (1974) shown in Figure 2.2. The transition boundaries were presented in a log-log plot using superficial phasic velocities of 1178 flow patterns observations for an air-water system in a pipe with inside diameters between 13 and 165mm.

As shown in Figure 5.14, this macro flow regime map presents very poor agreement with the present experimental data both with respect to the significant trends of the curves and the absolute locations for the  $S - A$  and  $I$  flow patterns. In this work, the majority of flow patterns ( $S - A$ ,  $I$ ) observed in the smallest channel tested are in the annular region of Mandhane's flow map, and a majority of the slug flow patterns match in both regime maps but transition lines are different.

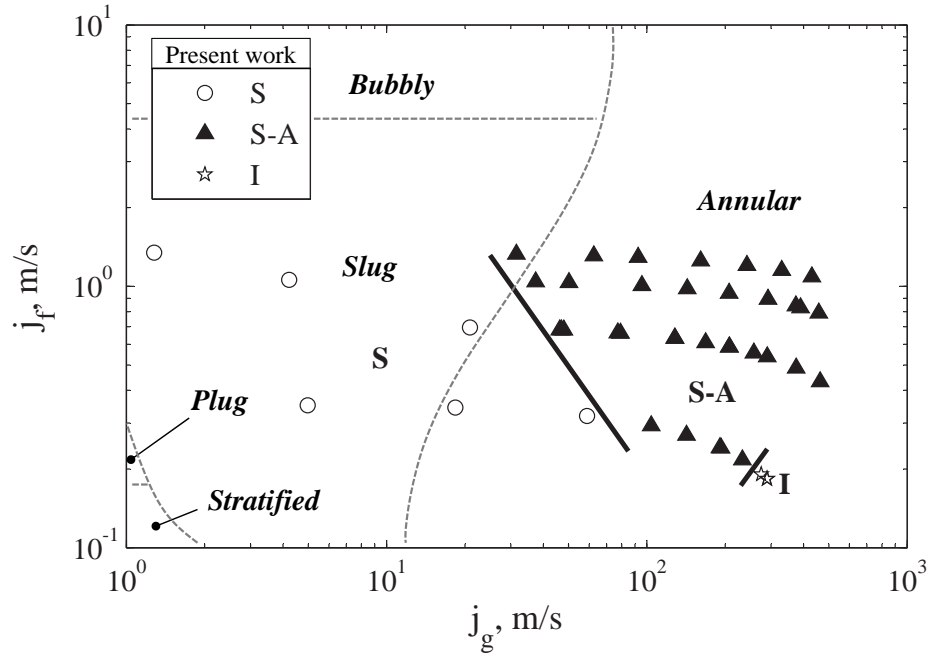


Figure 5.14: Comparison between present flow regime map ( $198 \times 241 \mu m$  microchannel) and the experimental transition lines of Mandhane et al. (1974)

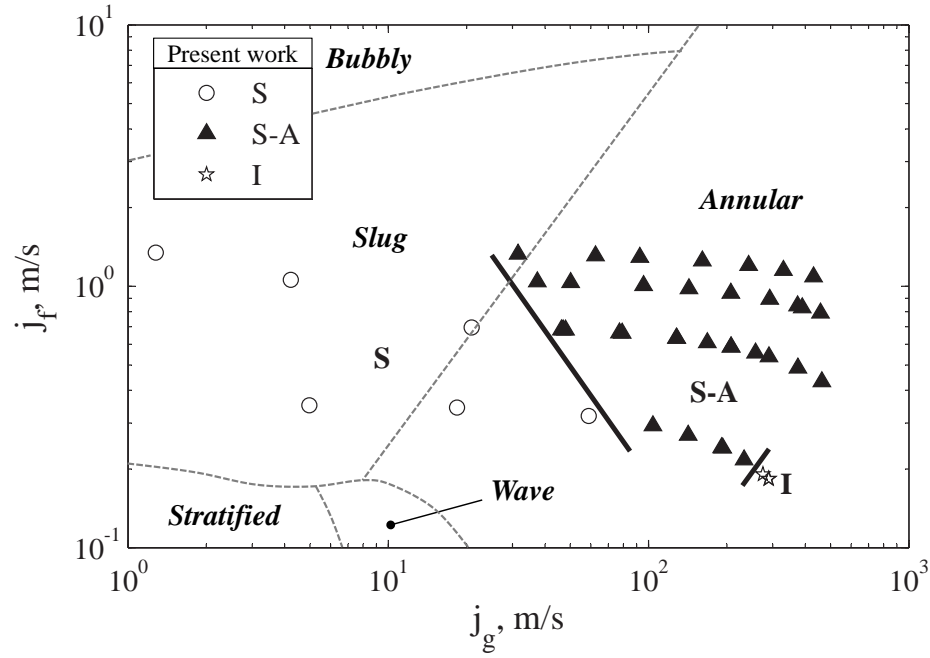


Figure 5.15: Comparison between present flow regime map ( $198 \times 241 \mu m$  microchannel) and transitions lines predicted by Taitel and Dukler (1976)



Figure 5.15 shows the experimental flow data for the  $198 \times 241 \mu m$  microchannel compared to predictions using the model for horizontal gas-liquid flow in the conventional size channel of Taitel and Dukler (1976). In general, traditional two-phase flow regimes maps, developed for mini and macroscale channels (with a hydraulic diameter larger than a millimeter), such as the widely adopted map by Mandhane et al. (1974) and the transition criteria developed by Taitel and Dukler (1976) for gas-liquid flow in horizontal channel cannot be applied for diabatic two-phase flow in microchannels. This can be attributed to the impact of surface tension, confinement effects, in addition to the coupled effects between heat and fluid mechanisms in diabatic systems which may lead to different flow regime maps.

### 5.7.2 Microscale flow regime maps

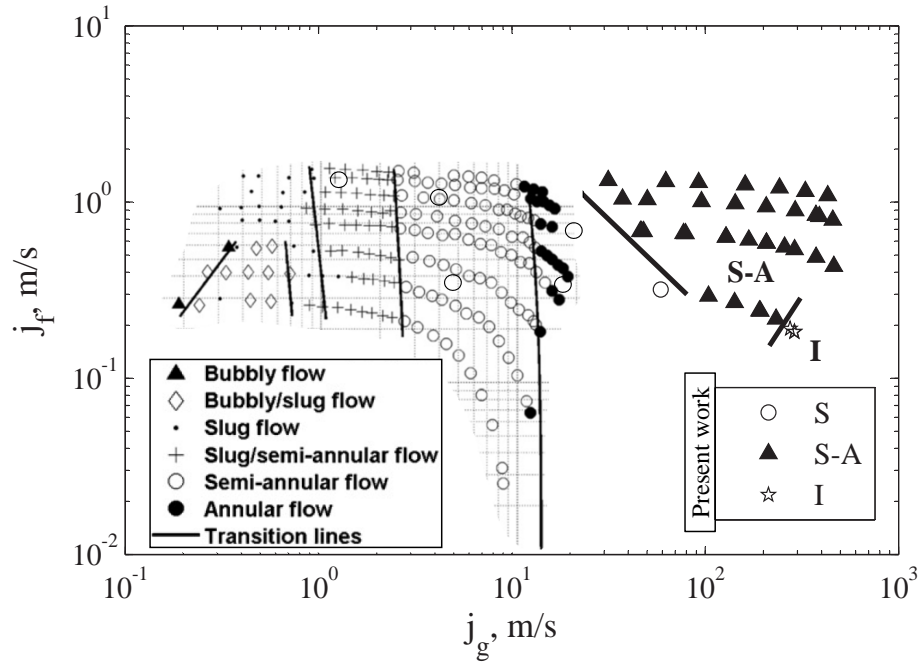


Figure 5.16: Comparison between flow regime maps: Present flow regime map ( $198 \times 241 \mu m$  microchannel) and pipe ( $D = 0.509 mm$ ) by Revellin and Thome (2007b)

Figure 5.16 shows a comparison between the  $198 \times 241 \mu m$  microchannel with the flow regime map by Revellin and Thome (2007b) obtained for R-134a in a pipe of  $0.509 \text{ mm}$  internal diameter and  $50 \text{ mm}$  length. Although, the geometry sizes are comparable, and both flow regime maps were obtained under diabatic conditions, the agreement is not satisfactory. It is important to mention that the thermophysical properties of R-134a differ significantly from those of water and the cross sectional areas of the geometries are also different.

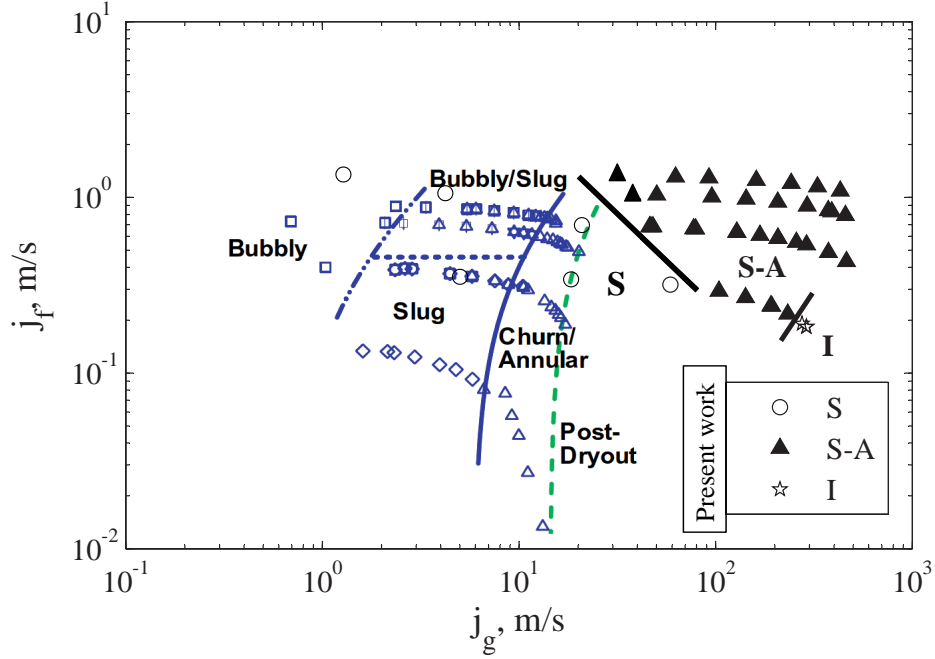


Figure 5.17: Comparison between flow regime maps: Present flow regime map ( $198 \times 241 \mu m$  microchannel) and minichannel ( $250 \times 400 \mu m$ ) by Harirchian and Garimella (2009b)

In Figure 5.17, the flow regime map for the smallest channel tested in this work and the one obtained by Harirchian and Garimella (2009b) are compared. In this case both geometries are for rectangular channels with comparable size and diabatic conditions. As in Figure 5.16 this flow map is for R-134a and their data are shifted to the left side. Again, only a small region of the slug flow data is consistent between these flow regime maps.

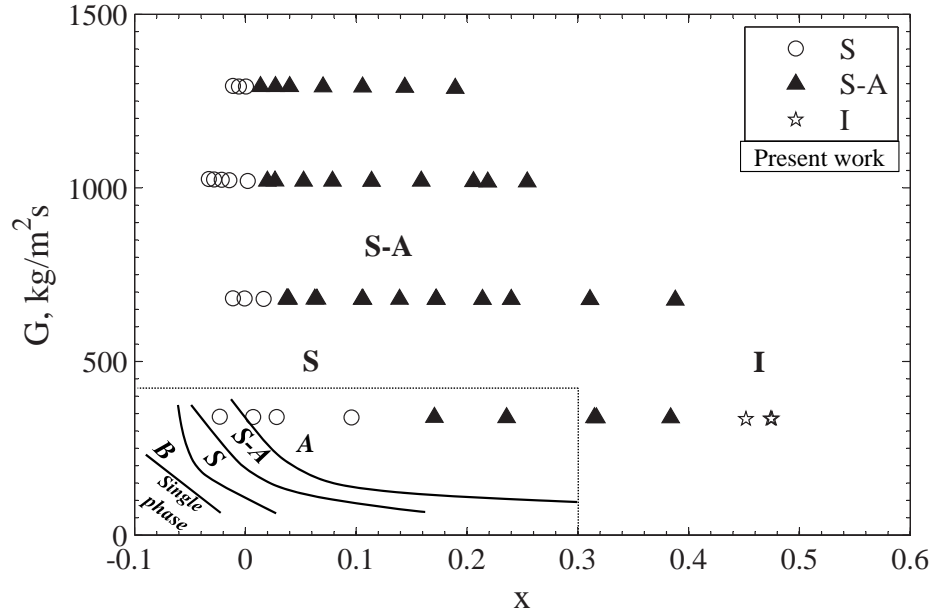


Figure 5.18: Comparison between flow regime maps: Present flow regime map ( $198 \times 241 \mu m$  microchannel) and microchannel ( $119 \times 173 \mu m$ ) by Singh et al. (2009)

Finally, in Figure 5.18 the  $198 \times 241 \mu m$  microchannel is compared with the experimental flow regime map obtained by Singh et al. (2009). Both flow regimes are for water as working fluid, rectangular channels with hydraulic diameters 141 and  $270 \mu m$ , and at diabatic conditions. The experimental data reported by Singh et al. (2009) are for mass flux and vapor quality up to  $425 kg/m^2s$  and 0.3 respectively (dot lines on Figure 5.18). In these flow regime maps, the change of the flow pattern from *bubbly* to *slug* and from *slug* to *slug-annular* is consistent but the flow transitions are located in very different regions.

In summary, the flow regime maps in Revellin and Thome (2007b); Harirchian and Garimella (2009b); Singh et al. (2009) among other publications, indicates a progressive change on the flow pattern which is consistent with the observations in this work. Typically, bubbly flow commences and develops into slug and annular flow as the vapor quality or superficial vapor velocity increases. All flow patterns observed in the microchannels are also found in macro size channels. However, the confinement of the bubbles in macrochannels play an important factor in the characteristics of the flow pattern and transitions. Stratified

flow was not observed in the microchannels because gravitational effects are neglected. Higher heat flux is required to reach *ONB* as the mass flux increases. This is associated with a higher saturation temperature (pressure increases in the channel) as the mass flux increases. Bubble departure diameter decreases with the heat flux and mass flux. The higher drag force in the bubbles due to higher mass flux causes quicker depart of the bubbles from the surface. The number of active cavities increases with the heat flux. This is consistent with boiling in macro and micro size geometries reported in other publications. The vapor slug length increases with the heat flux because the higher evaporative rate. Flow reversal is presented in single channel microevaporators and it is attributed to the expansion upstream of confined bubbles. Macro and micro flow regime maps are not comparable, and the differences are mainly attributed to the confinement of the bubbles. Re-wetting and pressure oscillations may play a crucial role and are likely responsible for the development and evolution of flow patterns.

# Chapter 6

## Experimental Heat Transfer Coefficient, $HTC$

In this chapter, the thermal performance of microevaporators is evaluated based on experimental boiling curves and the  $HTC$ . The boiling curves are presented as heat flux vs wall channel superheat at different mass fluxes. Maximum heat fluxes and channel wall temperature are reported to estimate the potential application of microevaporators with water as the working fluid in cooling systems for high heat flux. Finally, the experimental  $HTCs$  are compared with some published models.

### 6.1 Experimental Results

Heat transfer data in the microevaporators were recorded simultaneously with the flow visualization measurements as described in Chapter 5. Details of the experimental conditions and procedure are described in the Chapter 3 section 3.1.

Table 6.1: Results for thermal performance study (microchannel  $198 \times 241 \mu m$ )

$G, kg/m^2 s$	$Re$	$q_w, kW/m^2$	$T_w @ L/2, ^\circ C$	$T_{w, avg}, ^\circ C$	$T_w - T_{sat} @ L/2, ^\circ C$	$h_{tp}, kW/m^2 K$	$x_{out}$
340	204	200	98.6	99.0	0.28	712.5	0.01
340	205	264	99.5	99.7	1.06	250.4	0.03
339	218	401	101.5	101.7	2.79	143.4	0.10
339	216	604	103.1	103.3	3.83	157.8	0.17
338	225	740	103.8	104.1	4.63	160.0	0.24
338	226	947	105.3	105.5	5.59	169.5	0.32
338	225	946	105.4	105.6	5.70	165.8	0.31
338	228	1116	107.1	107.2	6.81	163.9	0.38
335	256	1238	116.0	115.9	13.92	89.0	0.47
335	256	1241	115.5	115.5	12.65	98.1	0.48
334	264	1242	131.0	131.2	29.03	39.5	0.45
1292	777	766	102.6	102.6	2.87	266.8	0.00
1292	778	895	104.1	104.2	4.19	213.5	0.01
1292	779	1028	105.2	105.3	5.05	203.5	0.03
1292	778	1162	106.0	106.1	5.67	205.0	0.04
1291	785	1437	107.6	107.6	6.65	216.0	0.07
1291	789	1778	109.4	109.4	7.74	229.7	0.11
1290	801	2112	112.1	112.1	9.22	229.0	0.14
1287	834	2436	115.7	115.7	10.86	224.4	0.19
1285	859	2764	119.1	119.0	12.48	221.5	0.23
1284	862	2762	119.3	119.2	12.64	218.5	0.23

Table 6.1 shows a summary of the results used to estimate the thermal performance of the microevaporator with the microchannel size  $198 \times 241 \mu m$ . More data at different flow conditions for this microchannel, and for the microevaporator with the minichannel size  $378 \times 471 \mu m$  are shown in Appendix G section G.7.

The local  $HTC$  is calculated at the middle of the channel which corresponds to the same location where the high-speed videos for the flow patterns are recorded. Details of the procedure for the estimation of the  $HTC$  are given in the Chapter 3 section 3.2.2. Equation 3.18 is used for the calculation of the local  $HTC$ , where the channel saturation temperature is estimated at the local pressure in the channel. The local  $HTC$  estimated at the middle of the channel represents the average  $HTC$  of the microevaporator.

## 6.2 Boiling curve

Boiling curves are plotted for the  $198 \times 241$  and  $378 \times 471 \mu m$  microevaporators in Figures 6.1 and 6.2 respectively in terms of the variation of wall heat flux with temperature difference between wall and saturated temperature at the end of the channel. The results are plotted at four mass fluxes in the range of 350 and  $1300 \text{ kg/m}^2\text{s}$  for a process path increasing the heat flux up to  $\approx 4400 \text{ kW/m}^2$  or until a maximum temperature in the microevaporator assembly unit reaches  $180^\circ\text{C}$ . Since this maximum temperature was reached by the cartridge heater, data points for the boiling curve were not possible at higher heat fluxes in some cases. The inlet temperature of the fluid was controlled at  $50^\circ\text{C}$  which corresponds to approximately  $50 \text{ K}$  of sub-cooling for all boiling curves.

A single-phase region which corresponds to the straight line portion of the boiling curve is observed before the  $ONB$  (see Figures 6.1 and 6.2). Based on the typical behavior of the boiling curve during pool or flow boiling, after  $ONB$  this linear behavior should disappear and the characteristic curvature of the boiling curve must appear. Since the channels experience incipient boiling (single-phase still dominating over two-phase flow), the curvature is not appreciable immediately after  $ONB$ . Using high-speed visualizations, the  $ONB$  was observed when the first bubbles forming on a crevice survive condensation.

The *ONB* shows the dependence on the mass flux, this was more evident in the channel size  $198 \times 241 \mu m$  where higher heat fluxes were observed at *ONB* as the mass flux increases.

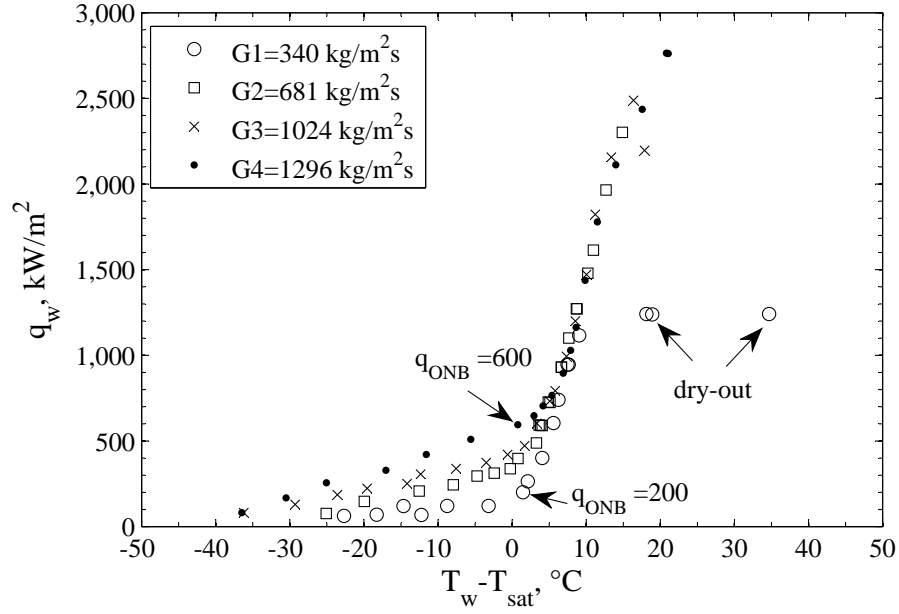


Figure 6.1: Boiling curves for microevaporator  $198 \times 241 \mu m$  microchannel

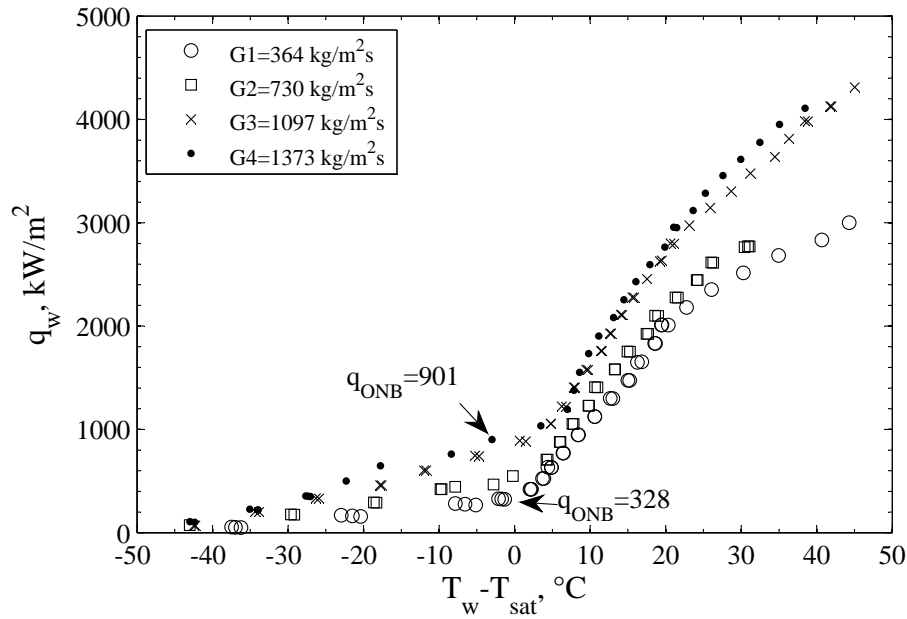


Figure 6.2: Boiling curves for minievaporator  $378 \times 471 \mu m$  minichannel



Wall superheat excursion or wall temperature overshoot, which is usually found after the initiation of *ONB* was not observed. After *ONB* or the incipient boiling region, the nucleate boiling region starts, which is characterized by the increasing of the slope on the boiling curve as the heat flux is increased.

The *CHF* is characterized in the boiling curve as a large increase in wall superheat with a small increase in heat flux. None of the experimental data reached *CHF* (dry-out condition), except the microevaporator with the smallest channel size ( $198 \times 241 \mu m$ ) and the lowest flow rate ( $G = 340 \text{ kg/m}^2\text{s}$ ) as shown in Figure 6.1. During *CHF*, film boiling was observed with an inverted annular flow pattern. Based on Figure 6.1, it seems that the *CHF* increases as the mass flux increases; this was also reported by Ali (2010); Bertscha et al. (2009).

As shown in Figure 6.1, the data converge into a single curve above 7 K of superheat, and beyond this point, there are no noticeable effects of mass flux on the boiling curve (except for  $G = 340 \text{ kg/m}^2\text{s}$  which reaches dry-out condition). Furthermore, there are no effects of the mass flux on the boiling curve after this superheat. This observation may support the dominance of nucleate boiling over a convection boiling mechanism after 8 K of superheat for the microchannel  $198 \times 241 \mu m$ . In contrast, for the larger channel  $378 \times 471 \mu m$  the boiling curves do not converge into a single curve as shown in Figure 6.2 indicating that convective boiling may dominates over nucleate boiling. Although similar observations have been reported by others authors, the experimental conditions (type of fluid, flow rates, channel size, etc.) are different. In addition, in this work the effects of non-uniform inlet flow observed in multiple channel evaporator have been isolated by using a single channel.

### 6.3 Heat Transfer Coefficient, $HTC$

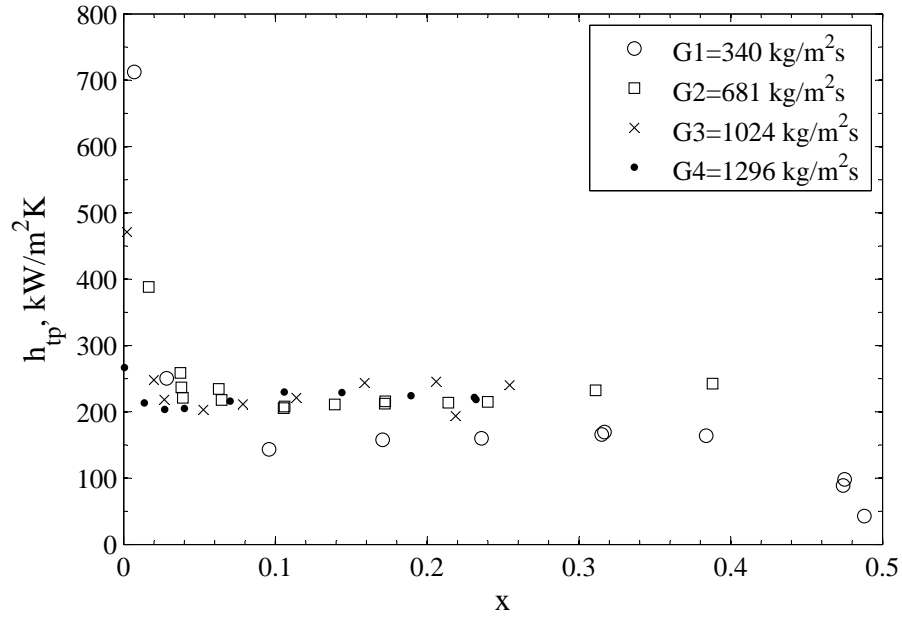


Figure 6.3: Average  $HTC$  vs vapor quality  $198 \times 241 \mu\text{m}$  microchannel

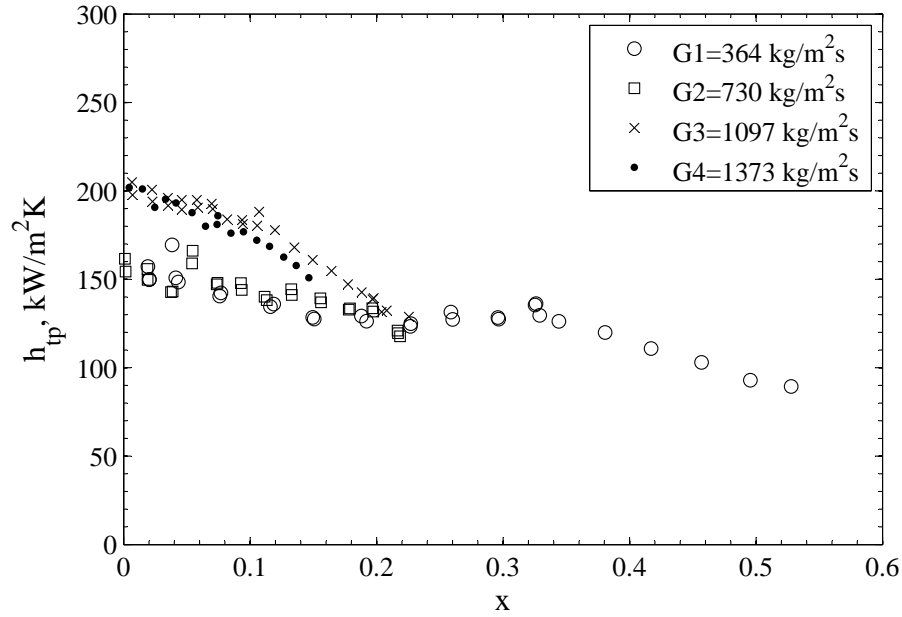


Figure 6.4: Average  $HTC$  vs vapor quality  $378 \times 471 \mu\text{m}$  minichannel

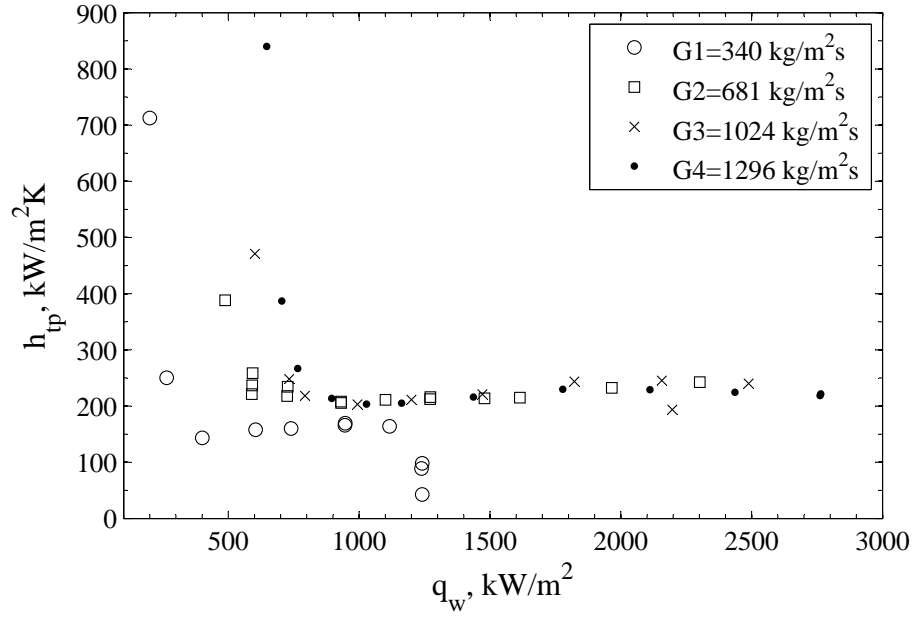


Figure 6.5:  $HTC$  vs heat flux  $198 \times 241 \mu m$  microchannel

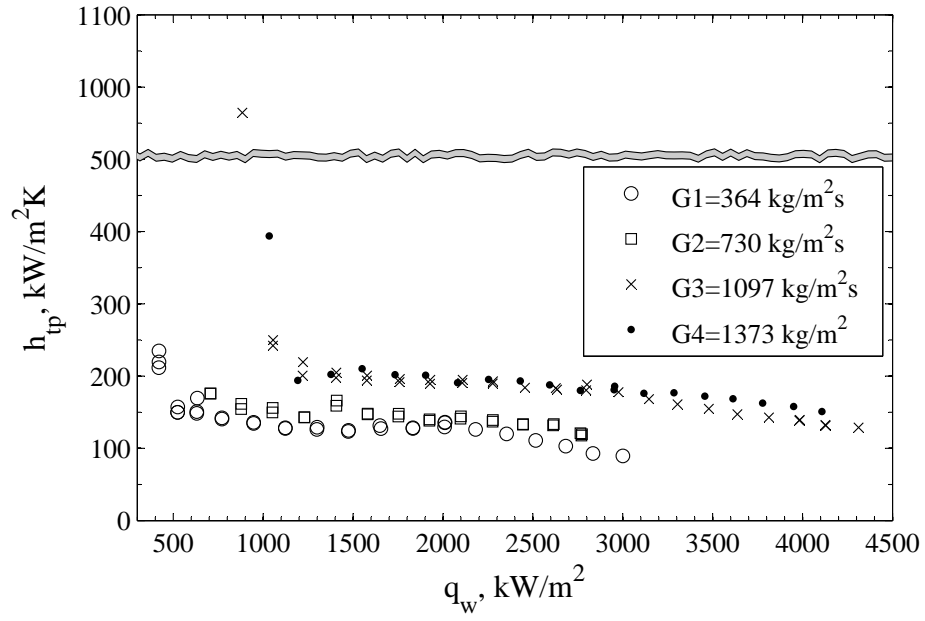


Figure 6.6:  $HTC$  vs heat flux  $378 \times 471 \mu m$  minichannel

The average  $HTC$  is plotted as a function of local quality at the channel exit (Figures 6.3 and 6.4) and heat flux (Figures 6.5 and 6.6) for the channel size  $198 \times 241 \mu m$  and  $378 \times 471 \mu m$ . The data covers four different mass fluxes over the entire range of qualities and heat fluxes possible with the current setup. The  $HTC$  decreases as the quality or heat flux increases; this similar trend has been reported by Steinke and Kandlikar (2004). The  $HTC$  is high at low values of quality or heat flux and then begins to sharply decline until dry-out conditions are reached. At this condition, the  $HTC$  drastically declines as shown in Figure 6.3 at a quality of  $x \approx 0.47$ .

Figure 6.5 shows that the  $HTC$  for the channel size  $198 \times 241 \mu m$  did not change with the mass flux after a heat flux of  $q_w \approx 900 \text{ kW/m}^2 K$  (except for the dry-out condition). This can also be supported from Figure 6.1, where the boiling curves also converge into a single curve after a heat flux of  $q_w \approx 900 \text{ kW/m}^2$ . Consequently, applying the macroscale logic (which indicates that when nucleate boiling dominates the transport, the boiling curve and  $HTC$  becomes virtually independent of the flow rate), the  $HTC$  for this channel size was predominantly controlled by nucleate boiling.

The high-speed visualizations confirm that nucleate boiling controls over convective boiling since slug and S-A flow patterns (S-A: slugs than expand until reach the total length of the channel) were the most observed during the experiments for this channel size. A similar analysis for the  $378 \times 471 \mu m$  minichannel size indicates that the  $HTC$  depends on the mass flux and the boiling curves did not converge into a single curve as shown in Figures 6.2 and 6.6. During the flow visualization for this channel size, all flow patterns were equally observed at higher heat fluxes (re-wetting and intermittent flow were very common), which may confirm that nucleate and convective boiling are both of equal importance.

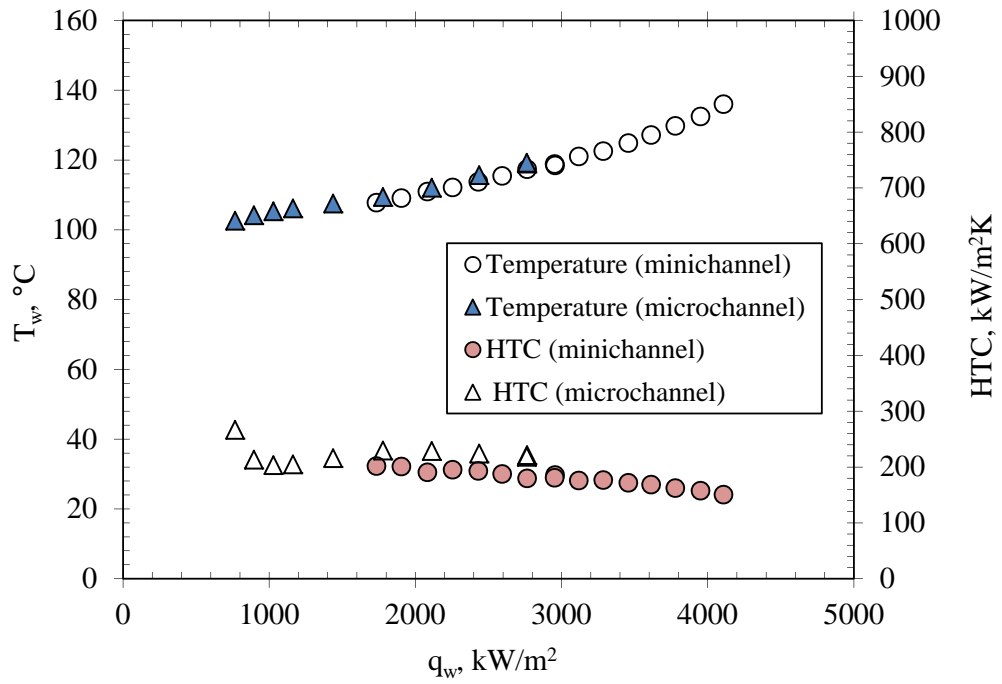


Figure 6.7: Microevaporators thermal performance curves at  $G \simeq 1300 \text{ kg/m}^2\text{s}$

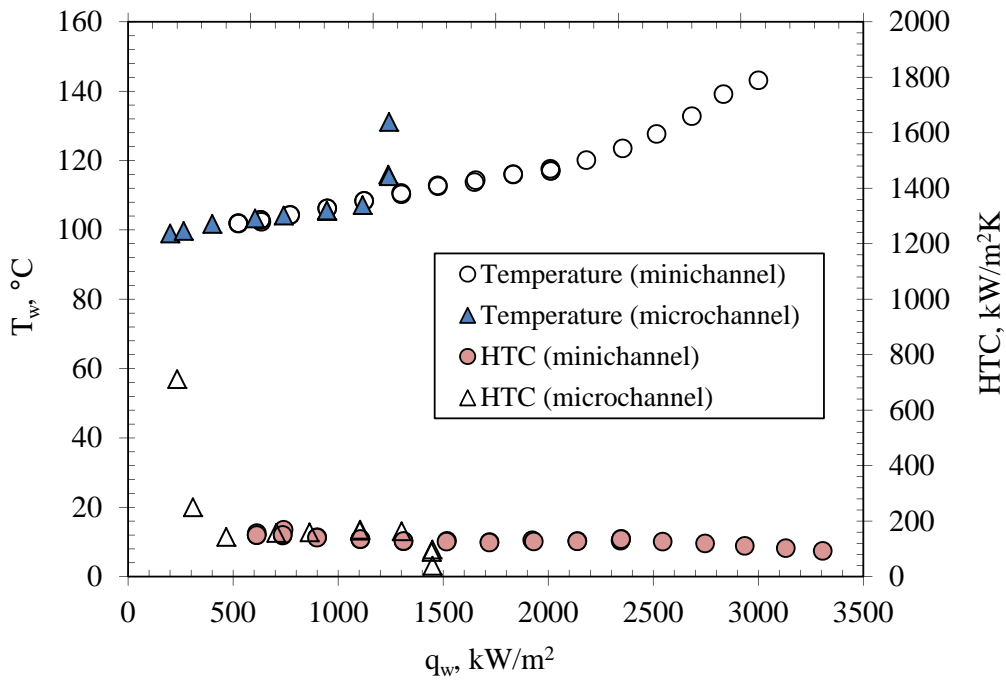


Figure 6.8: Microevaporators thermal performance curves at  $G \simeq 350 \text{ kg/m}^2\text{s}$

Figure 6.7 shows the channel wall temperature and  $HTC$  as a function of the heat flux for a mass flux  $G = 1300 \text{ kg/m}^2\text{s}$  in both microevaporators. This figure is more convenient when comparing the thermal performance between both microevaporators. From Figure 6.7, the wall temperature and  $HTC$  are comparable in both microevaporators for the same heat flux. A similar conclusion is obtained with other mass fluxes tested. The exception is for the mass flux  $G = 350 \text{ kg/m}^2\text{s}$  but only when dry-out occurred in the microchannel  $198 \times 241 \mu\text{m}$  as shown in Figure 6.8. Therefore, both microevaporators have comparable thermal performances when the dry-out condition is not present.

Figures 6.7 and 6.8 also show higher  $HTC$  and lower channel wall temperature at lower heat fluxes where sub-cooling boiling occurs. This may support the use of sub-cooled boiling for electronics cooling as suggested by Carey (2008).

In summary, the maximum heat fluxes dissipated are approximately  $280$  and  $440 \text{ W/cm}^2$  for the microevaporator with microchannel  $198 \times 241 \mu\text{m}$  and microevaporator with minichannel  $378 \times 471 \mu\text{m}$  respectively. These values of heat flux dissipation indicate that the microevaporators with water as the working fluid are an attractive solution for high heat flux cooling applications. The microevaporator with the minichannel is able to dissipate higher heat flux because it is possible to achieve higher superheat with this microevaporator without dry-out condition ( $T_w - T_{sat} \simeq 45^\circ\text{C}$  as shown in Figure 6.2 vs  $\simeq 22^\circ\text{C}$  in Figure 6.1).

## 6.4 Comparison of the experimental $HTCs$ with published correlations

Tables 6.2 and 6.3 shows the results for the experimental  $HTCs$  and the predicted values from the correlations in Table 2.1 for the  $198 \times 241 \mu\text{m}$  microchannel and  $378 \times 471 \mu\text{m}$  minichannel respectively. The results were obtained for mass fluxes between  $340$  and  $1367 \text{ kg/m}^2\text{s}$  and heat fluxes between  $264$  and  $4107 \text{ kW/m}^2\text{K}$  which cover a wide range of the experimental data in this thesis. Based on the  $HTC$  ratio ( $HTC_{model}/HTC_{experimental}$ ,

typically different than 1), the correlations indicate a poor prediction of the experimental *HTC*s which is also evidenced by the large Mean Average Error, *MAE*, between 37 and 67 % estimated from Equation 6.1.

The *MAE* for each model is reported in Tables 6.2 and 6.3 in addition to the percentage of predicted data within  $\pm 30\%$  error band which is very low (between 0 and 45 %). Larger *MAE* between 12 and 270 %, over and/or under predictions of experimental *HTC* using correlations from the open literature are very common as reported by (Megahed, 2010; Lee and Mudawar, 2008, 2004; Qu and Mudawar, 2003). Typically, the correlations are adjusted (calibrated) for the new set of experimental data through new expressions for the suppression and enhancement factors. The development of a model for two-phase flow *HTC* is beyond the scope of this thesis but the purpose of these comparisons is to illustrate the higher errors in the prediction of the *HTC* from traditional models that are not generated based on the flow patterns. Even the most successful correlation after “calibration”, predicts a maximum of 90 % of the data fall within the  $\pm 30\%$  band error and *MAE*  $\approx 15\%$ .

$$MAE = \frac{1}{n} \sum \left( \frac{|h_{exp} - h_{model}|}{h_{exp}} \times 100 \right) \quad (6.1)$$

Table 6.2: Results for experimental and predicted  $HTC$ 's ( $198 \times 241 \mu m$  microchannel)

bxa, $\mu m$	G, $kg/m^2 s$	q, $kW/m^2$	HTC, $kW/m^2 K$ , ratio (model/exp)						Flow pattern
			Experimental	Kandlikar	Gungor and Winterton	Schrock and Grossman	Lee and Mudawar	Lee and Garimella	
198x241	340	264	250	52 0.2	43 0.2	29 0.1	42 0.2	40 0.2	S
	339	604	158	131 0.8	93 0.6	66 0.4	44 0.3	57 0.4	S-A
	338	947	169	188 1.1	127 0.8	90 0.5	44.2 0.3	67 0.4	S-A
	338	1116	164	172 1.1	207 1.3	139 0.9	98.4 0.6	71 0.4	S-A
	335	1241	98	231 2.4	149 1.5	101 1.0	42.9 0.4	73 0.7	I
	680	488	388	46 0.1	68 0.2	45 0.1	46 0.1	53 0.1	S
	680	592	237	60 0.3	84 0.4	58 0.2	40 0.2	57 0.2	S-A
	679	931	208	102 0.5	129 0.6	93 0.4	75.6 0.4	68 0.3	S-A
	679	1614	215	161 0.8	196 0.9	142 0.7	74 0.3	79 0.4	S-A
	677	2302	243	210 0.9	247 1.0	174 0.7	73 0.3	82 0.3	S-A
	1020	602	471	42 0.1	85 0.2	55 0.1	48 0.1	57 0.1	S
	1020	793	218	58 0.3	111 0.5	75 0.3	42 0.2	64 0.3	S-A
	1019	1200	211	81 0.4	151 0.7	108 0.5	104 0.5	74 0.3	S-A
	1019	1823	244	113 0.5	206 0.8	153 0.6	99 0.4	81 0.3	S-A
	1017	2488	240	147 0.6	261 1.1	195 0.8	97 0.4	83 0.3	S-A
	1292	766	267	39 0.1	81 0.3	47 0.2	45 0.2	62 0.2	S
	1292	1028	203	52 0.3	128 0.6	87 0.4	42 0.2	70 0.3	S-A
	1291	1437	216	80 0.4	177 0.8	126 0.6	124 0.6	77 0.4	S-A
	1290	2112	229	118 0.5	247 1.1	179 0.8	116 0.5	83 0.4	S-A
	1285	2764	221	155 0.7	311 1.4	222 1.0	111 0.5	84 0.4	A
			MAE, %	55.9	39.0	47.8	67.0	66.9	
			Data 30 % band	30.0	45.0	30.0	0.0	5.0	



Table 6.3: Results for experimental and predicted  $HTCs$  ( $378 \times 471 \mu m$  minichannel)

bxa, $\mu m$	$G, kg/m^2 s$	$q, kW/m^2$	HTC, $kW/m^2 K$ , ratio (model/exp)						Flow pattern					
			Experimental	Kandlikar	Gungor and Winterton	Schrock and Grossman	Lee and Mudawar	Lee and Garimella						
378x471	365	525	219	36	0.2	53	0.2	41	0.2	23	0.1	53	0.2	B
	364	771	142	53	0.4	80	0.6	63	0.4	45	0.3	62	0.4	B-S
	363	1124	128	74	0.6	108	0.8	88	0.7	42	0.3	70	0.5	A
	362	1833	128	107	0.8	150	1.2	124	1.0	42	0.3	79	0.6	A
	363	2354	120	122	1.0	172	1.4	143	1.2	43	0.4	81	0.7	INT
	362	2683	103	133	1.3	182	1.8	148	1.4	43	0.4	81	0.8	INT
	361	2834	93	135	1.4	179	1.9	141	1.5	43	0.5	81	0.9	INT
	730	877	154	32	0.2	73	0.5	52	0.3	24	0.2	65	0.4	B-S
	729	1409	166	44	0.3	124	0.7	98	0.6	19	0.1	75	0.5	B-S
	727	2100	144	69	0.5	177	1.2	144	1.0	50	0.3	81	0.6	INT
	725	2445	133	81	0.6	201	1.5	163	1.2	68	0.5	82	0.6	INT
	723	2765	121	90	0.7	220	1.8	179	1.5	67	0.6	82	0.7	INT
	1094	1578	201	40	0.2	129	0.6	99	0.5	22	0.1	77	0.4	S
	1092	2109	195	51	0.3	175	0.9	138	0.7	103	0.5	81	0.4	S-A
	1092	2456	184	59	0.3	199	1.1	160	0.9	98	0.5	82	0.4	S-A
	1089	3146	168	76	0.5	248	1.5	200	1.2	92	0.5	81	0.5	S-A
	1087	4128	132	93	0.7	300	2.3	247	1.9	91	0.7	76	0.6	S-A
	1367	1904	201	65	0.3	142	0.7	108	0.5	24	0.1	80	0.4	S
	1367	2430	193	76	0.4	189	1.0	149	0.8	20	0.1	82	0.4	S-A
	1364	3118	176	99	0.6	240	1.4	193	1.1	114	0.6	81	0.5	S-A
	1361	3778	163	124	0.8	286	1.8	231	1.4	108	0.7	79	0.5	S-A
	1360	4107	151	133	0.9	306	2.0	248	1.6	107	0.7	76	0.5	A
			MAE, % Data 30 % band	51.4	44.9	37.1	63.6	47.5						
				25.0	40.0	45.0	0.0	10.0						

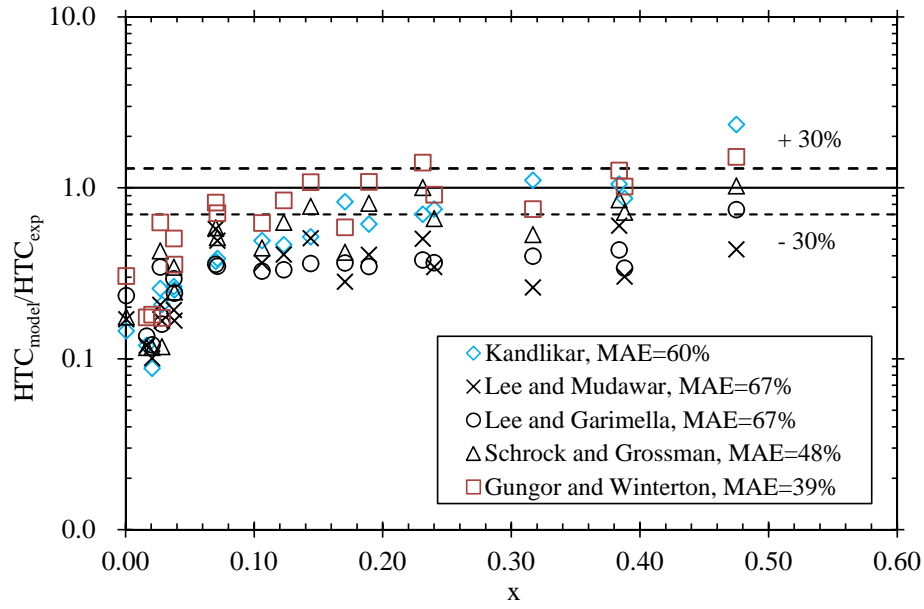


Figure 6.9: Comparison of saturated flow boiling  $HTCs$  ( $198 \times 241 \mu m$  microchannel)

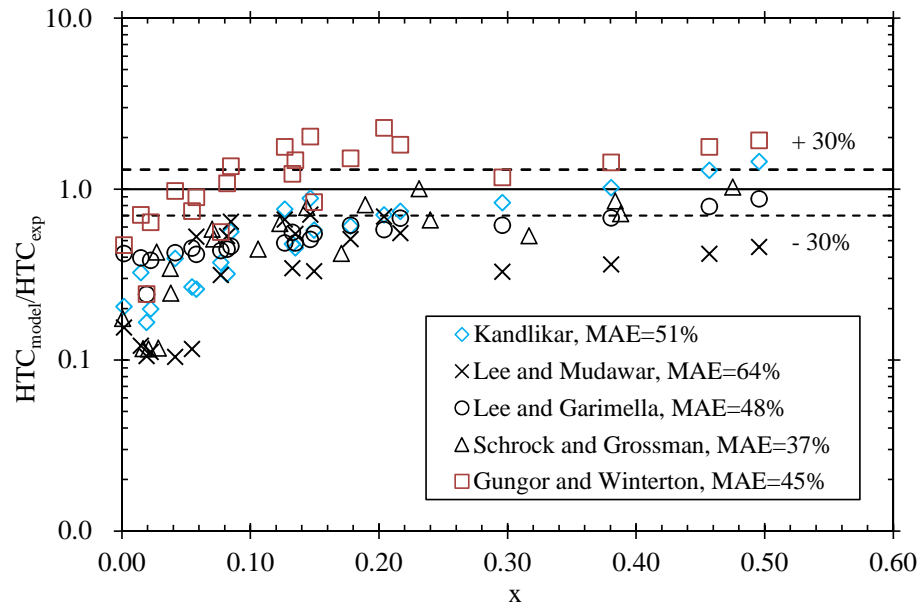


Figure 6.10: Comparison of saturated flow boiling  $HTCs$  ( $378 \times 471 \mu m$  minichannel)

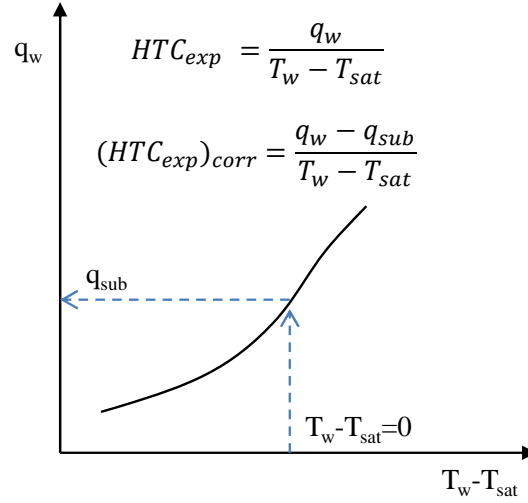


Figure 6.11: Estimation of heat flux due to sub-cooling using the boiling curve

Figures 6.9 and 6.10 compare the predicted and experimental  $HTCs$ , where higher errors in the prediction of the  $HTC$  can be mostly observed at lower qualities which is attributed to the sub-cooling in the experiments. The experimental  $HTCs$  can be corrected for sub-cooling by subtracting the heat flux attributed to sub-cooling ( $q_{sub}$ ) which can be obtained from the boiling curves (Figures 6.1 and 6.2) at  $T_w - T_{sat} = 0$  as illustrated in Figure 6.11.

Table 6.4:  $MAEs$  in the prediction of  $HTCs$  after sub-cooling correction

Variable	Kandlikar	Gungor and Winterton	Schrock and Grossman	Lee and Mudawar	Lee and Garimella	Channel bxa, $\mu m$
MAE, %	55.9	39.0	47.8	67.0	66.9	Microchannel
MAE (corrected), %	30.8	38.1	17.7	37.5	38.5	198x241
MAE, %	51.4	44.9	37.1	63.6	47.5	Minichannel
MAE (corrected), %	39.2	59.0	38.2	51.6	28.5	378x471

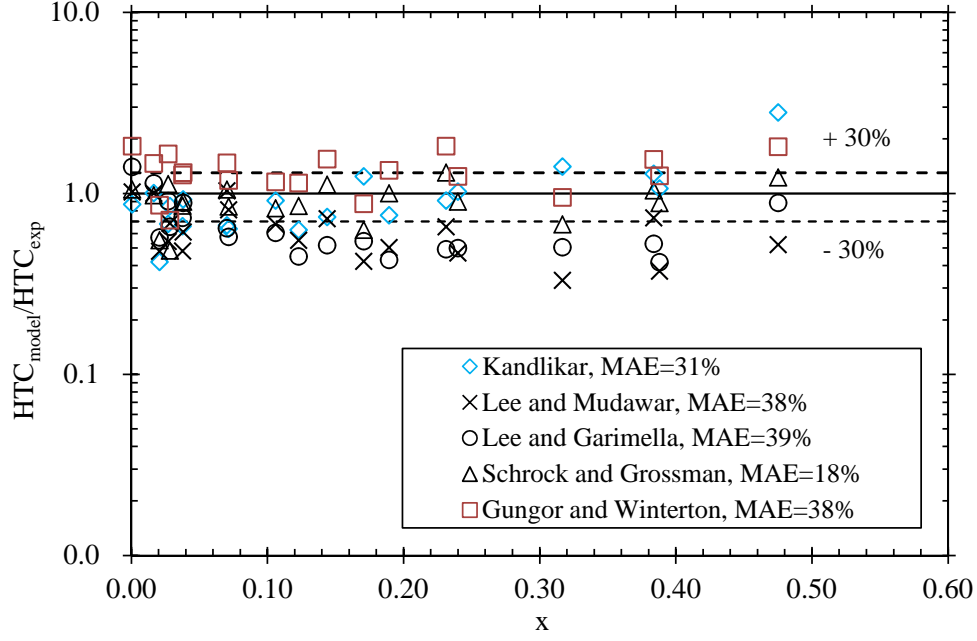


Figure 6.12: Comparison of saturated flow boiling  $HTCs$  after sub-cooling correction ( $198 \times 241 \mu m$  microchannel)

Figure 6.12 shows the ratio of  $HTCs$  (the experimental  $HTC$  is corrected by sub-cooling) versus the vapor quality for the microchannel evaporator. There is an appreciable improvement in the prediction of the  $HTCs$  after sub-cooling correction at low vapor qualities as seen in Figure 6.12 and evidenced by the reduction on the  $MAEs$  as shown in Table 6.5 with the exception of the Gungor and Winterton, and Schrock and Grossman's correlations for the minichannel evaporator, possibly because these two correlations are intended for conventional, larger geometries.

In summary, the proposed correlations from the literature are not able to predict the heat transfer coefficient with low mean average error. The degree of sub-cooling on the experiments must be taken into account for a proper comparison of heat transfer coefficients. Typically, the published correlations are “re-calibrated” through modifications of the suppression and enhanced factors where the flow patterns are not strictly considered. Therefore, modeling efforts considering individual flow patterns are strongly recommended rather than a single model covering the entire range of flow patterns. This requires exten-

sive data for the flow regime maps in microchannels prior to the development of analytical or empirical models.

# Chapter 7

## Conclusions and Recommendations

Microchannels heat exchangers are suitable for electronics cooling or applications where high heat fluxes are required. In future applications that might reach  $300 \text{ W/cm}^2$  in the next few years, new cooling technologies are required. Two-phase flow boiling in combination with microchannels may provide a potential solution for these applications.

An empirical or mathematical model of a physical phenomenon can be used to study or even optimize its performance. Unfortunately, based on the literature review, the heat transfer and pressure drop of boiling water in microchannels indicate several discrepancies between experimental data and analytical or empirical models. Each particular model or correlation was only able to predict the data from where they were obtained. In addition, there is not a generalized model for boiling two-phase flow which can predict the pressure drop or the heat transfer coefficient. Therefore, there is a serious need to conduct a comprehensive study of phase change phenomena in microchannels to understand the fundamental mechanisms involved in the process before attempting to develop any model.

In the present work, the experimental study was conducted in copper microevaporators to systematically investigate and analyze the flow boiling characteristics in mini and microchannels and identify their potential for cooling systems for high heat flux applications. Before the two-phase flow boiling study, single-phase experiments were performed. This study was necessary because the extensive research in the last decade in single-phase flow

in microchannels indicates discrepancies between the applicability of macroscale theories to microchannels. Reasons for the discrepancies are traditionally attributed to microscale effects that are not properly captured by the macroscale models. Due to a non-unified criterion in the applicability of macroscale theory to microchannels, an experimental study was conducted in micro heat exchangers with straight channels with hydraulic diameters approximately  $200\ \mu m$ .

The most important results in this work are summarized as follows with some recommendations based on the results found in this study.

## **7.1 Single-phase flow and heat transfer**

### **7.1.1 Applicability of macroscale theory to mini and microchannels**

The applicability of macroscale theory for friction factor and heat transfer coefficient to microchannel was confirmed for straight microchannels with hydraulic diameters up to  $200\ \mu m$ . The experimental and theoretical data show agreement within the range of the uncertainty of the experimental data.

The study in this thesis considered both fully developed and developing flow conditions for laminar flow which complement published data in the literature that only consider fully developed or turbulent flows. It is important to mention that based on the publications in the last two decades, the applicability of macroscale theories to microchannel was not clear. However, the most recent publications are more in favor of the applicability of macroscale theory to microchannels.

The pressure drop in microchannels is very difficult to measure and normally the experimental pressure drop includes pressure drop in bends, and contractions and expansions between the channel and headers. Therefore, the measured pressure drop must be corrected by these additional pressures (called minor losses) in order to properly identify the

experimental pressure drop along the microchannel. The minor losses have more impact in the calculation of the friction factor at higher Reynolds number because they are directly proportional to the second power of the velocity.

Single-phase liquid flow and heat transfer characteristics can be predicted using laminar flow theory in microchannels with water as the working fluid with hydraulic diameters as small as  $200\ \mu m$ . Deviation of the experimental data from the laminar fully developed theory begins at  $Re \simeq 500$ , and is attributed to entrance effects. A transition between fully developed and developing flow conditions is observed in the range of  $500 < Re \leq 1600$ . The early transition to turbulent flow in microchannels reported by several authors in the range of  $1000 < Re_{cr} < 1600$  was not observed.

### 7.1.2 Entrance length in microchannels

A proper identification of the entrance length in microchannels is a key factor in the study of transition from fully developed to developing laminar or turbulent flow. Therefore, numerical simulations were used to study the developing flows in rectangular microchannels, focusing on the entrance length and its dependence on the Reynolds number and the channel aspect ratio. New correlations for the entrance length were proposed for rectangular channels with  $100\ \mu m \leq d_h \leq 500\ \mu m$ , and  $0.5 \leq Re \leq 2000$  as shown in Table 4.1. In the present work, the proposed correlations contain not only more data points than correlations obtained experimentally but also the effects of the channel aspect ratio and low Reynolds number in the entrance length were also considered.

The results show that the dimensionless entrance length changes non-linearly with Reynolds number for  $Re \leq 50$ , while exhibiting a nearly-linear dependence within  $50 \leq Re \leq 1000$ . Similar behavior was reported from experimental published data (Ahmad and Hassan, 2006; Renksizbulut and Niazmand, 2006; Schlichting, 1979; Wiginton and Dalton, 1970).

The observed trends were found to be independent of the microchannel size for channel aspect ratio of one ( $b/a = 1$ ). This independence on the channel size on the entrance



length may also reinforce the applicability of macroscale theory for microchannels under these conditions.

The dimensionless entrance length increases with the channel aspect ratio at a given Reynolds number. The effect of channel aspect ratio gradually diminishes as the Reynolds number approaches  $Re \simeq 50$ .

## 7.2 Boiling two-phase flow

Several studies in the literature consider refrigerants as the working fluid. However, in the present study, water was used because it has the lowest thermal resistance compared with other coolants. This is very important for the development of cooling systems for high heat flux applications in the near future.

There are not enough data in the literature for boiling of water in mini and microchannels with rectangular cross sectional area. Also, the experimental data in microchannels normally are collected in microevaporators with multiple channels, where non-uniform flow distribution in the channels is typically observed. In order to have a better control of the flow distribution or flow rate per channel, the experimental data in this thesis were performed in microevaporators with a single straight channel. In addition, back flow controls (e.g. using check valves, controlled cavity sizes, etc.) were not implemented in the test rig in order to observe the natural behavior of the boiling mechanisms in microchannels.

High-speed videos, in addition to heat transfer and pressure drop data collected in the experimental microevaporators, permitted the generation of flow regime maps, and the evaluation of the thermal performance in microchannel evaporators. The flow regime maps were not comparable with macroscale flow regime maps, this difference may be attributed to the confinement of the bubbles. Differences between micro and macroscale flow regimes maps were also reported with refrigerants as the working fluid. The main conclusion in the boiling two-phase flow experiments are summarized as follow:

### 7.2.1 Two-phase flow visualizations

The high-speed visualizations confirm that the flow patterns depend on the mass flux, heat flux and channel size. The main flow patterns observed after the onset of nucleate boiling are bubbly, slug, churn, annular, wavy annular, and inverted annular flow. For a given mass flux and channel size, the flow regimes progress from one to another as the heat flux increases. However, it is possible that not all flow patterns mentioned above occur in a channel (e.g. bubbly flow was not observed in the  $198 \times 241 \mu m$  microchannel since the bubble was confined by the channel wall and slug flow commences almost immediately after the onset of nucleate boiling). The bubbly flow pattern was only observed at lower phasic superficial velocity and quickly changed to slug flow as the gas superficial velocity was increased.

The high-speed visualizations show that confinement effects are present in microchannels, where some bubbles grow in diameter until they reach the channel wall and then expand along the channel.

A detailed study in the ebullition cycle was not possible due to instabilities in the flow patterns and the rapid change of bubbly flow into annular flow. However, from the few steady flow patterns it was possible to observe that the ebullition cycle follows similar characteristics as reported by other authors Owhaib (2010); Ali (2010) (A decreasing of the bubble departure diameter, an increase of the number of active cavities, and an increase of the rate of growth of a vapor slug with the heat flux).

Reversed flow observed in the microevaporators, revealed that this was caused during the expansion upstream of confined bubbles. This may help to explain the reversal of flow also observed in multiple channel microevaporators, which has been mainly attributed to a non-uniform distribution of fluid between the channels.

During boiling two-phase flow, the pressure drop in a microchannel increased with the heat flux for a constant flow rate, unlike in a single-phase where the pressure drop is constant. Although, reversed flow was observed at lower heat fluxes, the pressure drop remained relatively unaffected by flow reversal at this condition. Pressure oscillation was

observed at higher heat flux and the amplitude of the oscillation increased with the heat flux.

Intermittent flow which was characterized by the presence of more than two flow patterns during a transitional flow was observed mainly at higher heat fluxes. The intermittent flow seemed to be caused by re-wetting of the channel walls. Therefore, re-wetting and pressure oscillations may play a crucial role and are likely responsible for the development and evolution of flow patterns. This characteristic “intermittent” flow in association with pressure oscillations could be the reason for the differences between several empirical models for heat transfer and pressure drop with experimental data.

The heat flux for the onset of nucleate boiling increases as the mass flux is increased. The associated reduction in the thermal boundary layer thickness may suppress the onset of nucleation until a higher wall superheat is attained. Since the critical heat flux was only observed for the smallest microchannel size and the lowest mass flux, it is likely that the critical heat flux can be avoided with higher mass flux and larger channel dimensions.

Flow patterns are closely coupled with the mass flux, heat flux and channel size. Bubbly and slug flow tends to appear at lower heat flux, and become annular and inverted at higher heat flux. A novel flow regime map plotted mass flux vs heat flux indicated that the flow transitions shift to a higher heat flux as the mass flux is increased.

There was an evident difference between macro and microscale flow regime maps. Unfortunately, there is not enough published flow regime maps in microchannels for diabatic conditions and water as the working fluid to compare. The flow regime maps developed in this work are a step forward for the understanding on the two-phase flow boiling mechanisms in mini and microchannels.

### **7.2.2 Boiling heat transfer and thermal performance on microevaporators**

Although, the effect of sub-cooling on the boiling curve was not reported in this work, experimental results for two different sub-cooling temperatures ( $\simeq 50$  and  $70$  K) show that

the boiling curve is shifted upward as the sub-cooling is increased. This behavior in the boiling curve with increasing sub-cooling or flow velocity was also reported by Carey (2008). Therefore, care must be taken when comparing boiling heat transfer coefficients at different sub-cooling.

The *ONB* is clearly shifted to higher heat flux as the mass flux and channel size is increased. Larger channels or higher mass flow can help avoid *CHF*. For the experimental microevaporators, the heat transfer coefficient was higher at lower vapor qualities or heat fluxes where the flow pattern is more likely to be bubbly or slug flow.

The high heat flux capacity in the microevaporators indicates the potential for high heat flux applications. The experimental results demonstrate that microevaporators with rectangular channels with hydraulic diameters of 218 or 419  $\mu m$ , water as the working fluid, and boiling as the heat transfer mechanism can dissipate heat fluxes of 280 or 440  $W/cm^2$  which make them a very attractive solution for cooling systems for high heat flux applications. The microevaporators were tested almost at atmospheric pressure where water boils at approximately 100  $^{\circ}C$ . This value of temperature is high for electronics cooling applications where maximum allowed chip temperature is approximately 85 – 90  $^{\circ}C$ . However, the saturation temperature of the water can be lowered having sub-atmospheric pressures in the cooling system. This is unlike fluorocarbons where the systems are pressurized to have a more convenient saturation temperature of refrigerants.

### 7.2.3 Heat transfer coefficient models

Analytical models for boiling in microchannels are very complex, and the required assumptions to solve these models restrict the ability to capture the “real” physics of boiling mechanisms. Also, most empirical correlations are not able to predict other experimental data, even under a similar range of operating conditions where the correlations were obtained. The complex nature of flow boiling in microchannels such as liquid-vapor interactions, bubble growth in the flow as well as in the thin film make analytical or empirical modeling of the two-phase flow a very difficult task.

A serious need was felt to conduct a comprehensive study of phase change phenomena in microchannels to understand the fundamental mechanisms involved in the boiling process before attempting any modeling. More accurate models for the heat transfer coefficient will be obtained if the modeling efforts are concentrated on each particular flow pattern. Therefore, flow regime maps with well defined flow patterns and transition lines may facilitate the modeling efforts.

## 7.3 Recommendations

- A further investigation in the effect of the inlet velocity profiles on the entrance length is suggested. At high Reynolds numbers, the dimensionless entrance length ( $L_e/d_h$ ) is linearly proportional to the Reynolds number; thus, the entrance length becomes independent of inlet velocity (Shah and London, 1978). On the other hand, at low Reynolds numbers, the dependence of the entrance length on the inlet velocity profile needs to be carefully considered.
- Use different working fluids (including air) and even smaller hydraulic diameters than  $200\ \mu m$  to identify a valid range for the applicability of macroscale theories to microchannels for fully developed and developing conditions. Also, flow visualization techniques should be used to study the transition from laminar to turbulent flow in single-phase flows in microchannels.
- Since, single-phase cooling systems are unable to meet demands for increasing heat load, an entropy generation minimization method is suggested in order to optimize the thermal performance and increase the heat dissipation capacity on these cooling systems. A multi variable optimization for channel depth, width, and wall thickness in an entropy generation model is suggested.
- A further study in the ebullition cycle in microchannels is suggested. This might require better control or elimination of the flow instabilities.

- A creation of a data bank of flow patterns at different channel sizes in order to allow a better identification of the transition lines in the flow regime maps. This might help in the generation of new flow regimes maps which probably can be plotted against different coordinates than the traditional superficial phasic velocities.
- Study the influence of the mass flux and channel size on the critical heat flux in order to identify safe operation of the system.
- A further study on two-phase flow boiling with water as the working fluid under sub-atmospheric pressure in order to have a suitable saturation temperature for cooling of electronics and the effects of sub-cooling water in the heat transfer.

# Permissions

## JOHN WILEY AND SONS LICENSE TERMS AND CONDITIONS

Sep 24, 2012

This is a License Agreement between Elmer Galvis ("You") and John Wiley and Sons ("John Wiley and Sons") provided by Copyright Clearance Center ("CCC"). The license consists of your order details, the terms and conditions provided by John Wiley and Sons, and the payment terms and conditions.

**All payments must be made in full to CCC. For payment instructions, please see information listed at the bottom of this form.**

License Number	2995570154813
License date	Sep 24, 2012
Licensed content publisher	John Wiley and Sons
Licensed content publication	Wiley Books
Book title	Design and Analysis of Heat Sinks
Licensed content author	Allan D. Kraus, Avram Bar-Cohen
Licensed content date	Sep 1, 1995
Type of use	Dissertation/Thesis
Requestor type	University/Academic
Format	Print and electronic
Portion	Figure/table
Number of figures/tables	1
Number of extracts	
Original Wiley figure/table number(s)	Figure 1.11
Will you be translating?	No
Order reference number	
Total	0.00 USD

[Terms and Conditions](#)

### TERMS AND CONDITIONS

This copyrighted material is owned by or exclusively licensed to John Wiley & Sons, Inc. or one of its group companies (each a "Wiley Company") or a society for whom a Wiley Company has exclusive publishing rights in relation to a particular journal (collectively WILEY). By clicking "accept" in connection with completing this licensing transaction, you agree that the following terms and conditions apply to this transaction (along with the billing and payment terms and conditions established by the Copyright Clearance Center Inc., ("CCC's Billing and Payment terms and conditions"), at the time that you opened your Rightslink account (these are available at any time at <http://myaccount.copyright.com>)

Terms and Conditions

1. The materials you have requested permission to reproduce (the "Materials") are protected



by copyright.

2. You are hereby granted a personal, non-exclusive, non-sublicensable, non-transferable, worldwide, limited license to reproduce the Materials for the purpose specified in the licensing process. This license is for a one-time use only with a maximum distribution equal to the number that you identified in the licensing process. Any form of republication granted by this licence must be completed within two years of the date of the grant of this licence (although copies prepared before may be distributed thereafter). The Materials shall not be used in any other manner or for any other purpose. Permission is granted subject to an appropriate acknowledgement given to the author, title of the material/book/journal and the publisher. You shall also duplicate the copyright notice that appears in the Wiley publication in your use of the Material. Permission is also granted on the understanding that nowhere in the text is a previously published source acknowledged for all or part of this Material. Any third party material is expressly excluded from this permission.

3. With respect to the Materials, all rights are reserved. Except as expressly granted by the terms of the license, no part of the Materials may be copied, modified, adapted (except for minor reformatting required by the new Publication), translated, reproduced, transferred or distributed, in any form or by any means, and no derivative works may be made based on the Materials without the prior permission of the respective copyright owner. You may not alter, remove or suppress in any manner any copyright, trademark or other notices displayed by the Materials. You may not license, rent, sell, loan, lease, pledge, offer as security, transfer or assign the Materials, or any of the rights granted to you hereunder to any other person.

4. The Materials and all of the intellectual property rights therein shall at all times remain the exclusive property of John Wiley & Sons Inc or one of its related companies (WILEY) or their respective licensors, and your interest therein is only that of having possession of and the right to reproduce the Materials pursuant to Section 2 herein during the continuance of this Agreement. You agree that you own no right, title or interest in or to the Materials or any of the intellectual property rights therein. You shall have no rights hereunder other than the license as provided for above in Section 2. No right, license or interest to any trademark, trade name, service mark or other branding ("Marks") of WILEY or its licensors is granted hereunder, and you agree that you shall not assert any such right, license or interest with respect thereto.

5. NEITHER WILEY NOR ITS LICENSORS MAKES ANY WARRANTY OR REPRESENTATION OF ANY KIND TO YOU OR ANY THIRD PARTY, EXPRESS, IMPLIED OR STATUTORY, WITH RESPECT TO THE MATERIALS OR THE ACCURACY OF ANY INFORMATION CONTAINED IN THE MATERIALS, INCLUDING, WITHOUT LIMITATION, ANY IMPLIED WARRANTY OF MERCHANTABILITY, ACCURACY, SATISFACTORY QUALITY, FITNESS FOR A PARTICULAR PURPOSE, USABILITY, INTEGRATION OR NON-INFRINGEMENT AND ALL SUCH WARRANTIES ARE HEREBY EXCLUDED BY WILEY AND ITS LICENSORS AND WAIVED BY YOU.

6. WILEY shall have the right to terminate this Agreement immediately upon breach of this Agreement by you.

7. You shall indemnify, defend and hold harmless WILEY, its Licensors and their respective directors, officers, agents and employees, from and against any actual or threatened claims, demands, causes of action or proceedings arising from any breach of this Agreement by you.

8. IN NO EVENT SHALL WILEY OR ITS LICENSORS BE LIABLE TO YOU OR ANY OTHER PARTY OR ANY OTHER PERSON OR ENTITY FOR ANY SPECIAL, CONSEQUENTIAL, INCIDENTAL, INDIRECT, EXEMPLARY OR PUNITIVE DAMAGES, HOWEVER CAUSED, ARISING OUT OF OR IN CONNECTION WITH THE DOWNLOADING, PROVISIONING, VIEWING OR USE OF THE MATERIALS REGARDLESS OF THE FORM OF ACTION, WHETHER FOR BREACH OF CONTRACT, BREACH OF WARRANTY, TORT, NEGLIGENCE, INFRINGEMENT OR OTHERWISE (INCLUDING, WITHOUT LIMITATION, DAMAGES BASED ON LOSS OF PROFITS, DATA, FILES, USE, BUSINESS OPPORTUNITY OR CLAIMS OF THIRD PARTIES), AND WHETHER OR NOT THE PARTY HAS BEEN ADVISED OF THE POSSIBILITY OF SUCH DAMAGES. THIS LIMITATION SHALL APPLY NOTWITHSTANDING ANY FAILURE OF ESSENTIAL PURPOSE OF ANY LIMITED REMEDY PROVIDED HEREIN.

9. Should any provision of this Agreement be held by a court of competent jurisdiction to be illegal, invalid, or unenforceable, that provision shall be deemed amended to achieve as nearly as possible the same economic effect as the original provision, and the legality, validity and enforceability of the remaining provisions of this Agreement shall not be affected or impaired

thereby.

10. The failure of either party to enforce any term or condition of this Agreement shall not constitute a waiver of either party's right to enforce each and every term and condition of this Agreement. No breach under this agreement shall be deemed waived or excused by either party unless such waiver or consent is in writing signed by the party granting such waiver or consent. The waiver by or consent of a party to a breach of any provision of this Agreement shall not operate or be construed as a waiver of or consent to any other or subsequent breach by such other party.

11. This Agreement may not be assigned (including by operation of law or otherwise) by you without WILEY's prior written consent.

12. Any fee required for this permission shall be non-refundable after thirty (30) days from receipt.

13. These terms and conditions together with CCC's Billing and Payment terms and conditions (which are incorporated herein) form the entire agreement between you and WILEY concerning this licensing transaction and (in the absence of fraud) supersedes all prior agreements and representations of the parties, oral or written. This Agreement may not be amended except in writing signed by both parties. This Agreement shall be binding upon and inure to the benefit of the parties' successors, legal representatives, and authorized assigns.

14. In the event of any conflict between your obligations established by these terms and conditions and those established by CCC's Billing and Payment terms and conditions, these terms and conditions shall prevail.

15. WILEY expressly reserves all rights not specifically granted in the combination of (i) the license details provided by you and accepted in the course of this licensing transaction, (ii) these terms and conditions and (iii) CCC's Billing and Payment terms and conditions.

16. This Agreement will be void if the Type of Use, Format, Circulation, or Requestor Type was misrepresented during the licensing process.

17. This Agreement shall be governed by and construed in accordance with the laws of the State of New York, USA, without regards to such state's conflict of law rules. Any legal action, suit or proceeding arising out of or relating to these Terms and Conditions or the breach thereof shall be instituted in a court of competent jurisdiction in New York County in the State of New York in the United States of America and each party hereby consents and submits to the personal jurisdiction of such court, waives any objection to venue in such court and consents to service of process by registered or certified mail, return receipt requested, at the last known address of such party.

#### **Wiley Open Access Terms and Conditions**

All research articles published in Wiley Open Access journals are fully open access: immediately freely available to read, download and share. Articles are published under the terms of the [Creative Commons Attribution Non Commercial License](#), which permits use, distribution and reproduction in any medium, provided the original work is properly cited and is not used for commercial purposes. The license is subject to the Wiley Open Access terms and conditions:

Wiley Open Access articles are protected by copyright and are posted to repositories and websites in accordance with the terms of the [Creative Commons Attribution Non Commercial License](#). At the time of deposit, Wiley Open Access articles include all changes made during peer review, copyediting, and publishing. Repositories and websites that host the article are responsible for incorporating any publisher-supplied amendments or retractions issued subsequently.

Wiley Open Access articles are also available without charge on Wiley's publishing platform, **Wiley Online Library** or any successor sites.

#### **Use by non-commercial users**

For non-commercial and non-promotional purposes individual users may access, download, copy, display and redistribute to colleagues Wiley Open Access articles, as well as adapt, translate, text- and data-mine the content subject to the following conditions:

- The authors' moral rights are not compromised. These rights include the right of "paternity" (also known as "attribution" - the right for the author to be identified as such) and "integrity" (the right for the author not to have the work altered in such a way that the author's reputation or integrity may be impugned).
- Where content in the article is identified as belonging to a third party, it is the obligation of the user to ensure that any reuse complies with the copyright policies of the owner of that content.
- If article content is copied, downloaded or otherwise reused for non-commercial research and education purposes, a link to the appropriate bibliographic citation (authors, journal, article title, volume, issue, page numbers, DOI and the link to the definitive published version on Wiley Online Library) should be maintained. Copyright notices and disclaimers must not be deleted.
- Any translations, for which a prior translation agreement with Wiley has not been agreed, must prominently display the statement: "This is an unofficial translation of an article that appeared in a Wiley publication. The publisher has not endorsed this translation."

### **Use by commercial "for-profit" organisations**

Use of Wiley Open Access articles for commercial, promotional, or marketing purposes requires further explicit permission from Wiley and will be subject to a fee. Commercial purposes include:

- Copying or downloading of articles, or linking to such articles for further redistribution, sale or licensing;
- Copying, downloading or posting by a site or service that incorporates advertising with such content;
- The inclusion or incorporation of article content in other works or services (other than normal quotations with an appropriate citation) that is then available for sale or licensing, for a fee (for example, a compilation produced for marketing purposes, inclusion in a sales pack)
- Use of article content (other than normal quotations with appropriate citation) by for-profit organisations for promotional purposes
- Linking to article content in e-mails redistributed for promotional, marketing or educational purposes;
- Use for the purposes of monetary reward by means of sale, resale, licence, loan, transfer or other form of commercial exploitation such as marketing products
- Print reprints of Wiley Open Access articles can be purchased from: [corporatesales@wiley.com](mailto:corporatesales@wiley.com)

Other Terms and Conditions:

BY CLICKING ON THE "I AGREE..." BOX, YOU ACKNOWLEDGE THAT YOU HAVE READ AND FULLY UNDERSTAND EACH OF THE SECTIONS OF AND PROVISIONS SET FORTH IN THIS AGREEMENT AND THAT YOU ARE IN AGREEMENT WITH AND ARE WILLING TO ACCEPT ALL OF YOUR OBLIGATIONS AS SET FORTH IN THIS AGREEMENT.

v1.7

**If you would like to pay for this license now, please remit this license along with your payment made payable to "COPYRIGHT CLEARANCE CENTER" otherwise you will be invoiced within 48 hours of the license date. Payment should be in the form of a check or money order referencing your account number and this invoice number RLNK500863834. Once you receive your invoice for this order, you may pay your invoice by credit card. Please follow instructions provided at that time.**

**Make Payment To:  
Copyright Clearance Center  
Dept 001  
P.O. Box 843006  
Boston, MA 02284-3006**

**For suggestions or comments regarding this order, contact RightsLink Customer Support: [customercare@copyright.com](mailto:customercare@copyright.com) or +1-877-622-5543 (toll free in the US) or +1-978-646-2777.**

**Gratis licenses (referencing \$0 in the Total field) are free. Please retain this printable license for your reference. No payment is required.**

---

## **PERMISSION INVOICE**

Inv. # P03B 22082

September 27, 2012

Elmer Galvis  
200 University Av. West  
Waterloo N2L 3G1  
Canada



**CAMBRIDGE**  
UNIVERSITY PRESS

32 Avenue of the Americas  
New York, NY 10013-2473, USA

[www.cambridge.org](http://www.cambridge.org)

Telephone 212 924 3900  
Fax 212 691 3239

## **REFERENCE**

ISBN: HB 9780521882767 PB Other  
Author: S. Mostafa Ghiaasiaan  
Title: TWO-PHASE FLOW, BOILING, AND CONDENSATION: IN CONVENTIONAL AND MINIATURE SYSTEMS  
Selection/pp.: Figure 4.13, 12.7 and 12.8

Additional: Copyright © 2008 S. Mostafa Ghiaasiaan. Reprinted with the permission of Cambridge University Press.

## **USE**

Reprint Title: Single-Phase and Boiling Flow in Microchannels with High Heat Flux  
Publisher: University of Waterloo  
Format: dissertation / thesis  
Quantity (Limit\*): 100  
Avail. Date: 2012

## **RIGHTS/ACKNOWLEDGEMENT**

Permission is granted for nonexclusive rights throughout the World in the English language for interior text editorial use in the format described above only, including non-profit editions for the blind and handicapped. Please fully acknowledge our material and indicate the copyright notice as it appears in our publication, followed by the phrase "Reprinted with the permission of Cambridge University Press."

All requests from third parties to reproduce this material must be forwarded to Cambridge University Press.

## **FEES/RESTRICTIONS**

**\$0.00**

\*This permission is restricted to the indicated format and quantity; for additional use, you must reapply for permission. This permission does not allow reprinting of any material copyrighted by or credited in our publication to another source; Cambridge disclaims all liability in connection with the use of such material without proper consent.

A COPY OF THIS INVOICE MUST ACCOMPANY PAYMENT. Payment is due upon receipt of invoice. Make check payable to Cambridge University Press, Attn: Rights and Permissions. (Fed. I.D. #: 13-1599108.)

This permission does not supersede permission that may be required from the original source indicated in our publication.

This permission requires that you send zero (0) copies of your publication directly to our author and zero (0) copy of your publication to this office upon availability.

Authorization:

Removed signature

Adam Hirschberg  
Rights and Permissions Associate  
[ahirschberg@cambridge.org](mailto:ahirschberg@cambridge.org)

# References

- Agostini, B., Fabbri, M., Park, J. E., Wojtan, L., Thome, J. R., and Michel, B. (2007). State of the art of high heat flux cooling technologies. *Heat Transfer Engineering*, 28(4):258–281.
- Ahmad, T. and Hassan, I. (2006). Experimental analysis of microchannel entrance length characteristics using microparticle image velocimetry. *ASME J. Fluids Eng.*, 132(4):041102.1–041102.13.
- Ali, R. (2010). *Phase change phenomena during fluid flow in micro channels*. Doctoral Thesis, Department of Energy Technology, Royal Institute of Technology, Stockholm, Sweden.
- Babcock and Wilcox (1992). *Steam: its generation and use (1922)*. S. C. Stultz and J. B. Kitto, New York.
- Bao, Z. Y., Fletcher, D. F., and Haynes, B. S. (2000). Flow boiling heat transfer of Freon R11 and HCFC123 in narrow passages. *Int. J. Heat Mass Tran.*, 43(18):3347–3358.
- Bar-Cohen, A., Ruder, Z., and Griffith, P. (1979). Thermal and hydrodynamic phenomena in a horizontal uniformly heated steam generating pipe. *J. Heat Transfer*, 109(3):739–745.
- Barlak, S., Yapıcı, S., and Sara, O. N. (2011). Experimental investigation of pressure drop and friction factor for water flow in microtubes. *Int. J. Therm. Sci.*, 50(3):361–368.

- Barnea, D. and Taitel, Y. (1976). *Encyclopedia of fluid mechanics*, volume 3. Gulf Publishing Company, Houston, Texas.
- Bertscha, S., Groll, E. A., and Garimella, S. V. (2008). Refrigerant flow boiling heat transfer in parallel microchannels as a function of local vapor quality. *Int. J. Heat Mass Tran.*, 51(19-20):4775–4787.
- Bertscha, S., Groll, E. A., and Garimella, S. V. (2009). Effects of heat flux, mass flux, vapor quality, and saturation temperature on flow boiling heat transfer in microchannels. *Int. J. Multiphase Flow*, 35(2):142–154.
- Brody, J. P. and Yager, P. (1996). Low Reynolds number micro-fluidic devices. *Solid State Sensor and Actuator Workshop, Hilton Head, SC, 2-6 June*, pages 105–108.
- Callizo, C. M. (2010). *Flow boiling heat transfer in single vertical channels of small diameter*. Doctoral Thesis, Department of Energy Technology, Royal Institute of Technology, Stockholm, Sweden.
- Carey, V. P. (2008). *Liquid-vapor phase-change phenomena*. Taylor & Francis Group, New York, 2<sup>nd</sup> edition.
- Celata, G. P., Cumo, M., Farello, G. E., Mariani, A., and Solimo, A. (1991). Flow pattern recognition in heated vertical channels: Steady and transient conditions. *Exp. Therm. Fluid Sci.*, 4(6):737–746.
- Celata, G. P., Cumo, M., and Zummo, G. (2004). Thermal-hydraulic characteristics of single-phase flow in capillary pipes. *Exp. Therm. Fluid Sci.*, 28(2-3):87–95.
- Celata, G. P., Morini, G. L., Marconi, V., McPhail, S. J., and Zummo, G. (2006). Using viscous heating to determine the friction factor in microchannels: An experimental validation. *Exp. Therm. Fluid Sci.*, 30(8):725–731.
- Chen, J. C. (1966). Correlation for boiling heat transfer to saturated fluids in convective flow. *Ind. Eng. Chem. Res. Process Des. Dev.*, 5(3):322–329.

- Chen, T. and Garimella, S. V. (2006). Measurements and high-speed visualizations of flow boiling of a dielectric fluid in a silicon microchannel heat sink. *Int. J. Multiphase Flow*, 32(8):957–971.
- Cheng, L., Ribatski, G., Moreno, Q., and Thome, J. R. (2008a). New prediction methods for CO<sub>2</sub> evaporation inside tubes, Part 1: A two-phase flow pattern map and a flow pattern based phenomenological model for two-phase flow frictional pressure drops. *Int. J. Heat Mass Tran.*, 51(1-2):111–124.
- Cheng, L., Ribatski, G., and Thome, J. R. (2008b). New prediction methods for CO<sub>2</sub> evaporation inside tubes, Part 2: An updated general flow boiling heat transfer model based on flow patterns. *Int. J. Heat Mass Tran.*, 51(1-2):125–135.
- Cheng, L., Ribatski, G., and Thome, J. R. (2008c). Two-phase flow patterns and flow-pattern maps: Fundamentals and applications. *Appl. Mech. Rev.*, 61(5):050802.1–050802.28.
- Coleman, H. W. and Steele, W. G. (1989). *Experimentation and uncertainty analysis for engineers*. John Wiley & Sons, New York.
- Collier, J. G. and Thome, J. R. (1994). *Convective Boiling and Condensation*. Clarendon Press, Oxford, 3<sup>th</sup> edition.
- Cornwell, K. and Kew, P. A. (1992). Boiling in small parallel channels. *Proc. CEC Conference on Energy Efficiency in Process Technology*, pages 624–628.
- Dang, T., Teng, J., and Chu, J. (2011). Influence of gravity on the performance index of microchannel heat exchangers-experimental investigations. *Proceedings of the World Congress on Engineering, July 6-8, London, UK*.
- Dukler, A. E. (1978). Modelling two-phase flow and heat transfer. *6th Int. Heat Transfer Conference, August 7-11, Toronto, Canada*.



- Ekberg, N. P., Ghiaasiaan, S. M., Abdel-Khalik, S. I., Yoda, M., and Jeter, S. M. (1999). Gas-liquid two-phase flow in narrow horizontal annuli. *Nuclear Engineering and Design*, 192(1):59–80.
- Felcar, H. O. M., Ribatski, G., and Jabardo, J. M. S. (2007). A gas-liquid flow pattern predictive method for macro-and-mini-scale round channels. *Department of Mechanical Engineering, Escola de Engenharia de São Carlos, University of São Paulo, and Escuela Politécnica Superior Mendizabal, Universidad de la Coruña*.
- Frankum, D. P., Wadekar, V. V., and Azzopardi, B. J. (1997). Two-phase flow patterns for evaporating flow. *Exp. Therm. Fluid Sci.*, 15(3):183–192.
- Gad-el-Hak, M. (1999). The fluid mechanics of microdevices. *ASME J. Fluids Eng.*, 121(1):7–33.
- Galvis, E. and Culham, R. (2010). Lower entropy generation in microchannels with laminar single phase flow. *ASME 8th International Conference on Nanochannels, Microchannels, and Minichannels Collocated with 3rd Joint US-European Fluids Engineering Summer Meeting, ICNMM2010*, pages 1491–1500.
- Galvis, E. and Culham, R. (2012). Measurements and flow pattern visualizations of two-phase flow boiling in single channel microevaporators. *Int. J. Multiphase Flow*, 42:52–61.
- Galvis, E., Jubran, B. A., XI, F., Behdinan, K., and Fawaz, Z. (2008). Numerical modeling of pin-fin micro heat exchangers. *Int. J. Heat Mass Tran.*, 44(6):659–666.
- Galvis, E., Yarusevych, S., and Culham, R. (2012). Incompressible laminar developing flows in microchannels. *ASME J. Fluids Eng.*, 134(1):014503.1–014503.4.
- Ghiaasiann, S. M. (2008). *Two-phase flow, boiling, and condensation in conventional and miniature systems*. Cambridge, New York.
- Giudice, S. D., Nonino, C., and Savino, S. (2007). Effects of viscous dissipation and temperature dependent viscosity in thermally and simultaneously developing laminar flows in microchannels. *Int. J. Heat Fluid Fl.*, 28(1):15–27.

- Gneilinski, V. (1976). New equations for heat and mass transfer in turbulent pipe and channel flow. *Int. Chem. Eng.*, 16(2):359–368.
- Gorenflo, D. (1993). *VDI-heat atlas*. VDI-Verlag GmbH, Dusseldorf, Germany, 6<sup>th</sup> edition.
- Gözükara, A. C. (2010). Analysis of single phase convective heat transfer in microchannels with variable thermal conductivity and viscosity. *ASME 10th Biennial Conference on Engineering Systems Design and Analysis, July 12-14, Istanbul, Turkey*.
- Gungor, K. E. and Winterton, R. H. S. (1986). A general correlation for flow boiling in tubes and annuli. *Int. J. Heat Mass Tran.*, 29(3):351–358.
- Guo, Z.-Y. and Li, Z.-X. (2003). Size effect on microscale single-phase flow and heat transfer. *Int. J. Heat Mass Tran.*, 46(1):149–159.
- Harirchian, T. and Garimella, S. V. (2009a). The critical role of channel cross-sectional area in microchannel flow boiling heat transfer. *Int. J. Multiphase Flow*, 35(10):904–913.
- Harirchian, T. and Garimella, S. V. (2009b). Effects of channel dimension, heat flux, and mass flux on flow boiling regimes in microchannels. *Int. J. Multiphase Flow*, 35(4):349–362.
- Harirchian, T. and Garimella, S. V. (2010). A comprehensive flow regime map for microchannel flow boiling with quantitative transition criteria. *Int. J. Heat Mass Tran.*, 53(13-14):2694–2702.
- Harirchian, T. and Garimella, S. V. (2012). Flow regime-based modeling of heat transfer and pressure drop in microchannel flow boiling. *Int. J. Heat Mass Tran.*, 55(4):1246–1260.
- Hetsroni, G., Mosyak, A., Pogrebnyak, E., and Yarin, L. P. (2005a). Fluid flow in microchannels. *Int. J. Heat Mass Tran.*, 48(10):1982–1998.
- Hetsroni, G., Mosyak, A., Pogrebnyak, E., and Yarin, L. P. (2005b). Heat transfer in micro-channels: Comparison of experiments with theory and numerical results. *Int. J. Heat Mass Tran.*, 48(25-26):5580–5601.

- Hewitt, G. F. (1978). *Measurement of two-phase flow parameters*. Academic Press, London.
- Hrnjak, P. and Tu, X. (2007). Single-phase pressure drop in microchannels. *Int. J. Heat Fluid Fl.*, 28(1):2–14.
- Hsieh, S. S., Huang, C. F., and Tsai, H. H. (2004). Liquid flow in a microchannel. *J. Micromech. Microeng.*, 14(4):436–445.
- Hsu, Y. Y. (1962). On the size range of active nucleation cavities on a heating surface. *J. Heat Trans-T ASME*, 84:207–216.
- Jacobi, A. M., Thome, J. R., and Zun, I. (2002). Heat transfer model for evaporation of elongated blubble flows in microchannels. *J. Heat Trans-T ASME*, 124(6):1131–1136.
- Jiang, X. N., Zhou, Z. Y., Yao, J., Li, Y., and Ye, X. Y. (1995). Micro-fluid flow in microchannel. *Proc. Transducers '95, Stockholm, Sweden*, pages 317–320.
- Judy, J., Maynes, D., and Webbs, B. W. (2002). Characterization of frictional pressure drop for liquid flows through microchannels. *Int. J. Heat Mass Tran.*, 45(17):3477–3488.
- Kakaç, S., Kosy, B., and Li, D. (2009). *Microfluidics based microsystems*. Springer, Netherlands.
- Kakaç, S., Shah, R. K., and Aung, W. (1987). *Handbook of single-phase convective heat transfer*. John Wiley & Sons, New York.
- Kandlikar, S. and Grande, W. (2002). Evolution of micro-channel flow passages-thermohydraulic performance and fabrication technology. *Proceedings of IMEECE, ASME International Mechanical Engineering Congress and Exposition, November 17-22, New Orleans, US*, page 1–13.
- Kandlikar, S. G. (1990). A general correlation for saturated two-phase flow boiling heat transfer inside horizontal and vertical tubes. *J. Heat Trans-T ASME*, 112(1):219–228.
- Kandlikar, S. G. (1991). A model for correlating flow boiling heat transfer in augmented tubes and compact evaporators. *J. Heat Trans-T ASME*, 113(4):966–972.

- Kandlikar, S. G. (2004). Heat transfer mechanisms during flow boiling in microchannels. *J. Heat Trans-T ASME*, 126(1):8–16.
- Kandlikar, S. G. (2006). Effects of liquid-vapor phase distribution on the heat transfer mechanisms during flow boiling in minichannels and microchannels. *Heat Transfer Eng.*, 27(1):4–13.
- Kandlikar, S. G. (2010). Scale effects on flow boiling heat transfer in microchannels: A fundamental perspective. *Int. J. Therm. Sci.*, 49(7):1073–1085.
- Kandlikar, S. G. and Balasubramanian, P. (2004). An extension of the flow boiling correlation to transition, laminar, and deep laminar flows in minichannels and microchannels. *Heat Transfer Eng.*, 25(3):86–93.
- Kandlikar, S. G., Garimella, S., Li, D., Colin, S., and King, M. R. (2006a). *Heat transfer and fluid flow in minichannels and microchannels*. Elsevier Ltd, Oxford.
- Kandlikar, S. G., Joshi, S., and Tian, S. (2003). Effect of surface roughness on heat transfer and fluid flow characteristics at low reynolds numbers in small diameter tubes. *Heat Transfer Eng.*, 24(3):4–16.
- Kandlikar, S. G., Kuan, W. K., Willistein, D., and Borrelli, J. (2006b). Stabilization of flow boiling in microchannels using pressure drop elements and fabricated nucleation sites. *J. Heat Trans-T ASME*, 128(4):389–396.
- Kandlikar, S. G., Shoji, M., and Dhira, V. K. (1999). *Handbook of phase change: Boiling and condensation*. Taylor & Francis, Philadelphia.
- Kattan, N., Thome, J. R., and Favrat, D. (1998). Flow boiling in horizontal tubes-part 1: Development of a diabatic two-phase flow pattern map. *ASME J. Heat Transfer*, 120(1):140–147.
- Keithley (2001). *Model 2700 multimeter data acquisition system: User’s manual*. Keithley Instruments, Inc.

- Khan, W. A., Yovanovich, M. M., and Culham, J. R. (2006). Optimization of microchannel heat sinks using entropy generation minimization method. *Twenty-Second Annual IEEE Semiconductor Thermal Measurement and Measurement Symposium, Dallas, TX, US*.
- Kim, J. (2009). Freview of nucleate pool boiling bubble heat transfer mechanisms. *Int. J. Multiphase Flow*, 35(12):1067–1076.
- Koo, J. and Kleinstreuer, C. (2004). Viscous dissipation effects in microtubes and microchannels. *Int. J. Heat Mass Tran.*, 47(14-16):3159–3169.
- Kraus, A. D. and Bar-Cohen, A. (1995). *Design and analysis of heat sinks*. John Wiley & Sons, New York.
- Lee, H. J. and Lee, S. Y. (2001). Heat transfer correlation for boiling flows in small rectangular horizontal channels with low aspect ratios. *Int. J. Multiphase Flow*, 27(12):2043–2062.
- Lee, J. and Mudawar, I. (2004). Two-phase flow in high-heat-flux micro-channel heat sink for refrigeration cooling applications: Part 2: heat transfer characteristics. *Int. J. Heat Mass Tran.*, 48(5):941–955.
- Lee, J. and Mudawar, I. (2005). Two-phase flow in high-heat-flux micro-channel heat sink for refrigeration cooling applications: Part 1: pressure drop characteristics. *Int. J. Heat Mass Tran.*, 48(5):928–940.
- Lee, J. and Mudawar, I. (2008). Fluid flow and heat transfer characteristics of low temperature two-phase micro-channel heat sinks: Part 2: subcooled boiling pressure drop and heat transfer. *Int. J. Heat Mass Tran.*, 51(17-18):4327–4341.
- Lee, J. H., Liu, D. Y., and Yao, S. (2010). Flow instability of evaporative micro-channels. *Int. J. Heat Mass Tran.*, 53(9-10):1740–1749.
- Lee, P.-S., Garimella, S. V., and Liu, D. (2005). Investigation of heat transfer in rectangular microchannels. *Int. J. Heat Mass Tran.*, 48(9):1688–1704.

- Lee, P.-S., Garimella, S. V., and Liu, D. (2008). Saturated flow boiling heat transfer and pressure drop in silicon microchannel arrays. *Int. J. Heat Mass Tran.*, 51(3-4):789–806.
- Lelea, D., Nishio, S., and Takano, K. (2004). The experimental research on microtube heat transfer and fluid flow of distilled water. *Int. J. Heat Mass Tran.*, 47(12-13):2817–2830.
- Lemczyk, T. and Molloy, D. (1995). Advanced engineering: NP-329 fluid properties, research report, revision 1. *LONG Manufacturing Ltd.*
- Li, H. and Olsen, M. G. (2006). Aspect ratio effects in turbulent and transitional flow in rectangular microchannels as measured with micro-piv. *ASME J. Fluids Eng.*, 128(2):305–331.
- Li, J., Peterson, G. P., and Cheng, P. (2004). Three-dimensional analysis of heat transfer in a micro-heat sink with single phase flow. *Int. J. Heat Mass Tran.*, 47(19-20):4215–4231.
- Liu, D. and Garimella, S. V. (2007). Flow boiling heat transfer in microchannels. *J. Heat Trans-T ASME*, 129(10):1321–1332.
- Mala, G. M. and Li, D. (1999). Flow characteristics of water in microtubes. *Int. J. Heat Fluid Fl.*, 20(2):152–148.
- Mandhane, J. M., Gregory, G. A., and Aiz, K. (1974). A flow pattern map for gas-liquid flow in horizontal pipes. *Int. J. Multiphase Flow*, 1(4):537–553.
- Maranzana, G., Perry, I., and Maillet, D. (2004). Mini- and micro-channels: influence of axial conduction in the walls. *Int. J. Heat Mass Tran.*, 47(17-18):3993–4004.
- Megahed, A. (2010). *Experimental investigation and analytical modeling of flow boiling characteristics in silicon microchannel arrays*. Doctoral Thesis, Department of Mechanical and Industrial Engineering, Concordia University, Montreal, Canada.
- Morini, G. L. (2004). Single-phase convective heat transfer in microchannels: a review of experimental results. *Int. J. Therm. Sci.*, 43(7):631–651.

- Morini, G. L. (2005). Viscous heating in liquid flows in microchannels. *Int. J. Heat Mass Tran.*, 48(17):3637–3647.
- Muzychka, Y. S. and M.M.Yovanovich (2010). Pressure drop in laminar developing flow in noncircular ducts: a scaling and modeling approach. *ASME J. Fluids Eng.*, 131(11):111105.1–111105.11.
- Natrajan, V. K. and Christensen, K. T. (2007). Microscopic particle image velocimetry measurements of transition to turbulence in microscale capillaries. *Exp. Fluids*, 43(1):1–16.
- Natrajan, V. K. and Christensen, K. T. (2010a). The impact of surface roughness on flow through a rectangular microchannel from the laminar to turbulent regimes. *Microfluidics and Nanofluidics*, 9(1):92–121.
- Natrajan, V. K. and Christensen, K. T. (2010b). Non-intrusive measurements of convective heat transfer in smooth and rough-wall microchannels: laminar flow. *Exp. Fluids*, 49(5):1021–1037.
- Natrajan, V. K. and Christensen, K. T. (2011). Non-intrusive measurements of transitional and turbulent convective heat transfer in a rectangular microchannel. *J. Micromech. Microeng.*, 21(8):08500.1–0850.19.
- Nukiyama, S. (1934). The maximum and minimum values of the heat  $Q$  transmitted from metal to boiling water under atmospheric pressure. *J. Jap. Soc. Mech. Eng.*, 37:367–374.
- Ong, C. L. and Thome, J. R. (2011). Macro-to-microchannel transition in two-phase flow: Part 1-two-phase flow patterns and film thickness measurements. *Exp. Therm. Fluid Sci.*, 35(1):37–47.
- Owhaib, W. (2010). *Experimental heat transfer, pressure drop, and flow visualization of R-134a in vertical mini/micro tubes*. Doctoral Thesis, Department of Energy Technology, Royal Institute of Technology, Stockholm, Sweden.

- Papautsky, I., Ameen, T., and Frazier, A. (2001). A review of laminar single-phase flow in microchannels. *ASME International Mechanical Engineering Congress and Exposition, Nov 11-16, New York, US*.
- Park, H. S. and Punch, J. (2008). Friction factor and heat transfer in multiple microchannels with uniform flow distribution. *Int. J. Heat Mass Tran.*, 51(17-18):4535–4543.
- Peng, X. F. and Peterson, G. P. (1996). Convective heat transfer and flow friction for water flow in microchannel structures. *Int. J. Heat Mass Tran.*, 39(12):2599–2608.
- Peng, X. F., Peterson, G. P., and Wang, B. X. (1994). Frictional flow characteristics of water flowing through rectangular microchannels. *Experimental Heat Transfer*, 7(4):249–264.
- Phillips, R. J. (1990). Microchannel heat sinks. *Advances in Thermal Modeling of Electronic Components and Systems*, Hemisphere, New York, Chap. 3.
- Qi, S. L., Zhang, P., Wang, R. Z., and Xu, L. X. (2007). Single-phase pressure drop and heat transfer characteristics of turbulent liquid nitrogen flow in microtubes. *Int. J. Heat Mass Tran.*, 50:1993–2001.
- Qu, W., Mala, G. M., and Li, D. (2000). Pressure driven water flows in trapezoidal silicon microchannels. *Int. J. Heat Fluid Fl.*, 43(3):353–364.
- Qu, W. and Mudawar, I. (2002). Experimental and numerical study of pressure drop and heat transfer in a single-phase micro-channel heat sink. *Int. J. Heat Mass Tran.*, 45(12):2549–2565.
- Qu, W. and Mudawar, I. (2003). Flow boiling heat transfer in two-phase micro-channel heat sinks-i. experimental investigation and assessment of correlation methods. *Int. J. Heat Mass Tran.*, 46(15):2755–2771.
- Ramiar, A. and Ranjbar, A. A. (2011). Effects of viscous dissipation and variable properties on nanofluids flow in two dimensional microchannels. *ASME Int. J. Eng.*, 24(2):131–142.



- Renksizbulut, M. and Niazmand, H. (2006). Laminar flow and heat transfer in the entrance region of trapezoidal channels with constant wall temperature. *ASME J. Heat Transfer*, 128(1):63–74.
- Revellin, R., Dupont, V., Ursenbacher, T., Thome, J. R., and Zun, I. (2006). Characterization of diabatic two-phase flows in microchannels: Flow parameter results for R-134a in a 0.5 mm channel. *Int. J. Multiphase Flow*, 32(7):755–774.
- Revellin, R. and Thome, J. R. (2007a). Experimental investigation of R134a and R245fa two-phase flow in microchannels for different flow conditions. *Int. J. Heat Fluid Fl.*, 28(1):63–71.
- Revellin, R. and Thome, J. R. (2007b). A new type of diabatic flow pattern map for boiling heat transfer in microchannels. *J. Micromech. Microeng.*, 17(4):788–796.
- Saisorn, S., Kaew-On, J., and Wongwises, S. (2010). Flow pattern and heat transfer characteristics of R-134a refrigerant during flow boiling in a horizontal circular mini-channel. *Int. J. Heat Mass Tran.*, 53(19-20):4023–4038.
- Schlichting, H. (1979). *Boundary layer theory*. McGraw-Hill, New York, 7<sup>th</sup> edition.
- Schrock, V. E. and Grossman, L. M. (1959). *Forced convection boiling studies*. Univeristy of California, Institute of Engineering Research, Report no. 73308-UCX-2182.
- Shah, R. K. and London, A. L. (1978). *Laminar flow forced convection in ducts: Advances in Heat Transfer, Supplement*, volume 1. Academic Press, New York.
- Sharp, K. V. and Adrian, R. J. (2004). Transition from laminar to turbulent flow in liquid filled microtubes. *Exp. Fluids*, 36(5):741–747.
- Sharp, K. V., Adrian, R. J., Santiago, J. G., and Molho, J. I. (2006). *Liquid flows in microchannels*, in *Gad-el-Hak, M(Ed), The MEMS Handbook*. Taylor & Francis Group, Philadelphia.

- Shen, S., Xu, J. L., Zhou, J. J., and Chen, Y. (2006). Flow and heat transfer in microchannels with rough wall surface. *Energy Conversion Management*, 47(11-12):1311–1235.
- Singh, S. G., Jain, A., Sridharan, A., Duttagupta, S. P., and Agrawal, A. (2009). Flow map and measurement of void fraction and heat transfer coefficient using an image analysis technique for flow boiling of water in a silicon microchannel. *J. Micromech. Microeng.*, 19(7):075004.1–075004.10.
- Sobhan, C. B. and Garimella, S. V. (2001). A comparative analysis of studies on heat transfer and fluid flow in micro-channels. *Microscale Thermophys Eng.*, 5(4):293–311.
- Steiner, D. (1993). Heat transfer to boiling saturated liquids. *VDI-Wärmeatlas (VDI Heat Atlas)*, Verein Deutscher Ingenieure, VDI-Gesellschaft Verfahrenstechnik und Chemieingenieurwesen (GCV), Düsseldorf, Chapter Hbb.
- Steinke, M. E. and Kandlikar, S. G. (2004). An experimental investigation of flow boiling characteristics of water in parallel microchannels. *J. Heat Trans-T ASME*, 126(4):518–526.
- Steinke, M. E. and Kandlikar, S. G. (2006). Single phase liquid friction factors in microchannels. *Int. J. Therm. Sci.*, 45(11):1073–1083.
- Taitel, Y. (1990). Flow regime transition in two-phase flow. *9th Int. Heat Transfer Conference, Jerusalem*.
- Taitel, Y. and Dukler, A. E. (1976). A model for predicting flow regime transitions in horizontal and near horizontal gas-liquid flow. *AIChE J.*, 22(1):47–55.
- Taitel, Y. and Dukler, A. E. (1977). Flow regime transitions for vertical upward gas-liquid flow: A preliminary approach through physical modelling. *AIChE 70th annual meeting, New York, US*.
- Taitel, Y., Lee, N., and Dukler, A. E. (1978). Transient gas-liquid flow in horizontal pipes: modeling the flow pattern transitions. *AIChE J.*, 24(5):920–934.

- Thome, J. R. (2004). Boiling in microchannels: a review of experiment and theory. *Int. J. Heat Fluid Fl.*, 25(2):128–139.
- Tso, C. P. and Mahulikar, S. P. (1998). The use of the brinkman number for single phase forced convective heat transfer in micro-channels. *Int. J. Heat Mass Tran.*, 41(12):1759–1769.
- Tso, C. P. and Mahulikar, S. P. (1999). The role of the brinkman number in analyzing flow transitions in micro-channels. *Int. J. Heat Mass Tran.*, 42(10):1813–1833.
- Tso, C. P. and Mahulikar, S. P. (2000). Experimental verification of the role of brinkman number in microchannels using local parameters. *Int. J. Heat Mass Tran.*, 43(10):1837–1849.
- Tuckerman, D. B. and Pease, R. F. W. (1981). High-performance heatsinking for vlsi. *IEEE Electronic Device Letters*, EDL-2(5):126–129.
- Tunc, G. and Bayazitoglu, Y. (2001). Heat transfer in microtubes with viscous dissipation. *Int. J. Heat Mass Tran.*, 44(13):2395–2403.
- Weisman, J., Duncan, D., Gibson, J., and Crawford, T. (1979). Effect of fluid properties and pipe diameter on two-phase flow pattern in horizontal lines. *Int. J. Multiph. Flow*, 5(6):437–462.
- Wiginton, C. L. and Dalton, C. (1970). Incompressible laminar flow in the entrance region of a rectangular duct. *ASME J. Appl. Mech.*, 37(3):854–856.
- Wu, H. Y. and Chen, P. (2003). An experimental study of convective heat transfer in silicon microchannels with different surface conditions. *Int. J. Heat Mass Tran.*, 46(14):2547–2556.
- Wu, H. Y. and Cheng, P. (2004). Boiling instability in parallel silicon microchannels at different heat flux. *Int. J. Heat Mass Tran.*, 47(17-18):3631–3641.

Yang, C. Y. and Lin, T. Y. (2007). Heat transfer characteristics of water flow in microtubes. *Exp. Therm. Fluid Sci.*, 32(2):432–439.

Yarin, L. P., Mosyak, A., and Hetsroni, G. (2009). *Fluid flow, heat transfer and boiling in micro-channels*. Springer-Verlag, Berlin Heidelberg.

# Appendices

# Appendix A

## Uncertainty Analysis

An uncertainty analysis of the experimental method, apparatus and data is performed in the following sections. The uncertainties were comparable with other values reported in the literature for microchannels. Typically, the uncertainty of calculated variables in microscale measurements is high (e.g. friction factor, heat transfer coefficient 15 – 25 %) due to error propagation.

### A.1 Method

The procedure used for the uncertainty analysis is based on the method described by Coleman and Steele (1989). Consider a general case in which a quantity  $R$  is determined from a set of measured values,  $X_j$ :

$$R = R(X_1, X_2, X_3, \dots, X_N) \quad (\text{A.1})$$

where each measured value  $X_j$  has an associated uncertainty represented by the notation  $\delta X_j$ , the effect of the uncertainty in  $X_j$  on the result  $R$  is calculated by:

$$\delta R_{X_j} = \frac{\partial R}{\partial X_j} \delta X_j \quad (\text{A.2})$$

where  $\delta R_{X_j}$  refers to the uncertainty in  $R$  as a result of the uncertainty in the  $X_j$  measurement. Then the uncertainty in the result is given in general form as:

$$\delta R = \pm \left\{ \left( \frac{\partial R}{\partial X_1} \delta X_1 \right)^2 + \left( \frac{\partial R}{\partial X_2} \delta X_2 \right)^2 + \dots + \left( \frac{\partial R}{\partial X_j} \delta X_j \right)^2 \right\}^{1/2} \quad (\text{A.3})$$

When  $R$  depends on a number of measured quantities and this dependence can be expressed in the form:

$$R = X_1^{C_1} X_2^{C_2} X_3^{C_3} \dots X_N^{C_N} \quad (\text{A.4})$$

the overall uncertainty is determined from the uncertainties of each of the individual measurements:

$$\frac{\delta R}{R} = \pm \left\{ \left( C_1 \frac{\delta X_1}{X_1} \right)^2 + \left( C_2 \frac{\delta X_2}{X_2} \right)^2 + \left( C_3 \frac{\delta X_3}{X_3} \right)^2 + \dots + \left( C_N \frac{\delta X_N}{X_N} \right)^2 \right\}^{1/2} \quad (\text{A.5})$$

The result of this equation is the overall uncertainty in  $R$  expressed as a percentage. The following section describes the uncertainty associated with the instrumentation and the method used in the measurements of each of the individual quantities.

## A.2 Uncertainty in Measured Values

### A.2.1 Temperature Measurements

All temperature measurements are performed using T-Type thermocouples and a Keithley 2700 data acquisition system. From the calibration specifications by Keithley (2001) the accuracy of T-Type thermocouple measurements relative to a simulated junction, such as the ice point cell used in these experiments, is:

$$\frac{\delta T}{T} = \pm \frac{0.2^\circ\text{C}}{T[^\circ\text{C}]} \quad (\text{A.6})$$

### A.2.2 Heater Voltage

The voltage to the cartridge resistance heater embedded in the copper block is measured using the Keithley data logger. For the range of voltages used in these tests,  $5V \leq V_{heater} \leq 95V$ , the corresponding accuracy of the measurements from the calibration specifications of the instrument (Keithley, 2001) are:

$$\delta V_{heater} = \pm (4.5 \times 10^{-5} \text{ Reading} + 9 \times 10^{-6} \text{ Range}) [V] \quad (\text{A.7})$$

For the 100 V range, the resulting expression for the uncertainty is:

$$\frac{\delta V_{heater}}{V_{heater}} = \pm \left( 4.5 \times 10^{-5} + \frac{9 \times 10^{-4} V}{V_{heater}[V]} \right) \quad (\text{A.8})$$

### A.2.3 Heater Current

The current in the heater is calculated based on the voltage drop across a calibrated shunt resistor:

$$I = \frac{V_{shunt}}{\Re} \quad (\text{A.9})$$

The uncertainty in the heater current is calculated by:

$$\frac{\delta I}{I} = \pm \left\{ \left( \frac{\delta V_{shunt}}{V_{shunt}} \right)^2 + \left( \frac{\delta \Re}{\Re} \right)^2 \right\}^{1/2} \quad (\text{A.10})$$

From the specifications for the data logger (Keithley, 2001) the uncertainty in the voltage reading across the shunt resistor is:

$$\delta V_{shunt} = \pm (3.0 \times 10^{-5} \text{ Reading} + 3.5 \times 10^{-5} \text{ Range}) [V] \quad (\text{A.11})$$

From the 100 mV range, the resulting expression for the uncertainty is :



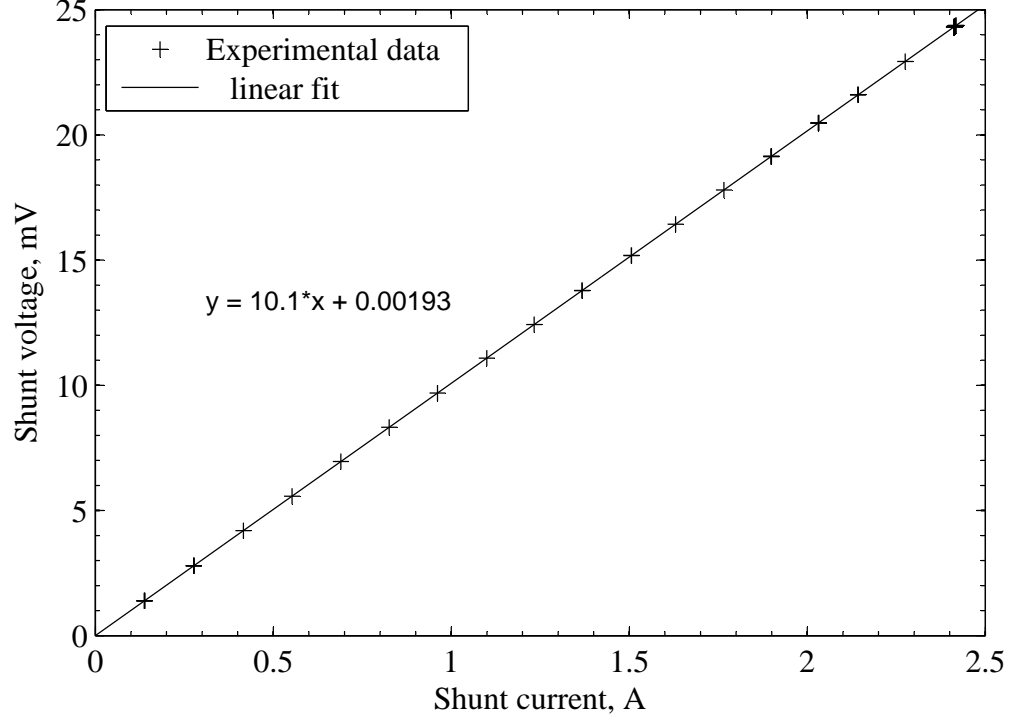


Figure A.1: Shunt resistance linear fit

$$\frac{\delta V_{shunt}}{V_{shunt}} = \pm \left( 3.0 \times 10^{-5} + \frac{3.5 \times 10^{-6} V}{V_{shunt} [V]} \right) \quad (\text{A.12})$$

The resistance of the shunt was measured during a calibration procedure at the start of the experimental tests. Using the Keithley data logger to measure current as the full range of voltages were applied to the shunt ( $0 < V_{shunt} \leq 25 \text{ mV}$ ), the resistance was calculated based on a linear fit of the voltage versus current data shown in Figure A.1

The uncertainty in the calculated resistance is determined by:

$$\frac{\delta \mathcal{R}}{\mathcal{R}} = \pm \left\{ \left( \frac{\delta V_{shunt}}{V_{shunt}} \right)^2 + \left( \frac{\delta I_{shunt}}{I_{shunt}} \right)^2 + \left( \frac{\delta L}{L} \right)^2 \right\}^{1/2} \quad (\text{A.13})$$

where the uncertainty associated with the liner fit of the data,  $\delta L/L$ , is the *RMS* % difference between the linear fit and the data.

$$\frac{\delta L}{L} = \pm 0.02\% = \pm 0.0002 \quad (\text{A.14})$$

The uncertainty in the current measurement is calculated for a 3 A range by (Keithley, 2001)

$$\frac{\delta I_{shunt}}{I_{shunt}} = \pm \left( 1.2 \times 10^{-3} + \frac{1.2 \times 10^{-4} A}{I_{shunt}[A]} \right) \quad (\text{A.15})$$

Substituting Equations A.12, A.14, and A.15 into Equation A.13, the uncertainty in the resistance at the lowest values of  $V_{shunt} = 1 \text{ mV}$  and  $I_{shunt} = 0.1 \text{ A}$  (where the uncertainty is higher) is determined as:

$$\frac{\delta \Re}{\Re} = \pm 0.0043 \quad (\text{A.16})$$

Combining the uncertainties of the shut voltage and resistance, the current uncertainty is:

$$\frac{\delta I}{I} = \pm \left\{ \left( 3.0 \times 10^{-5} + \frac{3.5 \times 10^{-6} V}{V_{shunt}[V]} \right)^2 + (0.0043)^2 \right\}^{1/2} \quad (\text{A.17})$$

#### A.2.4 Pressure

Since the outlet of the microchannel is at atmospheric pressure, the absolute pressure drop in the microchannel is measured using a Omega pressure sensor PX481A-060G5V located at the inlet of the microchannel. For the lowest pressure drop, an Omega PX26-005GV differential pressure sensor was used. These sensors convert the absolute pressure reading to voltage signal that is measured by the Keithley data acquisition system. The pressure drop reading is calculated using:

$$\Delta p \approx C.V_{pressure} \quad (\text{A.18})$$

where C is a constant correlation coefficient. The uncertainty in the pressure measurement is determined by:

$$\frac{\delta\Delta p}{\Delta p} = \pm \left\{ \left( \frac{\delta C}{C} \right)^2 + \left( \frac{\delta V_{pressure}}{V_{pressure}} \right)^2 \right\}^{1/2} \quad (\text{A.19})$$

The accuracy of the pressure gauge is determined from its calibration certificate:

$$\frac{\delta C}{C} = \pm 0.2\% \text{ of full scale for PX418A-060G5V} \quad (\text{A.20})$$

$$\frac{\delta C}{C} = \pm 1\% \text{ of full scale for PX26-005GV} \quad (\text{A.21})$$

Full scale for the transducer PX418A-060G5V is  $60 \text{ psi} = 4.1369 \times 10^5 \text{ Pa}$  and for the PX26-005GV is  $5 \text{ psi} = 3.4474 \times 10^4 \text{ Pa}$

$$\frac{\delta C}{C} = \pm \frac{827.38 \text{ Pa}}{p[\text{Pa}]} \text{ for PX418A-060G5V} \quad (\text{A.22})$$

$$\frac{\delta C}{C} = \pm \frac{344.74 \text{ Pa}}{p[\text{Pa}]} \text{ for PX26-005GV} \quad (\text{A.23})$$

For the 10 V range used by the data logger for reading the PX418A-060G5V transducer output signal, the corresponding uncertainty is:

$$\frac{\delta V_{pressure}}{V_{pressure}} = \pm \left( 3.0 \times 10^{-5} + \frac{5 \times 10^{-5} \text{ V}}{V_{pressure}[\text{V}]} \right) \quad (\text{A.24})$$

Based on these expressions, the uncertainty in the pressure readings for the for the PX418A-060G5V sensor can be calculated by:

$$\frac{\delta\Delta p}{\Delta p} = \pm \left\{ \left( \frac{827.38 \text{ Pa}}{p[\text{Pa}]} \right)^2 + \left( 3.0 \times 10^{-5} + \frac{5 \times 10^{-5} \text{ V}}{V_{pressure}[\text{V}]} \right)^2 \right\}^{1/2} \quad (\text{A.25})$$

For the 0.1 V range used by the data logger for reading the PX26-005GV transducer output signal, the corresponding uncertainty is:

$$\frac{\delta V_{pressure}}{V_{pressure}} = \pm \left( 3.0 \times 10^{-5} + \frac{35 \times 10^{-5} V}{V_{pressure}[V]} \right) \quad (\text{A.26})$$

Based on these expressions, the uncertainty in the pressure readings for the for the PX26-005GV sensor can be calculated by:

$$\frac{\delta \Delta p}{\Delta p} = \pm \left\{ \left( \frac{344.74 Pa}{p[Pa]} \right)^2 + \left( 3.0 \times 10^{-5} + \frac{35 \times 10^{-5} V}{V_{pressure}[V]} \right)^2 \right\}^{1/2} \quad (\text{A.27})$$

The  $V_{pressure}$  is related to pressure for the PX418A-060G5V and PX26-005GV sensor by:

$$V_{pressure} = \frac{\left( \frac{\Delta p[Pa]}{6894.75} + 15 \right)}{15}, \text{ for PX418A-060G5V} \quad (\text{A.28})$$

and for the PX26-005GV by:

$$V_{pressure} = \frac{p[Pa]}{689470}, \text{ for PX26-005GV} \quad (\text{A.29})$$

### A.2.5 Properties

Properties of water (liquid and vapor) were determined based on correlations of tabulated values as function of temperature presented by Lemczyk and Molloy (1995) and Babcock and Wilcox (1992). The correlations deviate from the tabulated values by less than 0.4 %. Therefore, the uncertainty in the fluid properties is:

$$\frac{\delta Property}{Property} = \pm 4.0 \times 10^{-3} \quad (\text{A.30})$$

## A.2.6 Channel Dimensions

The uncertainty in the microchannel width and depth were estimated based on twice the standard deviation ( $2\sigma$ ) of several measurements taken with a surface tester as:

- Microchannel 1: width  $241 \pm 9.6$  (3.9 %), depth  $198 \pm 9.3$  (4.7 %). Therefore:

$$\frac{\delta a}{a} = \frac{9.6}{241} = \pm 0.039 \quad \frac{\delta b}{b} = \frac{9.3}{198} = \pm 0.047 \quad (\text{A.31})$$

- Microchannel 2: width  $471 \pm 13.4$  (2.8 %), depth  $378 \pm 1.6$  (0.42 %). Therefore:

$$\frac{\delta a}{a} = \frac{13.4}{471} = \pm 0.028 \quad \frac{\delta b}{b} = \frac{1.6}{378} = \pm 0.004 \quad (\text{A.32})$$

See Appendix D for detailed data.

The channel length was measured using an electronic digital caliper with a resolution of  $\delta L = \pm 0.005 \text{ mm}$ . Since, the channel length is  $L = 21.9 \text{ mm}$ , the uncertainty in the channel is:

$$\frac{\delta L}{L} = \frac{0.005}{21.9} = \pm 0.000228 \quad (\text{A.33})$$

## A.2.7 Time

The timer function in the ExceLink data acquisition program is used to access the computer's system clock and record time values. The timer function has a  $1 \text{ ms}$  resolution; therefore the uncertainty in the time value is:

$$\frac{\delta t}{t} = \pm \frac{5 \times 10^{-4} \text{ s}}{t[\text{s}]} \quad (\text{A.34})$$

## A.3 Uncertainty in Calculated Quantities

### A.3.1 Mass flow, $\dot{m}$

The volumetric flow rate in the microchannel was measured using a Harvard Apparatus PHD2000 syringe pump and a McMillan Co. micro-turbine flow sensor for low and high flow rates respectively.

- Syringe pump  $1 \leq Q \leq 15 \text{ ml/min}$

The accuracy of the syringe pump was determined from its calibration certificate as  $\delta Q = 0.0002106 \text{ ml/min}$  for  $150 \text{ ml}$  plastic syringe. The mass flow can be expressed in terms of the volumetric flow rate as:

$$\dot{m} = Q * \rho \quad (\text{A.35})$$

Therefore the uncertainty in the mass flow rate can be calculated as:

$$\frac{\delta \dot{m}}{\dot{m}} = \pm \left\{ \left( \frac{\delta Q}{Q} \right)^2 + \left( \frac{\delta \rho}{\rho} \right)^2 \right\}^{1/2} \quad (\text{A.36})$$

The highest uncertainty in the flow rate is expected at the lowest flow rate. Therefore, substituting the uncertainty of the volumetric flow rate  $\delta Q = 0.0002106 \text{ ml/min}$ , the flow rate  $Q = 1 \text{ ml/min}$ , and the uncertainty of the density (Equation A.30), the lowest uncertainty for the flow rate reduces to  $\delta \dot{m}/\dot{m} = \pm 0.004$

- Micro gear pump  $15 < Q \leq 64 \text{ ml/min}$

For this range, the syringe pump was replaced for a micro gear pump and the flow rate was measured using a McMillan Co. micro-turbine flow sensor with uncertainty  $\delta Q = 0.4 \text{ ml/min}$ . Therefore with this setup, the maximum uncertainty in the flow rate is determined as  $\delta \dot{m}/\dot{m} = \pm 0.027$ .

### A.3.2 Channel cross sectional area, $A$

The cross sectional area of the channel is the product of the channel width and height.

$$A = ab \quad (\text{A.37})$$

Therefore, the uncertainty in the cross sectional area of the channel is:

$$\frac{\delta A}{A} = \pm \left\{ \left( \frac{\delta a}{a} \right)^2 + \left( \frac{\delta b}{b} \right)^2 \right\}^{1/2} \quad (\text{A.38})$$

Substituting the uncertainty in the channel dimensions (Equations A.31 and A.32) into Equation A.38 then:

$$\frac{\delta A}{A} = \pm(0.061 \text{ and } 0.029) \quad (\text{A.39})$$

On Equation A.39 0.061 and 0.029 corresponds to the smallest and biggest channel respectively.

### A.3.3 Channel surface area, $A_s$

The channel surface area can not be expressed in terms of a product of its variables. Therefore, Equation A.5 can not be used to calculate the uncertainty. For these cases the uncertainty can be calculated using the general form given in Equation A.3.

$$A_s = (a + 2b)L \quad (\text{A.40})$$

$$\delta A_s = \pm \left\{ \left( \frac{\partial A_s}{\partial a} \delta a \right)^2 + \left( \frac{\partial A_s}{\partial b} \delta b \right)^2 + \left( \frac{\partial A_s}{\partial L} \delta L \right)^2 \right\}^{1/2} \quad (\text{A.41})$$

$$\frac{\partial A_s}{\partial a} = L \quad \frac{\partial A_s}{\partial b} = 2L \quad \frac{\partial A_s}{\partial L} = a + 2b \quad (\text{A.42})$$

Substituting Equation A.42 into Equation A.41

$$\delta A_s = \pm \left\{ (L\delta a)^2 + (2L\delta b)^2 + [(a + 2b)\delta L]^2 \right\}^{1/2} \quad (\text{A.43})$$

The relative uncertainty can be obtained dividing Equation A.43 by  $A_s$  then:

$$\frac{\delta A_s}{A_s} = \pm \left\{ \left[ \frac{L}{(a + 2b)L} \delta a \right]^2 + \left[ \frac{2L}{(a + 2b)L} \delta b \right]^2 + \left[ \frac{(a + 2b)}{(a + 2b)L} \delta L \right]^2 \right\}^{1/2} \quad (\text{A.44})$$

Rearranging terms in Equation A.44, the uncertainty in the channel surface area can be expressed as:

$$\frac{\delta A_s}{A_s} = \pm \left\{ \left[ \left( \frac{a}{a + 2b} \right) \frac{\delta a}{a} \right]^2 + \left[ \left( \frac{2b}{a + 2b} \right) \frac{\delta b}{b} \right]^2 + \left( \frac{\delta L}{L} \right)^2 \right\}^{1/2} \quad (\text{A.45})$$

Substituting the channel uncertainties and dimensions in Equation A.45, the uncertainty in the channel surface area is 3.3 % and 1.1 % for the smaller and larger channel respectively.

### A.3.4 Channel perimeter, $P$

The perimeter of the channel is defined as:

$$P = 2(a + b) \quad (\text{A.46})$$

After using the general form (Equation A.3) and rearrangement of terms:

$$\frac{\delta P}{P} = \pm \left\{ \left[ \left( \frac{a}{a + b} \right) \frac{\delta a}{a} \right]^2 + \left[ \left( \frac{b}{a + b} \right) \frac{\delta b}{b} \right]^2 \right\}^{1/2} \quad (\text{A.47})$$

The uncertainties in the channel size ( $\delta a/a$ ,  $\delta b/b$ ) can be obtained from Equations A.31 and A.32.



### A.3.5 Hydraulic diameter, $d_h$

The hydraulic diameter is defined as:

$$d_h = \frac{4A}{P} = \frac{2ab}{a+b} \quad (\text{A.48})$$

After using the general form (Equation A.3) and rearrangement of terms, the uncertainty in the hydraulic diameter is:

$$\frac{\delta d_h}{d_h} = \pm \left\{ \left[ \left( \frac{b}{a+b} \right) \frac{\delta a}{a} \right]^2 + \left[ \left( \frac{a}{a+b} \right) \frac{\delta b}{b} \right]^2 \right\}^{1/2} \quad (\text{A.49})$$

The uncertainties in the channel dimensions can be obtained from Equations A.31 and A.32.

### A.3.6 Mass flux, $G$

$$G = \frac{\dot{m}}{A} \quad (\text{A.50})$$

$$\frac{\delta G}{G} = \pm \left\{ \left( \frac{\delta \dot{m}}{\dot{m}} \right)^2 + \left( \frac{\delta A}{A} \right)^2 \right\}^{1/2} \quad (\text{A.51})$$

where the uncertainty of the mass flow and channel cross sectional area can be obtained from Equation A.36, and Equation A.38 respectively.

### A.3.7 Reynolds number, $Re$

$$Re = \frac{ud_h}{\nu} = \frac{2\dot{m}}{(a+b)\mu} \quad (\text{A.52})$$

After applying the general form (Equation A.3) and rearrangement of terms:

$$\frac{\delta Re}{Re} = \pm \left\{ \left( \frac{\delta \dot{m}}{\dot{m}} \right)^2 + \left[ \left( \frac{a}{a+b} \right) \frac{\delta a}{a} \right]^2 + \left[ \left( \frac{b}{a+b} \right) \frac{\delta b}{b} \right]^2 + \left( \frac{\delta \mu}{\mu} \right)^2 \right\}^{1/2} \quad (\text{A.53})$$

where,  $\delta \dot{m}/\dot{m}$  can be obtained from Equation A.36

### A.3.8 Heat flux, $q_w$

- Single-phase: The heat flux during single-phase testing was calculated from:

$$q_w = \frac{\dot{m}c_p(T_{out} - T_{in})}{A_s} \quad (\text{A.54})$$

After applying the general form (Equation A.3) and rearrangement of terms:

$$\begin{aligned} \frac{\delta q_w}{q_w} = \pm \left\{ \left( \frac{\delta \dot{m}}{\dot{m}} \right)^2 + \left( \frac{\delta c_p}{c_p} \right)^2 + \left[ \left( \frac{T_{out}}{T_{out} - T_{in}} \right) \frac{\delta T_{out}}{T_{out}} \right]^2 \right. \\ \left. + \left[ \left( \frac{T_{in}}{T_{out} - T_{in}} \right) \frac{\delta T_{in}}{T_{in}} \right]^2 + \left( \frac{\delta A_s}{A_s} \right)^2 \right\}^{1/2} \end{aligned} \quad (\text{A.55})$$

where  $\delta A_s/A_s$  can be obtained from Equation A.44

- Two-phase flow: The heat flux in the microevaporator is defined as:

$$q_w = \frac{Q_{fluid}}{A_s} \quad (\text{A.56})$$

where the heat removed by the fluid ( $Q_{fluid}$ ) is determined by:

$$Q_{fluid} = Q_{total} - Q_{loss}(T_w) = Q_{total} - [m(T_w) + b] \quad (\text{A.57})$$

The total heat transfer rate  $Q_{total}$  is calculated base on the heater voltage and shunt voltage and resistance according to:

$$Q_{total} = \frac{V_{heater}V_{shunt}}{\mathfrak{R}} \quad (\text{A.58})$$

Therefore, the heat transfer rate by the fluid  $Q_f$  is:

$$Q_f = \left[ \left( \frac{V_{heater}V_{shunt}}{\mathfrak{R}} \right) - (mT_w + b) \right] \quad (\text{A.59})$$

Neglecting the uncertainties in the slope  $m$  and intercept  $b$ , and applying the general form (Equation A.3), the uncertainty in the heat removed by the fluid reduces to:

$$\begin{aligned} \delta Q_f = \pm \left\{ \left[ \left( \frac{V_{shunt}}{\Re} \right) \delta V_{heater} \right]^2 + \left[ \left( \frac{V_{heater}}{\Re} \right) \delta V_{shunt} \right]^2 \right. \\ \left. + \left[ \left( \frac{V_{shunt} V_{heater}}{\Re^2} \right) \delta \Re \right]^2 + [m \delta T_w]^2 \right\}^{1/2} \end{aligned} \quad (\text{A.60})$$

Dividing Equation A.60 by  $Q_f$ , the relative uncertainty in the heat rate for two-phase flow is:

$$\begin{aligned} \frac{\delta Q_f}{Q_f} = \pm \left\{ \left[ \left( \frac{1}{1 - \frac{(mT_w + b)\Re}{V_{shunt} V_{heater}}} \right) \frac{\delta V_{heater}}{V_{heater}} \right]^2 + \left[ \left( \frac{1}{1 - \frac{(mT_w + b)\Re}{V_{shunt} V_{heater}}} \right) \frac{\delta V_{shunt}}{V_{shunt}} \right]^2 \right. \\ + \left[ \left( \frac{1}{1 - \frac{(mT_w + b)\Re}{V_{shunt} V_{heater}}} \right) \frac{\delta \Re}{\Re} \right]^2 \\ \left. + \left[ \left( \frac{1}{\frac{V_{shunt} V_{heater}}{\Re m T_w} - 1 - \frac{b}{m T_w}} \right) \frac{\delta T_w}{T_w} \right]^2 \right\}^{1/2} \end{aligned} \quad (\text{A.61})$$

The relative uncertainty in the heat flux  $q_w$  can be calculated from:

$$\delta q_w = \pm \left\{ \left( \frac{\delta Q_f}{Q_f} \right)^2 + \left( \frac{\delta A_s}{A_s} \right)^2 \right\}^{1/2} \quad (\text{A.62})$$

The uncertainty in the rate of heat  $Q_f$ , heater voltage, shunt voltage, resistance, channel wall temperature, and channel surface area can be obtained from Equations A.61, A.8, A.12, A.13, A.6, and A.45 respectively.

### A.3.9 Heat transfer coefficient, $h$

- The local heat transfer coefficient for two-phase flow was calculated as:

$$h_{tp} = \frac{q_w}{(T_w - T_{sat})} \quad (\text{A.63})$$

After applying the general form (Equation A.3) and rearrangement of terms:

$$\frac{\delta h_{tp}}{h_{tp}} = \pm \left\{ \left( \frac{\delta q_w}{q_w} \right)^2 + \left[ \left( \frac{T_w}{T_w - T_{sat}} \right) \frac{\delta T_w}{T_w} \right]^2 + \left[ \left( \frac{T_{sat}}{T_w - T_{sat}} \right) \frac{\delta T_{sat}}{T_{sat}} \right]^2 \right\}^{1/2} \quad (\text{A.64})$$

The uncertainty in the heat flux, wall and saturated temperature can be obtained from Equations A.62, A.6, and A.30 respectively.

- The uncertainty in the local heat transfer coefficient for single-phase can be obtained from Equation A.64 just substituting the saturated temperature  $T_{sat}$  with the fluid temperature  $T_f$  and using Equation A.55 to estimate the uncertainty in the heat flux.

$$\frac{\delta h_{sp}}{h_{sp}} = \pm \left\{ \left( \frac{\delta q_w}{q_w} \right)^2 + \left[ \left( \frac{T_w}{T_w - T_f} \right) \frac{\delta T_w}{T_w} \right]^2 + \left[ \left( \frac{T_f}{T_w - T_f} \right) \frac{\delta T_f}{T_f} \right]^2 \right\}^{1/2} \quad (\text{A.65})$$

### A.3.10 Nusselt number, $Nu$

- The local Nusselt number for single-phase was defined as:

$$Nu = \frac{h d_h}{k_f} \quad (\text{A.66})$$

After applying the general form (Equation A.3) and rearrangement of terms:

$$\frac{\delta Nu}{Nu} = \pm \left\{ \left( \frac{\delta h_{sp}}{h_{sp}} \right)^2 + \left( \frac{\delta d_h}{d_h} \right)^2 + \left( \frac{\delta k_f}{k_f} \right)^2 \right\}^{1/2} \quad (\text{A.67})$$

The uncertainties in the local heat transfer coefficient for single-phase, the hydraulic diameter, and the thermal conductivity of the fluid can be obtained from Equations A.65, A.49, and A.30 respectively.

- The average Nusselt number for single-phase between the entrance of the channel and a location  $x$  was defined as:

$$\overline{Nu}_{o-x} = \frac{\overline{h}_{o-x} d_h}{k_f} \quad (\text{A.68})$$

The average heat transfer coefficient was defined as:

$$\overline{h}_{o-x} = \frac{q_{o-x}}{\Delta T_{\ell n}} \quad (\text{A.69})$$

where  $q_{o-x}$  is the heat flux and  $\Delta T_{\ell n}$  is the logarithmic mean temperature difference calculated as:

$$q_{o-x} = \frac{\dot{m} c_p (T_f - T_{in})}{(a + 2b)x} \quad (\text{A.70})$$

$$\Delta T_{\ell n} = \frac{(T_w - T_f) - (T_w - T_{in})}{\ell n \left( \frac{T_w - T_f}{T_w - T_{in}} \right)} \quad (\text{A.71})$$

The temperature of the fluid  $T_f$  at any location along the channel was estimated based on the inlet and outlet temperature as:

$$T_f = \frac{x(T_{out} - T_{in})}{L} + T_{in} \quad (\text{A.72})$$

After applying the general form (Equation A.3), the uncertainty in the average Nusselt number can be expressed as:

$$\frac{\delta \overline{Nu}_{o-x}}{\overline{Nu}_{o-x}} = \pm \left\{ \left( \frac{\delta \overline{h}_{o-x}}{\overline{h}_{o-x}} \right)^2 + \left( \frac{\delta d_h}{d_h} \right)^2 + \left( \frac{\delta k_f}{k_f} \right)^2 \right\}^{1/2} \quad (\text{A.73})$$

Assuming that the uncertainty of the logarithmic mean temperature is approximately  $\delta T/T$  (shown in Equation A.30), the uncertainty in the average Nusselt number can be expressed as:

$$\begin{aligned} \frac{\delta \overline{Nu}_{o-x}}{\overline{Nu}_{o-x}} \approx & \pm \left\{ \left( \frac{\delta \dot{m}}{\dot{m}} \right)^2 + \left( \frac{\delta c_p}{c_p} \right)^2 + \left[ \left( \frac{T_f}{T_f - T_{in}} \right) \frac{\delta T_f}{T_f} \right]^2 + \left[ \left( \frac{T_{in}}{T_f - T_{in}} \right) \frac{\delta T_{in}}{T_{in}} \right]^2 \right. \\ & \left. + \left( \frac{\delta A_s}{A_s} \right)^2 + \left( \frac{\delta T}{T} \right)^2 + \left( \frac{\delta d_h}{d_h} \right)^2 + \left( \frac{\delta k_f}{k_f} \right)^2 \right\}^{1/2} \end{aligned} \quad (\text{A.74})$$

The uncertainties in the mass flow, properties and temperature of the fluid, hydraulic diameter, and channel surface can be obtained from Equations A.6, A.30, A.36, A.45, and A.49.

### A.3.11 Friction factor, $f$

The single-phase friction factor was defined as:

$$f = \frac{\Delta p d_h}{L \rho V^2} = \frac{\Delta p \rho}{L \dot{m}^2} \left[ \frac{(ab)^3}{a+b} \right] \quad (\text{A.75})$$

After applying the general form (Equation A.3) and rearrangement of terms:

$$\begin{aligned} \frac{\delta f}{f} = & \pm \left\{ \left( \frac{\delta \Delta p}{\Delta p} \right)^2 + \left( \frac{\delta \rho}{\rho} \right)^2 + \left( \frac{\delta L}{L} \right)^2 + \left( 2 \frac{\delta \dot{m}}{\dot{m}} \right)^2 \right. \\ & \left. + \left[ \left( \frac{2a+3b}{a+b} \right) \frac{\delta a}{a} \right]^2 + \left[ \left( \frac{3a+2b}{a+b} \right) \frac{\delta b}{b} \right]^2 \right\}^{1/2} \end{aligned} \quad (\text{A.76})$$

The uncertainties in the pressure, density, and mass flow can be obtained from Equations A.25, A.30, and A.36 respectively. The uncertainties in the channels dimensions can be obtained from Equations A.31-A.33.

### A.3.12 Vapor quality, $x$

The vapor quality at the exit of the channel was calculated based on an energy balance as:

$$x = \frac{1}{h_{fg}} \left[ \frac{Q_f}{\dot{m}} - c_p(T_{sat} - T_{in}) \right] \quad (\text{A.77})$$

After applying the general form (Equation A.3) and rearrangement of terms, the uncertainty of the vapor quality reduces to:

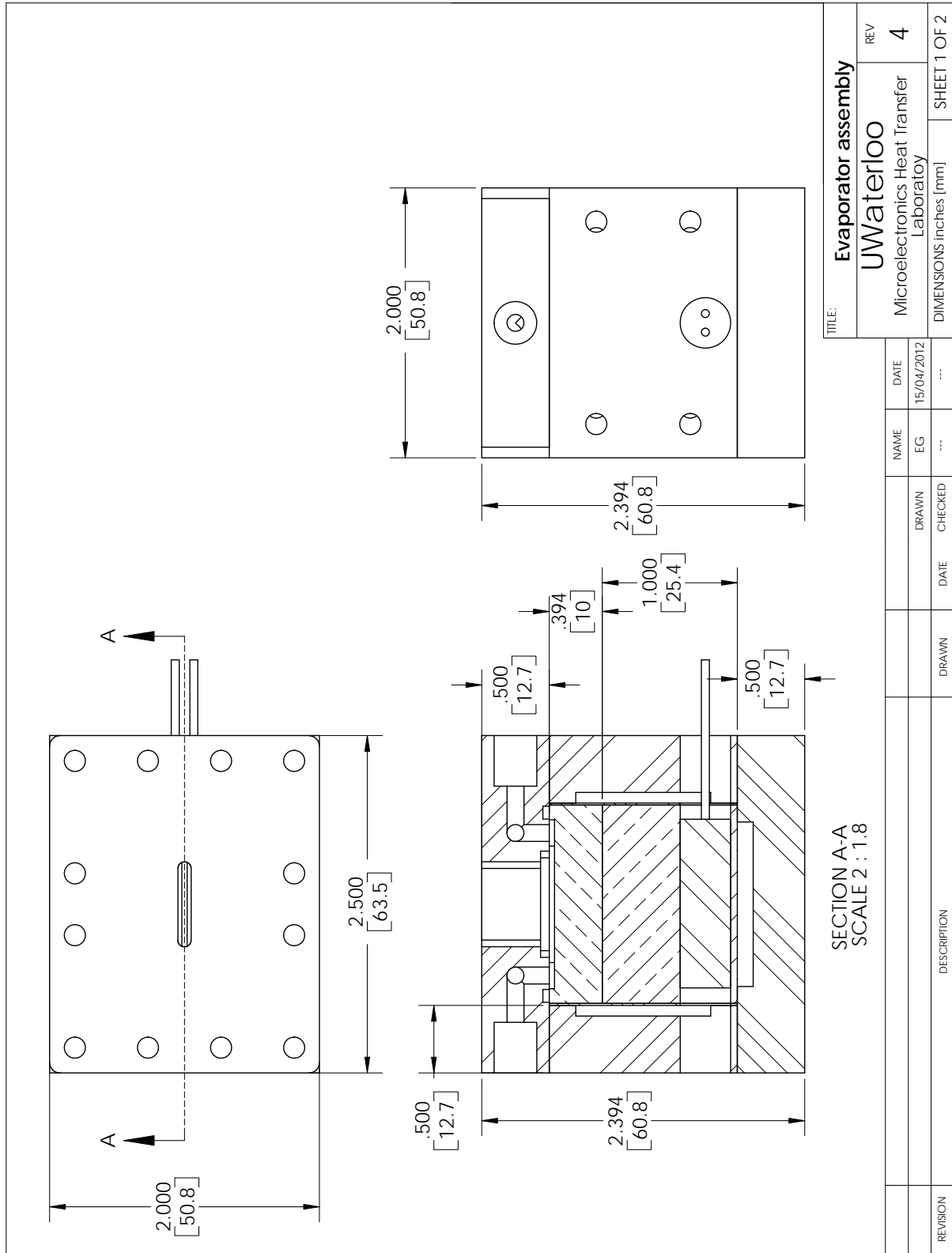
$$\begin{aligned} \frac{\delta x}{x} = & \pm \left\{ \left( \frac{\delta h_{fg}}{h_{fg}} \right)^2 + \left[ \frac{1}{1 - \frac{\dot{m} c_p (T_{sat} - T_{in})}{Q_{fluid}}} \frac{\delta Q_{fluid}}{Q_{fluid}} \right]^2 + \left[ \frac{1}{1 - \frac{\dot{m} c_p (T_{sat} - T_{in})}{Q_{fluid}}} \frac{\delta \dot{m}}{\dot{m}} \right]^2 \right. \\ & + \left[ \frac{1}{\frac{Q_{fluid}}{\dot{m} c_p (T_{sat} - T_{in})} - 1} \frac{\delta c_p}{c_p} \right]^2 + \left[ \frac{c_p T_{sat}}{\frac{Q_{fluid}}{\dot{m}} - c_p (T_{sat} - T_{in})} \frac{\delta T_{sat}}{T_{sat}} \right]^2 \\ & \left. + \left[ \frac{c_p T_{in}}{\frac{Q_{fluid}}{\dot{m}} - c_p (T_{sat} - T_{in})} \frac{\delta T_{in}}{T_{in}} \right]^2 \right\}^{1/2} \quad (\text{A.78}) \end{aligned}$$

The uncertainties in the heat removed by the fluid, heater voltage, shunt voltage, resistance, fluid properties, and mass flow can be obtained from Equations A.61, A.8, A.12, A.13, A.30, and A.36 respectively.

## Appendix B

# Detailed Drawings of Microevaporator Assembly Unit





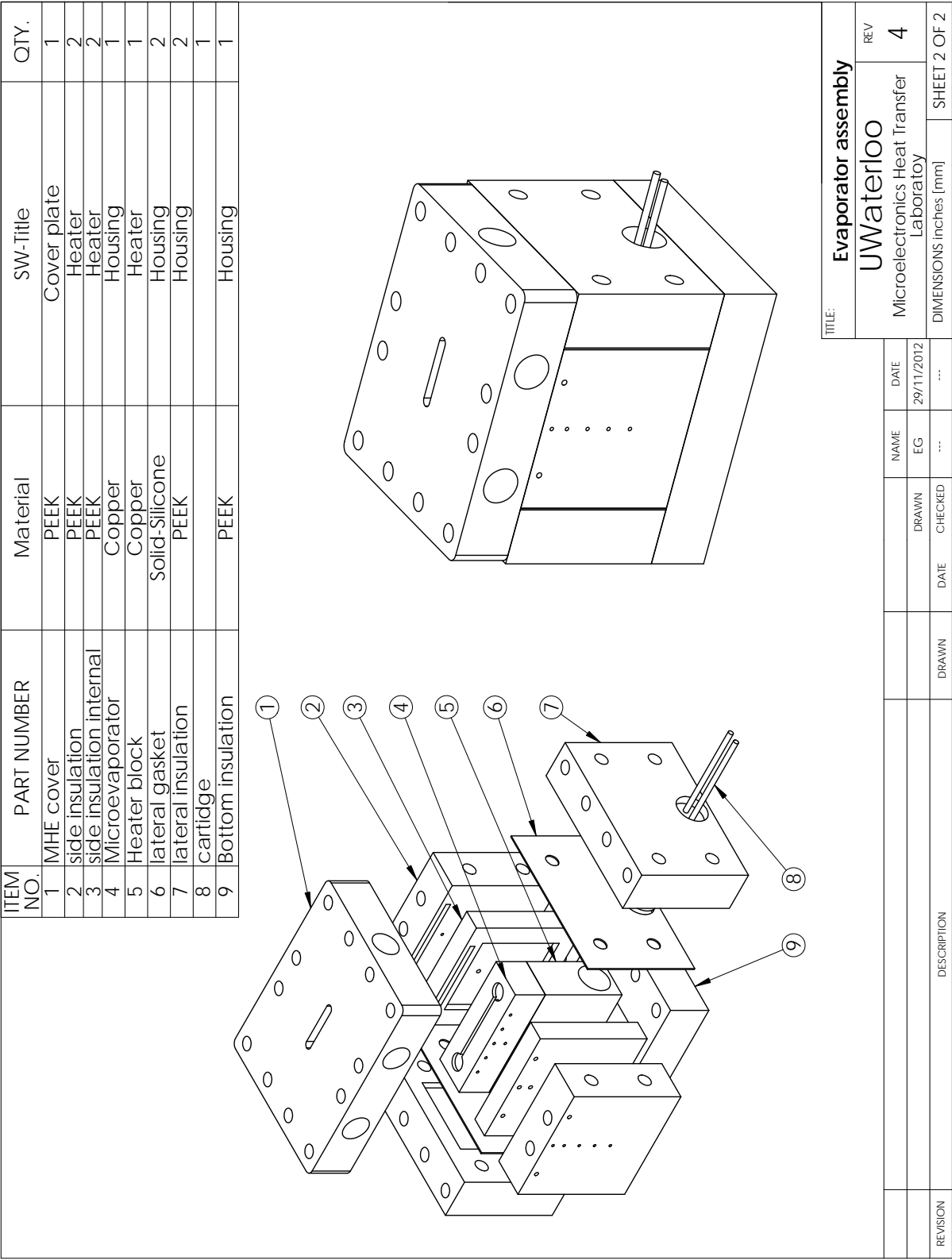
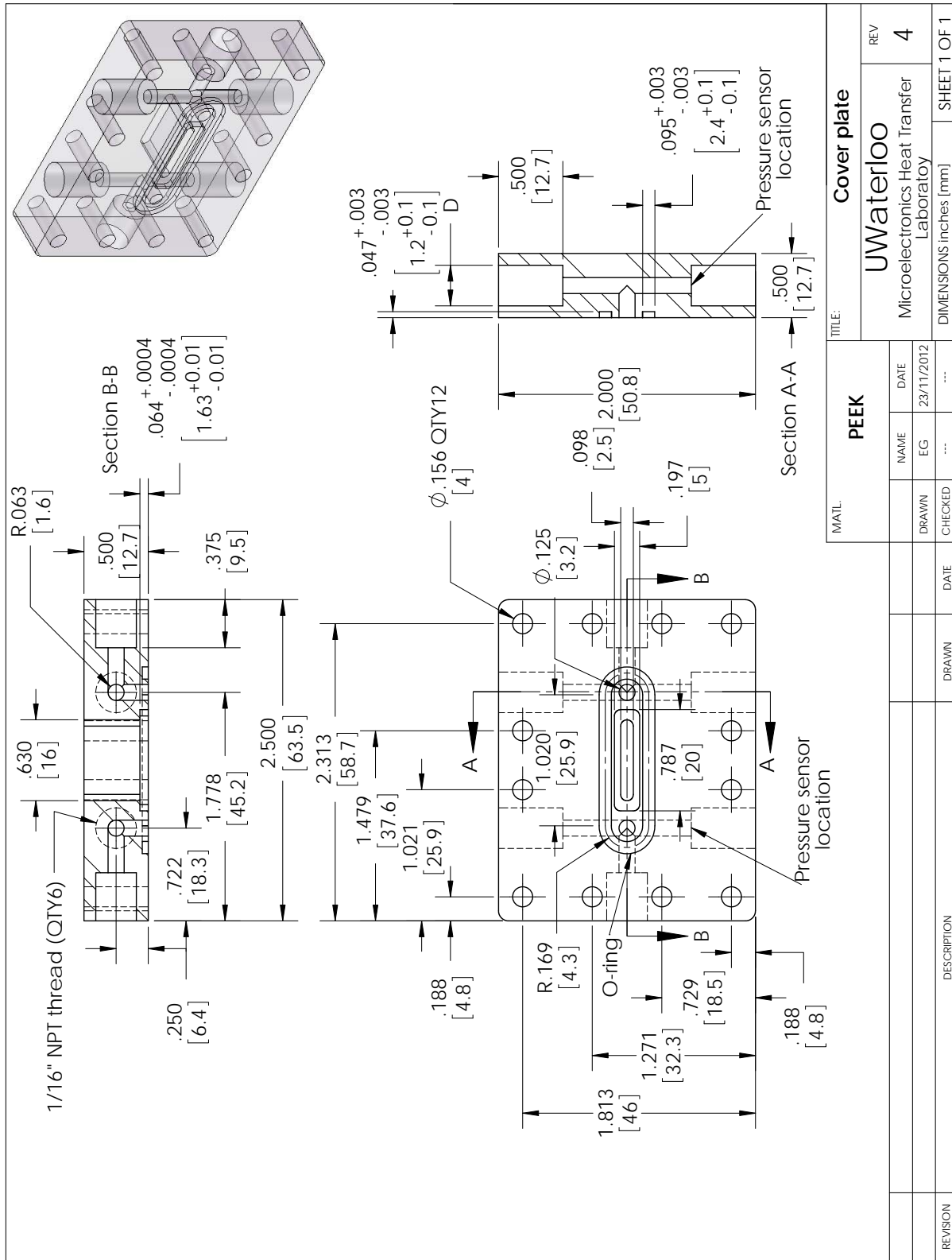


Figure B.2: Microevaporator assembly unit - isometric and exploded views



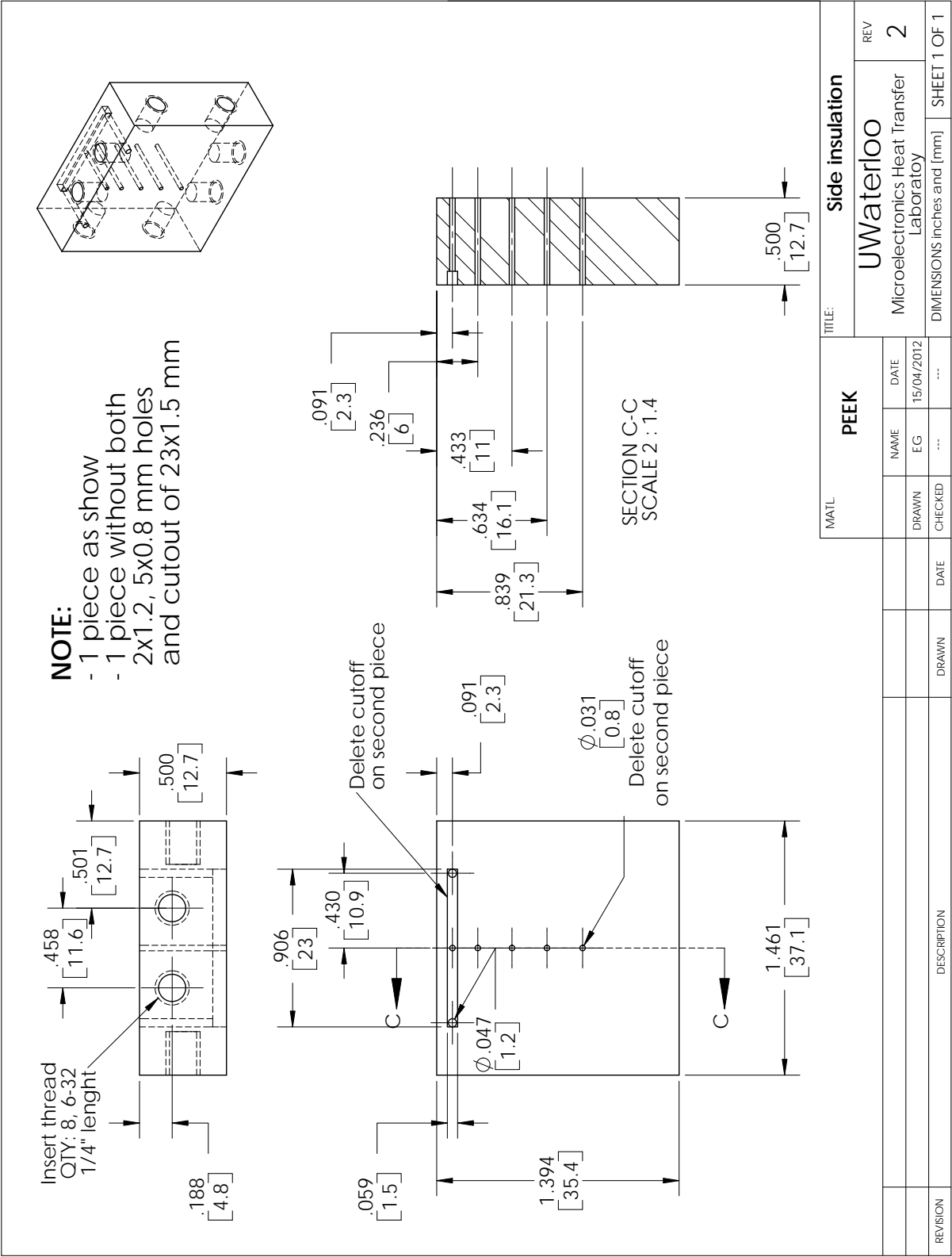


Figure B.4: Side insulation



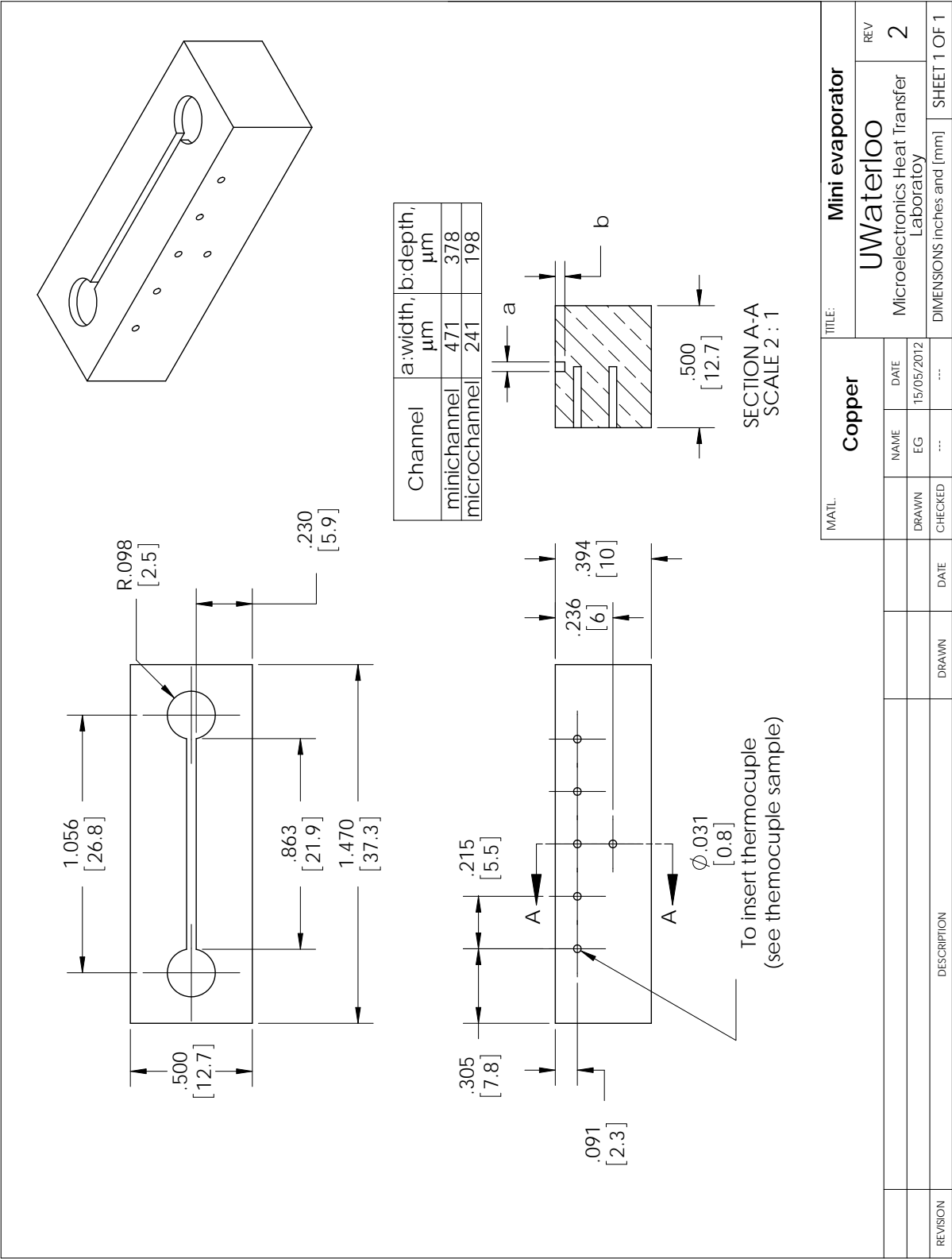


Figure B.6: Microevaporator single straight channel

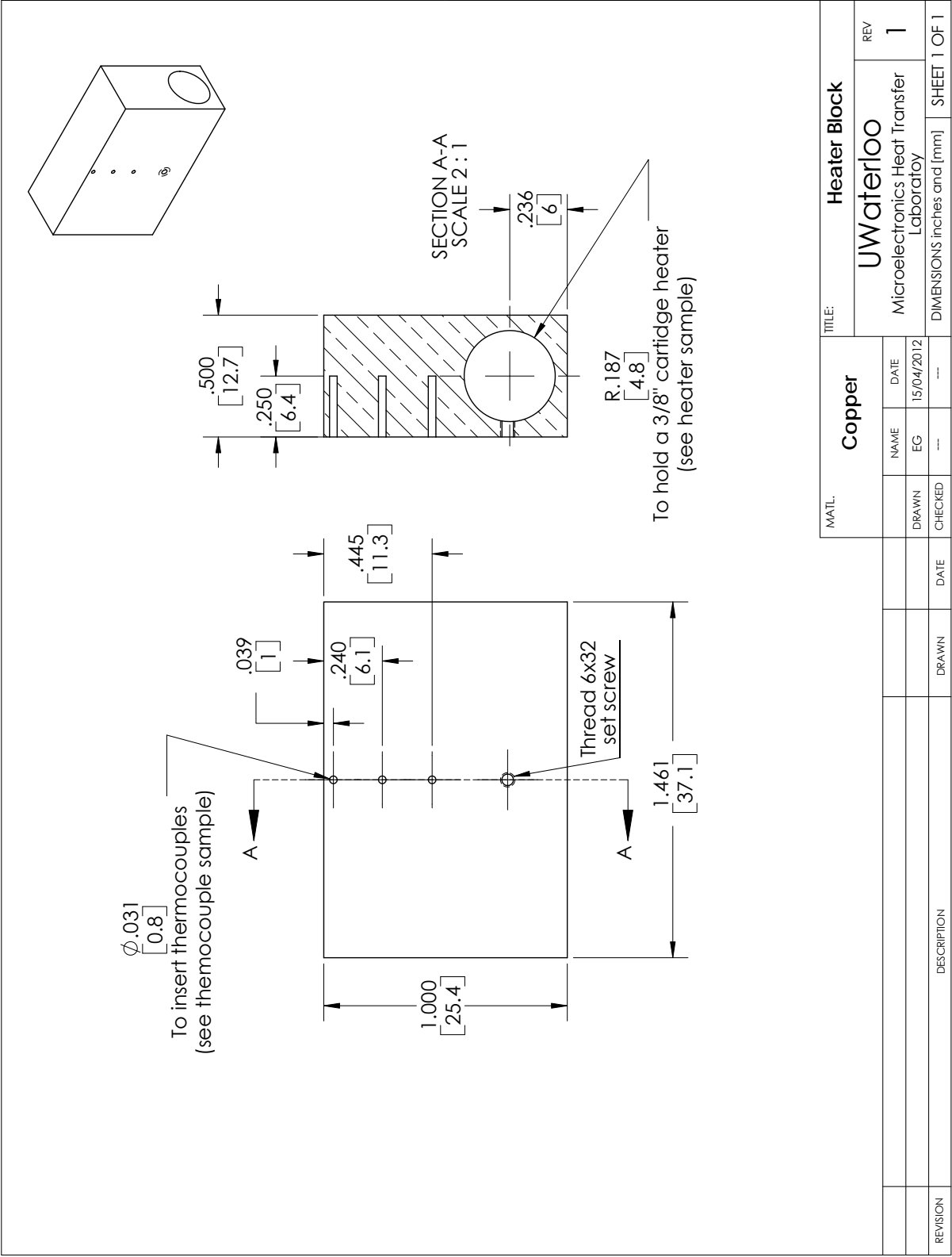


Figure B.7: Heater block

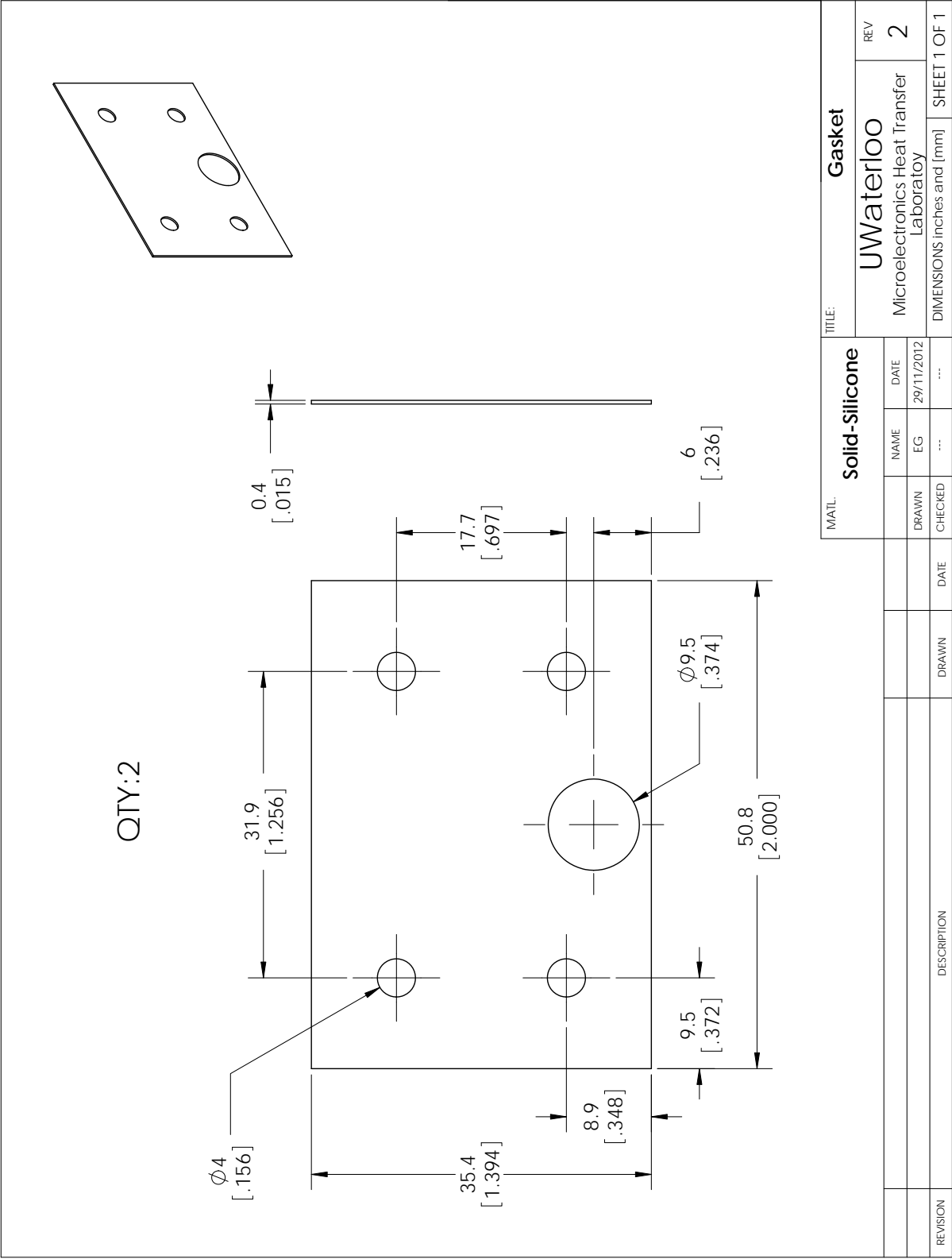


Figure B.8: Lateral gasket



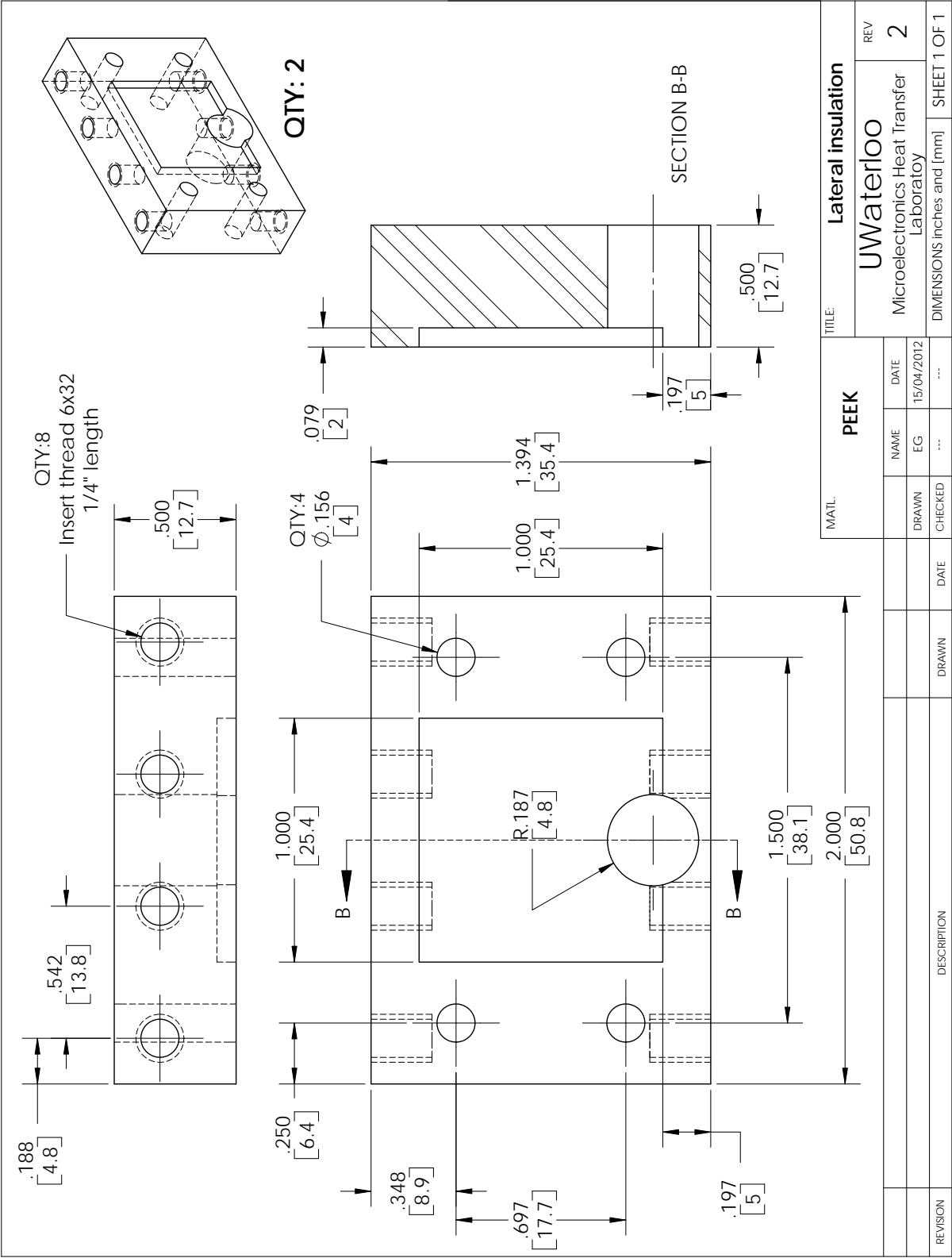


Figure B.9: Lateral insulation

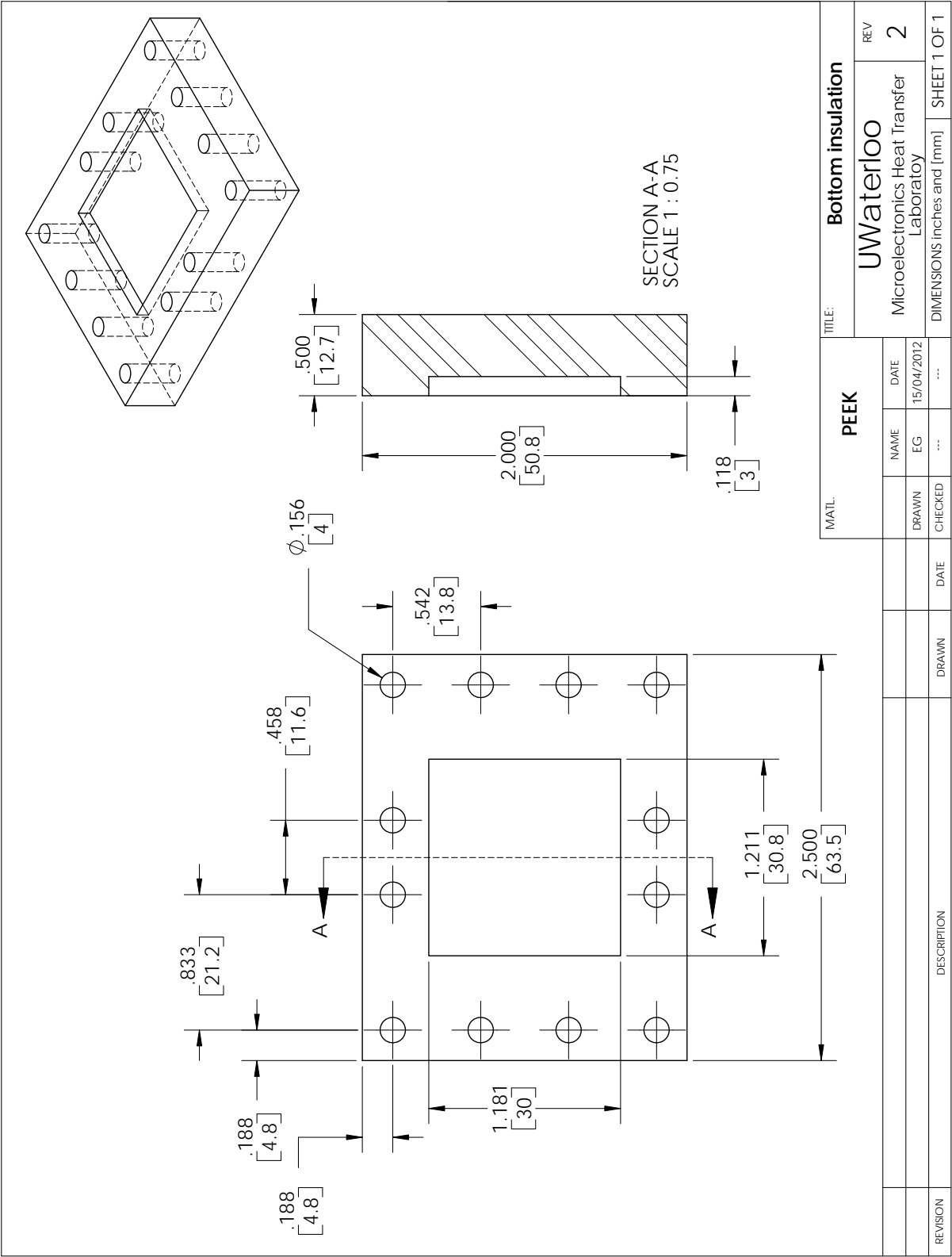


Figure B.10: Bottom insulation

# Appendix C

## Finite Element Models and Thermal Conductivity Measurements

### C.1 Finite Element Models, FEMs

In order to measure the thermal conductivity of the oxygen free copper in accordance with ASTM D5470, the gradient of temperature along the sample (rectangular bar  $13 \times 14 \times 53$  mm) was measured using six thermocouples located at different isothermal planes. The FEM shown in Figure C.1 was used to assist in the locations of the isothermal planes. Based on the FEM the thermocouples were equally spaced at 6 mm.

Similarly, the location of the thermocouples were also determined using a FEM for the cartridge heater and microevaporator as shown in Figure C.2. There are three thermocouples located at the heater block and five in the microevaporator.

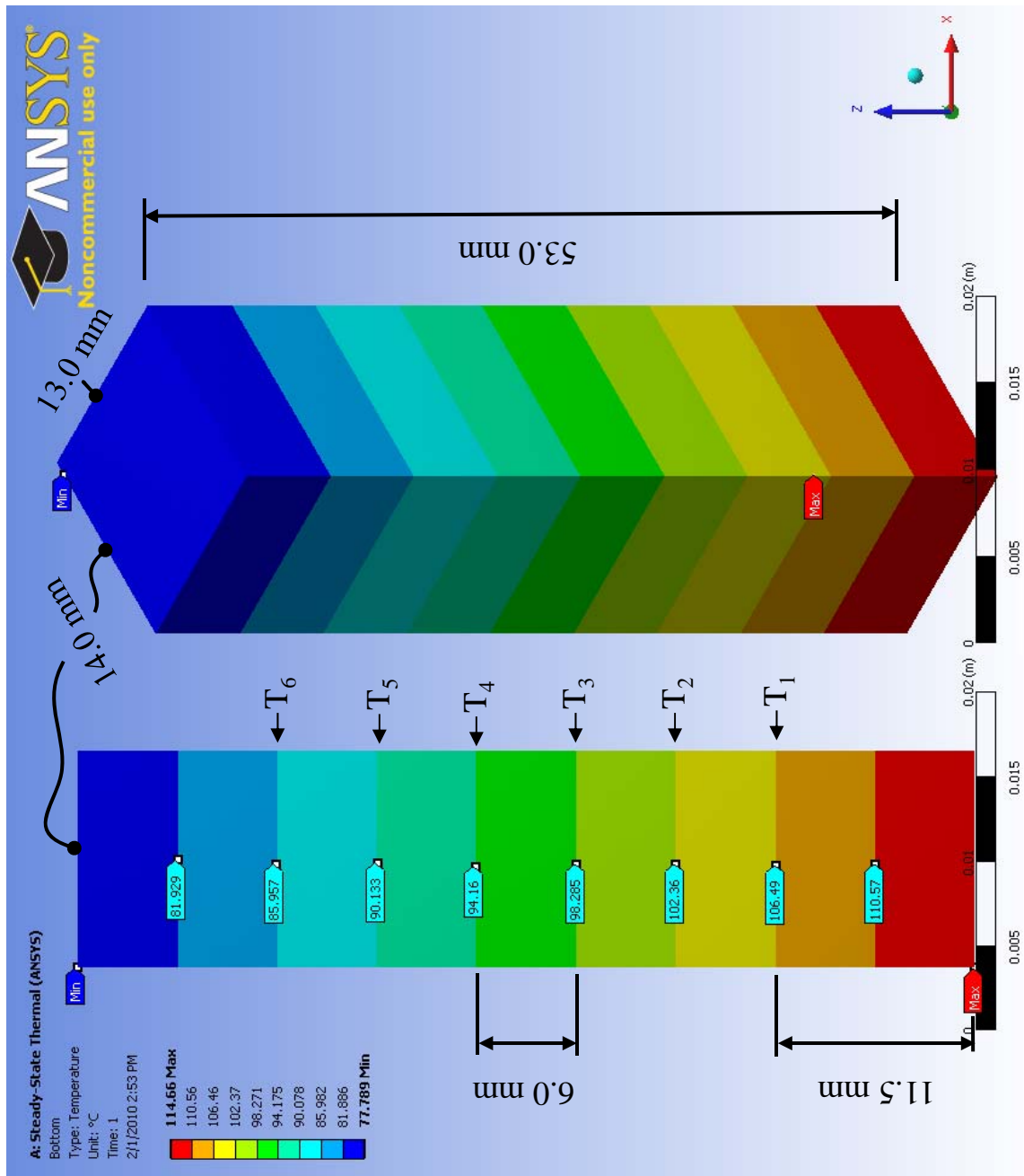
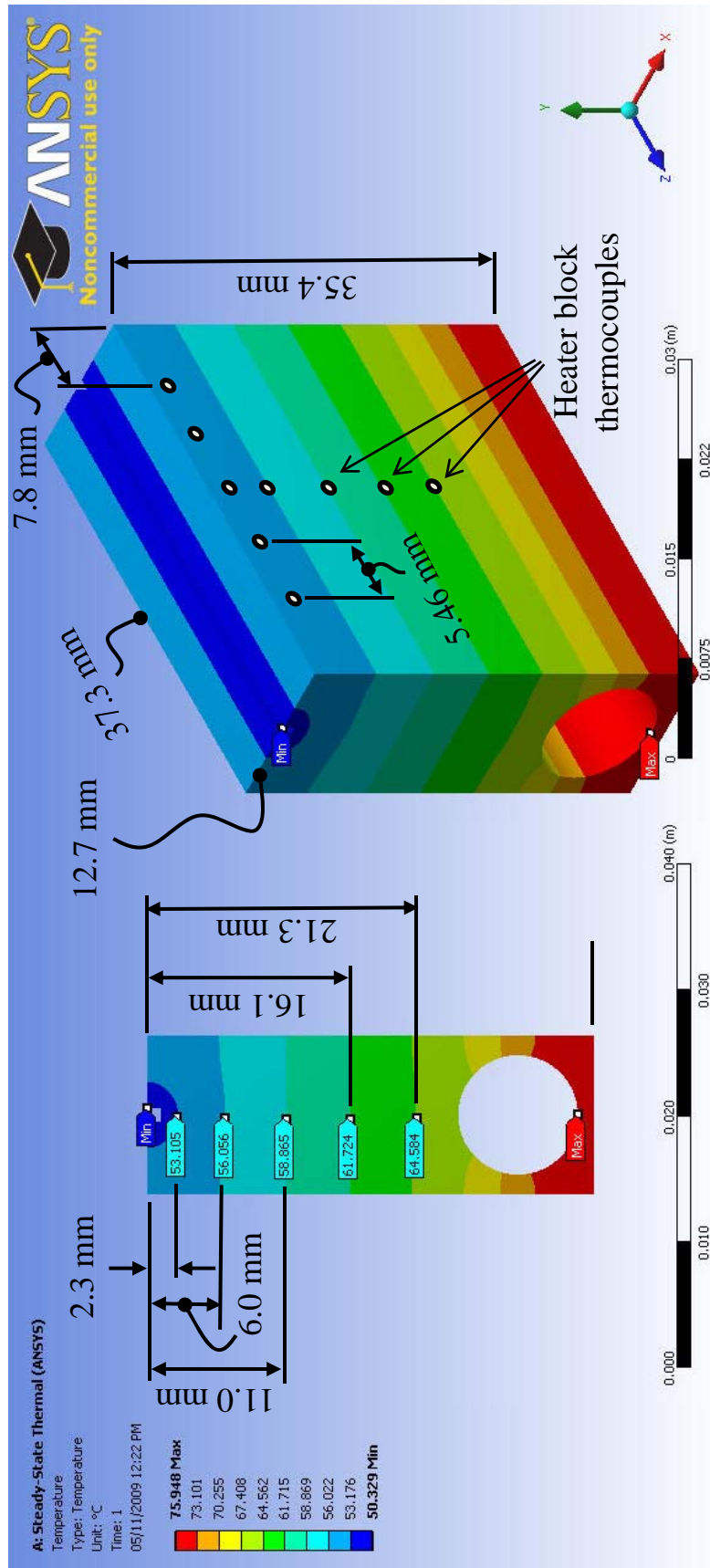


Figure C.1: FEM for thermocouple locations at isothermal planes in oxygen free copper sample



Note: All thermocouples are located at middle plane  
 (6.35 mm from the surface)

Figure C.2: FEM for thermocouple locations at isothermal planes in heater block and microevaporator

## C.2 Thermal conductivity

The thermal conductivity of the oxygen free copper was recorded for different temperatures (50, 70, 90, 110 and 120 °C) in a vacuum chamber. In order to evaluate the thermal conductivity using the ASTM D5470, measurements of the heat flow through the sample and the gradient of temperature are required. Figure C.3 shows the heat added and removed from the sample ( $Q$ ), the joint temperature ( $T_{joint}$ : temperature at the middle of the sample length), and the thermal conductivity as a function of time. The final value of the thermal conductivity is acquired when steady state is reached.

A typical gradient of temperature along the sample (temperature vs position) is shown in Figure C.4 for the 90°C case. Three straight lines are observed, the middle one represents the gradient of temperature in the sample (oxygen free copper), and the others are for the calibrated blocks (with known thermal conductivities) used to estimate the heat input and output during the experiment. The step in the straight lines represents the contact resistance between the sample and the calibrated blocks.

Table C.1 summarizes the data collected to calculate the thermal conductivity for all cases.

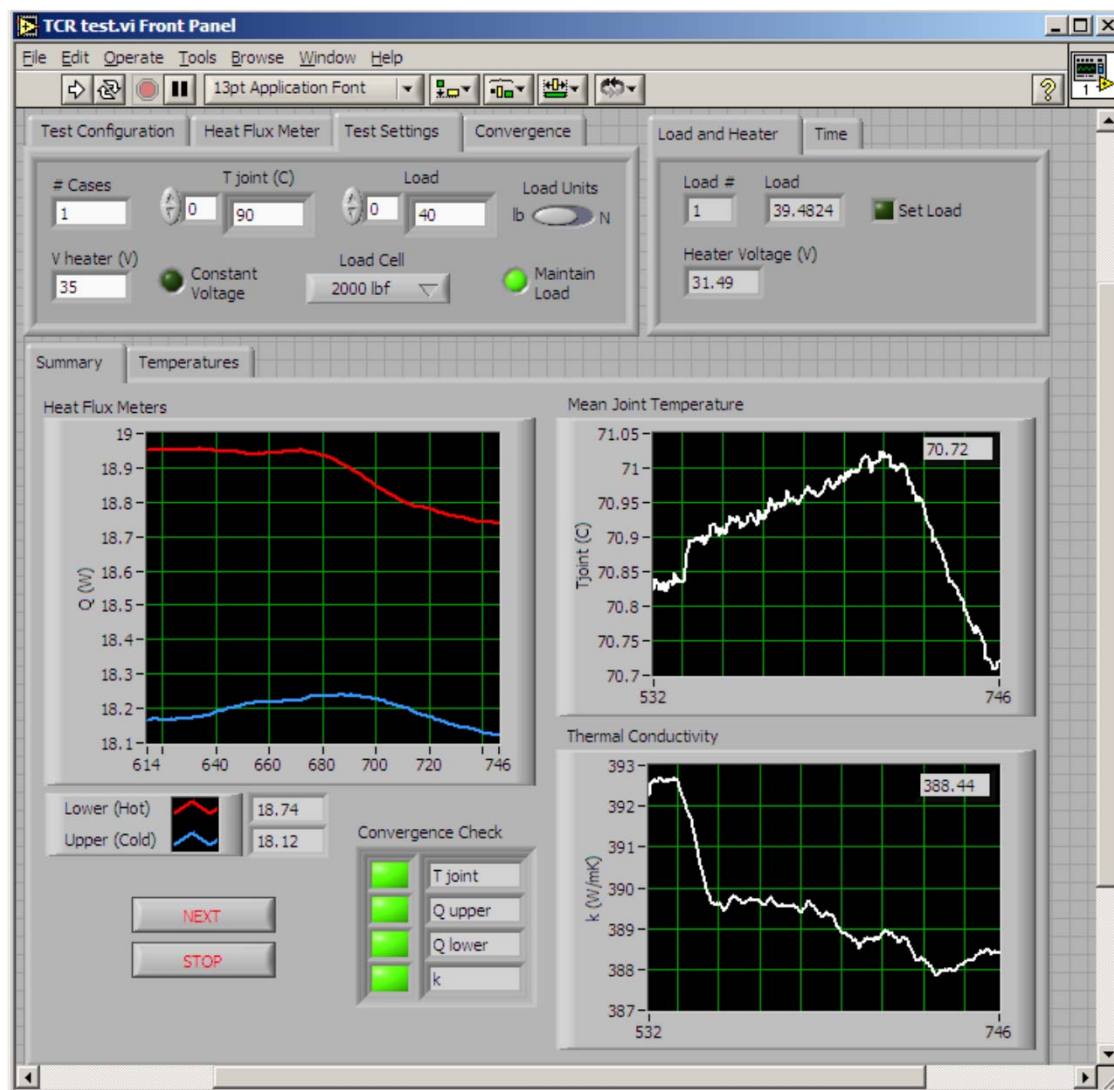


Figure C.3: Heat, sample temperature and conductivity vs time (case 70 °C)

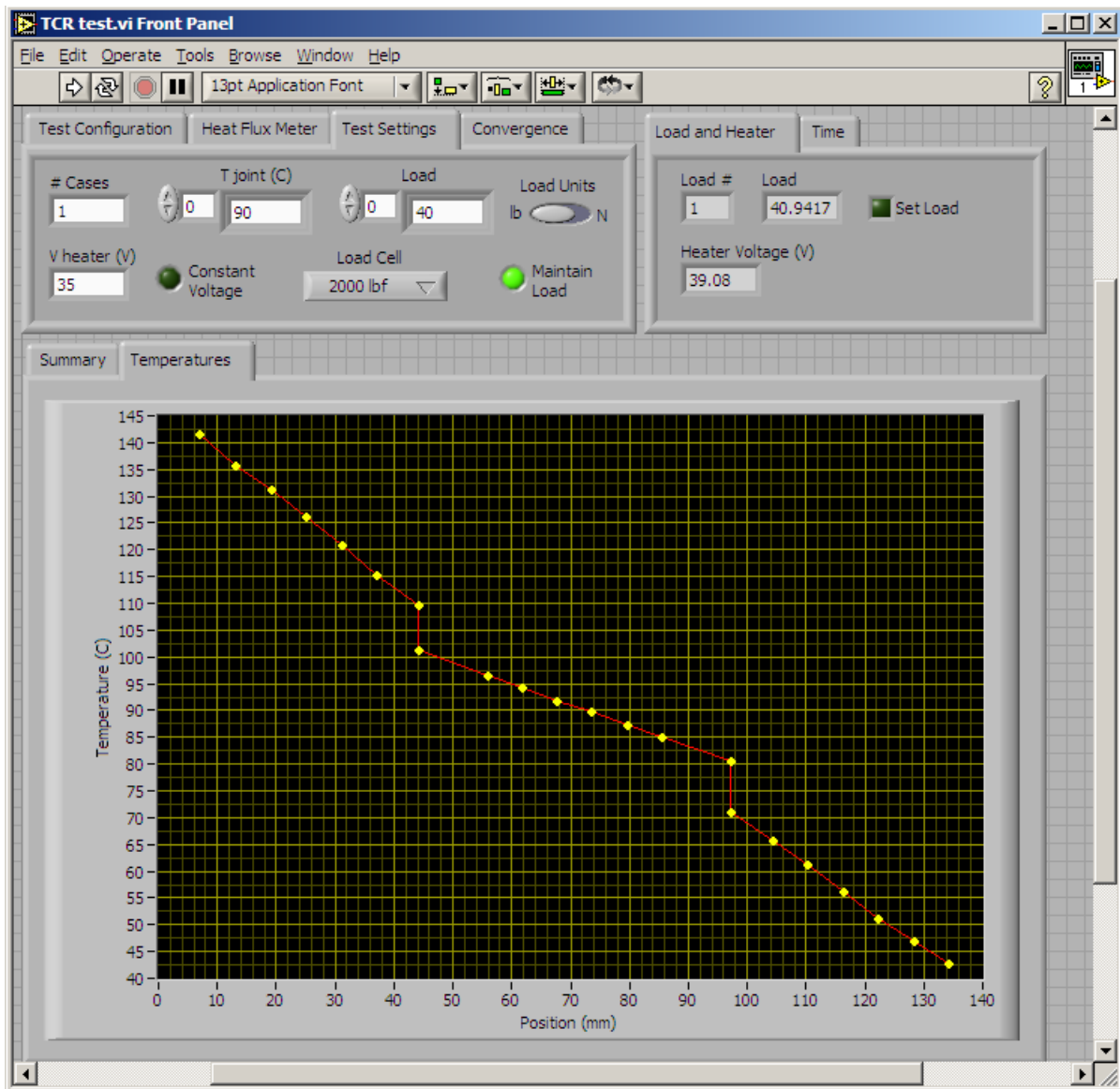


Figure C.4: Gradient of temperature in sample and calibrated blocks (case 90 °C)



Table C.1: Thermal conductivity measurement

<i>Cool bath, °C</i>	<i>Load, psi</i>	<i>Q<sub>upper</sub>, W</i>	<i>Q<sub>lower</sub>, W</i>	<i>T<sub>avg</sub>, °C</i>	<i>k, W/mK</i>
15.0	39.2	16.2	15.8	50.2	377.6
15.0	39.2	16.3	15.8	50.5	383.6
20.0	39.1	13.7	13.3	50.0	389.1
30.0	39.1	9.2	9.0	50.1	380.9
30.0	39.4	9.2	8.7	49.9	380.4
30.0	39.6	18.7	18.1	70.7	388.4
30.0	40.9	28.2	27.1	90.8	390.3
40.0	40.9	27.9	26.5	100.2	387.8
50.0	40.6	28.0	26.4	110.3	381.0
70.0	40.0	23.7	22.2	120.8	377.8

# Appendix D

## Channel Size Measurements

Microchannel 1				
channel width (a), $\mu\text{m}$		channel depth <sup>*</sup> (b), $\mu\text{m}$		
Surface tester	Microscope	Surface tester		
246	235	203		
244	240	194		
237	235			
242	240			
241	237			
234	235			
239	240			
236	237			
240	240			
239	234			
248	232			
247	232			
235	232			
236	238			
237				
233				
245				
245				
248				
243				
246				
246				
243				
234				
Average	241	236	Average	198
SD	4.8	3.0	SD	4.7
Measured with caliper	0.22	$\mu\text{m}$		$\mu\text{m}$
Methods difference	2.0%			
a =	241	$\mu\text{m}$	b =	198
+ -	9.6	$\mu\text{m}$	+ -	9.3
	4.0%			4.7%

\* Measured at channel header

Figure D.1: Dimension in microchannel

Microchannel 2					
channel width (a), $\mu\text{m}$		channel depth* (b), $\mu\text{m}$			
Surface tester	Microscope	Surface tester	Microscope	Surface tester	Microscope
480	470	378			
471	473	379			
481	470	377			
475	468				
478	471				
471	473				
471					
464					
470					
485					
475					
476					
480					
474					
468					
458					
462					
460					
469					
464					
468					
471					
469					
Average	471	Average	471	Average	378
SD	6.7	SD	1.8	SD	0.8
measured with caliper	0.49				
Methods difference	0.1%				
a =	471	b =	378		
+-	13.4	+-	1.6		
	2.8%		0.4%		

\* Measured at channel header

Figure D.2: Dimension in minichannel

# Appendix E

## Fluid Properties Correlations

All properties are determined based on correlations of tabulated data from Lemczyk and Molloy (1995) and Babcock and Wilcox (1992). The properties of the water are expressed as a function of the temperature  $T$ , valid for a temperature range between 273 and 400  $K$ .

### E.1 Thermal conductivity, $k$ ( $W/mK$ )

$$a = -2.76131$$

$$b = 3.40118 \times 10^{-1}$$

$$c = -8.38245 \times 10^{-3}$$

$$k = a + bT^{1/2} + cT$$

### E.2 Specific heat, $c_p$ ( $J/kgK$ )

$$a = 3.80507 \times 10^6$$

$$b = -1.02808 \times 10^6$$

$$c = 1.11160 \times 10^5$$

$$d = -6.00526 \times 10^3$$

$$e = 1.62081 \times 10^2$$

$$f = -1.7482$$

$$c_p = a + bT^{1/2} + cT + dT^{3/2} + eT^2 + fT^{5/2}$$

### **E.3 Density, $\rho$ ( $kg/m^3$ )**

$$a = -3.42584 \times 10^2$$

$$b = 1.64103 \times 10^2$$

$$c = -5.01225$$

$$\rho = a + bT^{1/2} + cT$$

### **E.4 Dynamic viscosity, $\mu$ ( $Pa.s$ )**

$$a = 3.16371 \times 10^1$$

$$b = -6.37804$$

$$c = 4.85827 \times 10^{-1}$$

$$d = -1.65190 \times 10^{-2}$$

$$e = 2.11278 \times 10^{-4}$$

$$\mu^{1/3} = a + bT^{1/2} + cT + dT^{3/2} + eT^2$$

### **E.5 Saturation temperature, $T_{sat}$ ( $^{\circ}C$ )**

A correlation for the saturation temperature as a function of the pressure was obtained from the tabulated data shown in Table E.1.

$$a = 4.63501 \times 10^1$$

$$b = 2.78155 \times 10^{-1}$$

$$T_{sat} = aP^b$$

In this correlation, the pressure  $P$  is in *psia* and the saturation temperature  $T_{sat}$  in degree Celsius,  $^{\circ}C$ . This correlation is valid for a range of pressure between 2.6 and 174 *psia*. These units were more convenient for the pressure transducers and data acquisition program.

Table E.1: Saturation temperature vs pressure (Babcock and Wilcox, 1992)

<i>Pressure, MPa</i>	<i>T<sub>sat</sub>, K</i>	<i>Pressure MPa</i>	<i>T<sub>sat</sub>, K</i>
0.0180	330.96	0.1600	386.47
0.0200	333.22	0.1800	390.09
0.0250	338.12	0.2000	393.38
0.0300	342.26	0.2500	400.59
0.0400	349.02	0.3000	406.70
0.0500	354.48	0.4000	416.78
0.0600	359.09	0.5000	425.01
0.0800	366.65	0.6000	432.00
0.1000	372.78	0.8000	443.59
0.1013	373.14	1.0000	453.06
0.1200	377.96	1.2000	461.14
0.1400	382.46		

## E.6 Liquid, $h_f$ and vapor, $h_g$ enthalpy and latent heat of vaporization, $h_{fg}$ ( $kJ/kg$ )

The following correlations for the enthalpy of the water in liquid and vapor phase, and the latent heat of vaporization were obtained from the tabulated data shown in Table E.2. In these correlations the temperature  $T$  is in  $^{\circ}C$  and the enthalpy and latent heat of vaporization is in  $kJ/kg$ . The valid range for these correlations is for  $16 \leq T \leq 188^{\circ}C$ .

- Enthalpy of liquid

$$a = 5.18384 \times 10^{-4}$$

$$b = 4.13514$$

$$c = 8.33566 \times 10^{-1}$$

$$h_f = aT^2 + bT + c$$

- Enthalpy of vapor

$$a = -3.30874 \times 10^{-3}$$

$$b = -2.05899$$

$$c = 2.49498 \times 10^3$$

$$h_g = aT^2 + bT + c$$

- Latent heat of vaporization

$$a = -2.79036 \times 10^{-3}$$

$$b = 2.076143$$

$$c = 2.49581 \times 10^3$$

$$h_{fg} = aT^2 + bT + c \quad \text{or} \quad h_{fg} = h_g - h_f.$$



Table E.2: Enthalpy and latent heat vs temperature (Babcock and Wilcox, 1992)

<i>Temperature, °C</i>	<i><math>h_f</math>, kJ/kg</i>	<i><math>h_g</math>, kJ/kg</i>	<i><math>h_{fg}</math>, kJ/kg</i>
15.84	65.5	2530.0	2464.5
17.50	72.4	2533.0	2460.6
21.08	87.5	2539.6	2452.1
24.08	100.1	2545.1	2445.0
28.97	120.7	2553.9	2433.2
32.88	137.2	2561.0	2423.8
36.16	151.0	2566.6	2415.6
41.51	173.7	2576.5	2402.8
45.81	191.8	2584.2	2392.4
49.42	207.1	2590.6	2383.5
52.55	220.3	2596.1	2375.8
55.32	231.9	2601.0	2369.1
57.81	242.4	2605.3	2362.9
60.07	251.9	2609.3	2357.4
64.97	272.6	2617.7	2345.1
69.11	289.9	2624.8	2334.9
75.87	318.3	2636.3	2318.0
81.33	341.3	2645.4	2304.1
85.94	360.6	2653.0	2292.4
93.50	392.3	2665.3	2273.0
99.63	418.0	2675.0	2257.0
99.99	419.5	2675.6	2256.1

Table E.2 Enthalpy and latent heat vs temperature (Babcock and Wilcox, 1992)  
(cont)

<i>Temperature, °C</i>	<i><math>h_f</math>, kJ/kg</i>	<i><math>h_g</math>, kJ/kg</i>	<i><math>h_{fg}</math>, kJ/kg</i>
104.81	439.7	2683.1	2243.4
109.31	458.6	2690.0	2231.4
113.32	475.5	2696.0	2220.5
116.94	490.8	2701.4	2210.6
120.23	504.7	2706.2	2201.5
127.44	535.2	2716.5	2181.3
133.55	561.2	2724.9	2163.7
143.63	604.3	2738.1	2133.8
151.86	639.8	2748.2	2108.4
158.85	670.1	2756.4	2086.3
170.44	720.7	2768.7	2048.0
179.91	762.5	2777.6	2015.1
187.99	798.5	2784.4	1985.9

# Appendix F

## Heat Loss Correlations for Microevaporators

In this appendix, the correlations for the heat loss from the test section as a function of the channel wall temperature are shown.

## F.1 Microchannel

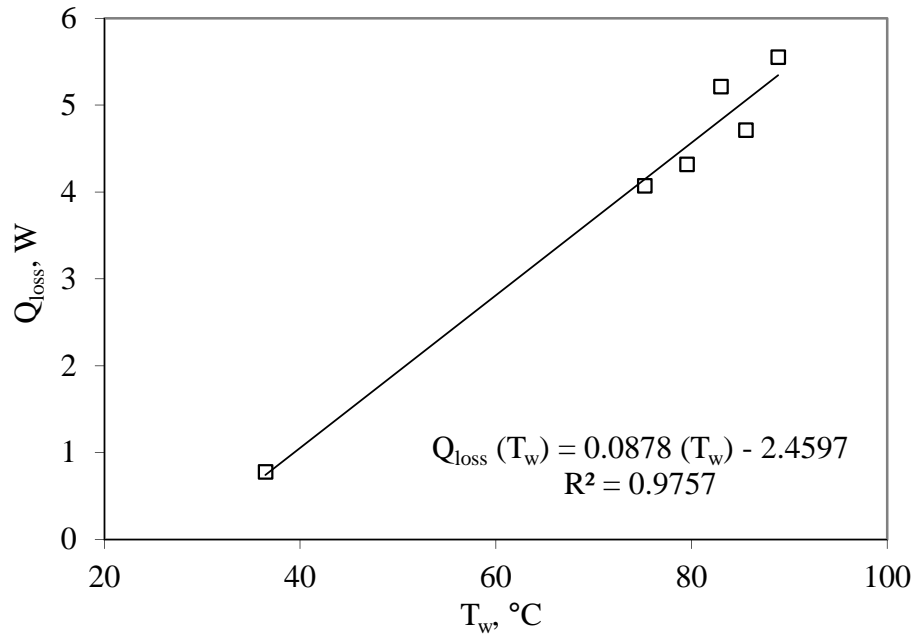


Figure F.1: Heat losses vs channel wall temperature, 1 ml/min ( $G \approx 350 \text{ kg/m}^2\text{s}$ )

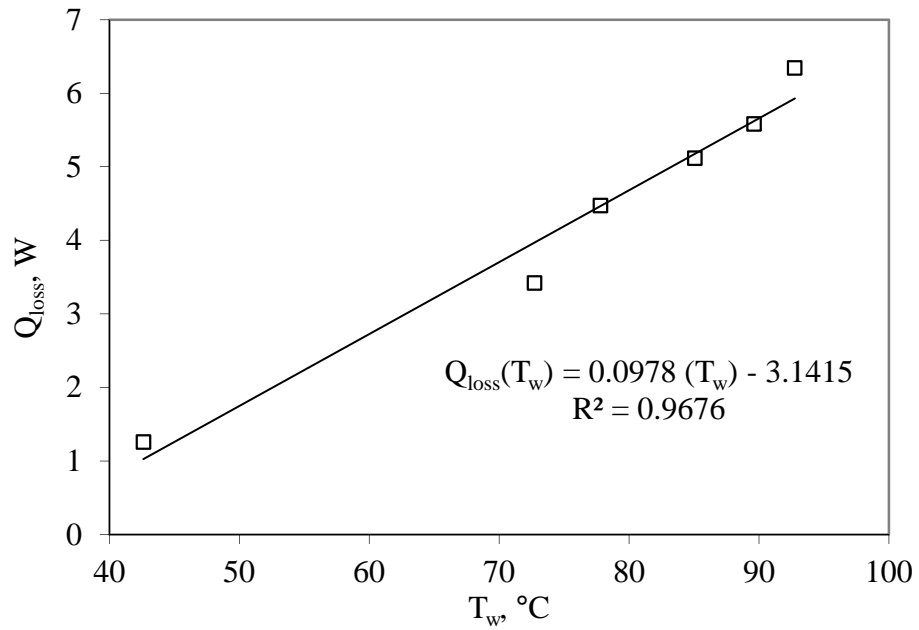


Figure F.2: Heat losses vs channel wall temperature, 2 ml/min ( $G \approx 700 \text{ kg/m}^2\text{s}$ )

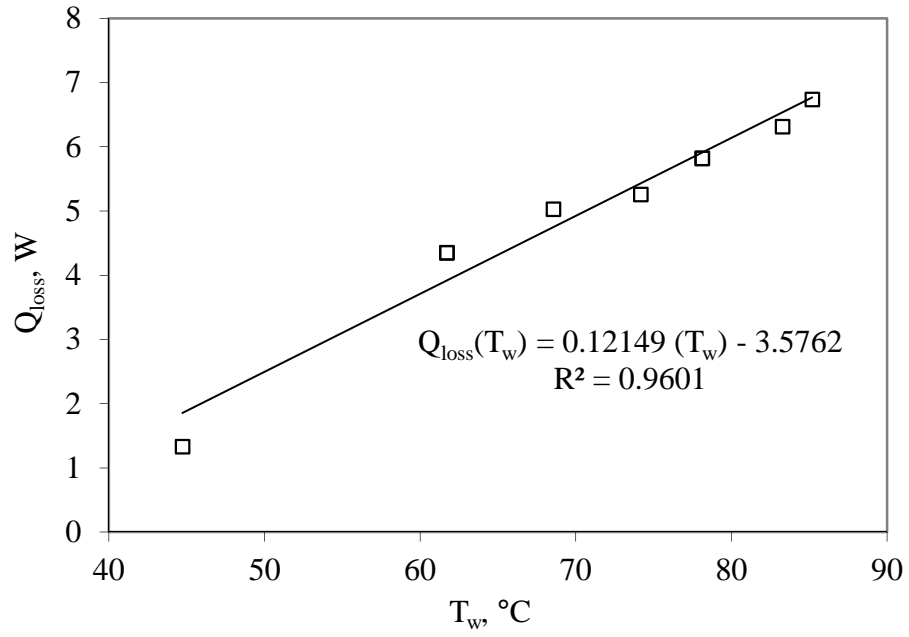


Figure F.3: Heat losses vs channel wall temperature, 3 ml/min ( $G \approx 1050 \text{ kg/m}^2\text{s}$ )

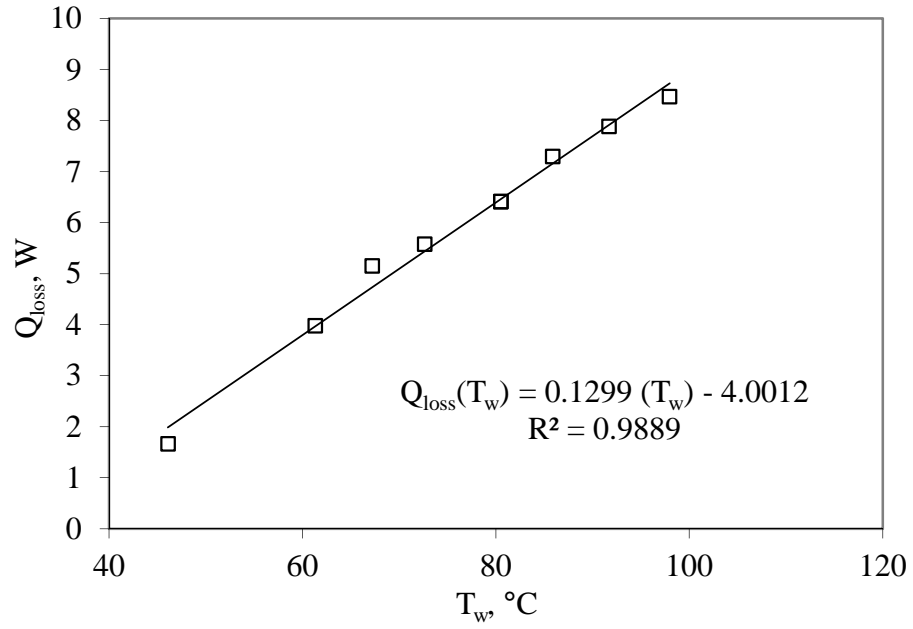


Figure F.4: Heat losses vs channel wall temperature, 3.8 ml/min ( $G \approx 1300 \text{ kg/m}^2\text{s}$ )

## F.2 Minichannel

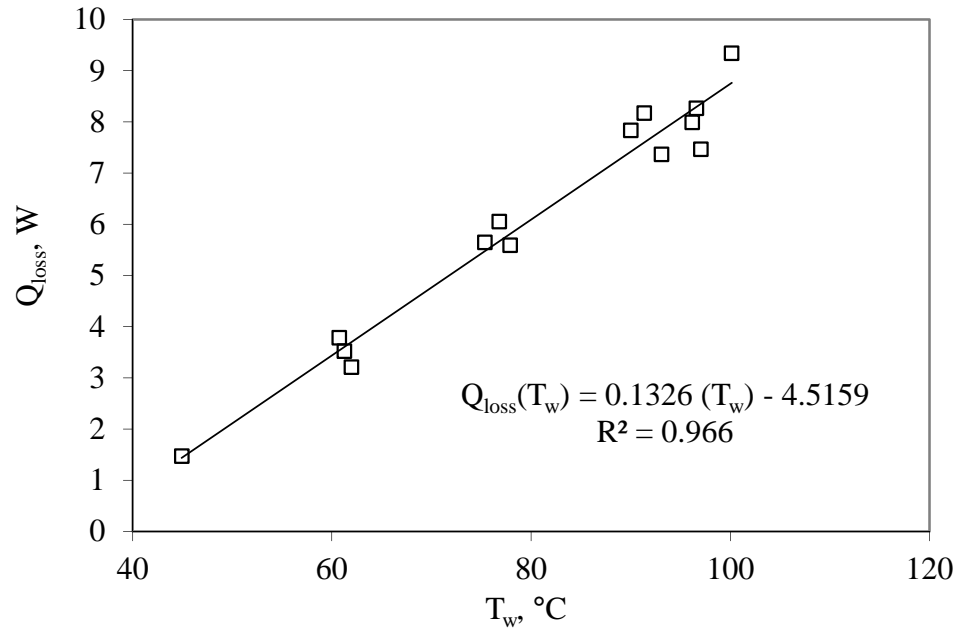


Figure F.5: Heat losses vs channel wall temperature, 4 ml/min ( $G \approx 350 \text{ kg/m}^2\text{s}$ )

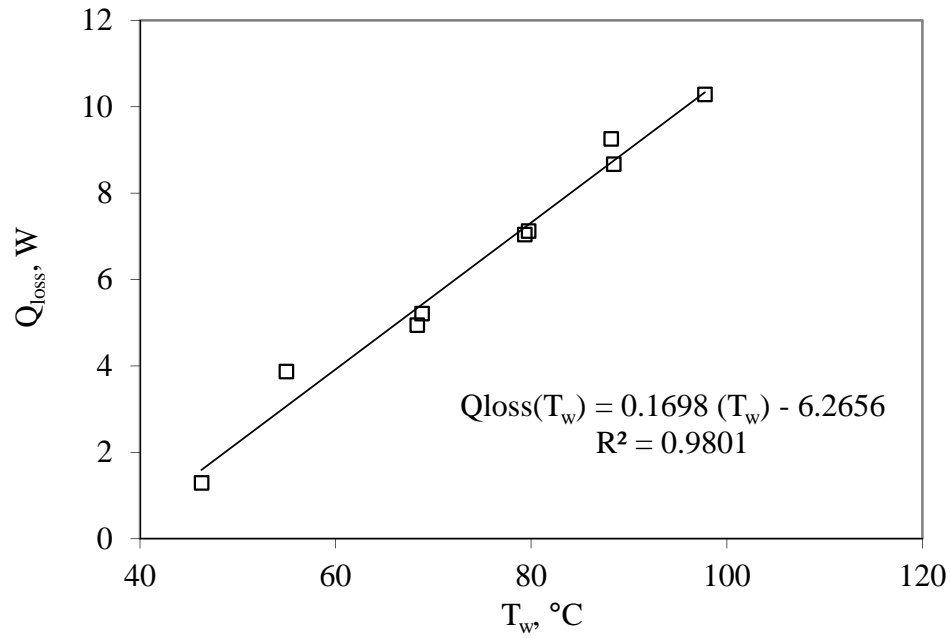


Figure F.6: Heat losses vs channel wall temperature, 8 ml/min ( $G \approx 700 \text{ kg/m}^2\text{s}$ )

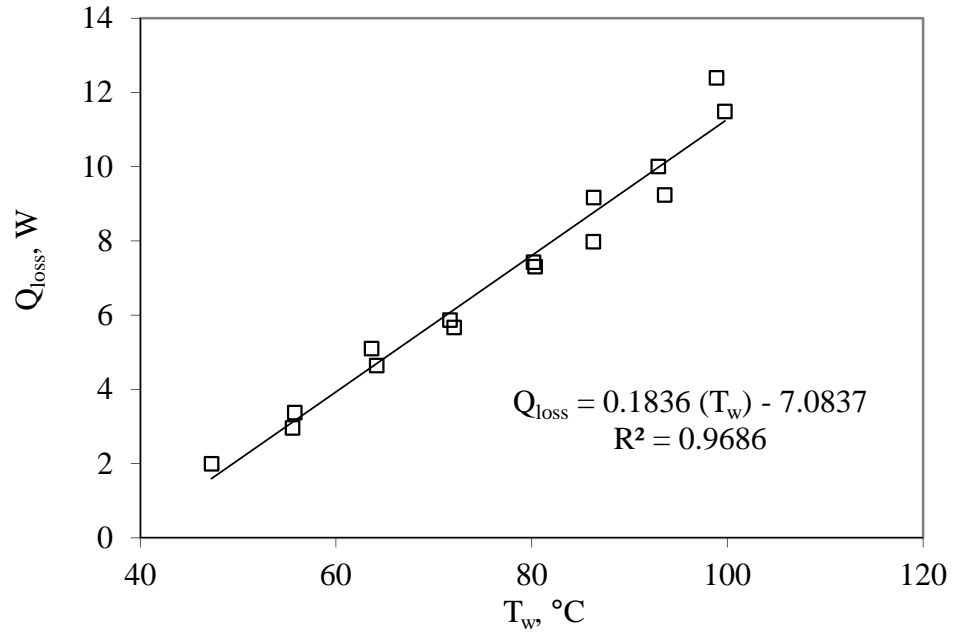


Figure F.7: Heat losses vs channel wall temperature, 12 ml/min ( $G \approx 1050 \text{ kg/m}^2\text{s}$ )

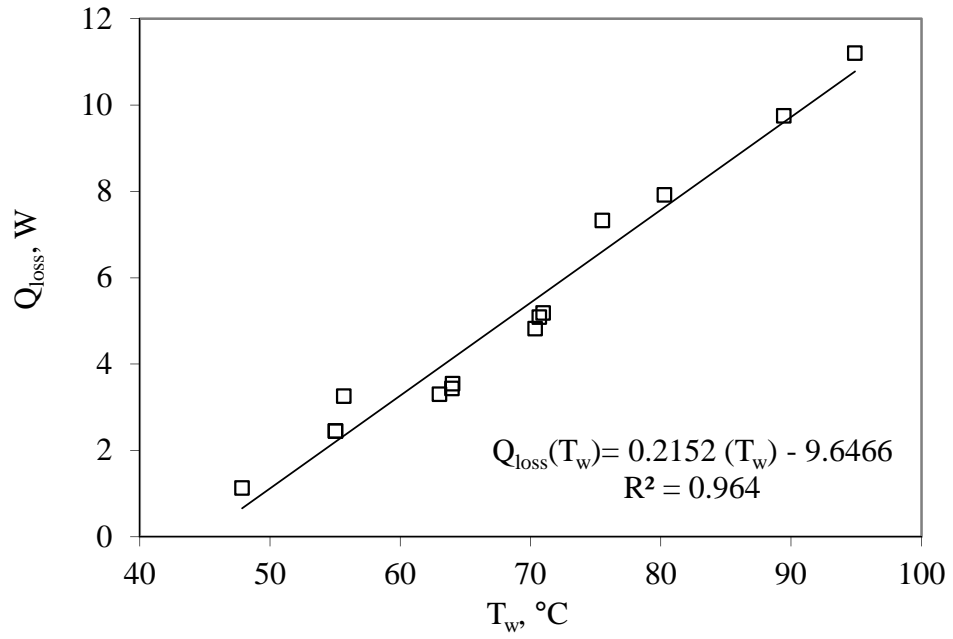


Figure F.8: Heat losses vs channel wall temperature, 15 ml/min ( $G \approx 1300 \text{ kg/m}^2\text{s}$ )

# Appendix G

## Experimental Data

### G.1 Single-phase friction factor for $198 \times 241 \mu m$ microchannel after pressure drop correction



Table G.1: Results for single-phase friction factor

<i>Mass flux, <math>\text{kg/m}^2 \text{ s}</math></i>	<i>Re</i>	<i>Pressure drop, kPa</i>	<i>f</i>	<i>Uncertainty, <math>\delta f/f</math></i>
348	85	3.6	0.147	0.28
696	167	8.3	0.085	0.19
1043	251	12.6	0.057	0.17
1391	335	16.1	0.041	0.17
1739	419	21.2	0.035	0.16
2087	503	25.5	0.029	0.16
2434	588	30.4	0.025	0.16
2782	686	33.5	0.021	0.16
3130	758	40.4	0.020	0.16
3130	759	39.8	0.020	0.16
3478	843	45.6	0.019	0.16
3825	928	50.9	0.017	0.16
4173	1013	55.2	0.016	0.16
4521	1098	61.2	0.015	0.16
4869	1183	68.7	0.014	0.16
5216	1268	75.2	0.014	0.16
5564	1353	81.1	0.013	0.17
5912	1440	89.1	0.013	0.17
6260	1525	95.2	0.012	0.17
5949	1521	93.2	0.013	0.17
6288	1608	103.1	0.013	0.17
6776	1730	117.1	0.013	0.17
6763	1724	117.8	0.013	0.17
7396	1826	134.4	0.012	0.17
7387	1880	134.6	0.012	0.17
8030	1996	151.9	0.012	0.16
8348	2074	172.0	0.012	0.16
8742	2182	178.1	0.012	0.16
9024	2257	188.0	0.011	0.16
9154	2294	197.6	0.012	0.16

Table G.1: Results for single-phase friction factor (cont)

<i>Mass flux, kg/m<sup>2</sup> s</i>	<i>Re</i>	<i>Pressure drop, kPa</i>	<i>f</i>	<i>Uncertainty, <math>\delta f/f</math></i>
9642	2420	214.7	0.011	0.16
10158	2550	236.9	0.011	0.16
9769	2452	219.5	0.011	0.16
9238	2315	205.2	0.012	0.16
4883	1240	66.5	0.014	0.16
5261	1332	75.7	0.014	0.17
5622	1421	88.7	0.014	0.17
6259	1580	109.8	0.014	0.17
7156	1807	132.9	0.013	0.17
6707	1694	123.3	0.014	0.17
7604	1923	144.2	0.012	0.17
7823	1980	149.8	0.012	0.16
8059	2040	167.1	0.013	0.16
8364	2118	175.5	0.012	0.16
8744	2216	188.7	0.012	0.16
8877	2250	190.2	0.012	0.16
9078	2304	194.4	0.012	0.16
9570	2433	209.9	0.011	0.16
9164	2334	195.6	0.012	0.16
5659	1445	82.2	0.013	0.17
5213	1333	71.2	0.013	0.16
4866	1241	65.7	0.014	0.16
4518	1152	58.4	0.014	0.16
4171	1063	54.0	0.015	0.16
3823	975	48.4	0.016	0.16
3477	861	42.0	0.017	0.16
3129	785	39.1	0.020	0.16
2781	708	33.8	0.022	0.16
2433	630	29.2	0.024	0.16
2260	557	26.6	0.026	0.16

Table G.1: Results for single-phase friction factor (cont)

<i>Mass flux, <math>\text{kg/m}^2 \text{ s}</math></i>	<i>Re</i>	<i>Pressure drop, kPa</i>	<i>f</i>	<i>Uncertainty, <math>\delta f/f</math></i>
1912	471	22.1	0.030	0.16
1565	385	18.4	0.037	0.17
1217	300	14.2	0.047	0.17
869	214	10.1	0.066	0.18
522	128	6.3	0.115	0.20
243	60	3.2	0.266	0.30

## G.2 Average Nusselt numbers for $198 \times 241 \mu\text{m}$ microchannel (isothermal boundary condition)

The experimental Nusselt numbers in Figure 4.9 correspond to Reynolds numbers between 190 and 2660 and Prandtl numbers between 3.8 and 5. However, the results in this table are for  $Re = 198$  and  $Pr = 3.8$  since a wide range of the experimental Graetz number is covered with this condition.

Table G.2: Results for Nusselt number for single-phase ( $Re = 198$ ,  $Pr = 3.8$ )

$\sqrt{Gz^{-1}}$	$\overline{Nu}$	Uncertainty, $\delta Nu/Nu$
0.08	47.7	0.29
0.10	32.1	0.20
0.11	24.3	0.15
0.13	19.7	0.12
0.14	16.6	0.11
0.15	14.4	0.10
0.16	12.7	0.09
0.17	11.4	0.08
0.18	10.4	0.08
0.19	9.6	0.07
0.20	8.9	0.07
0.20	8.3	0.07
0.21	7.8	0.07
0.22	7.4	0.07
0.23	7.0	0.06
0.23	6.7	0.06
0.24	6.4	0.06
0.25	6.2	0.06
0.25	5.9	0.06
0.26	5.8	0.06
0.26	5.6	0.06
0.27	5.4	0.06
0.28	5.3	0.06
0.28	5.2	0.06
0.29	5.0	0.06
0.29	4.9	0.06
0.30	4.9	0.06
0.30	4.8	0.06
0.31	4.7	0.06
0.31	4.7	0.06

Table G.2: Results for Nusselt number for single-phase ( $Re = 198$ ,  $Pr = 3.8$ ) (cont)

$\sqrt{Gz^{-1}}$	$\overline{Nu}$	Uncertainty, $\delta Nu/Nu$
0.32	4.6	0.06
0.32	4.6	0.06
0.33	4.6	0.06
0.33	4.5	0.06
0.34	4.5	0.06
0.34	4.5	0.06
0.35	4.6	0.06
0.35	4.6	0.06
0.36	4.6	0.06
0.36	4.7	0.06
0.37	4.8	0.06
0.37	4.8	0.06
0.37	4.9	0.06

### G.3 Vapor and liquid slug positions and lengths

Table G.3: Slug position microchannel  $198 \times 241 \mu m$  (10 watts, 1  $ml/min$ , video capture 20000  $fps$ )

$x_{o,t}, \mu m$	$x_{L, \Delta t}, \mu m$	Frame	Length, $\mu m$	Time, $\mu s$
0.0	309.7	92781	309.7	0.0
189.3	533.4	92791	344.1	0.5
387.1	791.5	92801	404.4	1.0
559.2	1041.0	92811	481.8	1.5
731.2	1299.1	92821	567.9	2.0
877.5	1574.4	92831	696.9	2.5
1041.0	1858.3	92841	817.3	3.0
1178.6	2125.0	92851	946.4	3.5
1299.1	2408.9	92861	1109.8	4.0
1436.7	2701.4	92871	1264.7	4.5
1540.0	3002.5	92881	1462.5	5.0
1634.6	3286.4	92890	1651.8	5.5

Table G.4: Slug position microchannel  $198 \times 241 \mu m$  (15 watts, 1  $ml/min$ , video capture 20000  $fps$ )

$x_{o,t}, \mu m$	$x_{L, \Delta t}, \mu m$	<i>Frame</i>	<i>Length, <math>\mu m</math></i>	<i>Time, <math>\mu s</math></i>
0.0	478.0	196200	478.0	0
111.6	653.6	196202	542.0	0.1
215.2	948.5	196204	733.3	0.2
302.9	1259.4	196206	956.5	0.3
395.5	1650.0	196208	1254.5	0.4
486.2	2136.1	196210	1649.9	0.5
613.7	2765.8	196213	2152.1	0.65

Table G.5: Slug position microchannel  $198 \times 241 \mu m$  (22.5 watts, 1  $ml/min$ , video capture 20000  $fps$ )

$x_{o,t}, \mu m$	$x_{L, \Delta t}, \mu m$	<i>Frame</i>	<i>Length, <math>\mu m</math></i>	<i>Time, <math>\mu s</math></i>
0.0	967.9	30028	967.9	0
70.1	1184.7	30029	1114.6	0.05
139.4	1370.5	30030	1231.1	0.1
216.8	1633.8	30031	1417.0	0.15
302.0	1835.1	30032	1533.1	0.2
356.0	2129.3	30033	1773.3	0.25
433.0	2446.8	30034	2013.8	0.3
472.0	2787.4	30035	2315.4	0.35

Table G.6: Slug position microchannel  $198 \times 241 \mu m$  (11 watts, 2 ml/min, video capture 20000 fps, vapor slug #1)

$x_{o,t}, \mu m$	$x_{L,\Delta t}, \mu m$	<i>Frame</i>	<i>Length, <math>\mu m</math></i>	<i>Time, <math>\mu s</math></i>
0	867.5	44083	867.5	0.0
187.6	1078.5	44088	890.9	0.3
375.1	1277.7	44093	902.6	0.5
562.7	1477.0	44098	914.3	0.8
750.2	1688.0	44103	937.8	1.0
937.8	1887.3	44108	949.5	1.3
1125.3	2098.3	44113	973.0	1.5
1312.9	2297.6	44118	984.7	1.8
1500.5	2508.6	44123	1008.1	2.0
1688.0	2707.9	44128	1019.9	2.3
1875.6	2907.1	44133	1031.5	2.5
2063.1	3118.1	44138	1055.0	2.8
2250.0	3317.0	44143	1067.0	3.0
2450.0	3516.7	44148	1066.7	3.3
2649.2	3716.0	44153	1066.8	3.5
2837.0	3927.0	44158	1090.0	3.8
3036.1	4138.0	44163	1101.9	4.0
3223.6	4337.3	44168	1113.7	4.3

Table G.7: Slug position microchannel  $198 \times 241 \mu m$  (11 watts, 2  $ml/min$ , video capture 20000  $fps$ , vapor slug #2)

$x_{o,t}, \mu m$	$x_{L, \Delta t}, \mu m$	<i>Frame</i>	<i>Length, <math>\mu m</math></i>	<i>Time, <math>\mu s</math></i>
0	890.9	44269	890.9	0.0
187.6	1101.9	44274	914.3	0.3
375.1	1312.9	44279	937.8	0.5
562.7	1523.9	44284	961.2	0.8
761.9	1723.2	44289	961.3	1.0
961.2	1934.2	44294	973.0	1.3
1172.0	2145.0	44299	973.0	1.5
1383.2	2356.1	44304	972.9	1.8
1594.2	2578.9	44309	984.7	2.0
1781.8	2789.9	44314	1008.1	2.3
1969.3	3012.6	44319	1043.3	2.5
2168.6	3223.6	44324	1055.0	2.8
2356.2	3434.6	44329	1078.4	3.0
2532.0	3645.6	44334	1113.6	3.3
2731.3	3856.6	44339	1125.3	3.5
2930.6	4079.4	44344	1148.8	3.8
3129.9	4278.6	44349	1148.7	4.0



Table G.8: Slug position microchannel  $198 \times 241 \mu m$  (11 watts, 2  $ml/min$ , video capture 20000  $fps$ , vapor slug #3)

$x_{o,t}, \mu m$	$x_{L, \Delta t}, \mu m$	<i>Frame</i>	<i>Length, <math>\mu m</math></i>	<i>Time, <math>\mu s</math></i>
0	1008.1	44358	1008.1	0.0
199.3	1207.4	44363	1008.1	0.3
375.1	1406.7	44368	1031.6	0.5
574.4	1617.7	44373	1043.3	0.8
762.0	1817.0	44378	1055.0	1.0
949.5	2028.0	44383	1078.5	1.3
1148.8	2227.4	44388	1078.6	1.5
1336.3	2438.2	44393	1101.9	1.8
1523.9	2637.5	44398	1113.6	2.0
1711.5	2848.5	44403	1137.0	2.3
1910.7	3059.5	44408	1148.8	2.5
2110.0	3270.5	44413	1160.5	2.8
2297.5	3493.2	44418	1195.7	3.0
2508.6	3704.2	44423	1195.6	3.3
2719.6	3950.4	44428	1230.8	3.5
2942.3	4173.1	44433	1230.8	3.8
3141.6	4407.6	44438	1266.0	4.0

Table G.9: Slug position microchannel  $198 \times 241 \mu m$  (11 watts, 2  $ml/min$ , video capture 20000  $fps$ , vapor slug #4)

$x_{o,t}, \mu m$	$x_{L,\Delta t}, \mu m$	<i>Frame</i>	<i>Length, <math>\mu m</math></i>	<i>Time, <math>\mu s</math></i>
0	1734.9	44440	1734.9	0.0
187.6	1957.6	44445	1770.0	0.3
375.1	2156.9	44450	1781.8	0.5
562.7	2379.6	44455	1816.9	0.8
750.2	2590.6	44460	1840.4	1.0
937.8	2801.6	44465	1863.8	1.3
1125.3	3012.6	44470	1887.3	1.5
1324.6	3223.6	44475	1899.0	1.8
1512.1	3434.6	44480	1922.5	2.0
1711.5	3645.6	44485	1934.1	2.3
1899.0	3856.6	44490	1957.6	2.5
2086.6	4079.6	44495	1993.0	2.8
2285.8	4290.4	44500	2004.6	3.0
2450.0	4454.5	44504	2004.5	3.2

Table G.10: Slug position microchannel  $198 \times 241 \mu m$  (12 watts, 2  $ml/min$ , video capture 20000  $fps$ )

$x_{o,t}, \mu m$	$x_{L,\Delta t}, \mu m$	<i>Frame</i>	<i>Length, <math>\mu m</math></i>	<i>Time, <math>\mu s</math></i>
0	892.2	166124	892.2	0.0
188.5	1093.3	166129	904.8	0.3
402.1	1319.5	166134	917.4	0.5
590.0	1520.5	166139	930.5	0.8
779.0	1721.0	166144	942.0	1.0
967.6	1935.2	166149	967.6	1.3
1168.0	2136.0	166154	968.0	1.5
1357.0	2350.0	166159	993.0	1.8
1558.0	2563.6	166164	1005.6	2.0
1784.4	2777.2	166169	992.8	2.3
1985.0	2990.8	166174	1005.8	2.5
2186.0	3217.0	166179	1031.0	2.8
2375.0	3443.0	166184	1068.0	3.0
2576.0	3644.0	166189	1068.0	3.3
2777.2	3857.9	166194	1080.7	3.5
2965.7	4059.0	166199	1093.3	3.8
3166.8	4285.2	166204	1118.4	4.0
3367.8	4486.2	166209	1118.4	4.3

## G.4 Bubble diameter

Table G.11: Bubble diameter microchannel  $198 \times 241 \mu m$

<i>Flow rate, ml/min</i>	<i>Heat, W</i>	<i>Bubble diameter, <math>\mu m</math></i>
1	10	230
	15	73
	20	65
2	10.5	96.7
	15	72.5
	20	71
	35	41
	40	39
3	12	61
	15	41
	19	31
	20	30
	26	20
3.8	17	40
	18	48
	19	39
	22	41
	24	31
	26	41
	30	43
	40	30

## G.5 Number of active cavities

Table G.12: Active cavities microchannel  $198 \times 241 \mu m$

<i>Flow rate, ml/min</i>	<i>Heat, W</i>	<i>Number of active cavities</i>
1	6	2
	7	3
	10	5
	10	7
2	10.5	1
	20	1
	25	1
	30	1
	35	2
	40	5
3	26	2
	35	2
	40	3
3.8	40	3
	45	4

## G.6 Two-phase flow pressure drop and channel wall temperature

Table G.13: Pressure drop microchannel  $198 \times 241 \mu m$ , mass flux  $G \simeq 340 \text{ kg/m}^2\text{s}$

<i>Heat flux, <math>\text{kW/m}^2</math></i>	<i>Channel wall temperature, <math>^{\circ}\text{C}</math></i>	<i>Pressure drop, kPa</i>	
		<i>kPa</i>	<i>psi</i>
63	75.3	2.7	0.4
69	79.6	2.5	0.4
80	85.6	2.4	0.3
95	83.0	2.7	0.4
110	88.9	2.5	0.4
120	94.4	2.5	0.4
200	99.0	3.3	0.5
264	99.7	3.8	0.6
401	101.7	6.3	0.9
604	103.3	10.1	1.5
740	104.1	10.1	1.5
947	105.5	13.7	2.0
946	105.6	13.9	2.0
1116	107.2	18.1	2.6
1238	115.9	32.7	4.7
1241	115.5	39.4	5.7
1242	131.2	32.4	4.7

Table G.14: Pressure drop microchannel  $198 \times 241 \mu m$ , mass flux  $G \simeq 680 \text{ kg/m}^2 s$

<i>Heat flux, <math>\text{kW/m}^2</math></i>	<i>Channel wall temperature, <math>^\circ\text{C}</math></i>	<i>Pressure drop, kPa</i>	
		<i>kPa</i>	<i>psi</i>
76	72.7	5.8	0.8
147	77.8	5.6	0.8
207	85.1	5.5	0.8
244	89.6	5.3	0.8
295	92.7	5.4	0.8
312	95.0	5.3	0.8
338	97.1	5.3	0.8
397	98.3	5.1	0.7
488	100.5	6.6	1.0
593	101.3	7.2	1.0
592	101.5	7.5	1.1
590	101.7	7.7	1.1
727	102.4	9.0	1.3
725	102.7	9.5	1.4
931	104.3	12.8	1.9
931	104.3	13.1	1.9
1101	105.4	15.6	2.3
1271	106.5	18.5	2.7
1272	106.4	18.5	2.7
1479	108.0	22.8	3.3
1614	108.8	24.8	3.6
1965	110.7	33.0	4.8
2302	113.0	43.5	6.3

Table G.15: Pressure drop microchannel  $198 \times 241 \mu m$ , mass flux  $G \simeq 1024 \text{ kg/m}^2\text{s}$

<i>Heat flux, kW/m<sup>2</sup></i>	<i>Channel wall temperature, °C</i>	<i>Pressure drop, kPa</i>	
		<i>kPa</i>	<i>psi</i>
81	61.7	10.0	1.5
81	61.7	10.0	1.5
129	68.6	9.8	1.4
185	74.2	9.2	1.3
223	78.1	9.1	1.3
223	78.1	9.1	1.3
251	83.3	9.4	1.4
306	85.2	8.8	1.3
339	89.8	8.8	1.3
373	93.9	8.5	1.2
420	96.7	8.5	1.2
472	99.0	9.1	1.3
602	100.6	10.4	1.5
733	102.4	11.2	1.6
793	103.1	11.8	1.7
994	104.7	14.4	2.1
1200	106.0	18.0	2.6
1471	107.6	23.0	3.3
1823	108.8	26.8	3.9
2157	111.2	35.7	5.2
2488	114.2	48.1	7.0
2197	115.6	53.2	7.7



Table G.16: Pressure drop microchannel  $198 \times 241 \mu m$ , mass flux  $G \simeq 1296 \text{ kg/m}^2\text{s}$

<i>Heat flux, kW/m<sup>2</sup></i>	<i>Channel wall temperature, °C</i>	<i>Pressure drop, kPa</i>	
		<i>kPa</i>	<i>psi</i>
81	61.3	11.4	1.7
167	67.2	11.0	1.6
256	72.6	11.0	1.6
329	80.5	10.6	1.5
329	80.5	10.6	1.5
420	85.9	10.2	1.5
509	91.7	10.2	1.5
595	98.0	9.8	1.4
647	100.1	10.5	1.5
705	101.4	12.3	1.8
766	102.6	13.7	2.0
895	104.2	15.6	2.3
1028	105.3	17.5	2.5
1162	106.1	19.0	2.8
1437	107.6	23.4	3.4
1778	109.4	29.6	4.3
2112	112.1	39.6	5.7
2436	115.7	57.0	8.3
2764	119.0	72.8	10.6
2762	119.2	73.4	10.6

Table G.17: Pressure drop minichannel  $378 \times 471 \mu m$ , mass flux  $G \simeq 730 \text{ kg/m}^2 s$

<i>Heat flux, kW/m<sup>2</sup></i>	<i>Channel wall temperature, °C</i>	<i>Pressure drop, kPa</i>	
		<i>kPa</i>	<i>psi</i>
55	60.8	3.0	0.4
52	61.3	3.1	0.5
49	62.0	2.9	0.4
157	77.9	3.0	0.4
170	75.4	3.2	0.5
163	76.8	3.1	0.5
276	91.3	3.5	0.5
268	93.1	3.5	0.5
283	90.0	3.5	0.5
324	97.0	3.6	0.5
328	96.2	3.7	0.5
326	96.6	3.6	0.5
421	100.1	3.8	0.5
420	100.3	3.8	0.5
420	100.3	3.7	0.5
525	101.8	4.8	0.7
524	102.0	4.9	0.7
524	102.0	4.9	0.7
634	102.4	5.4	0.8
631	102.9	6.3	0.9
631	102.9	6.6	1.0
771	104.3	8.0	1.2
771	104.3	8.1	1.2
947	106.3	11.1	1.6
947	106.2	11.2	1.6
1123	108.4	14.4	2.1
1124	108.4	14.7	2.1
1301	110.3	19.1	2.8
1299	110.7	20.2	2.9
1475	112.6	24.3	3.5

Table G.17: Pressure drop minichannel  $378 \times 471 \mu m$ , mass flux  $G \simeq 730 \text{ kg/m}^2\text{s}$  (cont)

<i>Heat flux, kW/m<sup>2</sup></i>	<i>Channel wall temperature, °C</i>	<i>Pressure drop, kPa</i>	
		<i>kPa</i>	<i>psi</i>
1474	112.9	24.8	3.6
1649	113.8	27.7	4.0
1655	114.3	28.7	4.2
1833	116.0	32.5	4.7
1832	116.1	32.3	4.7
2012	117.0	37.1	5.4
2009	117.6	36.3	5.3
2011	117.1	37.4	5.4
2181	120.1	41.2	6.0
2354	123.5	50.0	7.3
2516	127.7	60.0	8.7
2683	132.8	74.7	10.8
2834	139.2	91.6	13.3
3001	143.1	102.3	14.8

Table G.18: Pressure drop minichannel  $378 \times 471 \mu m$ , mass flux  $G \simeq 1097 \text{ kg}/m^2 s$

<i>Heat flux, <math>kW/m^2</math></i>	<i>Channel wall temperature, <math>^{\circ}C</math></i>	<i>Pressure drop, kPa</i>	
		<i>kPa</i>	<i>psi</i>
71	55.6	7.8	1.1
69	55.8	7.9	1.2
204	63.6	8.0	1.2
200	64.2	8.1	1.2
334	71.6	8.3	1.2
331	72.1	8.3	1.2
458	80.4	8.2	1.2
460	80.2	8.3	1.2
604	86.3	8.3	1.2
604	86.3	8.3	1.2
745	92.9	8.2	1.2
741	93.6	7.8	1.1
890	98.9	8.2	1.2
884	99.8	8.3	1.2
1055	103.0	8.1	1.2
1054	103.1	8.1	1.2
1222	104.3	8.5	1.2
1219	104.7	8.2	1.2
1407	105.7	9.8	1.4
1406	105.9	9.2	1.3
1578	107.3	13.4	1.9
1576	107.5	13.5	2.0
1759	109.1	17.0	2.5
1760	108.9	16.6	2.4
1930	110.2	20.4	3.0
1928	110.4	20.0	2.9
2109	111.5	23.4	3.4
2107	111.8	24.0	3.5
2278	113.0	27.2	3.9

Table G.18: Pressure drop minichannel  $378 \times 471 \mu m$ , mass flux  $G \simeq 1097 \text{ kg/m}^2\text{s}$  (cont)

<i>Heat flux, kW/m<sup>2</sup></i>	<i>Channel wall temperature, °C</i>	<i>Pressure drop, kPa</i>	
		<i>kPa</i>	<i>psi</i>
2277	113.3	28.1	4.1
2456	115.0	32.4	4.7
2628	116.6	36.9	5.3
2634	116.8	37.3	5.4
2801	117.8	41.1	6.0
2797	118.4	41.7	6.0
2976	120.3	47.3	6.9
3146	123.2	55.1	8.0
3305	126.0	63.5	9.2
3479	128.8	71.7	10.4
3638	132.3	81.8	11.9
3813	134.7	87.9	12.7
3982	137.4	94.1	13.6
3984	137.0	92.4	13.4
4126	140.8	103.7	15.0
4128	140.6	99.0	14.4
4312	144.1	113.1	16.4

Table G.19: Pressure drop minichannel  $378 \times 471 \mu m$ , mass flux  $G \simeq 1373 \text{ kg/m}^2 s$

<i>Heat flux, kW/m<sup>2</sup></i>	<i>Channel wall temperature, °C</i>	<i>Pressure drop, kPa</i>	
		<i>kPa</i>	<i>psi</i>
100	55.7	10.9	1.6
105	55.0	10.9	1.6
105	55.0	10.9	1.6
219	64.0	10.9	1.6
220	64.0	10.9	1.6
228	63.0	11.2	1.6
354	70.4	10.2	1.5
352	70.7	10.1	1.5
349	71.0	10.0	1.5
499	75.5	9.0	1.3
647	80.3	9.0	1.3
760	89.4	9.1	1.3
901	94.9	9.4	1.4
1034	101.5	9.7	1.4
1193	105.2	10.4	1.5
1377	105.9	11.2	1.6
1551	106.6	11.6	1.7
1733	107.8	12.2	1.8
1904	109.1	16.1	2.3
2082	111.0	19.5	2.8
2254	112.2	23.6	3.4
2430	113.8	28.5	4.1
2594	115.5	32.6	4.7
2764	117.4	35.7	5.2
2956	118.5	40.9	5.9

Table G.19: Pressure drop minichannel  $378 \times 471 \mu m$ , mass flux  $G \simeq 1373 \text{ kg/m}^2 s$  (cont)

<i>Heat flux, <math>\text{kW/m}^2</math></i>	<i>Channel wall temperature, <math>^{\circ}\text{C}</math></i>	<i>Pressure drop, <math>\text{kPa}</math></i>	
		<i><math>\text{kPa}</math></i>	<i><math>\text{psi}</math></i>
2952	118.9	41.4	6.0
3118	121.0	47.3	6.9
3285	122.6	52.3	7.6
3457	124.9	59.4	8.6
3613	127.2	67.9	9.8
3778	129.8	76.6	11.1
3951	132.5	86.5	12.5
4107	136.0	98.1	14.2

## G.7 Heat transfer coefficient

Table G.20: HTC microchannel  $198 \times 241 \mu m$

$G, kg/m^2 s$	$Re$	$q_w, kW/m^2$	$T_w @ L/2, ^\circ C$	$T_{w, avg} ^\circ C$	$T_w - T_{sat} @ L/2, ^\circ C$	$h_{tp}, kW/m^2 K$	$x_{out}$
680	407	488	100.0	100.5	1.26	388.3	0.02
680	409	593	101.1	101.3	2.29	258.7	0.04
680	411	592	101.4	101.5	2.50	236.7	0.04
680	413	590	101.6	101.7	2.67	221.2	0.04
680	409	727	102.2	102.4	3.10	234.5	0.06
680	413	725	102.5	102.7	3.33	217.9	0.06
679	416	931	104.1	104.3	4.53	205.6	0.11
679	417	931	104.1	104.3	4.48	208.0	0.11
679	418	1101	105.1	105.4	5.21	211.1	0.14
679	419	1271	106.3	106.5	5.99	212.4	0.17
679	419	1272	106.2	106.4	5.89	215.9	0.17
679	422	1479	107.8	108.0	6.92	213.9	0.21
679	422	1614	108.6	108.8	7.51	215.0	0.24
678	427	1965	110.5	110.7	8.46	232.4	0.31
677	444	2302	112.8	113.0	9.49	242.5	0.39
1020	613	602	100.5	100.6	1.28	471.1	0.00
1020	618	733	102.3	102.4	2.95	248.1	0.02
1020	617	793	103.1	103.1	3.63	218.3	0.03
1019	620	994	104.7	104.7	4.89	203.1	0.05
1019	620	1200	105.9	106.0	5.67	211.5	0.08
1019	622	1471	107.5	107.6	6.65	221.1	0.11
1019	621	1823	108.8	108.8	7.48	243.8	0.16
1018	632	2157	111.2	111.2	8.78	245.6	0.21
1017	645	2488	114.2	114.2	10.36	240.2	0.25
1017	649	2197	115.8	115.6	11.34	193.7	0.22



Table G.21: HTC minichannel  $378 \times 471 \mu m$

$G, kg/m^2 s$	$Re$	$q_w, kW/m^2$	$T_w @ L/2, ^\circ C$	$T_{w, avg} ^\circ C$	$T_w - T_{sat} @ L/2, ^\circ C$	$h_{tp}, kW/m^2 K$	$x_{out}$
365	420	525	101.9	101.8	3.34	157.2	0.02
365	421	524	102.0	102.0	3.50	149.7	0.02
365	422	524	102.0	102.0	3.50	150.0	0.02
365	418	634	102.3	102.4	3.74	169.4	0.04
364	429	631	103.0	102.9	4.25	148.5	0.04
364	425	631	102.9	102.9	4.18	150.8	0.04
364	439	771	104.4	104.3	5.42	142.3	0.08
364	438	771	104.4	104.3	5.48	140.5	0.08
363	449	947	106.4	106.3	7.04	134.5	0.12
363	453	947	106.3	106.2	6.96	136.0	0.12
363	452	1123	108.6	108.4	8.81	127.6	0.15
363	451	1124	108.6	108.4	8.75	128.5	0.15
363	460	1301	110.4	110.3	10.07	129.2	0.19
362	466	1299	110.8	110.7	10.29	126.3	0.19
362	471	1475	112.8	112.6	11.80	124.9	0.23
362	471	1474	113.0	112.9	11.94	123.4	0.23
362	470	1649	114.0	113.8	12.54	131.5	0.26
362	471	1655	114.6	114.3	13.00	127.3	0.26
362	475	1833	116.3	116.0	14.27	128.4	0.30
362	476	1832	116.4	116.1	14.38	127.4	0.30
362	471	2012	117.3	117.0	14.77	136.2	0.33
362	476	2009	118.0	117.6	15.50	129.6	0.33
362	470	2011	117.4	117.1	14.84	135.5	0.33
363	453	2181	120.3	120.1	17.28	126.2	0.34
363	460	2354	123.7	123.5	19.63	119.9	0.38
362	470	2516	127.9	127.7	22.69	110.9	0.42
362	482	2683	132.9	132.8	26.05	103.0	0.46
361	497	2834	139.1	139.2	30.50	92.9	0.50
361	499	3001	143.2	143.1	33.56	89.4	0.53

Table G.21: HTC minichannel  $378 \times 471 \mu m$  (cont.)

$G, kg/m^2 s$	$Re$	$q_w, kW/m^2$	$T_w @ L/2, ^\circ C$	$T_{w, avg}, ^\circ C$	$T_w - T_{sat} @ L/2, ^\circ C$	$h_{tp}, kW/m^2 K$	$x_{out}$
1368	1562	1733	108.1	107.8	8.59	201.9	0.00
1367	1576	1904	109.5	109.1	9.47	201.1	0.01
1367	1586	2082	111.3	111.0	10.91	190.7	0.02
1367	1587	2254	112.5	112.2	11.54	195.3	0.03
1367	1589	2430	114.1	113.8	12.58	193.2	0.04
1366	1615	2594	115.9	115.5	13.82	187.7	0.05
1365	1627	2764	117.8	117.4	15.36	180.0	0.06
1365	1635	2956	118.9	118.5	15.90	185.9	0.07
1365	1633	2952	119.4	118.9	16.31	181.0	0.07
1364	1648	3118	121.5	121.0	17.71	176.0	0.08
1364	1658	3285	122.9	122.6	18.58	176.8	0.09
1363	1672	3457	125.2	124.9	20.09	172.0	0.11
1362	1686	3613	127.5	127.2	21.42	168.6	0.12
1361	1704	3778	130.3	129.8	23.24	162.6	0.13
1361	1712	3951	133.1	132.5	25.04	157.8	0.14
1360	1725	4107	136.5	136.0	27.23	150.8	0.15

Table G.21: HTC minichannel  $378 \times 471 \mu m$  (cont)

$G, kg/m^2 s$	$Re$	$q_w, kW/m^2$	$T_w @ L/2, ^\circ C$	$T_{w, avg}, ^\circ C$	$T_w - T_{sat} @ L/2, ^\circ C$	$h_{fp}, kW/m^2 K$	$x_{out}$
730	826	878	104.1	104.0	5.43	161.6	0.00
730	831	877	104.3	104.1	5.68	154.4	0.00
729	839	1053	105.6	105.5	6.76	155.9	0.02
729	843	1052	106.0	105.7	7.02	149.7	0.02
729	854	1229	107.9	107.7	8.59	143.1	0.04
729	851	1229	108.0	107.8	8.61	142.8	0.04
729	851	1409	108.2	108.2	8.48	166.2	0.05
729	851	1407	108.6	108.5	8.85	159.0	0.05
728	864	1581	111.1	110.9	10.75	147.1	0.07
728	866	1581	111.1	110.8	10.69	148.0	0.07
728	875	1752	113.0	112.8	12.16	144.0	0.09
728	873	1754	112.7	112.4	11.86	147.9	0.09
727	884	1926	115.3	115.0	13.74	140.2	0.11
727	889	1925	115.5	115.2	13.92	138.2	0.11
727	896	2100	116.3	116.0	14.55	144.4	0.13
726	900	2097	116.7	116.4	14.86	141.1	0.13
726	918	2278	119.0	118.6	16.36	139.2	0.16
725	921	2276	119.3	119.0	16.61	137.0	0.16
724	943	2445	121.8	121.5	18.31	133.6	0.18
725	940	2445	121.9	121.6	18.40	132.9	0.18
724	952	2612	124.0	123.7	19.82	131.8	0.20
724	948	2616	123.6	123.3	19.58	133.6	0.20
723	969	2770	128.9	128.9	23.51	117.8	0.22
723	964	2765	128.1	128.2	22.85	121.0	0.22
723	965	2773	128.7	128.5	23.19	119.6	0.22

Table G.21: HTC minichannel  $378 \times 471 \mu m$  (cont.)

$G, kg/m^2 s$	$Re$	$q_w, kW/m^2$	$T_w @ L/2, ^\circ C$	$T_{w, avg}, ^\circ C$	$T_w - T_{sat} @ L/2, ^\circ C$	$h_{tp}, kW/m^2 K$	$x_{out}$
1095	1245	1407	106.1	105.7	6.87	204.9	0.01
1094	1249	1406	106.2	105.9	7.11	197.7	0.01
1094	1268	1578	107.5	107.3	7.86	200.7	0.02
1093	1272	1576	107.8	107.5	8.13	194.0	0.02
1093	1278	1759	109.3	109.1	9.18	191.7	0.04
1093	1276	1760	109.0	108.9	8.98	196.0	0.04
1093	1286	1930	110.4	110.2	9.90	194.9	0.05
1093	1288	1928	110.7	110.4	10.18	189.4	0.05
1092	1292	2109	111.7	111.5	10.82	194.9	0.06
1092	1297	2107	112.0	111.8	11.06	190.6	0.06
1092	1301	2278	113.2	113.0	11.82	192.8	0.07
1092	1307	2277	113.5	113.3	12.00	189.7	0.07
1092	1310	2456	115.4	115.0	13.35	183.9	0.08
1091	1318	2628	116.9	116.6	14.32	183.5	0.09
1091	1319	2634	117.1	116.8	14.53	181.3	0.09
1091	1328	2801	117.9	117.8	14.88	188.2	0.11
1091	1325	2797	118.6	118.4	15.50	180.4	0.11
1090	1338	2976	120.5	120.3	16.73	177.9	0.12
1089	1361	3146	123.4	123.2	18.72	168.1	0.14
1088	1382	3305	126.1	126.0	20.53	161.0	0.15
1087	1400	3479	129.0	128.8	22.48	154.8	0.16
1087	1413	3638	132.3	132.3	24.71	147.2	0.18
1087	1415	3813	134.9	134.7	26.72	142.7	0.19
1087	1408	3982	137.6	137.4	28.71	138.7	0.20
1087	1409	3984	137.3	137.0	28.58	139.4	0.20
1087	1417	4126	141.0	140.8	31.16	132.4	0.21
1087	1399	4128	140.7	140.6	31.38	131.5	0.20
1085	1441	4312	144.2	144.1	33.46	128.9	0.23